Controlled Illumination
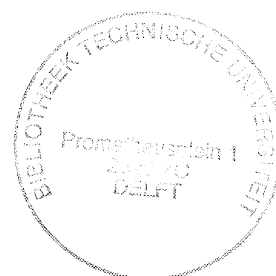# in
Prestack Seismic Migration

PROEFSCHRIFT

ter verkrijging van de graad van doctor
aan de Technische Universiteit Delft,
op gezag van de Rector Magnificus,
Prof. ir. K.F. Wakker
in het openbaar te verdedigen
ten overstaan van een commissie,
door het College van Dekanen aangewezen,
op dinsdag 21 februari 1995 te 16.00 uur
door

Walter Eduard Antonius RIETVELD

natuurkundig ingenieur

geboren te Rotterdam

Dit proefschrift is goedgekeurd door de promotor:

Prof. dr. ir. A. J. Berkhout

voor Suzanne

Preface

The research that forms the basis of this thesis has been carried out at the Laboratory of Seismics and Acoustics at the faculty of Applied Physics of the Delft University of Technology im the Netherlands.

This research started in March 1989 as part of the DELPHI (DELft PHilosophy on Inversion) consortium. I wish to thank the participating companies for making this research possible and for all the interest and comments they gave at sponsormeetings.

First of all I would like to thank my promotor professor Berkhout. The many ideas and discussions we had at any time of day were an ever stimulating environment to work in.

Also I wish to thank Kees Wapenaar. Apart from all the support on the everyday questions and foottraps a 'promovendus' encounters, his theoretical pushes-in-the-back to get everything right and his careful and endless proofreading, I will remember the personal contacts best, including 'de kleine Jodeljongen'.

For the moral, social, computer and geophysical support as one-of-the-boys first and later on as associate project leader, I wish to thank Eric Verschuur. I will never be able to look at a brown sweater without a smile on my face.

In modern geophysics it is almost impossible to come along without using computers. This is the appropriate place to thank the people in the group who try keep them running and keep back-ups of everything, including this thesis: Leen Buitelaar, Edo Bergsma and Henry de Bok. A special word of thanks I owe to Leen, who was always kind enough to get me some extra diskspace, without asking what happened to the other giga-bytes I had already occupied.

Special thanks to Jan-Willem de Bruijn who helped me in everything that has to do with software. I have maybe found one problem he could not solve, but I have forgotten which one it was ....

Working within the DELPHI consortium means working in a team. Here I wish to thank all my former colleagues: Niels Kinneging, Gerrit Blacquière, Henk Cox, Greg Haimé, Philippe Herrmann, Alex Geerlings, Gerd-Jan Lörtzer, Johan de Haas and Cees de Bruin. They got me on the road and helped me on the road in a nice environment.

I wish to apologize to all my current colleagues: Erwin Giling, Felix Herrmann, Riaz Alá'i, Nurul Kabir, Jan Thorbecke, Alexander Koek , Aart-Jan van Wijngaarden and Frank Dessing for keeping up with all the noise I produce and for all the times I was 'waltering' around thinking how to fix another unbelievable bug in my software. I also want to thank them for the time I had with them in Delft and at all the congresses we have attended together.

Thanks to Alexander Koek, Gerrit van Dijk and Gerard Faber, who have put a lot of effort to get the watertank measument facility up-and-running and got me the 3-D data I wanted (just) in time.

I wish to thank Paul Scholte for helping me designing the cover. It is nice to see an idea brought to life and improved. Also thanks to Peter van Hagen, for proofreading the 'Dutch' summary. After writing English for some months, the Dutch summary is probably the most underestimated part to write. It is good to have someone finding a lot of Dutch synonyms for all those English seismic terms.

All my friends are thanked for keeping me in contact with the rest of the world and get me startted every week with a 'fresh' mind. In that way they have constructively contributed to the research and the completion of this thesis, probably without knowing it.

Finally I wish to thank my parents and Paul and Irene. There is no business like home business. The silent support I got from them is modestly accepted and appreciated.

Bauke en Lotte, no problem is big enough to keep daddy's mind occupied when you are around. That helped to solve a lot of them.

Basically all credits and thanks go to Suzanne, who, if possible, would have written this thesis by herself just to help me. I could not have done this without you.

Table of contents

Introduction

1.1 Statement of the problem

The seismic method measures the response of the subsurface in space and time due to a known source wave field. In general, on land a dynamite source or a seismic vibrator is used; in the marine case an airgun source is used. The response is measured at the surface by a distribution of geophones (land) or hydrophones (marine), see Figure 1.1. In order to obtain a good quality image of the subsurface, these measurements are repeated for different source and receiver positions. The principle goal of the seismic method is to deduce from these measurements the structure of the subsurface. The transformation of the seismic *measurements* in the *space-time* domain to seismic *reflectivity* in the *space-depth* domain is called *seismic migration*.
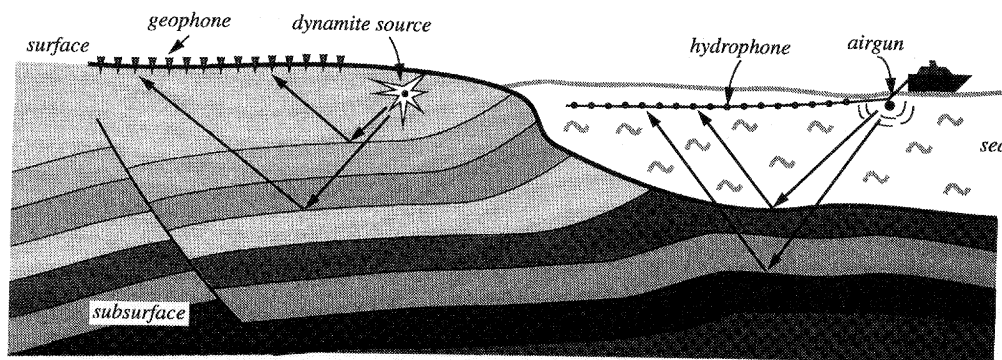
Figure 1.1 *The principle of acquisition of seismic measurements for the land case (left) and the marine case (right). Generally 240 geo-/hydrophones are used per source position. The seismic waves generated by the seismic source propagate through the subsurface, get reflected by the layer boundaries and propagate back to the surface where they are recorded by the geo-/hydrophones as a function of time.*

The transformation from surface measurements to *sub*surface structure requires knowledge of the way seismic waves propagate and reflect in the earth. This is described by *wave theory*. For *depth* migration a description of the main structures in the subsurface is also required. This description is generally referred to as the *macro model*. The way waves propagate through inhomogeneous media is a very complex process and the actual computation of a depth image from the seismic measurements is therefore a computational intensive method. Nowadays most 3-D surveys are migrated using a data-reduction method first, the so-called CMP stacking method, followed by a so-called *poststack* migration.

The goal of this thesis is to develop an efficient way to perform *prestack depth migration*.

1.2 Areal shot record technology

Since the size of the source is small compared to the average wavelength in the seismic signal, the source for one shot record is spatially considered a *point* source. As already mentioned, since, the number of shot records may amount to many thousands, the use of *prestack* migration methods is economically not yet attractive.

The method described in this thesis reduces the number of shot records that have to be processed. The reduction is obtained by *combining* shot records due to a source with a spatial extension: a so-called *areal* source. An example of an areal source is a *plane-wave* source or a *line* source. The way to combine the shot records can be seen as an example of the application of Huygens' principle, see Figure 1.2.

Since the response of such an *areal* source can still be described by the wave equation (it is still a physical experiment), wave-equation based migration algorithms can be used. As long as the number of constructed *areal* shot record is much less than the number of field shot records, the method of areal shot record migration will be a more economical approach to prestack depth migration than the conventional shot record migration scheme.

1.3 Outline of this thesis

In this thesis an efficient approach to prestack depth migration is discussed based on the use of areal shot record technology.

Chapter 2 describes the method of areal shot record synthesis. The method will be derived using the matrix notation (Berkhout, 1985). In *chapter 3* the method of controlled illumination will be introduced. This method makes it possible to construct areal sources at the surface in such a way that a specific part of the subsurface, for instance a potential reservoir, is illuminated by a prespecified source wave field, for instance a plane wave. In *chapter 4* the first application of the method of controlled illumination it is shown, i.e. the verification of the macro model used in prestack depth migration.
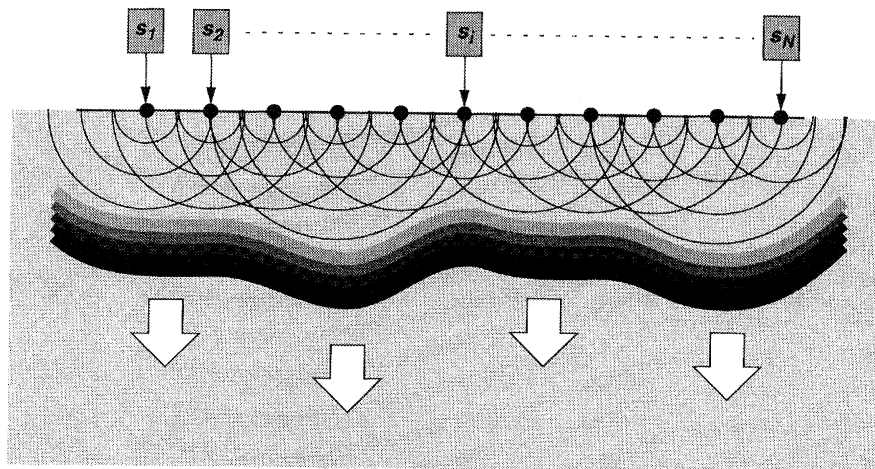
Figure 1.2 *Huygens' principle illustrated. The wave field which will propagate into the subsurface is constructed by taking the envelope over all the wave fronts of the individual point sources. The specific shape of the wave front is determined by the amplitude of the individual point sources and the time at which they start, denoted by* s_i.

In *chapter 5* the depth migration of areal shot records is discussed and illustrated on a simple synthetic example. It is shown that the migration of *areal* shot records is a generalization of the well-known *shot record* migration.

In *chapter 6* results are shown on a complex synthetic dataset (the Marmousi dataset), and on a field dataset. It is shown that the method of *areal shot record migration* in combination with the concept of *controlled illumination* provides an efficient tool to prestack depth migration. Also the concept of Fresnelzone filtering is introduced and applied to the field dataset to increase the signal-to-noise ratio in the final migrated section.

Finally, in *chapter 7* the extension to the 3-D case is discussed and illustrated on a synthetic and a watertank data set.

In *appendix A* the matrices used in the theoretical derivations are described in more detail. In *appendix B* the influence of incomplete acquisition on the amplitudes as obtained after areal shot record synthesis and migration are discussed; the notion the Fresnel zone and its implication in migration is illustrated.
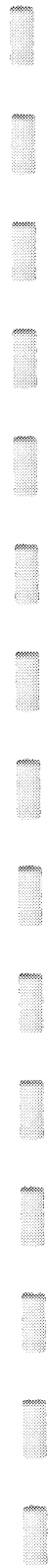
Areal shot record technology

2.1 Introduction

So far, elaborate prestack processes such as inversion and migration have always been applied to data configurations as acquired in the field, i.e. to common shot gathers, common receiver gathers, common midpoint gathers or common offset gathers. As the acquisition of seismic measurements has shifted from two-dimensional (2-D) to three-dimensional (3-D) surveys, this approach to prestack processing may not be optimum from an economic point of view. Moreover, the total amount of data obtained from 3-D surveys is so large, that *full* prestack processing in a true 3-D sense is not yet feasible, even on current supercomputers.

In this chapter an alternative to full prestack processing is presented, based on the synthesis of an *areal* source at the surface. The related synthesized response is referred to as an *areal* shot record, and can be used as input for accurate migration and/or inversion processes.

A special case of the synthesis of areal shot records is the plane-wave stacking method. In the past, several authors have published on this method. Taner (1976, 1978) as well as Schultz and Claerbout (1978) show plane-wave stacking procedures. Temme (1984) computes migrated sections using plane-wave migration. Whitmore and Garing (1990) show the use of prestack migration in the common angle domain to estimate interval velocities. Many papers have been published on the subject of slant stacking, τ-p and Radon transforms (Gardner and Lu, 1991). All of these methods construct *plane waves* at the surface. The use of *non*plane areal sources for optimum illumination of reservoirs was proposed at a DELPHI[1] sponsor meeting in 1989; research on the subject started in the second half of 1989. In 1992 the concepts of areal shot record technology (synthesis, migration) were introduced in the open literature (Berkhout, 1992) and illustrated on synthetic examples (Rietveld et al., 1992). An important feature of the

1. DELPHI is a consortium of international companies, that finances a research program at the Laboratory of Seismics and Acoustics in Delft.

proposed areal shot record technology is that the areal sources are allowed to be complex and that modifications during downward extrapolation are taken into account.

In this chapter first the forward model for seismic reflection experiments will be reviewed (the 'WRW' model), followed by a discussion on the synthesis of areal sources, and the general processing scheme for areal shot record technology.

2.2 Review of the forward model

In this section the forward model for 3-D acoustic seismic reflection measurements is briefly reviewed. For a more detailed description of this forward model, the reader is referred to Berkhout (1985, 1993) and to Wapenaar (1993) for a matrix presentation and an integral representation, respectively.

In practice, seismic measurements are always discrete in time and space. Consequently, imaging is always a discrete process and the theory should be discrete. The forward model for reflection measurements, used here, is presented as a *discrete* model as well.

For linear wave theory in a time-invariant medium, the imaging problem may be described in the temporal frequency domain without any loss of generality. Moreover, as our recording has a finite duration T we only need to consider a finite number of frequencies N per seismic trace, where

$$N = (f_{max} - f_{min})\, T, \tag{2.1}$$

$f_{max} - f_{min}$ being the temporal frequency range of interest. A typical number for N equals 250.

Taking into account the discrete property on the one hand and the allowed representation by independent frequency components on the other hand, vectors and matrices are preeminently suited for the mathematical description of the recorded seismic data. For instance, considering one shot record, one element i of the so-called measurement vector $\vec{P}^-(z_0)$ contains the complex number (defining amplitude and phase for the Fourier component under consideration) related to the recorded signal at one location $(x,y)_i$ of acquisition plane z_0 (one detector position).

Note that in the forward model as described here the propagation direction of the waves is indicated by the superscript + for downward propagation, and superscript − for upward propagation. As already mentioned, the model describes monochromatic experiments. For notation convenience the argument ω for angular frequency, is omitted. The contents of the matrices used in the forward model are described in more detail in appendix A.

If the vector $\vec{S}^+(z_0)$ represents one Fourier component of the downward travelling source wave field at the data acquisition surface z_0, then we may write:

$$\vec{S}^+(z_m) = W^+(z_m, z_0)\, \vec{S}^+(z_0), \tag{2.2}$$

where $\vec{S}^+(z_m)$ is the monochromatic downward travelling source wave field at depth level z_m and $W^+(z_m,z_0)$ represents the operator describing downward propagation from z_0 to z_m. Operator W^+ is represented by a complex-valued *matrix*, where each *column* equals one Fourier component of the response for all (x,y) at depth level z_m due to *one* specific dipole at the surface z_0. Note that for laterally homogeneous media W^+ becomes a Toeplitz matrix, i.e. the elements along any diagonal are constant.

At any depth level z_m reflection may occur. For each Fourier component reflection may be described by a general linear operator $R(z_m)$[1],

$$\vec{P}_m^-(z_m) = R(z_m)\, \vec{S}^+(z_m), \tag{2.3}$$

where $\vec{P}_m^-(z_m)$ is the monochromatic upward travelling reflected wave field at depth level z_m due to the inhomogeneities at depth level z_m only. Matrix $R(z_m)$ represents the reflection operator, where each column describes the response of a monochromatic dipole source at z_m for one specific grid point at z_m. If the reflection is *not* locally reacting, the column describes the angle dependent reflection. If there exists no angle dependence, $R(z_m)$ is a diagonal matrix with angle *in*dependent reflection coefficients.

Finally, the reflected wave field at z_m travels up to the surface,

$$\vec{P}_m^-(z_0) = W^-(z_0,z_m)\, \vec{P}_m^-(z_m), \tag{2.4}$$

where $\vec{P}_m^-(z_0)$ is one Fourier component of the reflected wave field at data acquisition surface z_0 and $W^-(z_0,z_m)$ equals the operator describing upward propagation from z_m to z_0. Each column of W^- equals one Fourier component of the response at z_0 due to one specific dipole at depth level z_m.

Equations (2.2), (2.3) and (2.4) may now be combined to one matrix equation for the reflection response (Figure 2.1):

$$\vec{P}^-(z_0) = \sum_{m=1}^{M} \vec{P}_m^-(z_0),$$

$$= [\sum_{m=1}^{M} W^-(z_0,z_m)\, R(z_m)\, W^+(z_m,z_0)]\, \vec{S}^+(z_0), \tag{2.5a}$$

or, for a continuous formulation in z,

$$\vec{P}^-(z_0) = \int_{z_0}^{\infty} [W^-(z_0,z)\, R(z)\, W^+(z,z_0)\, dz]\, \vec{S}^+(z_0). \tag{2.5b}$$

---

1. Matrix $R(z_m)$ is generally written as $R^+(z_m)$, describing the reflection properties for downward propagating wave fields. For notational convenience the superscript + is omitted.

a

b
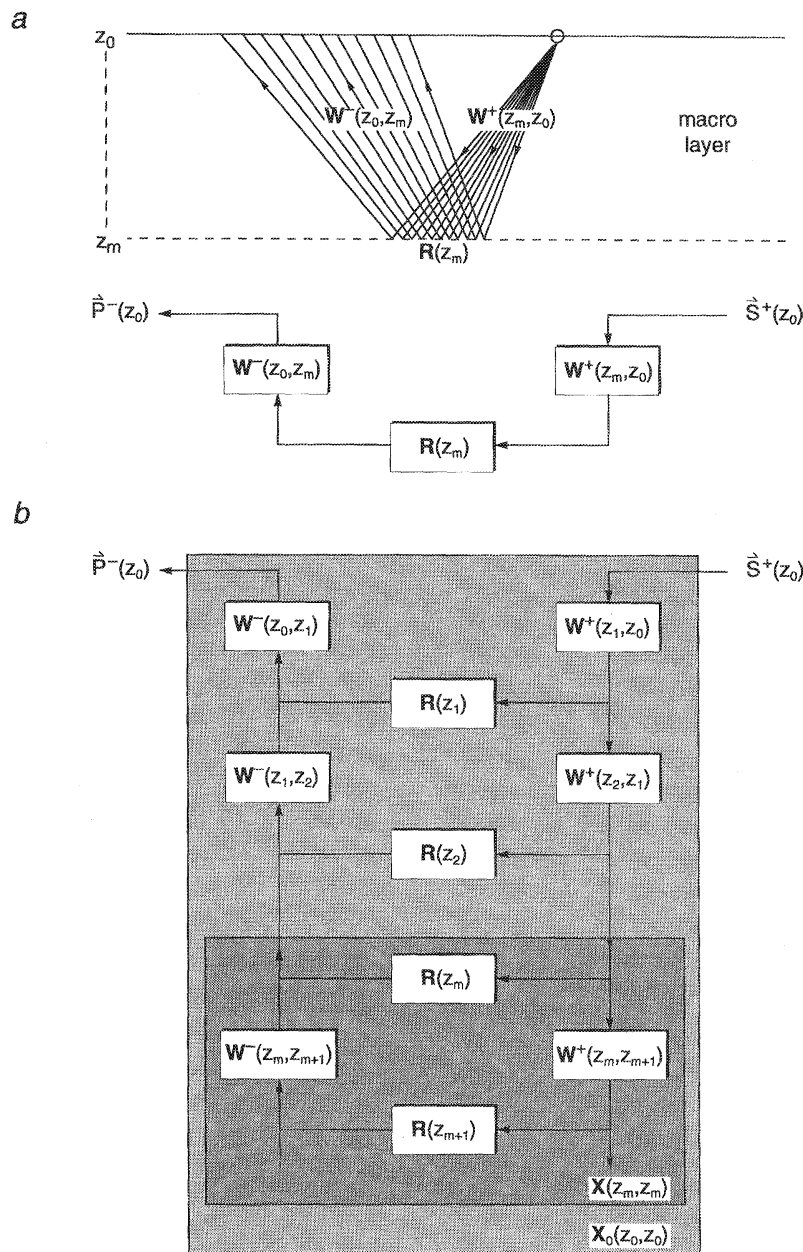
Figure 2.1 (a) *Propagation and reflection for one point source and one reflecting depth level* (z_m), *ignoring the reflectivity of the surface* (z_0);

(b) *Response at the reflection-free surface* $(z = z_0)$ *due to reflection in half space* $z \geq z_0$, *ignoring internal multiples and transmission losses. Indicated are the definitions of the pulsresponses* $X_0(z_0, z_0)$ *and* $X(z_m, z_m)$, *which includes the reflection of the depth level* z_m. *Note that in practice* z_m *does not coincide with a geological boundary.*

Equation (2.5a) may be rewritten as:

$$\vec{P}^{-}(z_0) = X_0(z_0,z_0)\ \vec{S}^{+}(z_0),\qquad\qquad\qquad\qquad (2.5c)$$

where $X_0(z_0,z_0)$ is the half-space reflection operator at depth level z_0 due to inhomogeneities at $z > z_0$. Note that $X_0(z_0,z_0)$ does *not* include the reflection of depth level z_0. The matrix element (i,j) of $X_0(z_0,z_0)$ may be considered as one Fourier component of the reflection response at position $(x,y)_i$ on surface z_0 due to a unit dipole source at position $(x,y)_j$ on the same surface z_0. For further details the reader is referred to Berkhout (1985, chapter VI).

The multi-experiment formulation of equation (2.5c) yields:

$$P^{-}(z_0) = X_0(z_0,z_0)\ S^{+}(z_0),\qquad\qquad\qquad\qquad (2.5d)$$

where one column of $S^{+}(z_0)$ defines the induced source function of one monochromatic experiment, and the related column of the measurement matrix $P^{-}(z_0)$ defines the monochromatic version of the measured signals of that experiment.

So far we have not discussed the effect of multiple scattering and the interaction of the sources and receivers with the free surface. However, in the stepwise inversion scheme, as described in the open literature by Berkhout and Wapenaar (1990), the interaction of the sources and receivers with the free surface, together with the multiples related to the free surface are removed by a surface-related preprocessing process (Verschuur et al., 1992). Therefore the simplified forward model of equation (2.5a) describes the data *after* preprocessing.

If we define the half-space reflection operator $X(z_m,z_m)$ at depth level z_m due to inhomogeneities at $z \geq z_m$ by matrix $X(z_m,z_m)$, then it follows from equation (2.5a) that we may write:

$$X(z_m,z_m) = \sum_{n\,=\,m}^{\infty} W^{-}(z_m,z_n)\ R(z_n)\ W^{+}(z_n,z_m),\qquad \text{for } m=1,2,\dots \qquad (2.6a)$$

with

$$W^{-}(z_m,z_m) = W^{+}(z_m,z_m) = I. \qquad\qquad\qquad\qquad (2.6b)$$

Note that $X(z_m,z_m)$ includes the reflection of depth level z_m.

Hence the half-space reflection operator at the surface z_0 due to the half space $z > z_0$ can be rewritten as:

$$X_0(z_0,z_0) = \sum_{i\,=\,1}^{m-1} W^{-}(z_0,z_i)\ R(z_i)\ W^{+}(z_i,z_0) +$$

$$W^{-}(z_0,z_m)\ R(z_m)\ W^{+}(z_m,z_0) +$$

$$\sum_{i\,=\,m+1}^{\infty} W^{-}(z_0,z_i)\ R(z_i)W^{+}(z_i,z_0). \qquad\qquad (2.7a)$$

The first term of equation (2.7a) describes the pulse response of the subsurface for $z < z_m$. The second term describes the pulsresponse of the reflecting level z_m. The third term describes the pulse response of the half-space $z > z_m$. Equation (2.7a) can be rewritten as:

$$X_0(z_0, z_0) = \sum_{i=1}^{m-1} W^-(z_0, z_i) \, R(z_i) \, W^+(z_i, z_0) \; +$$

$$W^-(z_0, z_m) \, X(z_m, z_m) \, W^+(z_m, z_0). \tag{2.7b}$$

In the following we will concentrate on the synthesis of areal shot records from the prestack data, as described by the forward model of equation (2.5d).

2.3 Synthesis of areal shot records

Considering the forward model as derived in the previous section, the incident wave field $\vec{S}^+(z_m)$ at depth level z_m is given by:

$$\vec{S}^+(z_m) = W^+(z_m, z_0) \, \vec{S}^+(z_0), \tag{2.8a}$$

or for a range of experiments:

$$S^+(z_m) = W^+(z_m, z_0) \, S^+(z_0). \tag{2.8b}$$

We now synthesize an areal source at the surface z_0 from the differently positioned local sources that are related to the different experiments. If $\vec{\Gamma}(z_0)$ is the complex-valued synthesis operator, the synthesized wave field at the surface z_0 equals:

$$\vec{S}^+_{syn}(z_0) = S^+(z_0) \, \vec{\Gamma}(z_0), \tag{2.9a}$$

and the incident wave field at depth level z_m due to this areal source equals:

$$\vec{S}^+_{syn}(z_m) = W^+(z_m, z_0) \, S^+(z_0) \, \vec{\Gamma}(z_0). \tag{2.9b}$$

From equation (2.5d) it follows that the resulting areal shot record is given by:

$$\vec{P}^-_{syn}(z_0) = X_0(z_0, z_0) \, \vec{S}^+_{syn}(z_0), \tag{2.10a}$$

or, using also equation (2.9a):

$$\vec{P}^-_{syn}(z_0) = P^-(z_0) \, \vec{\Gamma}(z_0). \tag{2.10b}$$

Note that if all individual sources are identical dipole sources on a regular grid, i.e.,

$$S^+(z_0) = S(\omega) \, I, \tag{2.10c}$$

where I is the unity matrix, equation (2.9a) may be simplified to:
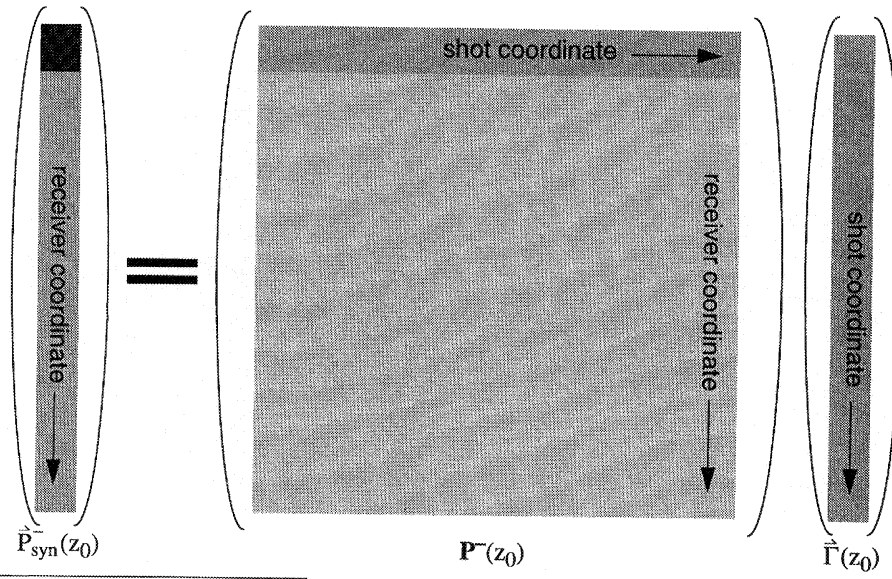
Figure 2.2   *Schematic overview of the synthesis process. Each shot position is weighted with the appropriate value of the synthesis operator, followed by a stacking in the common receiver direction, i.e. along the shot coordinate.*

$$\vec{S}^{+}_{syn}(z_0) = S(\omega)\, \vec{\Gamma}(z_0),\tag{2.10d}$$

meaning that the synthesis operator $\vec{\Gamma}(z_0)$ is the 'spike' version of the areal source $\vec{S}^{+}_{syn}(z_0)$, i.e. deconvolved for the source wavelet $S(\omega)$.

From equation (2.10b) it can be seen that at every shot position each frequency component is multiplied with the according value of the synthesis operator $\vec{\Gamma}(z_0)$ (Figure 2.2). Hence, in the time domain, the synthesis process can be explained as follows: each shot record is convolved with one trace of the synthesis operator, and subsequently, the resulting shot records are stacked per common receiver position, resulting in the areal shot record.

For the special situation of a horizontal plane wave at the surface z_0, the synthesis operator reads:

$$\vec{\Gamma}(z_0) = (1,\, 1,\, \ldots ,\, 1)^{T},\tag{2.11}$$

The synthesis operator as given by equation (2.11) is characteristic for conventional synthesis methods. For slant stack procedures the synthesis operator may be written as:

$$\vec{\Gamma}(z_0) = (e^{-j\omega p x_1},\, e^{-j\omega p x_2},\, \ldots ,\, e^{-j\omega p x_N})^{T},\tag{2.12a}$$

with the rayparameter p defined by:
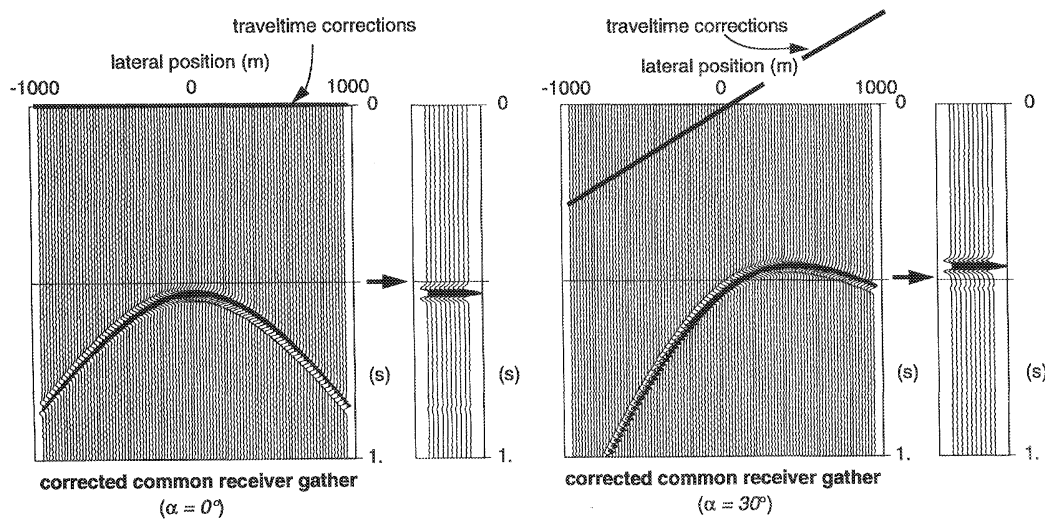
Figure 2.3 *Corrected common receiver gathers (CRG) for a (surface) illumination angle of 0° and 30°. Indicated are the traveltime corrections that have been applied to the original CRG. The areal source response is shown at the right hand side of the CRGs. This one trace is shown 10 times for display purposes. Note how the main contribution, around the apex of the event in the CRG shifts. Also note that the steep dip events may get aliased during the synthesis process.*

$$p = \frac{\sin \alpha}{c_0}, \qquad\qquad\qquad (2.12b)$$

where ω is the angular frequency, c_0 the velocity (distribution) just below the surface, and α the emergence angle of the plane wave. Figure 2.3 shows a common receiver gather (CRG) for a homogeneous medium containing one horizontal reflector after application of the synthesis operator according to equation (2.12a) for $\alpha=0°$ and $\alpha=30°$. Indicated are the traveltime corrections applied to the original CRG. The trace of the areal shot record after summing all traces of the corrected CRG is also shown. Note how the main contribution, around the apex of the event in the CRG shifts. Also note that the steep dip events may get aliased during the synthesis process. In appendix B it is argued that the main contribution to the areal shot record response is defined by the *Fresnel zone* around the apex of the events in the corrected CRGs.

If it is allowed to apply reciprocity, each shot record may be interpreted as a common receiver gather. The synthesis process may then be done per shot record, meaning that each shot record will result in one trace of the final areal shot record.

For synthesis operators defined by equation (2.12a) it is also possible to synthesize the areal shot records via the Radon domain, or the wavenumber-frequency domain. However, from the formulation of equation (2.9a) it can be seen that we do not have to restrict ourselves to plane waves from the surface: any kind of source wave field can be modelled, as long as the sampling of the individual sources at the surface allows us to do so.
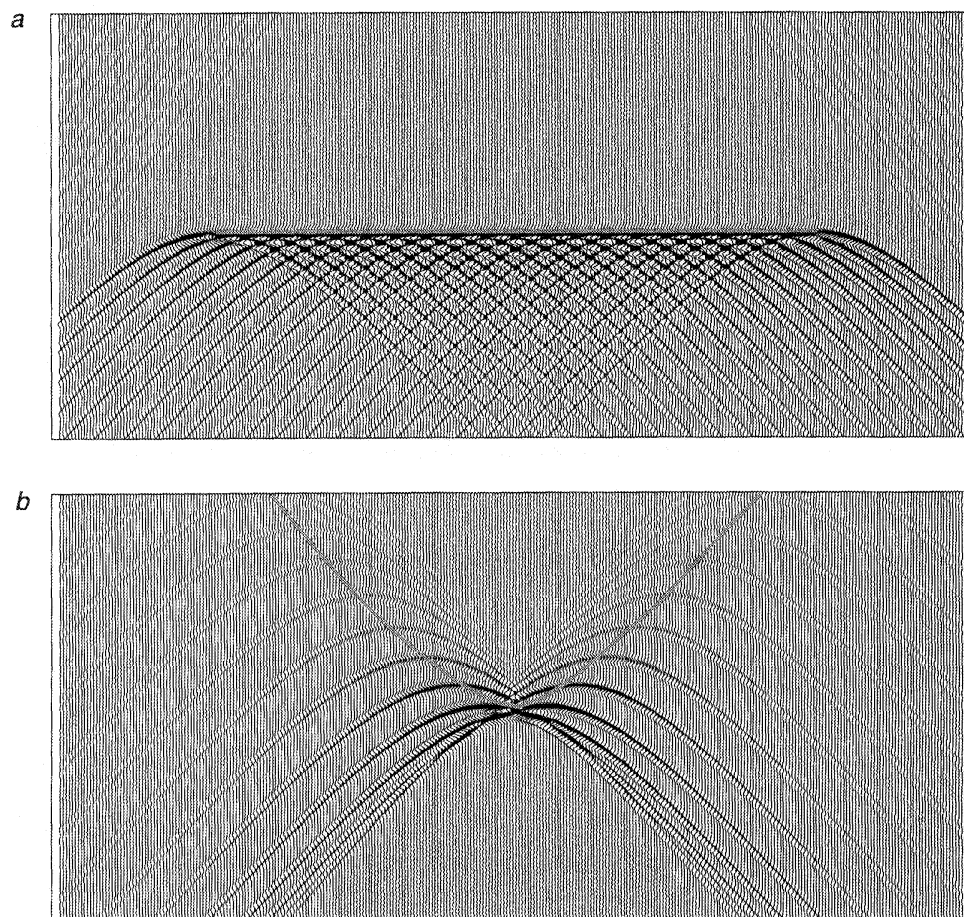
Figure 2.4 *Two areal shot records, build from sparse sampled shot records. (a) For a horizontal plane wave as areal source wave field. (b) For a* focussing *areal source wave field. Note how the shot records contribute to the areal shot record. The well-sampled areal shot record is the envelope of the shifted shot record. The synthesis operator cuts through the apices of the shot records (dotted line). For the plane wave the synthesis operator and the areal shot record to-be coincide.*

Finally, as illustration of the synthesis process partly synthesized areal shot records are shown for a model containing one horizontal reflector at $z = 400m$. A horizontal plane-wave response is synthesized and the response of an areal source wavefield which illuminated only *one* point of the reflector, a so-called *focus point* illumination. Different types of illumination and their use are discussed in Chapter 4, 5 and 6 of this thesis. Only 21 shot records are used in the synthesis process with a source sampling of *200m*. The geophone sampling is *20m*. The results are shown in Figure 2.4. Each shot record is shifted in time and scaled in amplitude according to the synthesis operator and finally stacked at the proper receiver positions. If the shot records are
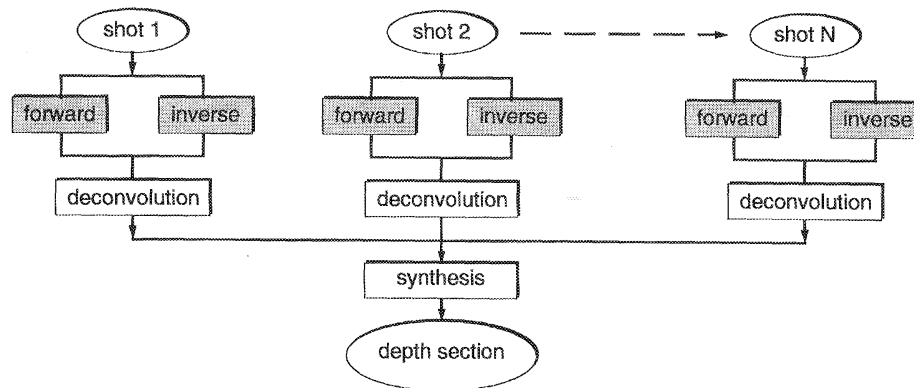
Figure 2.5 *Scheme for prestack shot record migration. Note that the synthesis occurs* after *the migration.*

sufficiently fine sampled, the areal shot record will contain an event which is the *envelope* of all the shifted individual shot records.

2.4 Areal shot record processing scheme

Figure 2.5 shows the scheme for conventional processing of preprocessed prestack data. This processing may be redatuming or migration. If we follow the shot record approach (Berkhout, 1985), we see that each shot record is processed individually, followed by a post-processing synthesis process (Common Depth Point stacking). During this post-processing synthesis process, all results of the individually processed shot records are combined into the final processing result. Because all shot records are processed individually, this method is very flexible, especially for irregularly sampled data. However like in 3-D surveys, the number of shot records becomes too large, hence, the processing of all shot records individually becomes a cumbersome job.

If, prior to the migration process, the prestack data is synthesized into areal shot records (Figure 2.6), the number of shot records is reduced, and prestack processing is feasible, even for 3-D surveys. Instead of the post-processing synthesis process (CDP stacking), a pre-processing synthesis is performed, which makes a user-defined subselection of the prestack data volume. After the migration process, all individually migrated *areal* shot record results can be combined in a final (weighted) addition step (Figure 2.7). As long as the number of constructed areal shot records is less than the number of shot records in the survey, the areal shot record route will be more economic. Note that although shot records are combined into *one* areal shot record, the method is still a *prestack* method.
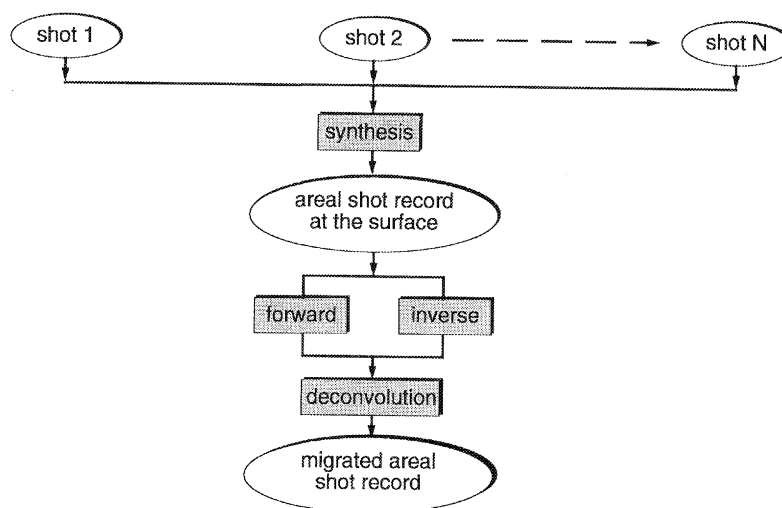
Figure 2.6 *Areal shot record migration scheme. Note that the synthesis occurs before the migration.*
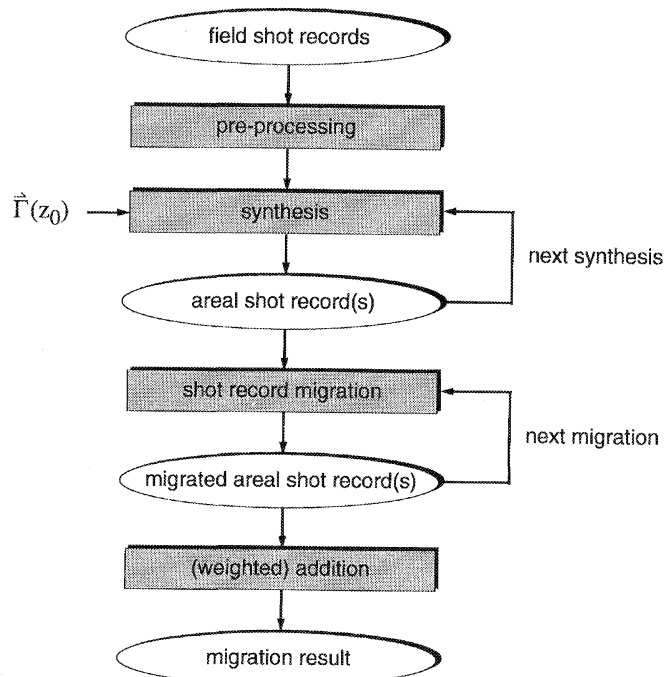
Figure 2.7 *Total areal shot record processing scheme; the results for the different areal shot records, i.e. for different source wave fields, are combined after depth migration.*

Controlled illumination

3.1 Introduction

In the previous chapter the concept of areal shot record technology has been described. The method consists of a synthesis process, in which many point source responses are combined into one areal source response. From the formulation used in the previous chapter, it was made clear that any kind of surface source wave field can be synthesized. In this chapter we will focus on the design of areal source wave fields at the surface, in such a way, that the incident source wave field at a specific target zone has a predefined shape. This principle has been called *controlled illumination*. We will show how the synthesis operator, describing the source wave field at the surface, can be constructed, so that the control of the source wave field is put at the target. The method will be compared with full prestack redatuming techniques.

3.2 Controlled illumination

In this section we will focus on the theoretical aspects of the controlled illumination process, and we will illustrate the principle with a synthetic example. For the example consider the subsurface model as depicted in Figure 3.1, where the acquisition spread consists of 128 shots and 128 receivers in a fixed spread configuration with a spacing of 12m. A zero-phase Ricker wavelet is used (Figure 3.1). The modeling for the example is done by a 2-D acoustic finite-difference scheme.

3.2.1 The design of the synthesis operator

First recall equation (2.9b):

$$\vec{S}_{syn}^+(z_m) = W^+(z_m, z_0)\, \vec{S}_{syn}^+(z_0) = W^+(z_m, z_0)\, S^+(z_0)\, \vec{\Gamma}(z_0), \tag{3.1}$$
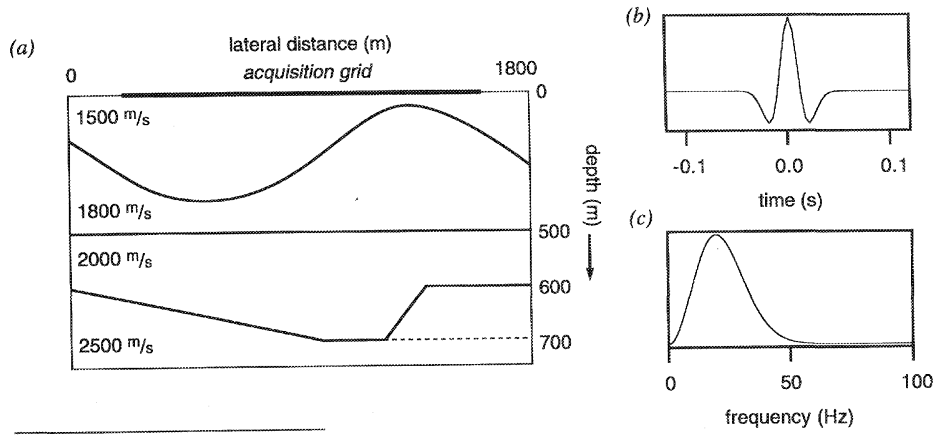
Figure 3.1 *The subsurface model used for the example (a). On the right-hand side the source wavelet (b) and its spectrum (c) are shown.*

describing the incident source wave field $\vec{S}_{syn}^+(z_m)$ at depth level z_m due to an areal source wave field $\vec{S}_{syn}^+(z_0)$ at the surface z_0. For controlled illumination we want to *define* the source wave field $\vec{S}_{syn}^+(z_m)$ at depth level z_m, and *design* the synthesis operator $\vec{\Gamma}(z_0)$ accordingly. Then, by inverting equation (3.1), the synthesis operator $\vec{\Gamma}(z_0)$ follows:

$$\vec{\Gamma}(z_0) = [S^+(z_0)]^{-1} \, F^+(z_0,z_m) \, \vec{S}_{syn}^+(z_m), \tag{3.2}$$

where $F^+(z_0,z_m)$ is the inverse of the propagation operator $W^+(z_m,z_0)$. Note that $[S^+(z_0)]^{-1}$ means correction for the source (arrays) as used in the field (deconvolution for signature and directivity).

If we assume that the deconvolution process for the directivity has already been applied during the preprocessing step, then we may write:

$$S^+(z_0) = S(\omega) \, I, \tag{3.3}$$

simplifying equation (3.2) to:

$$\vec{\Gamma}(z_0) = [S(\omega)]^{-1} \, F^+(z_0,z_m) \, \vec{S}_{syn}^+(z_m). \tag{3.4}$$

Next we define (in analogy with equation (2.10d)) the desired source wave field $\vec{S}_{syn}^+(z_m)$ as:

$$\vec{S}_{syn}^+(z_m) = S(\omega) \, \vec{\Gamma}(z_m). \tag{3.5}$$

Substitution of equation (3.5) into equation (3.4) yields:

$$\vec{\Gamma}(z_0) = F^+(z_0,z_m) \, \vec{\Gamma}(z_m). \tag{3.6a}$$

The inverse propagation operator $F^+(z_0,z_m)$ can be approximated by the complex conjugate of the propagation operator $W^-(z_0,z_m)$, see e.g. Wapenaar and Berkhout (1989):
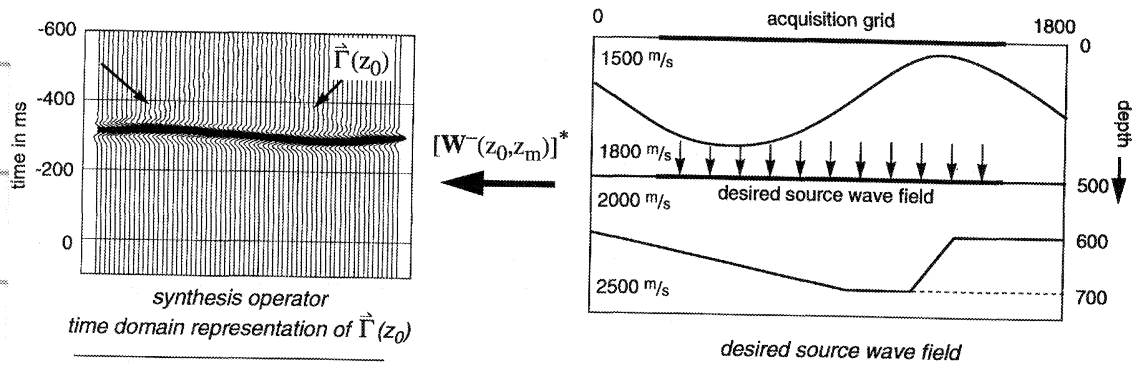
Figure 3.2 *Time domain representation of the designed synthesis operator $\vec{\Gamma}(z_0)$. Note that the diffractions in $\vec{\Gamma}(z_0)$ are needed to avoid them in $\vec{S}^+_{syn}(z_m)$. In this simple example a horizontal plane wave at depth level z_m was chosen. For display purposes the synthesis operator is convolved with the wavelet of Figure 3.1.*

$$F^+(z_0,z_m) = [W^+(z_m,z_0)]^{-1} \approx [W^-(z_0,z_m)]^*, \tag{3.6b}$$

simplifying equation (3.6a) to:

$$\vec{\Gamma}(z_0) = [W^-(z_0,z_m)]^* \vec{\Gamma}(z_m), \tag{3.6c}$$

where * denotes that the complex conjugate should be taken.

Taking the complex conjugate of the propagation operator W^- means reversing the sign of the phase, which is equivalent with reversing the *time* axis in the time domain. So synthesis operator $\vec{\Gamma}(z_0)$ is defined as the areal source wave field $\vec{\Gamma}(z_m)$ propagated back to the surface z_0. Hence, synthesis operator $\vec{\Gamma}(z_0)$ can be constructed from the desired wave field at the target, if the propagation properties of the overburden are known. Recall the relationship between the synthesis operators and the synthesized wave fields:

$$\vec{S}^+_{syn}(z_m) = S(\omega) \vec{\Gamma}(z_m), \text{ and } \vec{S}^+_{syn}(z_0) = S(\omega) \vec{\Gamma}(z_0). \tag{3.7}$$

If we define our desired source wave field $\vec{S}^+_{syn}(z_m)$ at the target as shown in Figure 3.2 (right), we end up with the time domain representation of the $\vec{\Gamma}(z_0)$ in Figure 3.2 (left). Note that the synthesis operator is designed in such a way that the incident wave field will arrive at depth level z_m at $t = 0$.

3.2.2 The application of the synthesis operator to the shot records

First recall the forward model of equation (2.5d) for the half-space response at the surface:

$$P^-(z_0) = X_0(z_0,z_0) S^+(z_0). \tag{3.8a}$$

If we ignore the response of the overburden $(z < z_m)$ we may rewrite equation (3.8a) as:

$$P^-(z_0 \mid z \geq z_m) = [W^-(z_0,z_m) X(z_m,z_m) W^+(z_m,z_0)] S^+(z_0), \tag{3.8b}$$
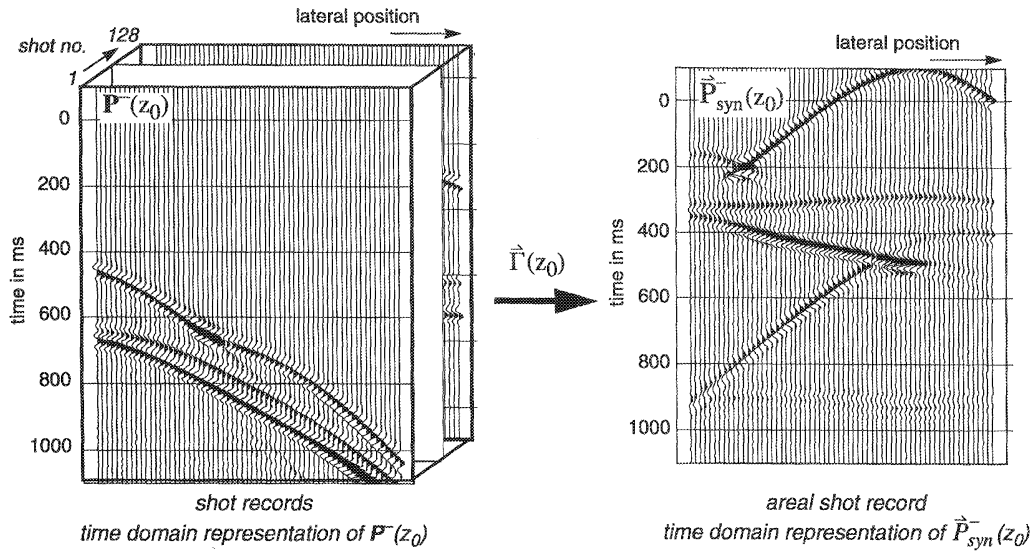
Figure 3.3 *Application of the synthesis operator $\vec{\Gamma}(z_0)$ to the data, yielding one* areal *shot record. In the synthesized result the source is the plane wave source at $z = 500m$; the receivers are at the surface.*

where $P^-(z_0 \mid z \geq z_m)$ indicates that only reflection for $z \geq z_m$ are considered. $P^-(z_0 \mid z \geq z_m)$ will further be denoted by simply $P^-(z_0)$.

Applying the synthesis operator $\vec{\Gamma}(z_0)$ to the data matrix $P^-(z_0)$ we obtain:

$$\vec{P}^-_{syn}(z_0) = P^-(z_0)\, \vec{\Gamma}(z_0), \qquad\qquad (3.9a)$$

or, according to equations (3.5), (3.6a) and (3.8b),

$$\vec{P}^-_{syn}(z_0) = W^-(z_0,z_m)\, X(z_m,z_m)\, \vec{S}^+_{syn}(z_m), \qquad\qquad (3.9b)$$

or

$$\vec{P}^-_{syn}(z_0) = X_0(z_0,z_m)\, \vec{S}^+_{syn}(z_m), \qquad\qquad (3.9c)$$

with

$$X_0(z_0,z_m) = W^-(z_0,z_m)\, X(z_m,z_m). \qquad\qquad (3.9d)$$

This result shows clearly that the areal shot record $\vec{P}^-_{syn}(z_0)$, as obtained by applying vector $\vec{\Gamma}(z_0)$ to the data $P^-(z_0)$, is the response at the surface z_0 due to the desired source wave field $\vec{S}^+_{syn}(z_m)$ at depth level z_m. The result of the application of the synthesis operator $\vec{\Gamma}(z_0)$ (Figure 3.2) to the data matrix $P^-(z_0)$, yielding one areal shot record $\vec{P}^-_{syn}(z_0)$, is shown in Figure 3.3 for the situation of a horizontal plane wave at z_m=500m:
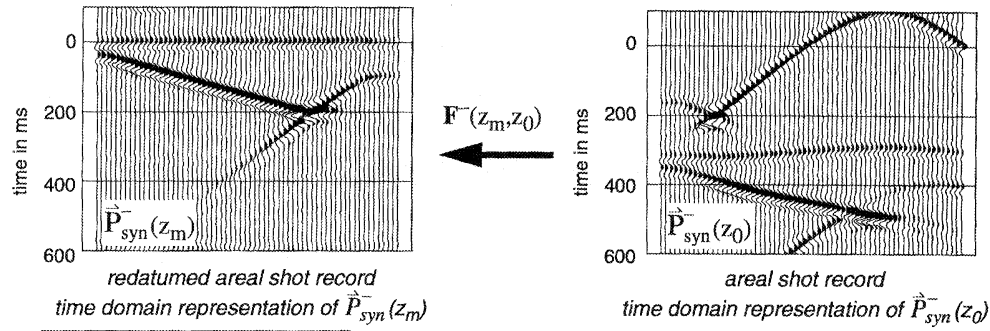
Figure 3.4 *The synthesized response after redatuming, meaning that the receivers are repositioned from z_0 to z_m.*

$$\vec{S}^{+}_{syn}(z_m{=}500m) = S(\omega) \; [1, 1, 1, \dots, 1]^{T}. \qquad (3.10)$$

3.2.3 Redatuming after synthesis

To obtain the redatumed areal shot record at depth level z_m due to the desired source wave field $\vec{S}^{+}_{syn}(z_m)$, the propagation effects that the overburden has on the received wave field must be removed by inverting for $W^{-}(z_m,z_0)$:

$$\vec{P}^{-}_{syn}(z_m) = F^{-}(z_m,z_0) \; \vec{P}^{-}_{syn}(z_0). \qquad (3.11)$$

Upon substitution of equation (3.9b), we obtain:

$$\vec{P}^{-}_{syn}(z_m) = X(z_m,z_m) \; \vec{S}^{+}_{syn}(z_m). \qquad (3.12)$$

The result is depicted in Figure 3.4 and shows the response at depth level z_m due to the desired source wave field $\vec{S}^{+}_{syn}(z_m)$. Note that the extrapolation, as described by equation (3.11), is done for only *one* synthesized areal shot record instead of for all individual shot records, thus speeding up the calculations by a factor of the order of the number of shot records. The actual structure in the target can be clearly seen after migration of the redatumed response, Figure 3.5.
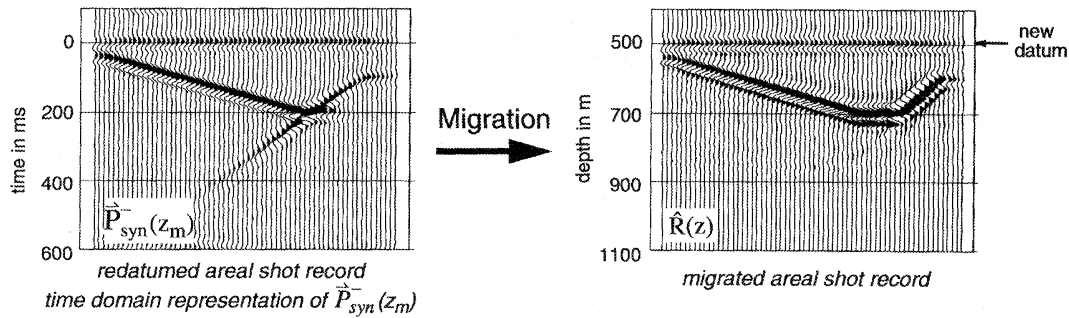
Figure 3.5 *Migration of the redatumed synthesized response.*
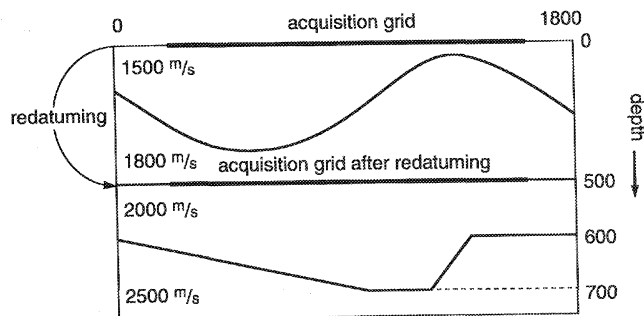
Figure 3.6 *The principle of redatuming: transformation of the acquisition level from the surface to another level somewhere in the subsurface.*

3.2.4 Comparison with full prestack redatuming

Prestack redatuming

The purpose of redatuming is to transform the data in such a way that the acquisition level is transported from the surface (initial 'datum') to another level (new 'datum') somewhere in the subsurface (Figure 3.7); (Kinneging, 1990). From the forward model, as described in section 2.2, it is simple to construct the formulas for such a prestack redatuming scheme.

Removing the propagation effects from the forward model (equation (2.7a)) means applying the inverse of the propagation operators $W^+(z_m, z_0)$ and $W^-(z_0, z_m)$:

$$X(z_m, z_m) = F^-(z_m, z_0)\, X_0(z_0, z_0)\, F^+(z_0, z_m), \tag{3.13a}$$

where $X(z_m, z_m)$ contains only causal events, and

$$F^-(z_m, z_0) = [W^-(z_m, z_0)]^{-1} \approx [W^+(z_m, z_0)]^*, \tag{3.13b}$$

and

$$F^+(z_0, z_m) = [W^+(z_0, z_m)]^{-1} \approx [W^-(z_0, z_m)]^*. \tag{3.13c}$$

Equation (3.13a) gives the general scheme for prestack redatuming (Berkhout, 1985, chapter VII). Redatuming as described by equation (3.13a) can be carried out in a two-step way: first the extrapolation of the receivers to the target:

$$X(z_m, z_0) = F^-(z_m, z_0)\, X(z_0, z_0), \tag{3.14a}$$

followed by the extrapolation of the sources:

$$X(z_m, z_m) = X(z_m, z_0)\, F^+(z_0, z_m). \tag{3.14b}$$

Equations (3.14a) and (3.14b) describe in a concise way redatuming according to the well-known SG method (Shot-Geophone method). The detailed algorithm follows directly from the way matrices should be multiplied.

For practical applications redatuming according to equations (3.14a) and (3.14b) may not be the most efficient solution. For 3-D applications in particular, it involves a cumbersome data reordering process in between the two steps. Similar to shot record migration (Figure 2.5), it is possible to derive an alternative scheme where the redatuming is performed per shot record (see e.g. Wapenaar and Berkhout, 1989, chapter XI), thereby avoiding the data reordering process and allowing irregular source positions.

Although from a data handling point of view the shot record method is much simpler than the SG method, still a lot of computational effort is involved, particularly in 3-D.

Comparison

For a comparison of the method of controlled illumination with the previously described full prestack redatuming scheme, we substitute equation (3.13a) into equation (3.12):

$$\vec{P}_{syn}^{-}(z_m) = F^{-}(z_m, z_0)\, X_0(z_0, z_0)\, F^{+}(z_0, z_m)\, \vec{S}_{syn}^{+}(z_m), \text{ or} \tag{3.15a}$$

$$\vec{P}_{syn}^{-}(z_m) = F^{-}(z_m, z_0)\, X_0(z_0, z_0)\, \vec{S}_{syn}^{+}(z_0). \tag{3.15b}$$

This shows, that synthesizing after redatuming (equation (3.15a)) is fully equivalent to synthesizing sources at the surface in the sense of equation (3.9a) according to a synthesis operator defined by equation (3.4) and extrapolating the receivers afterwards, according to equation (3.11). Hence, no accuracy is lost. It may also be stated here, that no assumption whatsoever is made on the form of the desired source wave field $\vec{S}_{syn}^{+}(z_m)$. This vector may have any form, thus describing any desired illumination. Figure 3.7 shows the result of the synthesis before and after redatuming. The equivalence confirms our theoretical expectation.
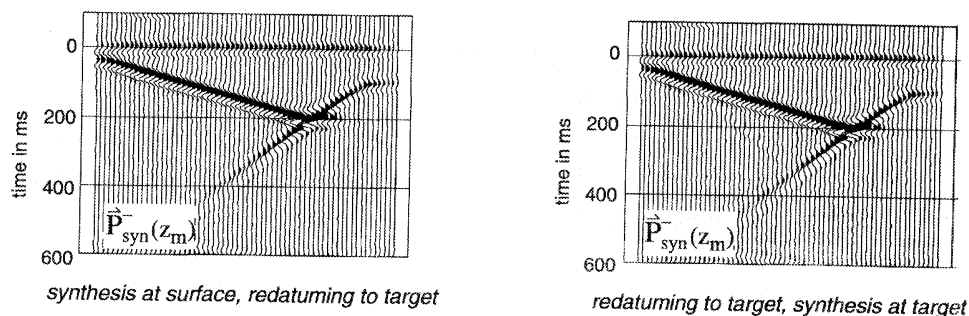
Figure 3.7   The result of synthesis before and after redatuming
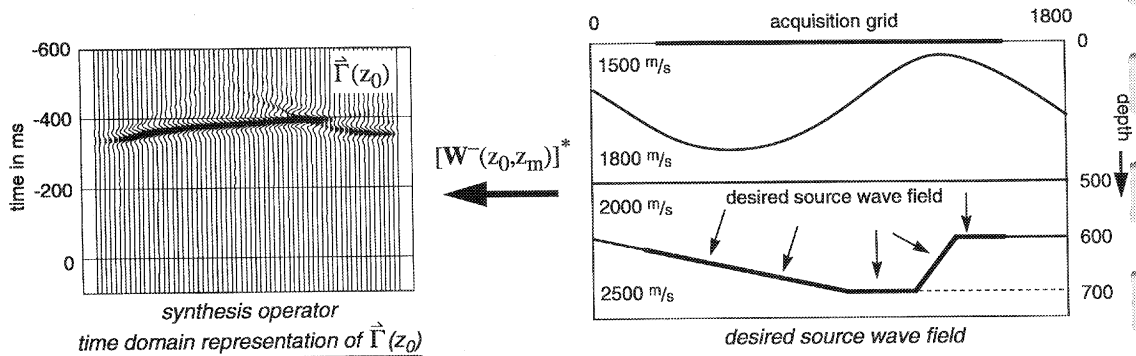
Figure 3.8 *The calculated synthesis operator according to the defined illumination and the macro model. For display purposes the synthesis operator is convolved with the wavelet of Figure 3.1.*

3.2.5 Illumination of a complex interface

In the next example, we will use the same model as shown in Figure 3.1. However, instead of a plane-wave illumination at a depth of 500m, this time the third reflector will be illuminated normal incidence, to show the flexibility of the method with respect to the type of illumination.

First the synthesis operator is calculated (Figure 3.8). Application of the synthesis operator to the data leads to the areal shot record as depicted in Figure 3.9. This areal shot record is the response at the surface due to the specified areal source at the third boundary of the model. After extrapolation of the receivers, we are left with the redatumed response, Figure 3.10. Although
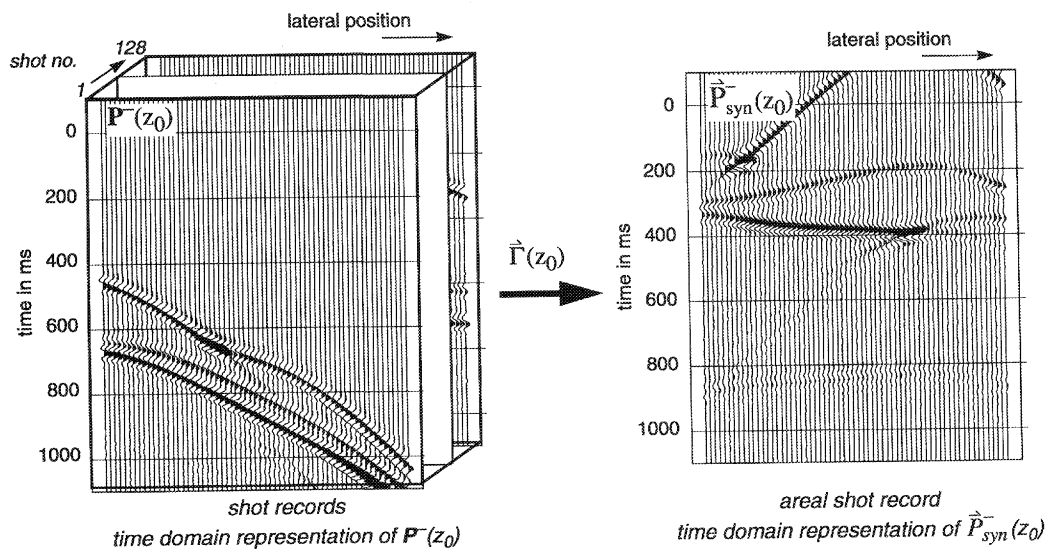
Figure 3.9 *Application of the synthesis operator to the data, yielding one areal shot record.*
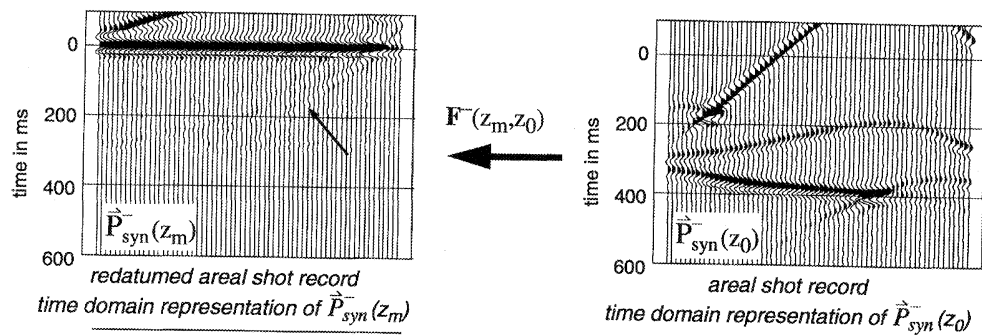
Figure 3.10 *The synthesized response after downward extrapolation at the received wave field. Since the diffraction energy from the target boundary is not entirely present in the surface data, the redatumed result shows some truncation artifacts indicated by the arrow.*

the redatuming level has a complicated shape, it can be clearly seen that the redatumed response has only one event at $t = 0$ for every lateral position, thus showing that the third boundary is illuminated perfectly, normal incidence.

Macro model verification by means of controlled illumination

4.1 Introduction

In the previous chapter the method of controlled illumination has been described. Because the method of controlled illumination involves wave field extrapolation, a description of the propagation properties of the subsurface must be available. The model quantifying the propagation effects of wave fields through the subsurface, is generally known as the *macro* model. The concept of the macro model and its use in depth migration was proposed by Berkhout (1985). To obtain macro models prestack migration techniques can be used (Cox, 1991; Al-Yahya, 1989; Jeannot, 1986; a.o.). For instance, at several lateral positions velocity analyses are performed by looking at the coherency in image gathers, focus panels or common depth point gathers.

In this chapter a new method for the verification of macro models is introduced, using the technique of controlled illumination. With this method it is possible to verify *local* macro velocities as well as an *entire* macro boundary in 2-D or 3-D. First the relation between the synthesis operator and the areal shot record is shown for different types of illumination assuming a correct macro model. This relationship is illustrated with a simple synthetic example and on field data. Next the influence of errors in the macro model is evaluated; it is shown that different types of illumination should be used to detect a *velocity* error or a *boundary* error.

4.2 Relation between the synthesis operator and the areal shot record for a correct macro model

First we recall the forward model for the one-reflector case (Figure 4.1):

$$P^-(z_0) = W^-(z_0,z_m)\, R(z_m)\, W^+(z_m,z_0)\, S^+(z_0),\qquad(4.1)$$

$P^-(z_0)$ ◄─────────────────────────────────────── $S^+(z_0)$

$W^-(z_0,z_m)$ $W^+(z_m,z_0)$

$R(z_m)$
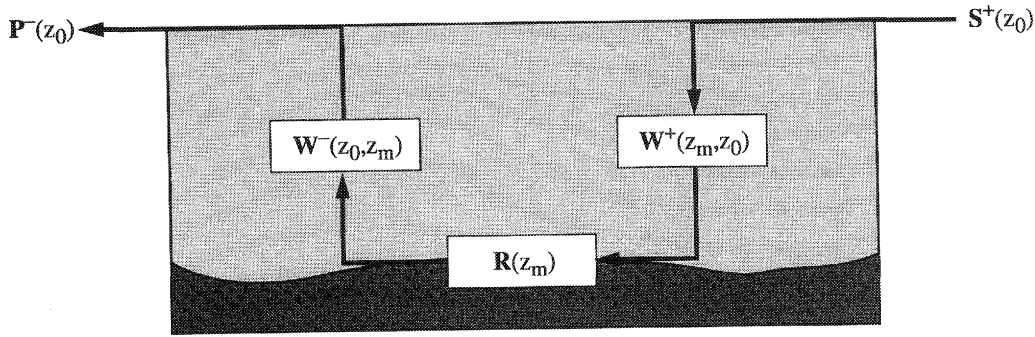
Figure 4.1 *Forward model for a model with one reflector. Note that the reflector may have any shape.*

in which $S^+(z_0)$ represents the source matrix, $W^+(z_m,z_0)$ the propagation matrix, describing the downward propagation from the surface z_0 to the reflector z_m, $R(z_m)$ the reflectivity matrix, describing the angle-dependent reflectivity for all points along the reflector, $W^-(z_0,z_m)$ the propagation matrix, describing the upward propagation from the reflector z_m to the surface z_0, and $P^-(z_0)$ being the monochromatic data matrix.

Note that the depth coordinate z_m is *not* restricted to one depth level; it can be a function of x and y, depending on the structure of the macro boundaries:

$$z_m = z_m(x,y), \qquad m = 1,2,... \tag{4.2}$$

For notational convenience the (x,y) arguments are omitted in the formulas.

Defining z_m according to equation (4.2) means that the description of the forward model, equation (4.1), is an approximation, since for the extrapolation of a wave field from an arbitrary shaped interface both particle velocity and pressure are required. Equation (4.1) takes only account for the pressure or the velocity, since it is based on the Rayleigh I or II integral. This approximation, however, does not effect the results shown in this chapter.

If we assume that the data is corrected for directivity in the preprocessing step, source matrix $S^+(z_0)$ simplifies to:

$$S^+(z_0) = I \, S(\omega), \tag{4.3}$$

with I the identity matrix and $S(\omega)$ the source signature.

In chapter 3 it was shown that the synthesis operator $\vec{\Gamma}(z_0)$ for a specified incident wave field $\vec{\Gamma}(z_m)$ the synthesis operator $\vec{\Gamma}(z_0)$ is given by (Figure 4.2):

$$\vec{\Gamma}(z_m) = W^+(z_m,z_0) \, \vec{\Gamma}(z_0), \tag{4.4a}$$

or
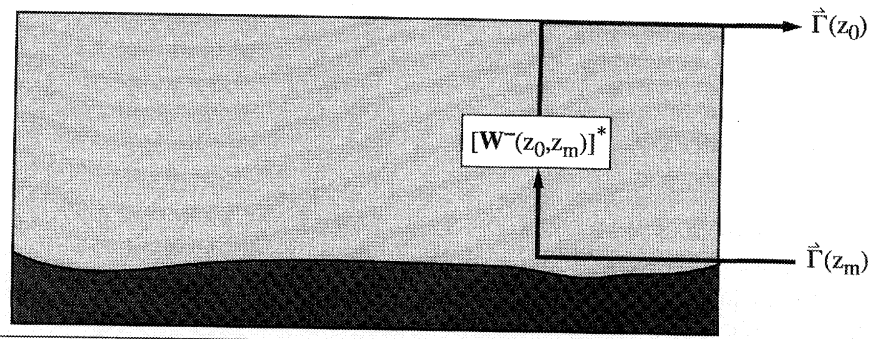
Figure 4.2 *Schematic view on the calculation of the synthesis operator for controlled illumination.*

$$\vec{\Gamma}(z_0) = F^+(z_0,z_m)\,\vec{\Gamma}(z_m), \tag{4.4b}$$

where $F^+(z_0,z_m)$ is the inverse of the forward extrapolation operator $W^+(z_m,z_0)$. Using the matched filter approach, equation (4.4a) changes to:

$$\vec{\Gamma}(z_0) = [W^-(z_0,z_m)]^*\,\vec{\Gamma}(z_m), \tag{4.4c}$$

where $[W^-(z_0,z_m)]^*$ describes the complex conjugate of the forward extrapolation operator from the surface z_0 to the target level z_m.

Application of the synthesis operator $\vec{\Gamma}(z_0)$ to the data $P^-(z_0)$ yields the areal shot record $\vec{P}_{syn}^-(z_0)$, (Figure 4.3):

$$\vec{P}_{syn}^-(z_0) = W^-(z_0,z_m)\,R(z_m)\,\vec{\Gamma}(z_m)\,S(\omega), \tag{4.5a}$$

or defining:

$$S(\omega) = 1, \text{ for all } \omega \text{ in the seismic band width}, \tag{4.5b}$$
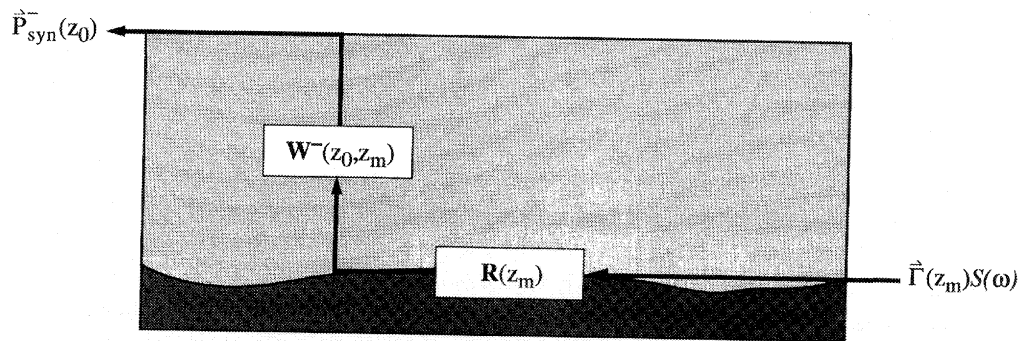
Figure 4.3 *Model after synthesis for controlled illumination.*

$$\vec{P}_{syn}^{-}(z_0) = W^{-}(z_0,z_m)\, \vec{R}(z_m), \tag{4.5c}$$

in which:

$$\vec{R}(z_m) = R(z_m)\, \vec{\Gamma}(z_m). \tag{4.5d}$$

From equations (4.4c) and (4.5c) we can see that if we define the desired source wave field $\vec{\Gamma}(z_m)$ at a macro boundary with reflectivity properties $R(z_m)$, and the propagation properties $W^{-}(z_0,z_m)$ are estimated correctly, we should be able to find a relation between the areal shot record $\vec{P}_{syn}^{-}(z_0)$ and the synthesis operator $\vec{\Gamma}(z_0)$. This will be discussed in the next sections for different types of illuminating source wave fields, i.e. different types of $\vec{\Gamma}(z_m)$.

4.2.1 Focus point illumination

The first type of illumination we will discuss is the *focus point* illumination:

$$\vec{\Gamma}_i(z_m) = \vec{I}_i = [0, \dots ,0,1,0, \dots ,0]^T, \tag{4.6a}$$

where the index i represents the lateral position $(x,y,)_i$ at which the focussing point is positioned at z_m.

For this specific type of illumination we see that equation (4.5d) can be rewritten as:

$$\vec{R}(z_m) = \vec{R}_i(z_m), \tag{4.6b}$$

where $\vec{R}_i(z_m)$ is the ith column of the reflectivity matrix $R(z_m)$. It thus represents a secondary point source with a directivity pattern given by the angle-dependent reflectivity property of the reflector at position $(x,y)_i$. Using equation (4.6b), we may write:

$$\vec{P}_{syn,i}^{-}(z_0) = W^{-}(z_0,z_m)\, \vec{R}_i(z_m), \tag{4.7a}$$

and

$$[\vec{\Gamma}_i(z_0)]^* = W^{-}(z_0,z_m)\, \vec{I}_i(z_m), \tag{4.7b}$$

where * denotes that the complex conjugate should be taken. Hence the inverse Fourier transforms of $\vec{P}_{syn,i}^{-}(z_0)$ and $[\vec{\Gamma}_i(z_0)]^*$ are equal in traveltime, but may differ in amplitude due to the angle-dependent reflection coefficient at $(x,y)_i$.

Figure 4.4 shows the synthesis operator and the synthesized areal shot record for a focus point illumination at the second boundary in the model of Figure 3.1 in chapter 3. The middle event in the areal shot record is the event corresponding to the illuminated boundary. The other two events in the areal shot record as shown in Figure 4.4 are the reflections of the first and third boundary due to the areal source wave field, defined by synthesis operator shown in the same figure. Note the good match between the reflection of the second reflector in the areal shot record and the complex conjugate of the synthesis operator. In Figure 4.4 also the 1-D cross--

time domain representation of $[\vec{\Gamma}(z_0)]^*$
complex conjugate of synthesis operator

time domain representation of $\vec{P}_{syn}(z_0)$
areal shot record

directivity

1D cross-correlation
along the time axis
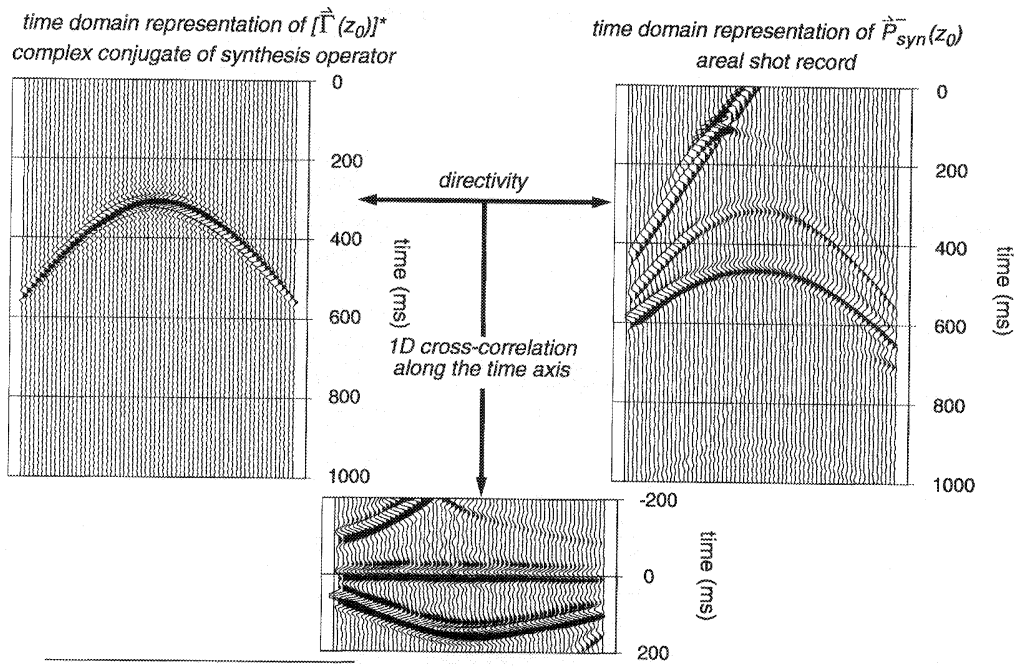
Figure 4.4 *The complex conjugate of the synthesis operator for a focus point illumination of the second boundary (left), and its areal shot record (right). Note that in the correlation display the event at t=0 aligns perfectly, indicating that the correct macro model is used.*

correlation along the time axis of the areal shot record with the synthesis operator is shown. Note the perfect alignment of the event at $t=0$, indicating that the correct macro model for the synthesis operator was used.

4.2.2 Normal incidence illumination

In this section we will discuss the *normal incidence* illumination of a macro boundary, i.e.:

$$\vec{\Gamma}(z_m) = \vec{\Gamma}_0(z_m) = [1,1, \dots ,1]^T. \tag{4.8}$$

If we assume that the reflectivity properties along the reflector do not change, we can rewrite equation (4.5d) as:

$$\vec{R}(z_m) = r_0 \, \vec{\Gamma}_0(z_m), \tag{4.9}$$

where r_0 is the normal incidence reflection coefficient of the illuminated boundary. Hence, we may now write:

$$\vec{P}_{syn}(z_0) = r_0 \, W^-(z_0,z_m) \, \vec{\Gamma}_0(z_m), \tag{4.10a}$$

and

time domain representation of $[\vec{\Gamma}^-(z_0)]^*$
complex conjugate of synthesis operator

time domain representation of $\vec{P}^-_{syn}(z_0)$
areal shot record
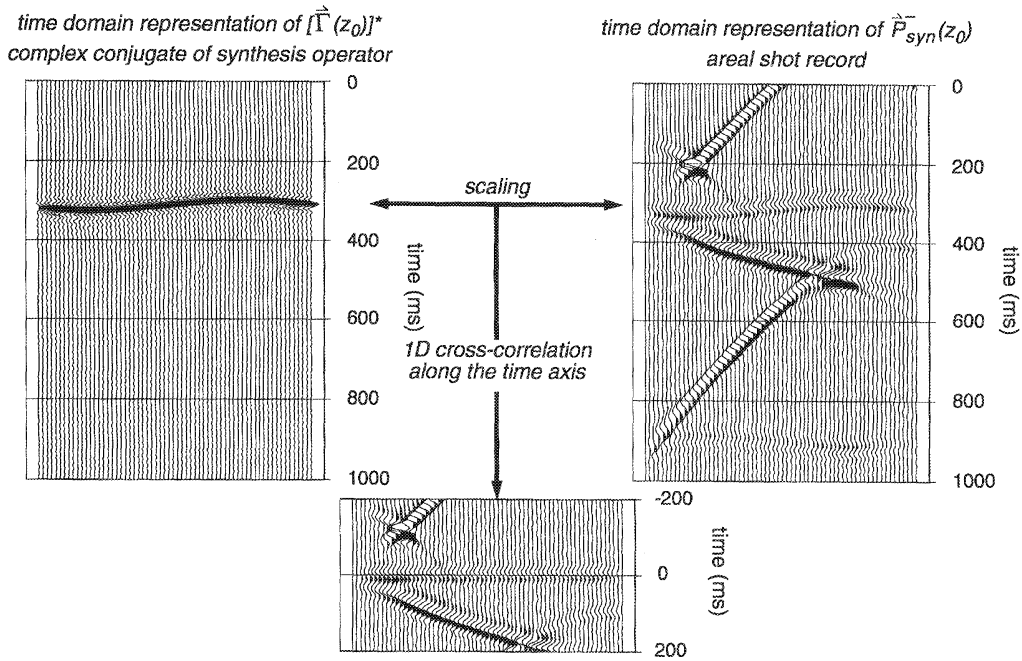
Figure 4.5 *The complex conjugate of the synthesis operator for a normal incidence illumination of the second boundary of the model (left), and its areal shot record (right). Note that in the correlation display the event at t=0 aligns perfectly.*

$$[\vec{\Gamma}^-_0(z_0)]^* = W^-(z_0, z_m)\, \vec{\Gamma}^-_0(z_m),$$

(4.10b)

yielding

$$\vec{P}^-_{syn}(z_0) = r_0\, [\vec{\Gamma}^-(z_0)]^*.$$

(4.10c)

Figure 4.5 shows the synthesis operator for a normal incidence illumination of the second boundary and its synthesized areal shot record. Note the good match between the reflection of the second reflector in the areal shot record and the complex conjugate of the synthesis operator. In Figure 4.5 also the 1-D cross-correlation along the time axis of the areal shot record with the synthesis operator is shown. Note the perfect alignment of the event at $t=0$, indicating that the correct macro model was used to compute the synthesis operator.

4.2.3 Non-normal incidence illumination

For a non-normal incidence illuminating source wave field with a constant p value, we find:

$$\vec{\Gamma}(z_m) = \vec{\Gamma}_p(z_m) = (e^{-j\omega p x_1},\ e^{-j\omega p x_2},\ \dots,\ e^{-j\omega p x_N})^T,$$

(4.11)

for the 2-D case. For this source wave field, again assuming that the reflection properties along the reflector do not change, we see that equation (4.5d) can be rewritten as:

time domain representation of $[\vec{\Gamma}(z_0)]^*$
complex conjugate of synthesis operator
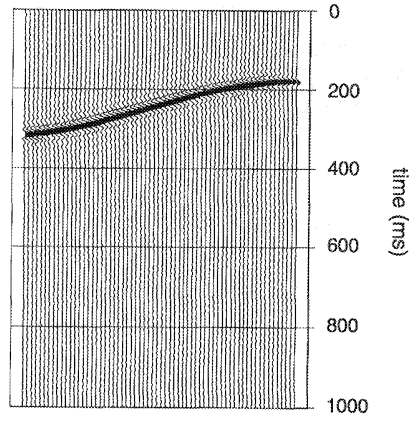
time domain representation of $\vec{P}_{syn}^-(z_0)$
areal shot record
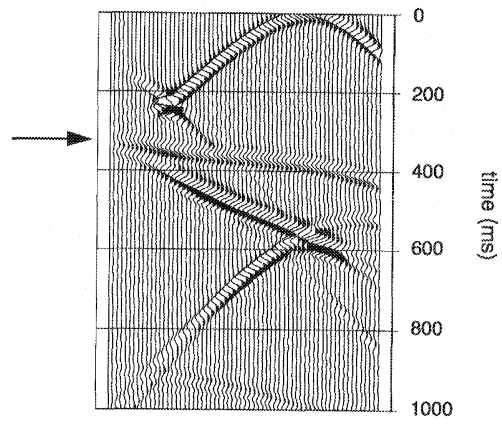
Figure 4.6   *The synthesis operator for illumination of the second boundary of the model with a incident plane wave field with an angle of $10°$ (left), and the areal shot record (right).*

$$\vec{R}(z_m) = r_p\,\vec{\Gamma}(z_m), \tag{4.12a}$$

where r_p is the reflection coefficient for the rayparameter p of the illuminated boundary. Hence we may now write:

$$\vec{P}_{syn}^-(z_0) = r_p\,W^-(z_0,z_m)\,\vec{\Gamma}_p(z_m), \tag{4.13a}$$

and

time domain representation of $[\vec{\Gamma}(z_0)]^*$
complex conjugate of synthesis operator
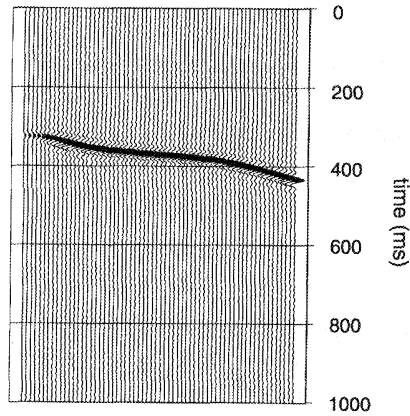
time domain representation of $\vec{P}_{syn}^-(z_0)$
areal shot record
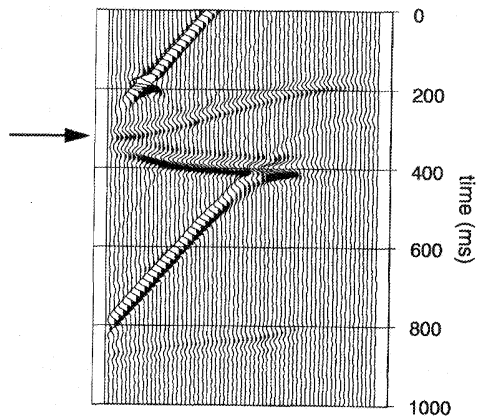
Figure 4.7   *The synthesis operator for illumination of the second boundary of the model with a incident plane wave field with an angle of $-10°$ (left), and the areal shot record (right).*

(a)   *(b)*
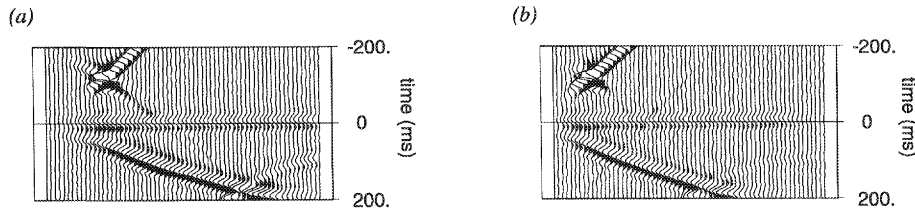
Figure 4.8 *Cross correlations along the time axis*
(a) the areal shot record for an illumination angle of 10° with the synthesis operator for an illumination angle of –10°.
(b) the areal shot record for an illumination angle of –10° with the synthesis operator for an illumination angle of 10°.

$$[\vec{\Gamma}_p(z_0)]^* = W^-(z_0, z_m)[\vec{\Gamma}_p(z_m)]^*. \tag{4.13b}$$

Figure 4.6 shows the areal shot record for an illumination of the second boundary with a rayparameter of approx. 96.5 μs/m (10°), together with the synthesis operator used for this synthesis. Figure 4.7 shows the same sections, but then for an illuminating source wave field with a rayparameter of approx. –96.5 μs/m (–10°), hence in this case:

$$\vec{\Gamma}_p(z_m) = [\vec{\Gamma}_{-p}(z_m)]^*. \tag{4.14a}$$

As can be seen from Figures 4.6 and 4.7, the illuminated boundary in the areal shot records shows up in the same way as the event in the synthesis operators, but with *opposite* angles.

Figure 4.8a shows the cross-correlation between the areal shot record for an illumination angle of 10° with the synthesis operator for an illumination angle of –10°. Figure 4.8b shows the cross-correlation between the areal shot record for an illumination angle of –10° with the synthesis operator for an illumination angle of 10°. Again the alignment at *t=0* shows that the correct macro model was used for the modelling of the synthesis operator.

Note that since we have used the correct macro model for the modeling of the synthesis operator, i.e. the traveltimes are correct, a comparison of the areal shot record $\vec{P}_{syn}^-(z_0)$ and the complex conjugate of the synthesis operator $\vec{\Gamma}(z_0)$ yields information on the *angle-dependent reflectivity* of the reflector.

4.3 Illustration on field data

In this section we will show results obtained on a field data set. The macro model is shown in Figure 4.9. The macro boundaries that we want to verify are indicated in the figure. They are the top and the bottom boundary of a layer with a horizontal gradient.

For the top of the gradient layer the synthesis operator was calculated for a normal incidence illumination. The areal shot record was computed and cross-correlated along the time axis with
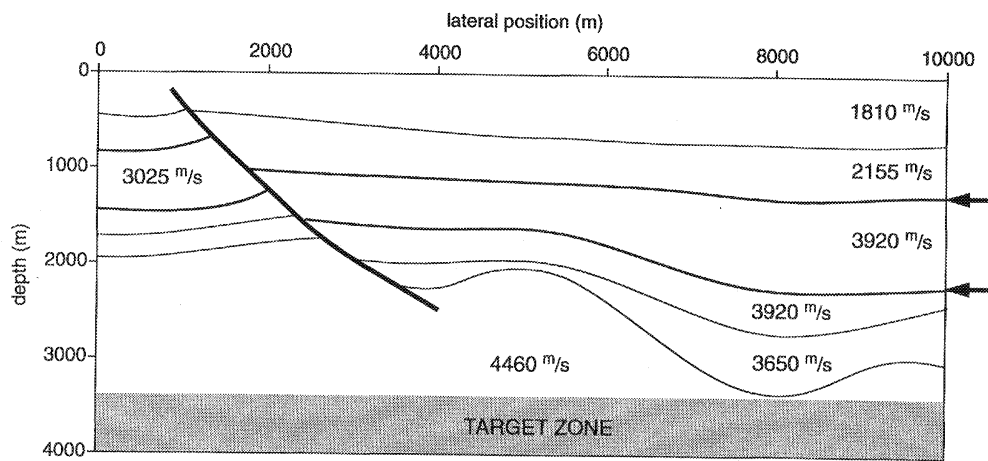
Figure 4.9 *Estimated macro model for the field data example (courtesy NAM). Indicated are the boundaries that will be validated.*

the synthesis operator. The result of these three steps are shown in Figure 4.10. In the areal shot record a traveltime track of the synthesis operator is overlaid. Note that overall of the cross-correlation aligns well along $t=0$, indicating that the macro boundary is well estimated.

For the bottom of the gradient layer the synthesis operator was calculated for a normal incidence illumination. The areal shot record was computed and cross-correlated along the time axis with the synthesis operator. The result of these three steps are shown in Figure 4.11. In the areal shot record a traveltime track of the synthesis operator is overlaid. Note that at the right hand side of the cross-correlation the event aligns rather well along $t=0$, indicating that the macro model is well estimated at that side of the model. At the left hand side of the section the model is less well resolved.

Finally the synthesis operator is calculated for a point source illumination of the bottom of the gradient layer. The point source is situated at a lateral position of 5000m. The areal shot record is computed and cross correlated along the time axis with the synthesis operator. The result of these three steps is shown in Figure 4.12. In the areal shot record a traveltime track of the synthesis operator is overlaid. Note that in the cross-correlation the events aligns rather well along $t=0$, indicating that the model is rather well estimated at the focus point.

From the three examples we see that indeed the technique of controlled illumination can be used to verify the macro model. One of the main advantages is that for the evaluation of the macro boundaries especially the *lateral* coherence is very well controlled, even over complex structures.
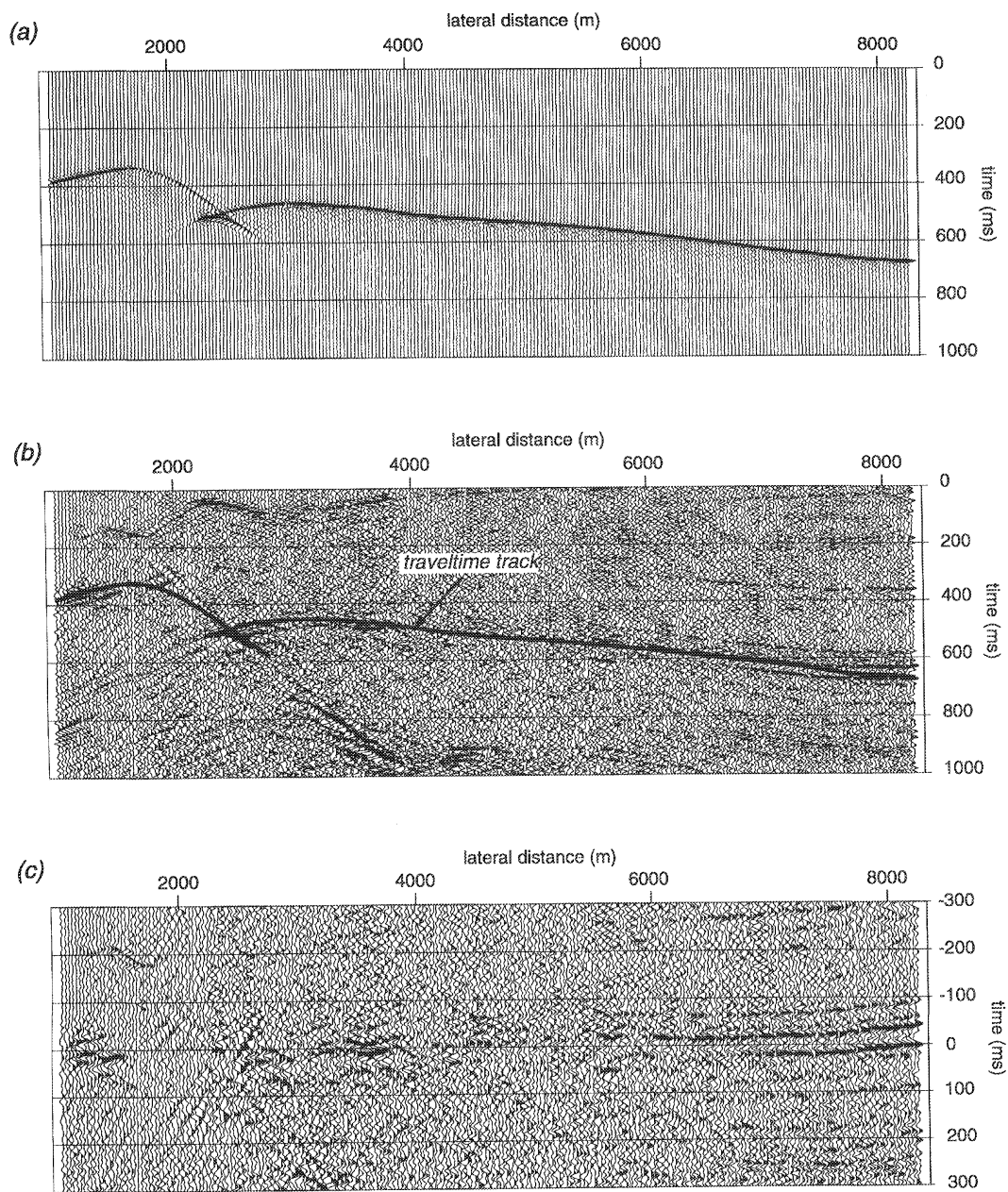
Figure 4.10 (a) *Time domain representation of the complex conjugate of the synthesis operator for a normal incidence illumination of the top boundary of the gradient layer; (b) the areal shot record, synthesized according to the synthesis operator from (a); (c) the cross-correlation along the time axis of the complex conjugate of the synthesis operator and the areal shot record. Note the reasonable alignment of the event at t=0 at the right side of the section. Note also that in (b) a traveltime track of the synthesis operator is overlaying the areal shot record.*
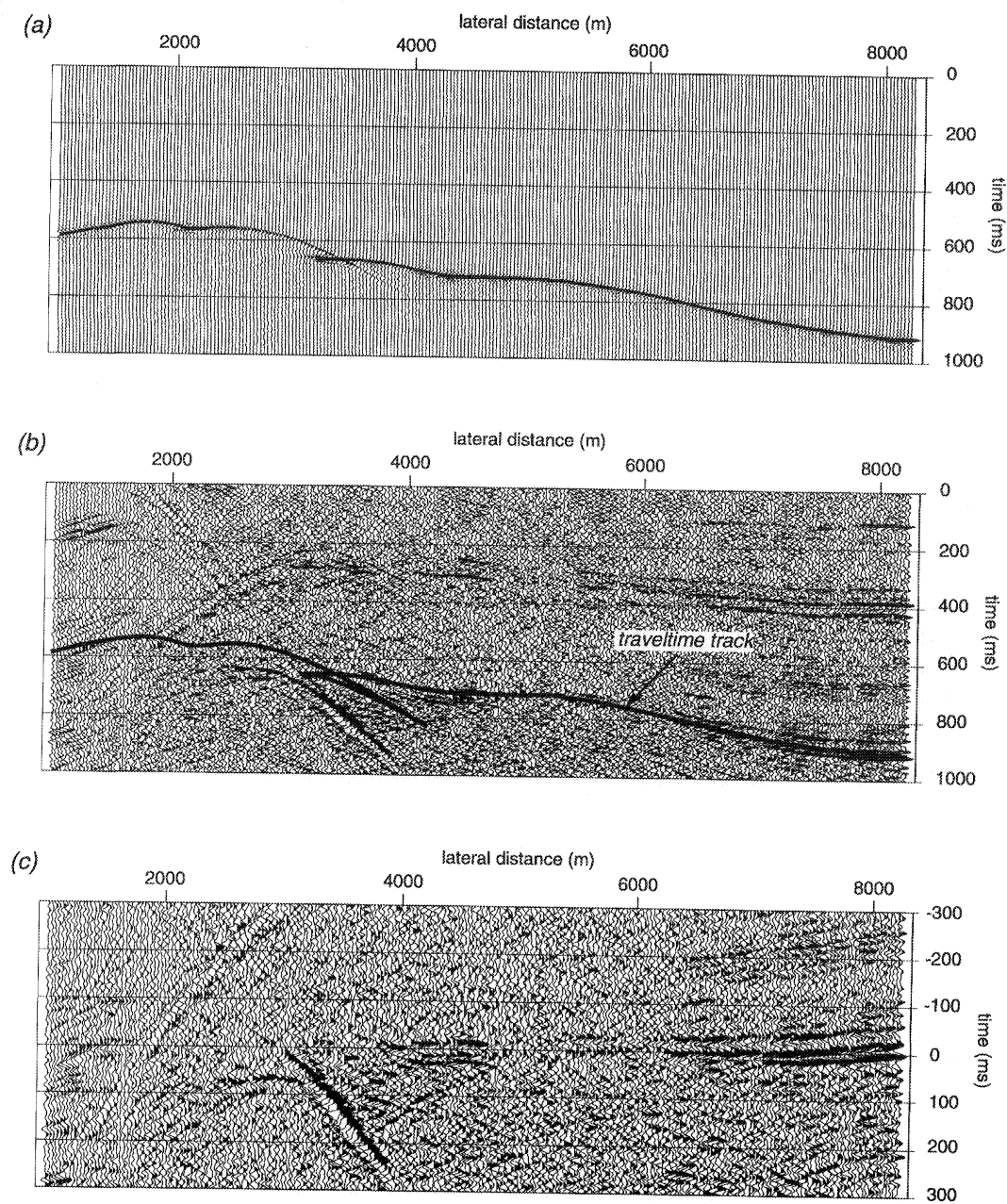
Figure 4.11 (a) *Time domain representation of the complex conjugate of the synthesis operator for a normal incidence illumination of the bottom boundary of the gradient layer; (b) the areal shot record, synthesized according to the synthesis operator from (a); (c) the cross-correlation along the time axis of the complex conjugate of the synthesis operator and the areal shot record. Note the reasonable alignment of the event at t=0 at the right side of the section. Note also that in (b) a traveltime track of the synthesis operator is overlaying the areal shot record.*
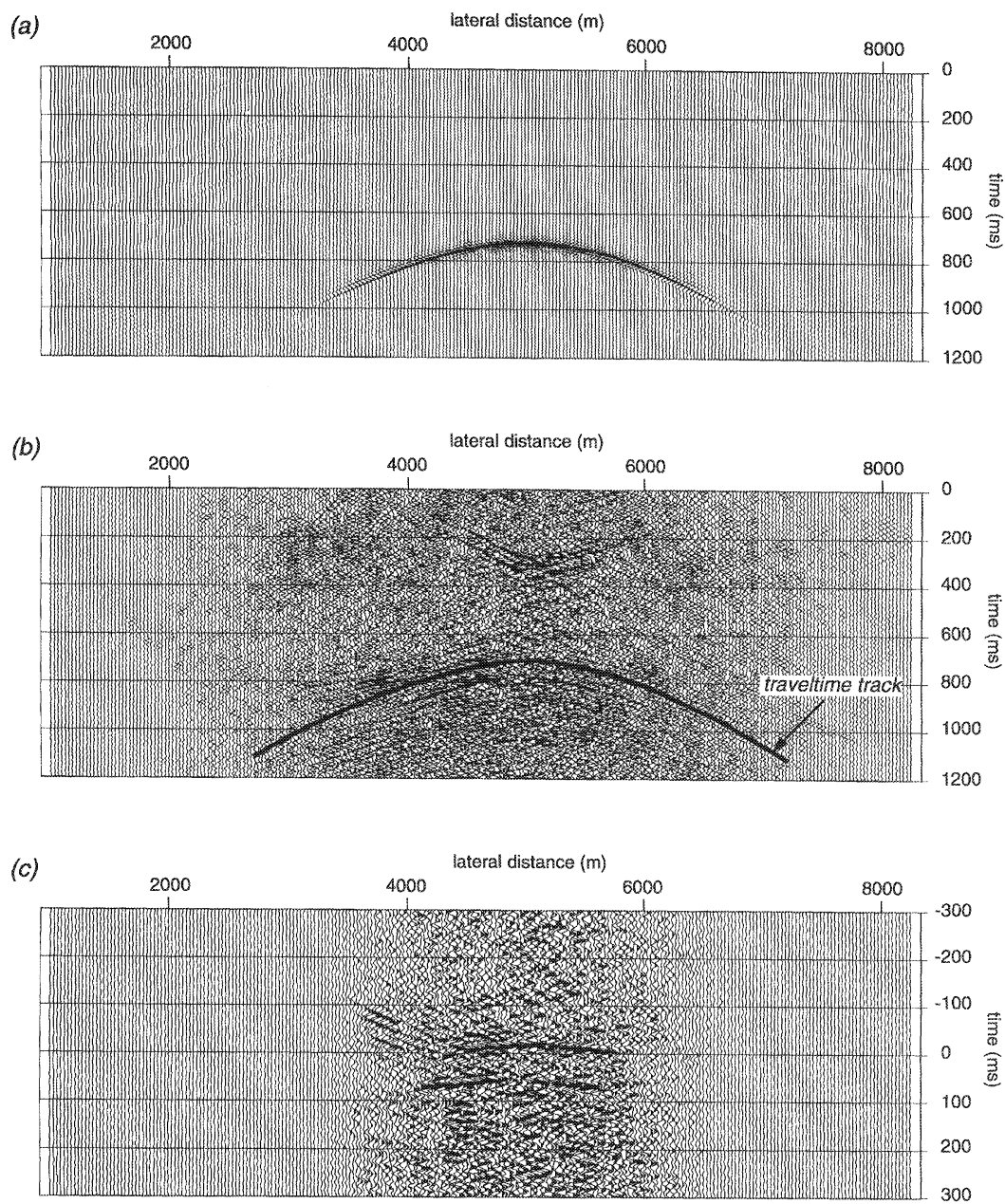
Figure 4.12 (a) *Time domain representation of the complex conjugate of the synthesis operator for a point illumination of the bottom boundary of the gradient layer at 5000m; (b) the areal shot record, synthesized according to the synthesis operator from (a); (c) the cross-correlation along the time axis of the complex conjugate of the synthesis operator and the areal shot record. Note that in (b) a traveltime track of the synthesis operator is overlaying the areal shot record.*

4.4 Conclusions

In this chapter we have introduced a new method to evaluate macro boundaries and macro velocities, based on the method of controlled illumination. The method is based on the relation between the synthesis operator and the related areal shot record. If the desired source wave field at a macro boundary is a normal incident wave field or a focus point, the events of the illuminated boundary will occur identically in the synthesis operator and in the related areal shot record (Figure 4.4 and 4.5). If the desired source wave field is non-normal incidence, a relation can be found between the areal shot record and the synthesis operator of the opposite illumination angle (Figure 4.6 and 4.7). A 1-D cross-correlation along the time axis between the correct synthesis operator and the areal shot record should result in an event aligning along the $t=0$ axis. Results on field data showed that these gathers indeed contain important information that can be used to evaluate the quality of the macro model *prior to prestack migration*.

Areal shot record migration

5.1 Introduction

In chapter 2 the principle of areal shot record technology has been described. In chapter 3 it has been shown that the construction of areal shot records from prestack data can be done in such a way that a specific part of the subsurface is illuminated by a user-defined source wave field. In this chapter we will show that the areal shot records can be migrated using the same scheme as the conventional shot record migration scheme. Two approaches to the combination 'controlled illumination - depth migration' are proposed as well as illustrated on a simple example. Finally the important issue of imaging is discussed.

5.2 Areal shot record migration

We recall the forward model after synthesis (equation (2.10a)):

$$\vec{P}_{syn}^{-}(z_0) = X_0(z_0,z_0) \, \vec{S}_{syn}^{+}(z_0),$$

(5.1a)

with

$$\vec{S}_{syn}^{+}(z_0) = S^{+}(z_0) \, \vec{\Gamma}(z_0).$$

(5.1b)

For the migration of the areal shot record, $\vec{P}_{syn}^{-}(z_0)$, the source wave field $\vec{S}_{syn}^{+}(z_0)$ is forward extrapolated to a range of depth levels z_i:

$$\vec{S}_{syn}^{+}(z_i) = W^{+}(z_i,z_0) \, \vec{S}_{syn}^{+}(z_0),$$

(5.2a)

and the areal shot record $\vec{P}_{syn}^{-}(z_0)$ is inverse extrapolated to the same range of depth levels z_i:

$$\vec{P}_{syn}^{-}(z_i) = [W^{-}(z_0,z_i)]^{-1} \; \vec{P}_{syn}^{-}(z_0) \tag{5.2b}$$

followed by imaging (see section 5.4):

$$\hat{R}(x_j,y_k,z_i) = \frac{1}{N}\sum_{\omega} P_{syn}^{-}(x_j,y_k,z_i,\omega) \, / \, S_{syn}^{+}(x_j,y_k,z_i,\omega), \tag{5.2c}$$

where $P_{syn}^{-}(x_j,y_k,z_i,\omega)$ represents the jth element of the kth subvector of $\vec{P}_{syn}^{-}(z_i)$, and $S_{syn}^{+}(x_j,y_k,z_i,\omega)$ represents the jth element of the kth subvector of $\hat{S}_{syn}^{+}(z_i)$. $\hat{R}(x_j,y_k,z_i)$ represents the estimated reflectivity at (x_j,y_k) of depth level z_i. N is the number of frequency components. Note that the actual implementation of a migration process based on equations (5.2a), (5.2b) and (5.2c) can either be recursive or non-recursive. It is obvious that when wave fields are extrapolated through inhomogeneous media, wavefront distortions should be taken into account. This applies to any kind of source, including point sources. Figure 5.1 shows a a horizontal plane source wave field propagating through an inhomogeneous macro model (the Marmousi model, see coming section 6.2). Note that the incident wave field at target level z_m is not a plane wave field due to the inhomogeneities of the overburden. This means that the only way to migrate (areal) shot records properly is *depth* migration.

Note that if we define the synthesis operator $\vec{\Gamma}(z_0)$ as:

$$\vec{\Gamma}(z_0) = [0, \, ..., \, 0, \, 1, \, 0, \, ..., \, 0]^T, \tag{5.3}$$

the described migration scheme becomes the conventional shot record migration scheme. Figure 5.2 shows the general scheme for (areal) shot record migration. Note that the synthesis operator can be designed target oriented.

5.3 Areal shot record migration after controlled illumination

An areal shot record, synthesized using the method of controlled illumination, migrated according to the previously described scheme (Figure 5.2), will result in a depth image for *all* depth levels z_i. The incident source wave field, however, is constructed in such a way that it will have a predefined shape at the target zone. Figure 5.3 shows the model used to illustrate the principle of areal shot record migration combined with controlled illumination. For the illuminating source wave field a horizontal plane wave is chosen at a depth of 450 m. The synthesis operator is modeled using the true model (Figure 5.4a) and the prestack data is synthesized using this operator, resulting in the areal shot record as shown in Figure 5.4b. Migration of this areal shot record using the scheme as described in the previous section results in the depth image as shown in Figure 5.5. Note that the depth image is obtained by the migration of *one* areal shot record only.

Another option is to extrapolate the receivers downward to the target zone (redatuming), after the synthesis for controlled illumination, but prior to the migration:
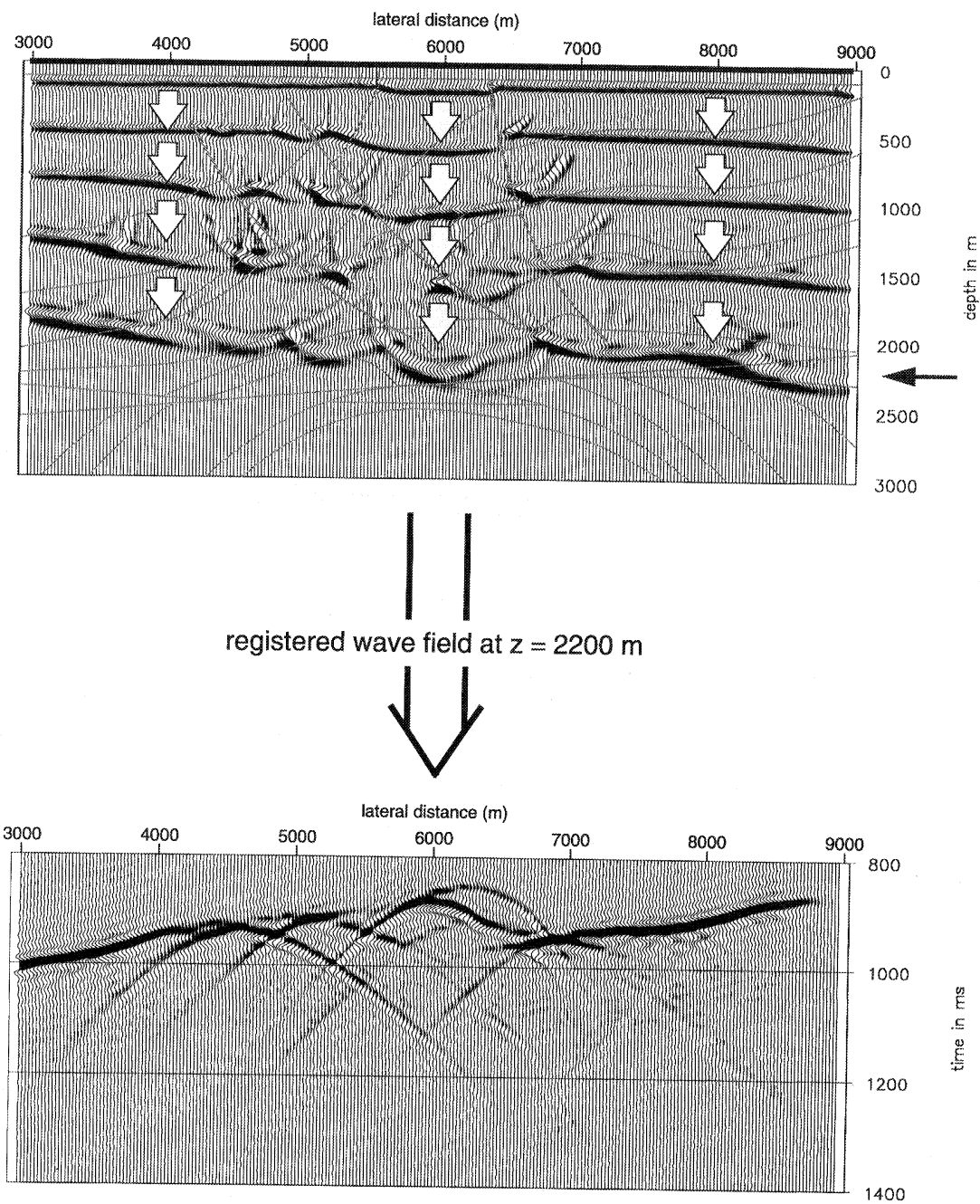
Figure 5.1 *A horizontal plane wave at the surface; snapshots in the Marmousi model (top). Areal source wave field at the target (z=2200m) due to the horizontal plane wave at the surface (bottom). Note the irregular and complex illumination of the target zone.*
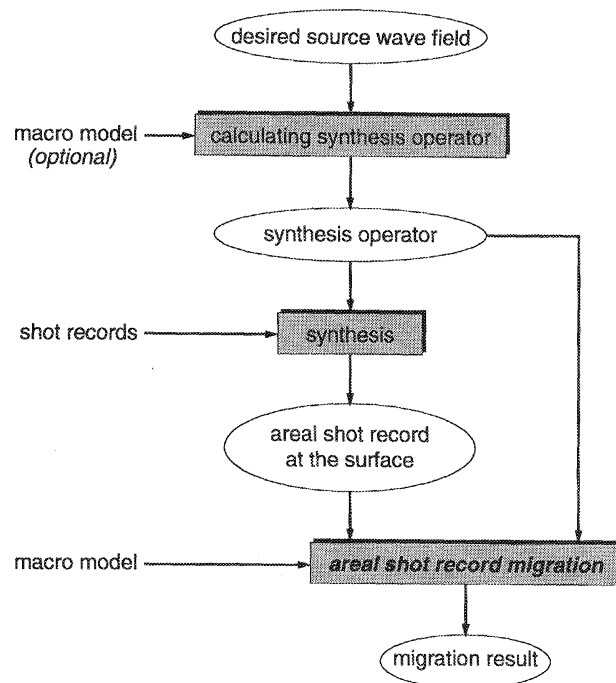
Figure 5.2   *Scheme for areal shot record migration. Note that the desired source wave field may be chosen target oriented (controlled illumination). The output is for all depth levels.*

$$\vec{P}_{syn}^{-}(z_m) = [W^{-}(z_0, z_m)]^{-1} \, X(z_0, z_m) \, \vec{S}_{syn}^{+}(z_m), \tag{5.4}$$

$X(z_0, z_m)$ being defined according to equation (3.9d), and to perform the migration only inside the target zone, using the extrapolated data:

$$\vec{P}_{syn}^{-}(z_m) = X(z_m, z_m) \, \vec{S}_{syn}^{+}(z_m), \tag{5.5a}$$

layer	c (m/s)	ρ (g/cc)
1	2400	1.
2	3000	1.6
3	3000	2.1
4	4100	2.2
5	3700	2.3
6	4200	2.
7	3500	1.8
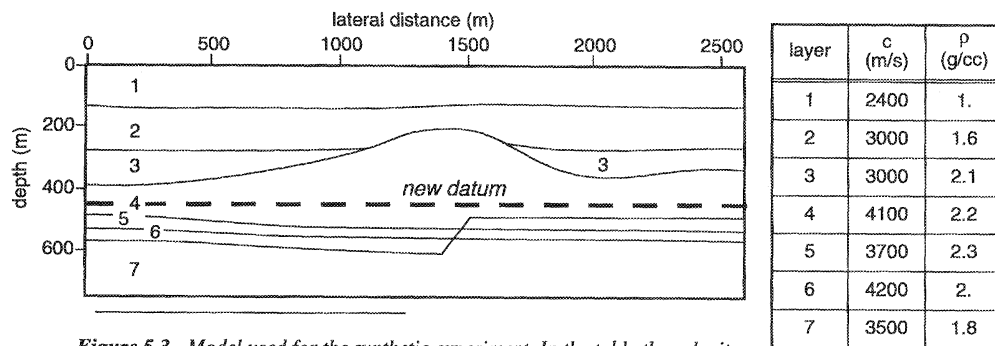
Figure 5.3   *Model used for the synthetic experiment. In the table the velocity c and density ρ per layer are indicated.*

time domain representation of $\vec{\Gamma}(z_0)$: the synthesis operator

time domain representation of $\vec{P}_{syn}^{-}(z_0)$: the areal shot record
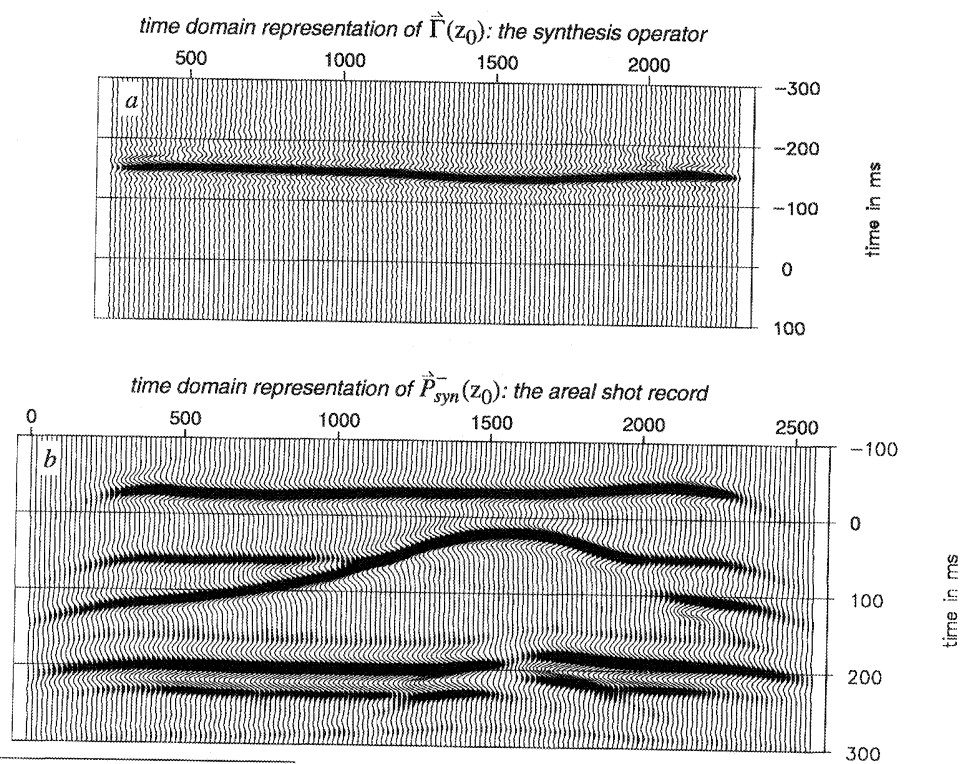
Figure 5.4 (a) Synthesis operator for a horizontal plane wave illumination at $z = 450$ m.
(b) Areal shot record; note that the source is the pre-defined source wave field (horizontal plane wave) at the target upper boundary, while the receivers are still positioned at the surface.
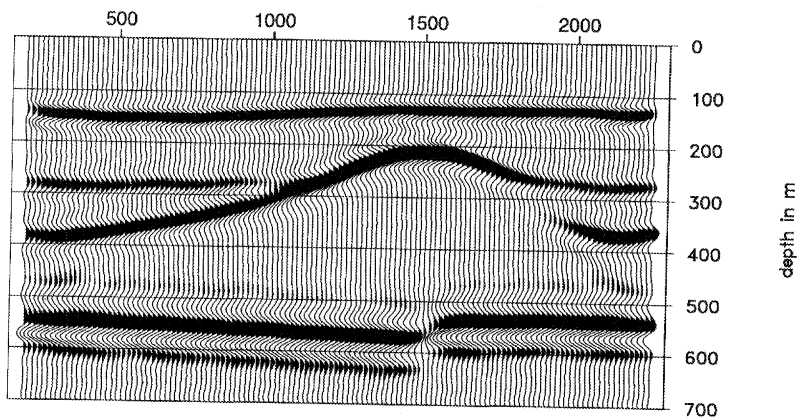
Figure 5.5 Result of migrating the areal shot record of Figure 5.4b, for all depth levels.

```
                    ┌─────────────────────────┐
                    │  desired source wave field │──────────────┐
                    │      at the target       │                │
                    └─────────────────────────┘                │
                              │                                 │
                              ▼                                 │
macro model ──────▶  ▓▓ calculating synthesis operator ▓▓       │
                              │                                 │
                              ▼                                 │
                    ┌─────────────────────────┐                │
                    │    synthesis operator   │                │
                    └─────────────────────────┘                │
                              │                                 │
                              ▼                                 │
shot records ──────▶  ▓▓▓▓▓▓▓ synthesis ▓▓▓▓▓▓▓                │
                              │                                 │
                              ▼                                 │
                    ┌─────────────────────────┐                │
                    │    areal shot record     │                │
                    │      at the surface      │                │
                    └─────────────────────────┘                │
                              │                                 │
                              ▼                                 │
macro model ──────▶  ▓▓ downward extrapolation ▓▓               │
                              │                                 │
                              ▼                                 │
                    ┌─────────────────────────┐                │
                    │    areal shot record     │                │
                    │      at the target       │                │
                    └─────────────────────────┘                │
                              │                                 ▼
macro model ──────▶  ▓▓ areal shot record migration ▓▓
                     ▓▓          in the target     ▓▓
                              │
                              ▼
                    ┌─────────────────────────┐
                    │    image of the target   │
                    └─────────────────────────┘
```
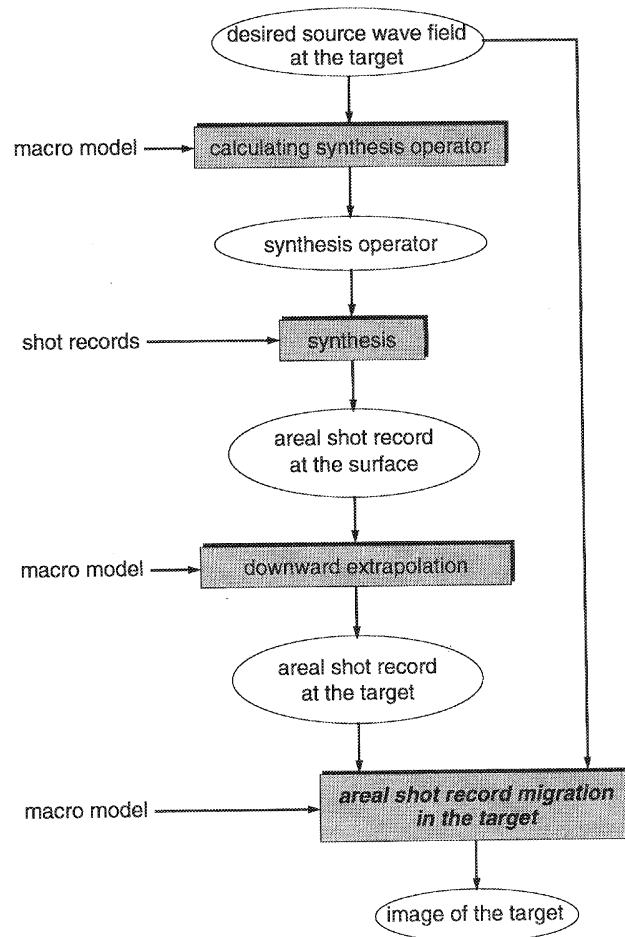
Figure 5.6   *Scheme for target oriented areal shot record migration, consisting of target oriented synthesis at the surface* (controlled illumination), *downward extrapolation to the target and migration in the target.*

and the user-defined source wave field:

$$\vec{S}^{+}_{syn}(z_m) = \vec{\Gamma}(z_m)\, S(\omega). \tag{5.5b}$$

The total processing flow for this scheme is shown in Figure 5.6. If the source signature is known, the synthesis operator can be convolved with this wavelet, leaving a depth section after areal shot record migration deconvolved for the source signature. Figure 5.7a shows the areal shot record of Figure 5.4b after downward extrapolation to a depth of 450 m. Figure 5.7b shows the result after migration in the target zone only.
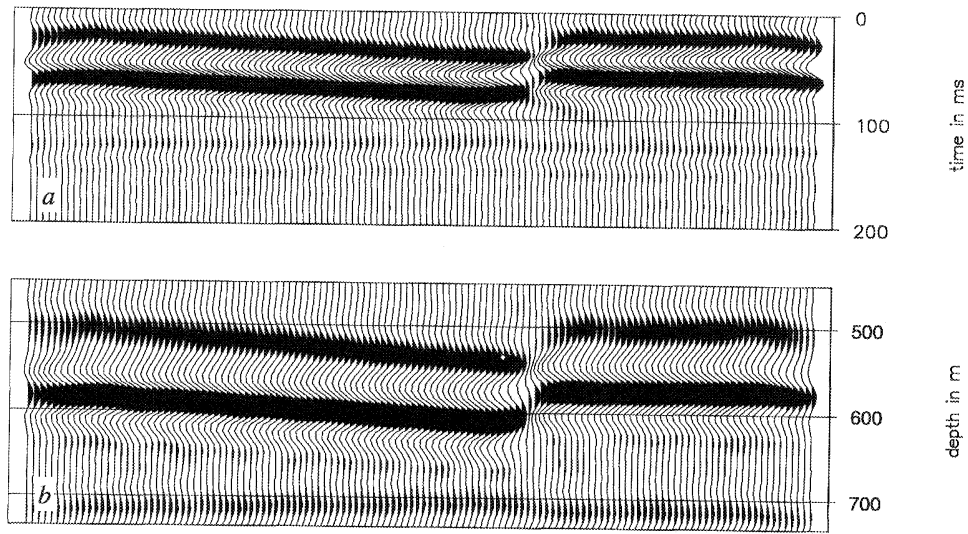
Figure 5.7 (a) Areal shot record after downward extrapolation of the receivers. This areal shot record represents the target response due to the pre-defined desired source wave field (i.e. a downgoing plane wave at depth level $z = 450m$).
(b) Result of target oriented areal shot record migration.

5.4 Imaging

In the migration process the major part of the computations is taken by the extrapolation of the wave fields through the macro model. Different types of migration make use of different types of extrapolation algorithms, in which there is a trade-off between accuracy and efficiency. The second part of the migration process is the imaging. The imaging principle relates the incident, illuminating, wave field at a position in the subsurface to the reflected wave field via the local reflectivity properties at that specific position. In this section we will show that the imaging principle is just as important as the quality of the extrapolation: an accurate extrapolation might still result in a bad image, if the imaging is not done properly. We will review the imaging principle for prestack depth migration and look at several practical implementations.

Recall the forward model for a homogeneous medium containing one reflector at depth z_m:

$$P^-(z_0) = W^-(z_0, z_m)\, R(z_m)\, W^+(z_m, z_0)\, S^+(z_0). \tag{5.6}$$

Extrapolation of both the prestack data $P^-(z_0)$ and the source wave fields $S^+(z_0)$ to the reflector depth z_m yields:

$$P^-(z_m) = R(z_m)\, S^+(z_m), \tag{5.7a}$$

hence

$$R(z_m) = P^-(z_m) \, [S^+(z_m)]^{-1}, \tag{5.7b}$$

relating the full reflectivity matrix $R(z_m)$, containing all angle-dependent information of depth level z_m to the incident and reflected wave fields $S^+(z_m)$ resp. $P^-(z_m)$, see Appendix A. Note that in the one-layer case, although both $P^-(z_m)$ and $S^+(z_m)$ represent monochromatic experiments, the full reflectivity matrix $R(z_m)$ can be estimated.

For the multi-layer case, the forward model for multiple-free data is given by:

$$P^-(z_0) = X_0(z_0, z_0) \, S^+(z_0). \tag{5.8a}$$

After extrapolation to depth level z_m, we obtain:

$$P^-(z_m) = X(z_m, z_m) \, S^+(z_m), \tag{5.8b}$$

hence

$$X(z_m, z_m) = P^-(z_m) \, [S^+(z_m)]^{-1}. \tag{5.8c}$$

Note that, neglecting transmission losses[1], $X(z_m, z_m)$ is defined as:

$$X(z_m, z_m) = R(z_m) + X_0(z_m, z_m), \tag{5.8d}$$

hence contains both the reflectivity properties $R(z_m)$ of depth level z_m, and amplitude and phase distorted reflectivity information of other depth levels, $X_0(z_m, z_m)$. It is possible to retrieve the full reflectivity information, i.e. the full reflectivity matrix $R(z_m)$, by a weighted addition, in which each frequency component of $X(z_m, z_m)$ is transformed into the linear Radon domain, and summed along lines of constant rayparameter (de Bruin, 1992). In the Radon domain the reflectivity matrix $\tilde{R}(z_m)$ is independent of the frequency, whereas $\tilde{X}_0(z_m, z_m)$ is frequency dependent. To obtain a good estimate of the reflectivity at z_m we can sum all frequencies, because all terms $\tilde{R}(z_m)$ add up coherently, whereas the terms $\tilde{X}_0(z_m, z_m)$ will interfere destructively:

$$\hat{\tilde{R}}(z_m) = \frac{1}{N} \sum_{\omega} \tilde{X}(z_m, z_m), \tag{5.9}$$

with N being the number of frequency components. Equation (5.9) can be interpreted as taking the linear Radon transform of the prestack data $P^-(z_m)$ deconvolved for the incident source wave fields $S^+(z_m)$, and selecting the data at $\tau = 0$ and $p = 0$.

As described in section 5.2, in (areal) shot record migration the reflectivity estimate is based on:

$$\vec{P}^-(z_m) = R(z_m) \, \vec{S}^+(z_m). \tag{5.10}$$

---

1. The complete expression in equation (5.8d) reads: $X(z_m, z_m) = R(z_m) + T^+(z_m) \, X_0(z_m, z_m) \, T^-(z_m)$,

   where $T^+(z_m)$ and $T^-(z_m)$ represent the transmission operator for down- and upgoing waves resp. at depth z_m

Only in very few cases the full angle-dependent reflectivity is required. For AVO, AVA and stratigraphic inversion techniques, angle-dependent reflectivity is used to relate the seismic reflections to lithologic contrasts (de Bruin, 1992) or rock and pore parameters (de Haas, 1992, Lörtzer, 1990). In general a so-called 'wide-angle zero-offset reflectivity' is sufficient for structural imaging. In that case only the elements along the diagonal of matrix $R(z_m)$ are estimated. Each element can be obtained by dividing one element of vector $\vec{P}^-(z_m)$ by the corresponding element of the vector $\vec{S}^+(z_m)$. Hence the imaging can also be formulated as (see equation (5.2c)):

$$\hat{R}(x_j, y_k, z_m) = \frac{1}{N}\sum_\omega P^-(x_j, y_k, z_m, \omega) \, / \, S^+(x_j, y_k, z_m, \omega),\qquad(5.11a)$$

or

$$\hat{R}(x_j, y_k, z_m) = \frac{1}{N}\sum_\omega \frac{P^-(x_j, y_k, z_m, \omega)\,[S^+(x_j, y_k, z_m, \omega)]^*}{\left| S^+(x_j, y_k, z_m, \omega) \right|^2}.\qquad(5.11b)$$

To ensure stability in the inversion in equation (5.11a), a crude estimate of $\hat{R}(x_j, y_k, z_m)$ is obtained by leaving out the scaling with the local source wave field. This leads to the most simple implementation of the imaging principle, the so-called *correlation* version (Claerbout, 1971):

$$\hat{R}(x_j, y_k, z_m) = \frac{1}{N}\sum_\omega P^-(x_j, y_k, z_m, \omega)\,[S^+(x_j, y_k, z_m, \omega)]^*.\qquad(5.12)$$

For more inhomogeneous macro models (see e.g. Figure 5.1) the source wave field can be severely distorted, such that we also have to take the amplitude variation of the illuminating source wave field into account. Hence we have to use equation (5.11b) for the imaging. Due to the inhomogeneities, shadow zones may occur, i.e. places where the amplitude of the source wave field is very small. To ensure that the solution remains stable, we have to stabilize the inversion:

$$\hat{R}(x_j, y_k, z_m) = \frac{1}{N}\sum_\omega \frac{P^-(x_j, y_k, z_m, \omega)\,[S^+(x_j, y_k, z_m, \omega)]^*}{\left| S^+(x_j, y_k, z_m, \omega) \right|^2 + \varepsilon^2},\qquad(5.13)$$

where ε is a stabilization constant.

Using equation (5.13) to relate an incident wave field to a reflected wave field via a reflection coefficient can be done if the incident wave field consists of only *one* event. If the incident wave field consists of more than one wave field with different local angles of incidence, an *average* reflection coefficient will be obtained. Note that with the help of controlled illumination we are able to construct a wavefront with only one incident wavefront at any position in the subsurface.

This means that we are able to obtain the angle-dependent reflection coefficient from our data in a user-specified area, allowing for further litho-stratigraphic inversion.

Another approach to get a best broad-band estimate of the reflectivity is based on the following relation:

$$P^-(x_j, y_k, z_m, \omega) = R(x_j, y_k, z_m) \, S^+(x_j, y_k, z_m, \omega), \qquad \text{for all } \omega. \tag{5.14}$$

The least-squares estimate of $R(x_j, y_k, z_m)$ is based on the relation:

$$E = \sum_\omega \left| P^- (x_j, y_k, z_m, \omega) - R(x_j, y_k, z_m, \omega) \, S^+ (x_j, y_k, z_m, \omega) \right|^2 = minimum. \tag{5.15a}$$

The least-squares estimate of $R(x_j, y_k, z_m)$ yields:

$$\frac{\partial E}{\partial R} = 0 \tag{5.15b}$$

hence

$$\hat{R}(x_j, y_k, z_m) = \frac{\displaystyle\sum_\omega \left[P^- (x_j, y_k, z_m, \omega) \right] \left[S^+ (x_j, y_k, z_m, \omega) \right]^*}{\displaystyle\sum_\omega \left| S^+ (x_j, y_k, z_m, \omega) \right|^2}. \tag{5.15c}$$

The nominator of equation (5.15c) represents the zero time part of the cross-correlation of the incident and reflected wave field at depth z_m, i.e. the image after correlation (equation (5.12)). The denominator represents the zero-time part of the auto-correlation of the incident wave field. For practical implementation we have to stabilize equation (5.15c), leaving:

$$\hat{R}(x_j, y_k, z_m) = \frac{\displaystyle\sum_\omega \left[P^- (x_j, y_k, z_m, \omega) \right] \left[S^+ (x_j, y_k, z_m, \omega) \right]^*}{\displaystyle\sum_\omega \left| S^+ (x_j, y_k, z_m, \omega) \right|^2 + \varepsilon^2}. \tag{5.15d}$$

Equation (5.15d) gives a more stable estimate of the reflection coefficient than equation (5.13), since there every frequency has to be stabilized separately, whereas in this case only the zero-time part of the auto-correlation has to be stabilized.

To illustrate the three derived imaging principles we will conduct an experiment in which we let the incident source wave field at target level z_m of Figure 5.1 (the Marmousi model) reflect at a horizontal interface with an angle *in*dependent reflection coefficient yielding unity. At the reflector at z_m the reflected wave field $\overset{\frown}{P}^-(z_m)$ is in that case equal to the incident wave field $\overset{\frown}{S}^+(z_m)$.

The result after imaging using the conventional correlation technique (equation (5.12)) is shown in Figure 5.8a. Note that parts that have a weak illumination are imaged worse, since we do not correct for amplitude variations of the incident wave field.

The result after imaging using the *stabilized inversion* (equation (5.13)) is shown in Figure 5.8b for three different stabilization factors $|\varepsilon|^2$, *0.1, 0.01* and *0.001*. Note that with a decreasing stabilization factor the result improves and almost reaches the ideal flat response with unit amplitude. For the larger stabilization factor the results tends to a scaled version of the *correlation* output as expected. Note that in this case the stabilization factors should be related to the amplitude of each monochromatically migrated result. The amplitudes of these vary in this experiment between *.01* and *2.5*. It is obvious that the value of the stabilization factor is of great importance for the quality of the image.In the next chapter we will show how the stabilization factor should be chosen in practice.

The result after imaging using the *least-squares* estimate (equation (5.15d)) is shown in Figure 5.8c. Also three different stabilization factors $|\varepsilon|^2$ are used, *0.1, 0.01* and *0.001*. The results are comparable to the results of the stabilized inversion, although the amplitude behaviour is slightly smoother. Note that in this case the stabilization factor should be related to the amplitude of the auto-correlation function of the incident source wave field at *t=0*. In this case this is equal to the result of the imaging using the correlation technique. It can be seen that the amplitude varies between *.1* and *1.1*. The results look smoother since the stabilization is performed *after* averaging over all relevant frequency components.

It may be concluded from these experiments that by scaling an image with the amplitude of the incident wave field, monochromatically or broad-band, it is necessary to obtain true-amplitude depth images. The influence of the stabilization factor on the depth image and the values chosen in practical situations is one of the aspects of areal shot record migration, that will be discussed in the next chapter.

5.5 Imaging angle-dependent reflectivity using controlled illumination

The local reflection coefficient, as derived in the previous subsection, equation (5.11a), represents in the conventional shot record migration after stacking of all individually migrated shot records, the *wide-angle zero-offset* reflectivity. With controlled illumination it is possible to construct an incident plane wave at a specific depth level or boundary. If we migrate the associated areal shot record we can relate the estimated reflection coefficient at the specified depth level or boundary to the angle-dependent reflection coefficient via the specified angle of illumination. This way we are able to construct the angle-dependent reflectivity curve point-by-point. To obtain the *absolute* value of the reflection coefficient the wavelet $S(\omega)$ should be known. We will illustrate this by a simple one reflector example. Two models are considered (Figure 5.9), a density contrast and a combined velocity-density contrast. The acquisition geometry consists of a fixed spread, ranging from *-3000* to *3000m*. The source positions cover the same range.
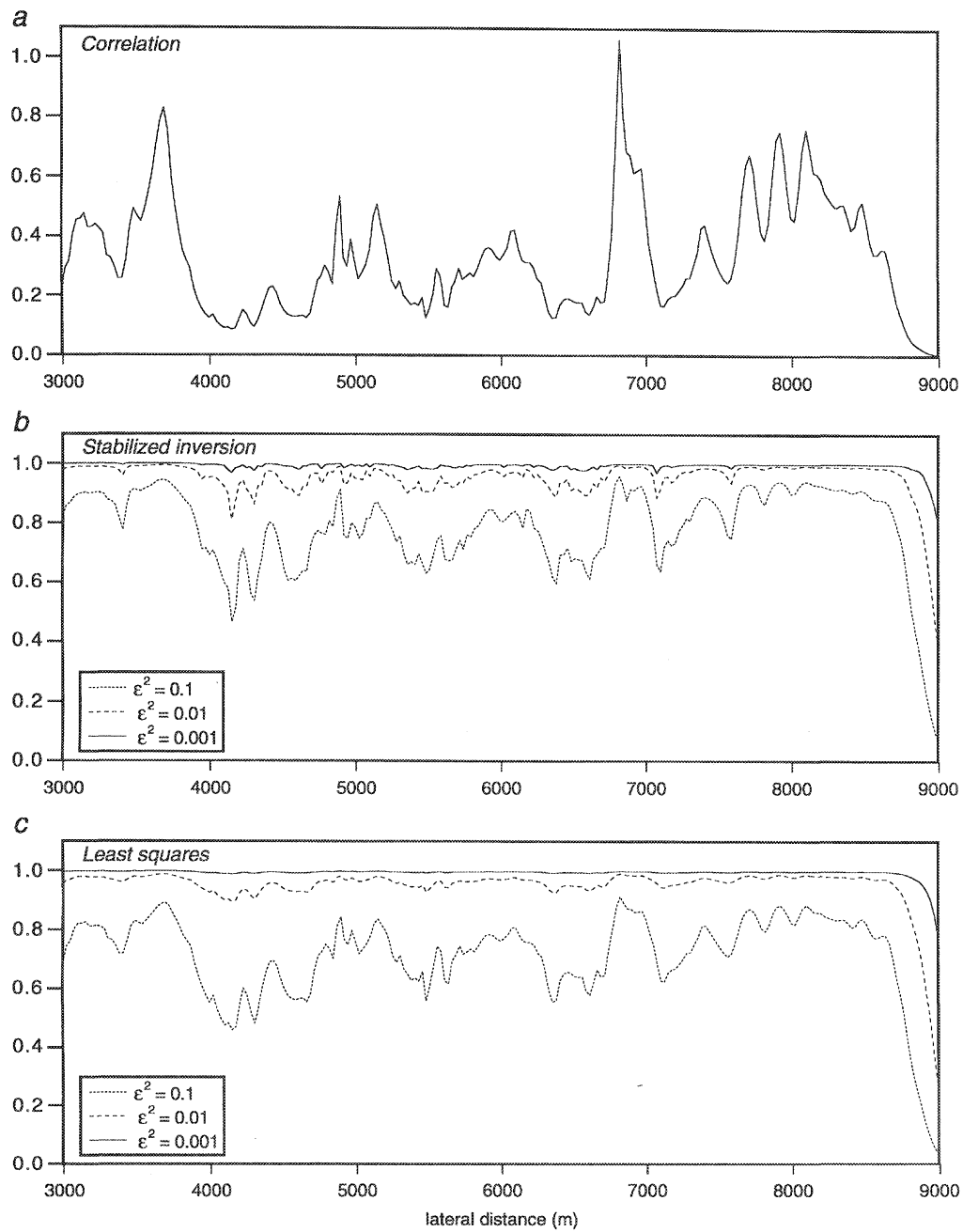
**Figure 5.8** *Image at a horizontal reflector for the incident wave field as shown in Figure 5.1 for different types of imaging. (a) correlation; (b) stabilized inversion for different stabilization factors; (c) least squares for different stabilization factors. Note the significant difference in the quality of the image. The importance of scaling with the amplitude of the incident source wave field is evident.*
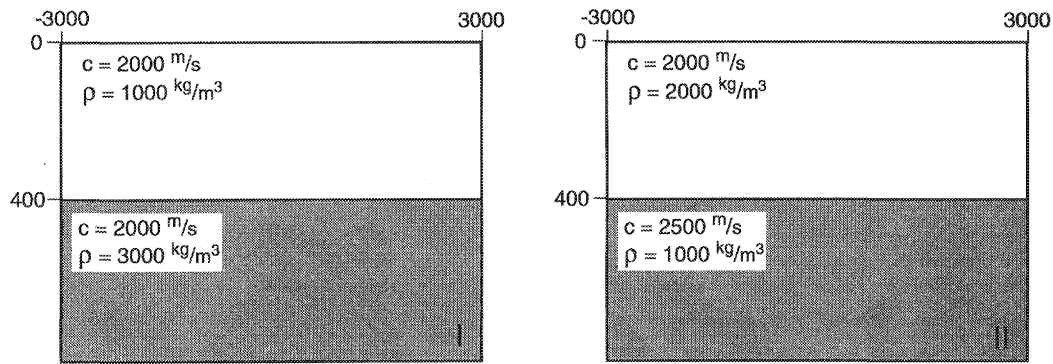
Figure 5.9 *The two models used to illustrate the imaging of angle-dependent information using controlled illumination. Model I is a density contrast over a horizontal interface at depth z=400m. Model II is a combined velocity-density contrast over a horizontal interface at depth z=400m. The acquisition geometry consists in both cases of a fixed spread, ranging from -3000 to 3000m. The source positions cover the same range.*

Target-oriented plane-wave responses are synthesized for rayparameters ranging from $p = 0$ $\mu s/m$ to $p = 400 \, \mu s/m$ for both experiments. All areal shot records are migrated. Figure 5.10 shows one depth section for $p = 200 \, \mu s/m$ (which corresponds to an angle of approx. $24°$) for the density contrast. For one lateral position the amplitude at the reflector is picked for all rayparameters and plotted in Figure 5.11 together with the theoretical angle-dependent reflection curves for both models. The results show that in both cases the error is less than 5% for rayparameters smaller than $p = 360 \, \mu s/m$ (which corresponds to an angle of approx. $46°$). If the critical angle is approached ($p_{crit.} = (c_2)^{-1} = 400 \, \mu s/m$) for the combined velocity-density contrast, the imaging principle, extracting a local reflection coefficient, is no longer valid.

In conclusion we may state that by constructing incident plane waves at a specific depth level or boundary, it is possible to extract angle-dependent reflection curves from the seismic data for that specific depth or boundary after migration.
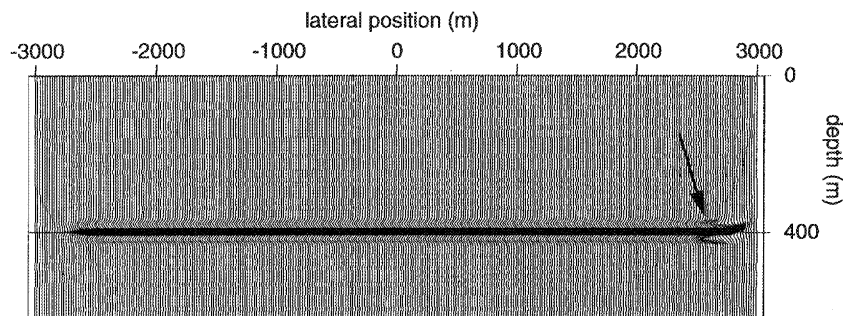
Figure 5.10 *Depth image of model I for a incident plane wave at depth z=400m, rayparameter p=200 $\mu s/m$ (approx. 24°). The arrow indicates an artifact due to the aperture limitation of the experiment.*
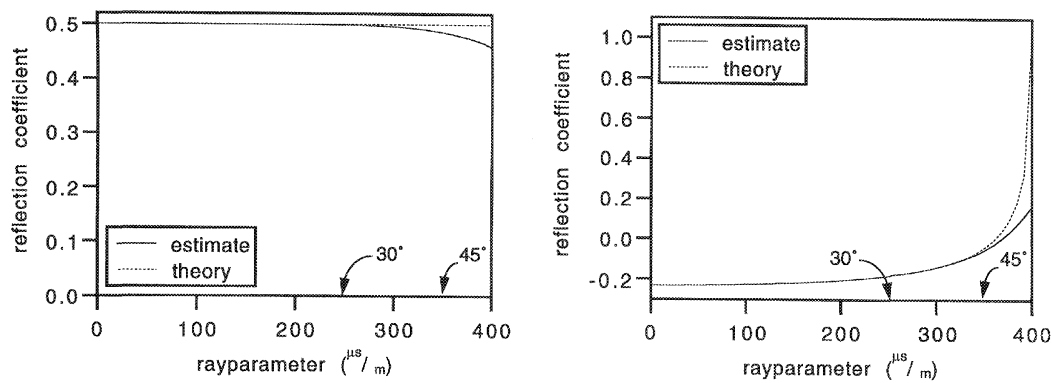
Figure 5.11 *Estimated and theoretical angle-dependent reflection coefficients for model I (left) and model II (right). For both cases the estimated curves give an error of less than 5% till a rayparameter p=360 $^{\mu s}/m$ (approx. 46°).*

In Chapter 4 it was shown, that if a *focus point* illumination is defined somewhere in the sub-surface, and if the macro model for the construction of the synthesis operator is correct, then the complex conjugate of the synthesis operator and the response of the focus point in the areal shot record are equal in traveltime and different in amplitude (subsection 4.2.1, equations (4.7a) and (4.7b)). The amplitude difference is caused by the angle-dependent reflectivity at the focus point (i.e. one column of the reflectivity matrix). Note that in this case the angle-dependent curves are obtained *prior* to migration. The use of focus point illumination in macro model estimation and AVO analysis is discussed by Berkhout (1995) and is beyond the scope of this thesis.

6

Examples

6.1 Introduction

In this chapter we will show results on the combination 'controlled illumination - depth migration' for a realistic synthetic dataset (Marmousi) and on a field dataset, a land case. On the Marmousi dataset also the influence of the different types of imaging will be shown for different types of source wave fields, both surface and target oriented. The results will be compared with the result after full prestack depth migration. All the examples are on two-dimensional (2-D) seismic lines. The extension of the method to 3-D will be discussed in chapter 7.

6.2 The Marmousi dataset

In this example we will show results on the well-known Marmousi dataset. This synthetic dataset was used as a blind test experiment to evaluate the quality of the industries inversion and prestack depth migration methods. The results of this blind test were presented during a workshop at the 52nd EAEG Meeting in Copenhagen (Versteeg and Grau, 1991).

In this section areal shot records will be synthesized for a plane wave *at the surface* and for a plane wave *at the target* (*controlled illumination*). Both areal shot records will be migrated by the areal shot record migration scheme using the *true* velocity model. The results will be compared with the result after full prestack depth migration and with the result of the migration of *one* shot record. Also the combination of results for different illuminating source wave fields will be shown. First a brief discussion of the model and the dataset will be given. Next, the preprocessing results will be discussed. For a more detailed description of the model, dataset and the preprocessing, the reader is referred to Versteeg and Grau (1991).
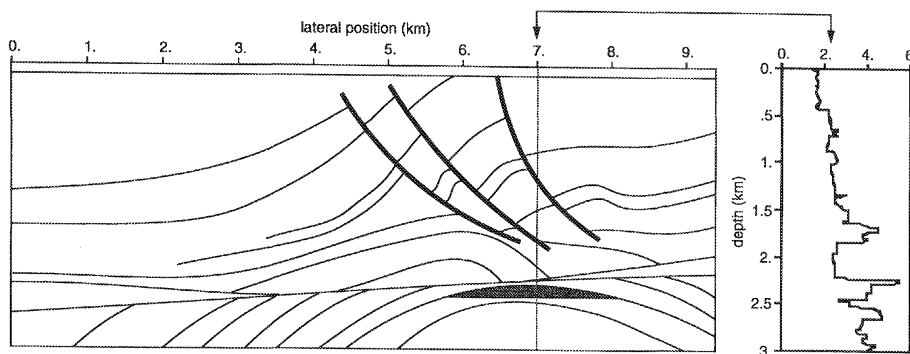
Figure 6.1   *An artist impression of the Marmousi model. Only some strong reflectors are indicated to obtain a feeling for the main structures in the model. Indicated is the potential reservoir. A velocity-log at x = 7000m is shown at the right hand side.*

6.2.1 The model and the dataset

An artist impression of the model is shown in Figure 6.1. Only some major interfaces are indicated to obtain a feeling for the main structures in the model. Next to the model a well-log is shown for a lateral position of 7000 m, showing the detail in this synthetic model.

The data was modeled with an acoustic finite difference scheme, second order both in space and time. The acquisition geometry is a marine acquisition (end of spread) containing 96 geophone groups, with an initial offset of 200 m. The number of shots modeled was 240. The source and receiver spacing was 25 m. The first shot was positioned at 3000 m; the last shot was positioned at 8975 m. The data has a length of 4s with a sampling interval of 4 ms.

6.2.2 Preprocessing

Surface-related preprocessing was applied in a two-step approach (Berkhout et al., 1991). First the thin layer reverberations were removed. After this, the surface-related multiple elimination technique was applied. The removal of the water layer reverberations improved the data significantly by sharpening the wavelet (Figure 6.2). Because the reflections in the first shallow layers of the model are weak due to the low contrasts, the multiple elimination technique did not improve the data very much. Finally the missing near offsets were interpolated using the CMP interpolation technique (DELPHI, Vol. I, Ch. 3, 1990). The required NMO velocities were based on the post-stack velocity estimates.

6.2.3 The shot record approach to prestack depth migration

In Chapter 2 the scheme for prestack shot record migration was shown (Figure 2.5). This scheme is applied for the whole 2-D line. Reciprocity is applied to all shot records to avoid edge effects during the extrapolation. After the depth migration of all the individual shot records, the depth sections are stacked in a true Common Depth Point sense. The source wave field is modelled as a band-limited pulse, with unit amplitude in the frequency domain. The frequency
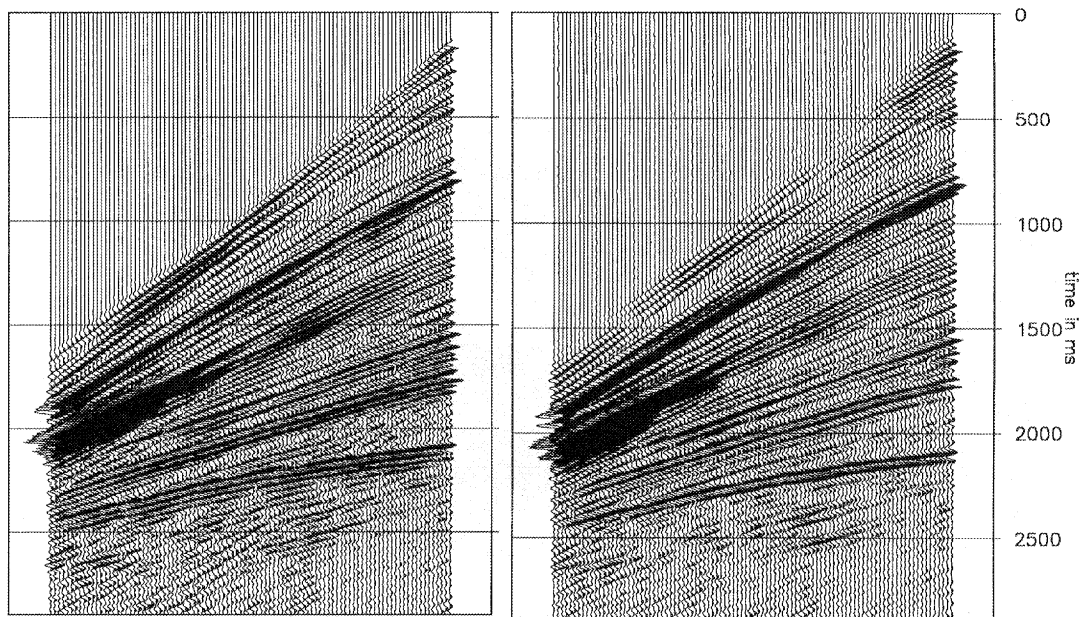
Figure 6.2 (a) Shot 40 of the Marmousi dataset; (b) Shot 40 after the removal of the thin layer reverberations.

range used in all migrations in this section ranges from 5 to 50Hz (185 frequency components). The result is shown in Figure 6.3. For the imaging the correlation was used. Since the fold at every depth point is large (approx. 240, i.e. the number of shot records) the influence of neglecting the amplitude variation in the source wave field during the imaging as discussed in Chapter 5, is not severe.

Figure 6.4 shows the result of the migration of *one* shot record at a source position of 6000m. The depth image shows weak illuminated positions, indicated by the arrows. These areas are not visible in the image after full prestack migration. Figure 6.5 shows an image gather at 6000m. The image gather shows the depth trace at the specified surface position for all individually migrated shot records. The prestack migration result is obtained by stacking all the traces in each image gather. Obviously areas indicated in Figure 6.4 are illuminated by other shot records. The horizontal alignment of the events in the image gathers indicate that a correct macro model is used for the migration. In complex media however, it is the influence of the illumination by the source wave field which makes the use of image gathers for macro model verification and estimation difficult.

The imaging principle used to obtained the results as shown in Figure 6.4 was the correlation (equation (5.12)). As was argued in section 5.4, for a true amplitude image the depth image should be scaled before or after imaging with the amplitude of the incident source wave field. In Figure 6.6 the result after migration of *one* shot record at a source position of 6000m is

lateral position (m)
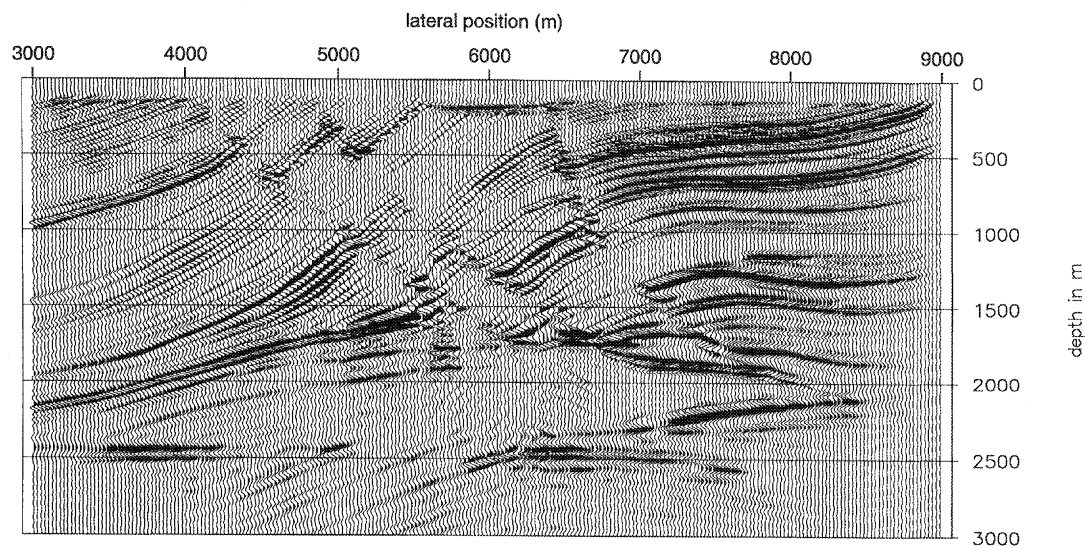
Figure 6.3   Depth image after full prestack depth migration, using the true velocity model.

lateral position (m)
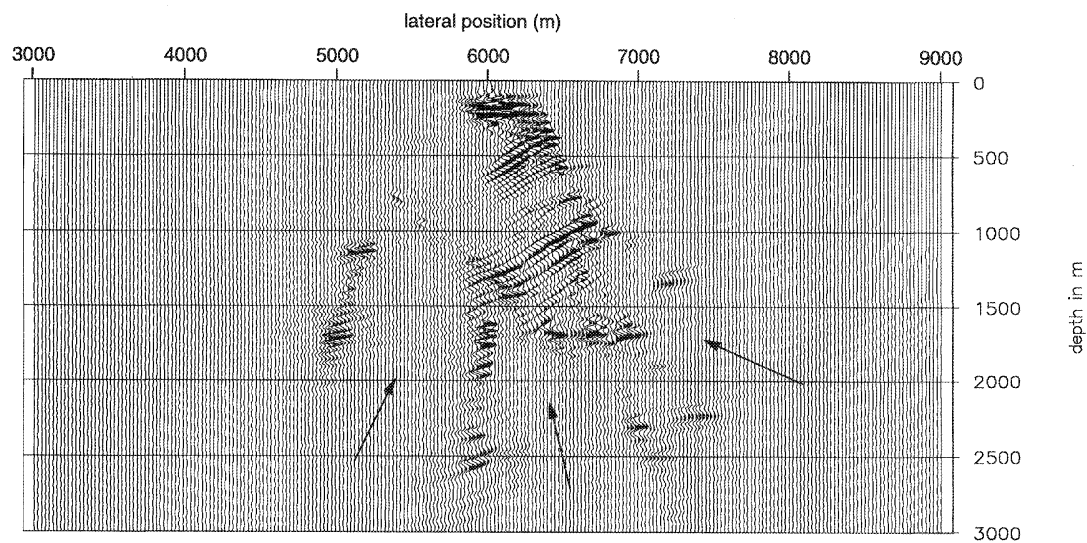
Figure 6.4   Depth image after depth migration of one shot record using the true velocity model. Indicated are the areas with a weak illumination. Prior to the migration reciprocity is applied to simulate a split spread acquisition geometry. This image is clipped at –15dB of the maximum value in the image.
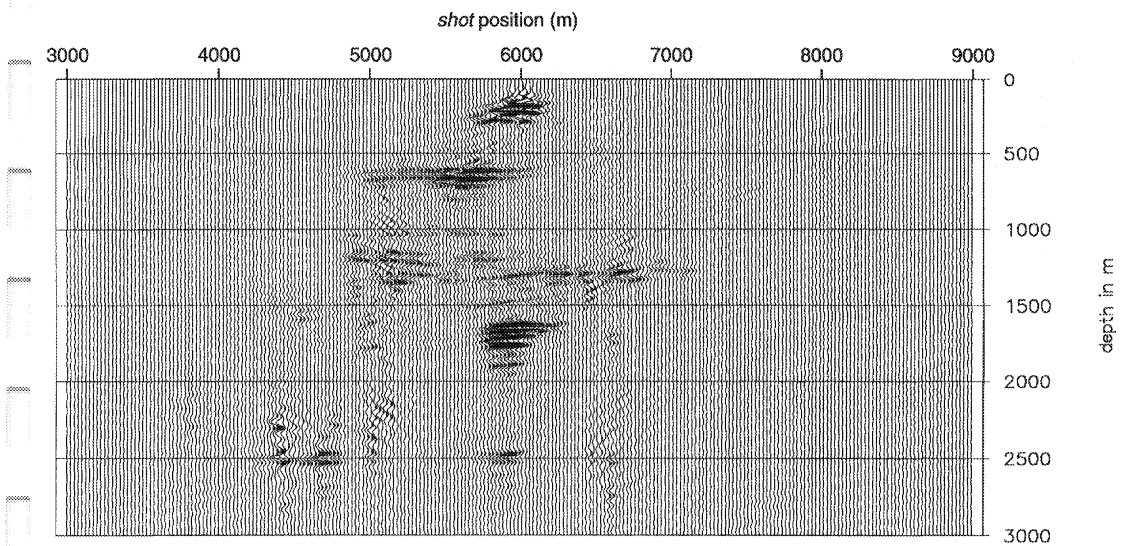
Figure 6.5 *Image gather at surface position 6000m. The image gather shows the depth image at 6000m for every individual shot record. Note the horizontal alignment of the events in the gather, indicating that the correct macro model was used for the migration. Also note the amplitude variations across the gather due to the change in illumination caused by the inhomogeneities of the macro model.*
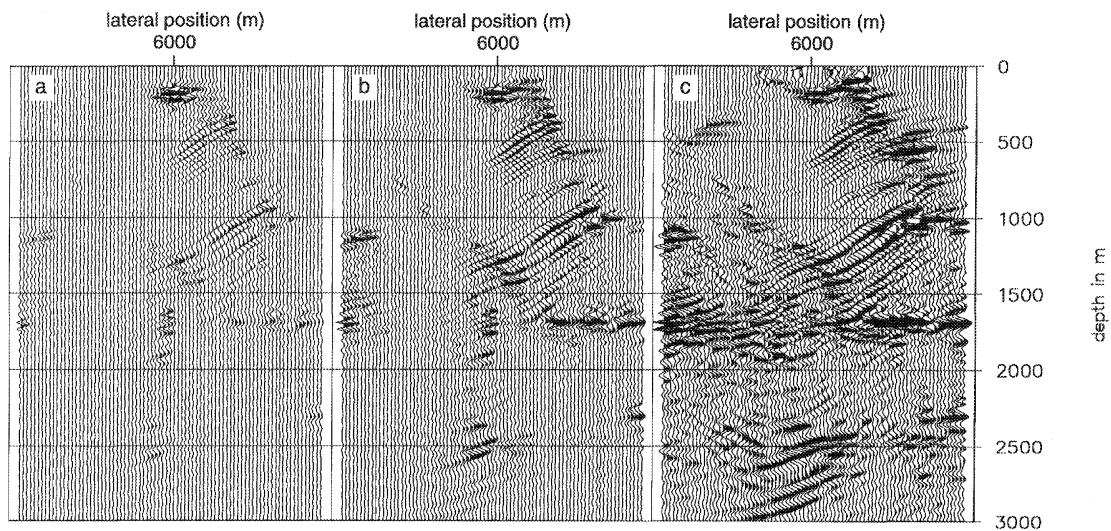
Figure 6.6 *Depth image after depth migration of one shot record using the true velocity model using the stabilized inversion as imaging principle. Results for three different stabilization factors are shown: $|\epsilon|^2 = 0.1$ (a); $|\epsilon|^2 = 0.01$ (b), and $|\epsilon|^2 = 0.001$ (c). All images are clipped at −6dB of the maximum value in the individual images. Notice the difficulty to find one stabilization factor to get a proper image at every depth level.*
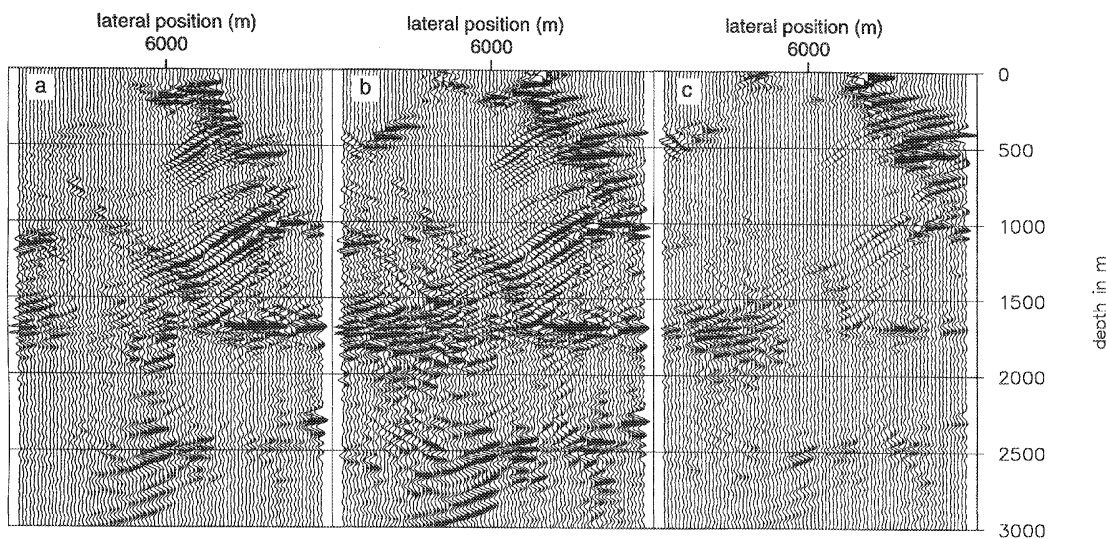
Figure 6.7   *Depth image after depth migration of one shot record using the true velocity model using the least-squares imaging as imaging principle.Results for three different stabilization factors are shown: $|\varepsilon|^2 = 1$. (a); $|\varepsilon|^2 = 0.1$ (b), and $|\varepsilon|^2 = 0.01$ (c). All images are clipped at $-6\mathrm{dB}$ of the maximum value in the individual images. Notice that if the stabilization factor is chosen too small, artifacts are blown up in the depth image.*

shown using stabilized inversion for the imaging. Results for 3 different stabilization factors are shown, $|\varepsilon|^2 = 0.1$, $|\varepsilon|^2 = 0.01$, and $|\varepsilon|^2 = 0.001$. Note how more reflectors become visible with decreasing stabilization factor. Also note the difficulty to find *one* stabilization factor to get a proper image at *all* depth levels. This is due to the fact that the amplitude of the incident source wave field changes with $1/\sqrt{r}$. The stabilization factor should be chosen fractional to the amplitude of the incident wave field, or at least be space dependent. The implementation of such a stabilization is not straight forward, since each frequency component would require a separate space dependent stabilization, which will have influence on the shape of the wavelet in the depth image.

In Figure 6.7 the result after migration of *one* shot record at a source position of 6000m using the least-squares approach for the imaging is shown. Results for 3 different stabilization factors are shown, $|\varepsilon|^2 = 1.$, $|\varepsilon|^2 = 0.1$, and $|\varepsilon|^2 = 0.01$. Note that this stabilization factor is broad-band, whereas the stabilization factor used in the stabilized inversion act on monochromatic images. The maximum value in the broad-band auto-correlation function of the source wave field (which is used to correct for the incident source wave field) has in this case a maximum amplitude of *186.*, but varies in the region directly below the source position at a depth range from 1000 to 2000m between *2.* and *1.* Since the correction for the amplitude of the incident source wave field is done in a broad-band sense, the stabilization factor can be chosen small. Again, it is difficult to find *one* stabilization factor to get a proper image at all depth levels. A space dependent stabilization should be able to do this. The implementation is again not straight forward, but is feasible when using the least-squares approach to the imaging principle.

6.2.4 Plane wave synthesis followed by areal shot record migration

In this subsection we will synthesize surface oriented areal shot records, i.e. plane-wave source wave fields at the surface. The result of the synthesis for a horizontal plane wave *at the surface* is shown in Figure 6.8. During the synthesis reciprocity was applied to simulate a split spread acquisition to avoid artifacts during the extrapolation. Figure 6.9 shows the depth section obtained by areal shot record migration with the true velocity model. For the imaging the correlation is used. We observe a fair image of the upper part of the section, whereas the deeper part (the target zone) is not imaged properly. This is due to the fact that the source wave field is severely distorted by the inhomogeneities of the model. Figure 6.10 shows the incident source wave field at a depth of 2200 m.

If for the imaging principle the stabilized inversion is used, we obtain a depth section as shown in Figure 6.11 ($|\varepsilon|^2 = 0.1$). To see the influence of the stabilization factor, three depth sections are shown in Figure 6.12 for a stabilization of $|\varepsilon|^2 = 0.1$, $|\varepsilon|^2 = 0.01$, and $|\varepsilon|^2 = 0.001$, i.e. approx. 10%, 1% and 0.1% of the average amplitude of the monochromatic source wave field. Only the middle part of the depth section is shown. It can be seen that the image does not improve considerably. The instabilities caused by the significant 'notches' in the illuminating source wave field outshine the reflections.

If for the imaging principle the least squares approach is used, we obtain a depth section as shown in Figure 6.14 ($|\varepsilon|^2 = 20.$). To see the influence of the stabilization factor, three depth
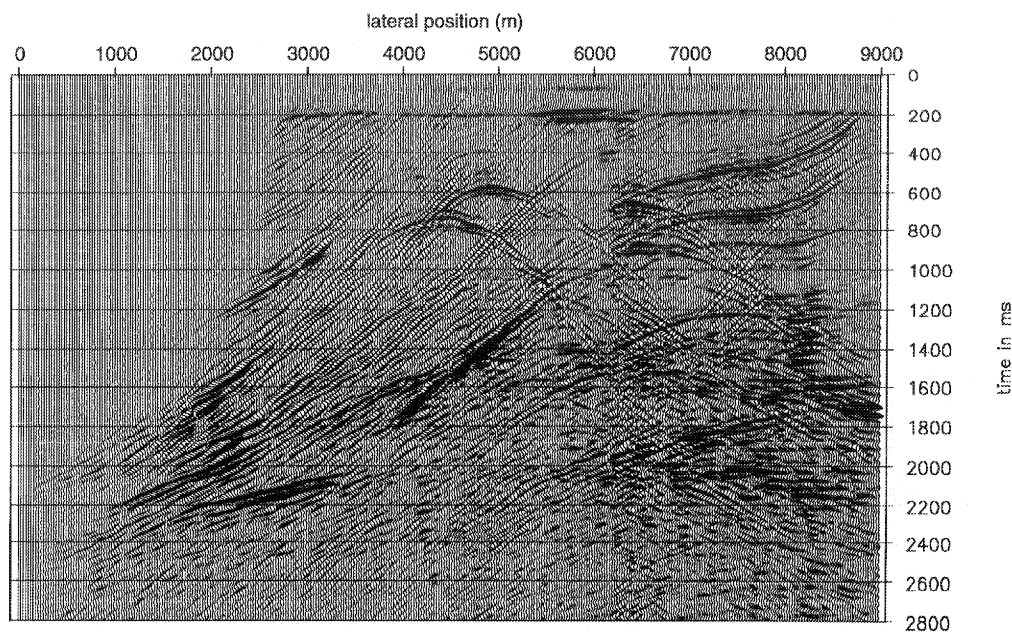

Figure 6.8   *Result after synthesis for a plane wave* at the surface *(conventional wave stack). Note the effect of the acquisition geometry at the left of this section.*

lateral position (m)
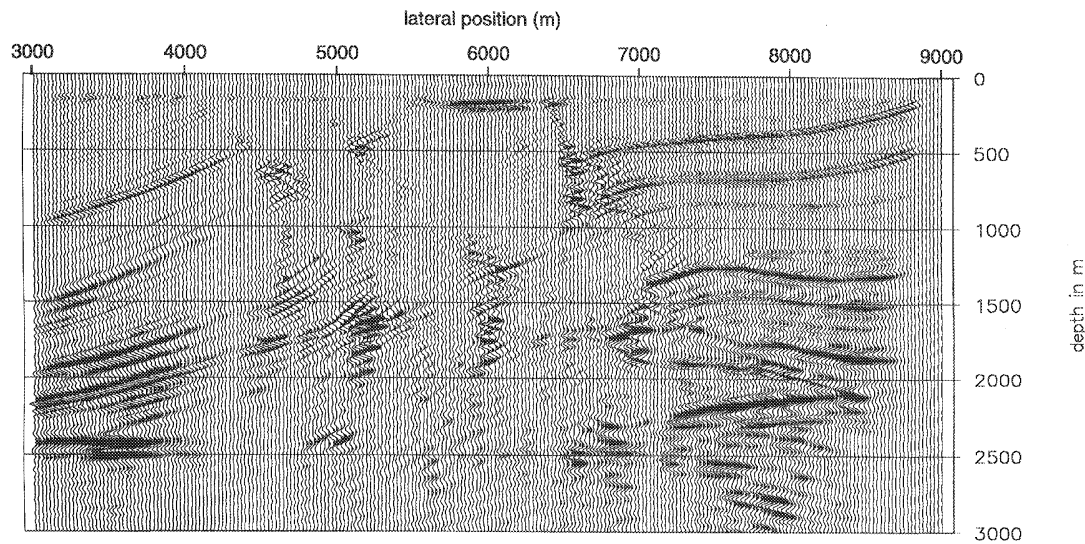
Figure 6.9 *Depth section after areal shot record migration of the conventional plane wave stack (Figure 6.8) using the true velocity model. Only the center part (directly beneath the areal surface source) is displayed. Note the bad image quality around the target (2500m).*

sections are shown in Figure 6.14. Only the middle part of the depth section is shown. For the stabilization $|\varepsilon|^2 = 20.$, $|\varepsilon|^2 = 2.$, and $|\varepsilon|^2 = 0.2$ are chosen, i.e. approx. 10%, 1% and 0.1% of the broad-band amplitude of the source wave field. Clearly there are more events visible compared with the result after correlation (Figure 6.9). The quality of the image however, does not improve with decreasing stabilization factor: again the image is distorted by the instabilities due to the notches in the illuminating source wave field. If the stabilization factors are chosen too small, even for shallow reflections instabilities are visible, damaging the proper reflections. The quality of the depth section in the target zone ($z>2500m$) is poor due to the complexity of the

lateral position (m)
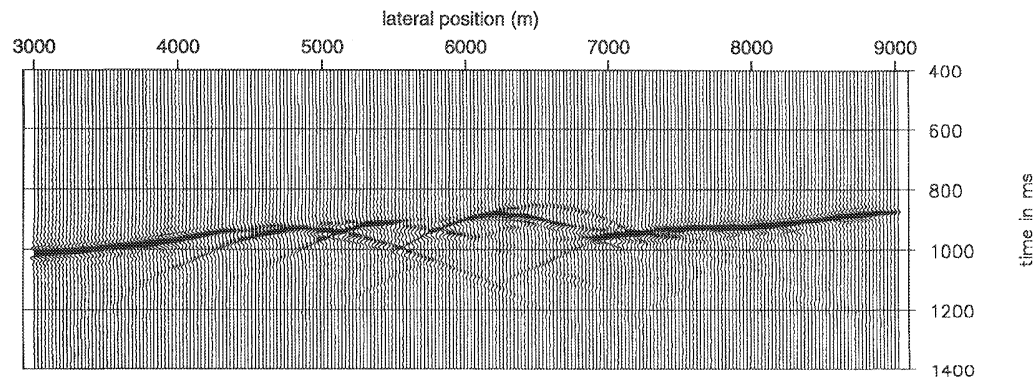
Figure 6.10 *The source wave field after propagation through the model, registered at z = 2200m. Note the severe complexity. Strong amplitude variations occur along the wave front due to the inhomogeneities of the*
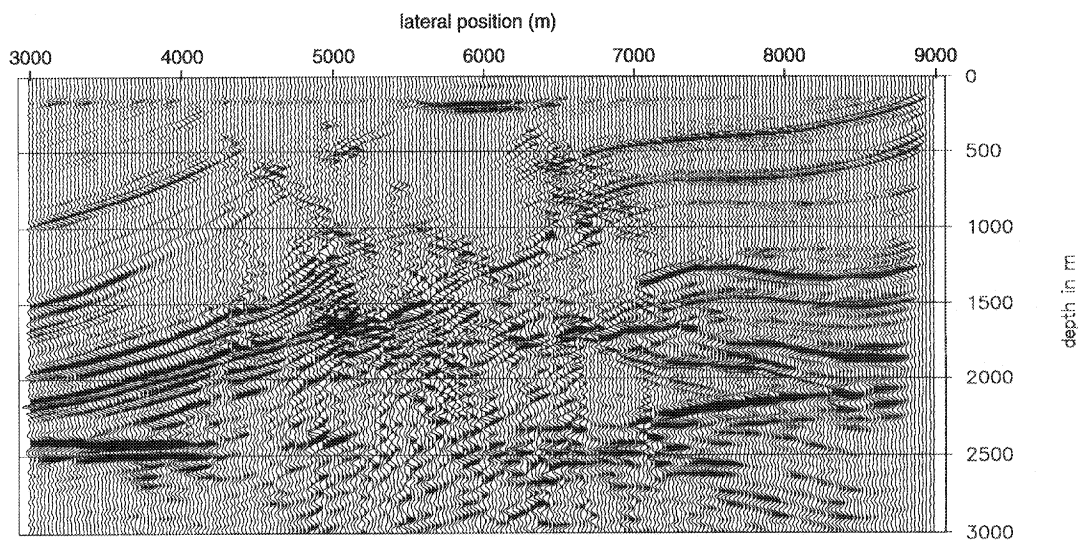
Figure 6.11 Depth image after depth migration of one areal shot record (p=0) using the true velocity model using the stabilized inversion as imaging principle using a stabilization factor $|\epsilon|^2=1$. The image is clipped at −6dB of the maximum value in the image. Note how instabilities 'propagated' through the depth section and outshine the proper imaged reflections.
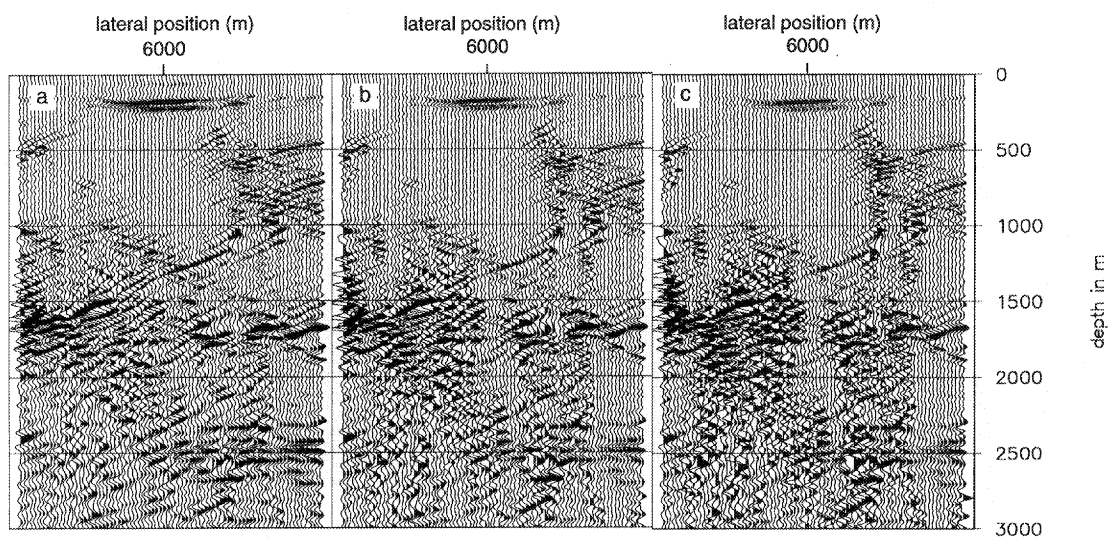
Figure 6.12 Depth image after depth migration of one areal shot record (p=0) using the true velocity model using the stabilized inversion as imaging principle.Results for three different stabilization factors are shown: $|\epsilon|^2=1$. (a); $|\epsilon|^2=0.01$ (b), and $|\epsilon|^2=.001$ (c). All images are clipped at −6dB of the maximum value in the individual images. Surface positions from 5000 to 7000 m are shown.

lateral position (m)

Figure 6.13 *Depth image after depth migration of one areal shot record (p=0) using the true velocity model using the least-squares imaging as imaging principle for a stabilization factor of $|\varepsilon|^2=20$. The image is clipped at −6dB of the maximum value in the image.*

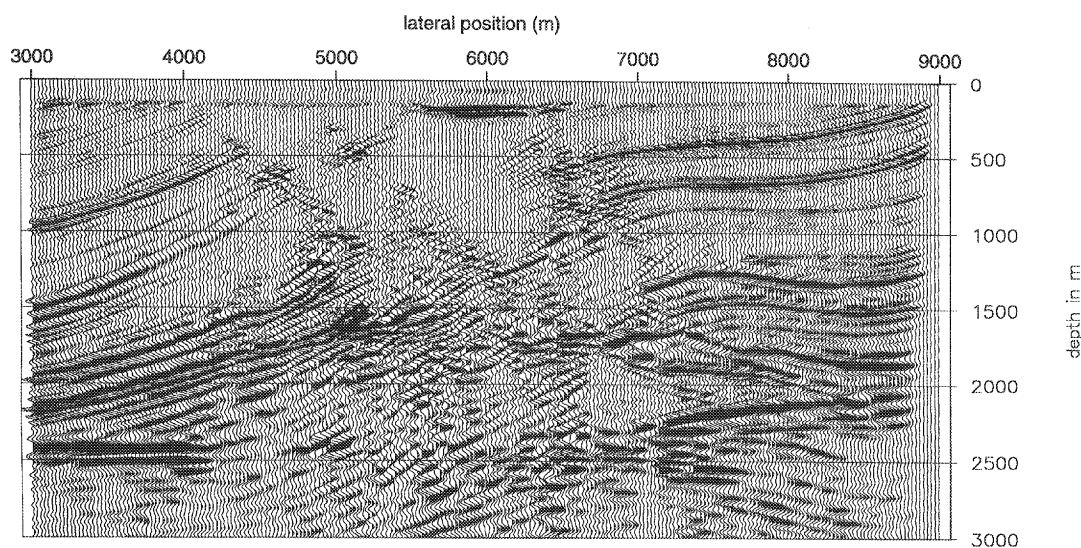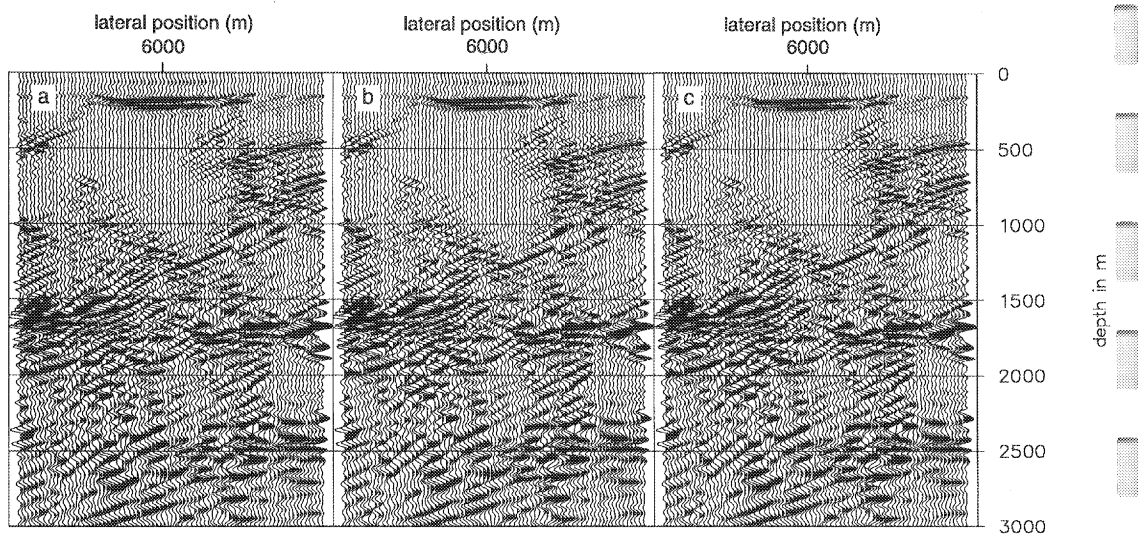**Figure 6.14** *Depth image after depth migration of one areal shot record (p=0) using the true velocity model using the least-squares imaging as imaging principle. Results for three different stabilization factors are shown: $|\varepsilon|^2=20$. (a); $|\varepsilon|^2=2$. (b), and $|\varepsilon|^2=0.2$ (c). All images are clipped at −6dB of the maximum value in the individual images. Notice that there are only minor differences between the three results, indicating that the influence of the stabilization factor is negligible.*

incident source wave field there. In fact, due to this complexity the imaging principle does not hold anymore: there is not *one* incident wavefront, hence an average reflection coefficient is imaged.

From the results shown in this subsection we may conclude that although for one areal shot record a depth image is obtained for all lateral positions, the complexity of the source wave field can make it impossible to get a proper image of the subsurface, even if the true model is used in the depth migration process.

6.2.5 Synthesis for controlled illumination followed by areal shot record migration

For the synthesis for controlled illumination we must first define our desired source wave field. As illuminating source wave field a horizontal plane wave is chosen at a depth level of $z = 2200m$. The synthesis operator was modeled using the true depth model, and is shown in Figure 6.15. The areal shot record after synthesis is shown in Figure 6.16. Again reciprocity is applied during the synthesis process to simulate a split-spread acquisition geometry. Applying the areal shot record migration scheme, we obtain the depth section as shown in Figure 6.17. As imaging principle the correlation is used. Here we observed a good image in the deeper part of the section, whereas the upper part gives a weak image of the faults. Note that opposite to the conventional surface oriented areal shot record synthesis, in this case the source wave field *at the surface* is complex, which gets simpler during the extrapolation through the overburden and ends up as a simple horizontal plane wave at the user-defined target.

If for the imaging principle the stabilized inversion is used ($|\epsilon|^2 = 0.1$), we see a spectacular improvement of the image in the upper part of the section (Figure 6.18). Also the deeper part of the of the depth section has improved. Only some minor instabilities are visible in shallow part of the depth section. If we compare the results as obtained by synthesis for a plane wave
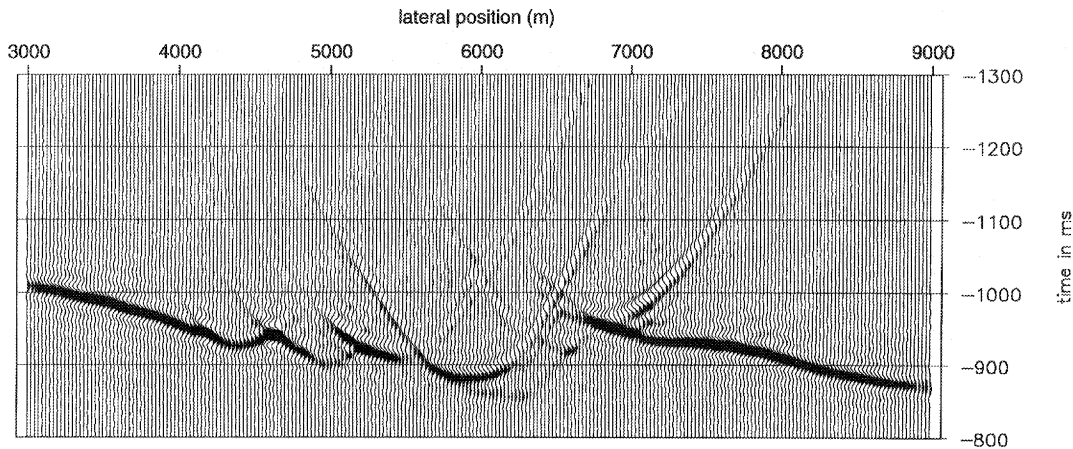
Figure 6.15 *Areal source wave field at the surface ($z = 0m$) to create a horizontal plane wave illumination at depth level $z = 2200m$.*

lateral position (m)
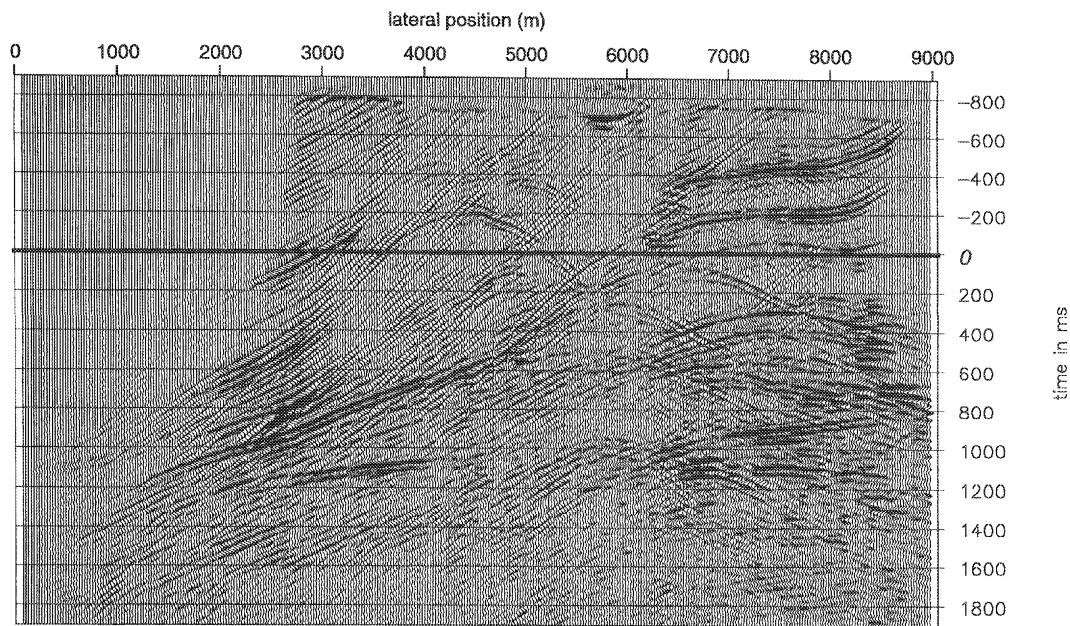
Figure 6.16 *Areal shot record after controlled illumination by a horizontal plane wave at depth level z = 2200m.*

lateral position (m)
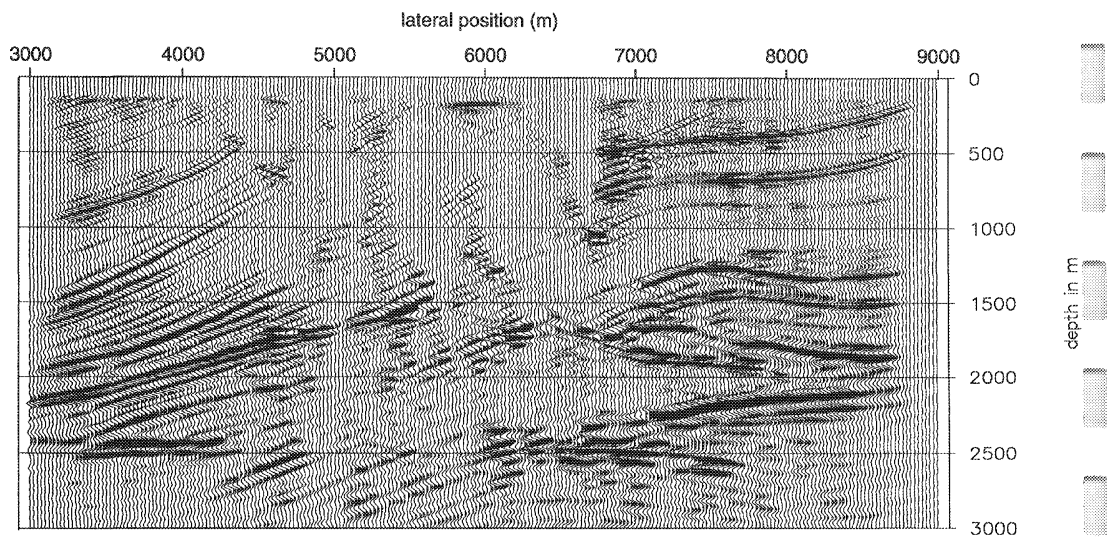
Figure 6.17 *Depth section obtained by migrating the areal shot record of Figure 6.16, using the correlation approach for the imaging (equation (5.12)).*
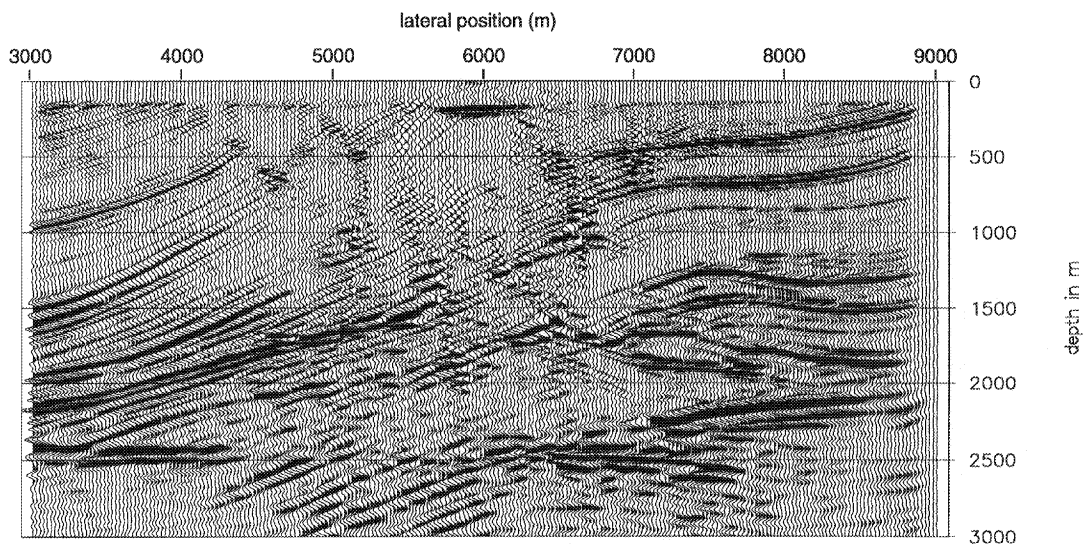
Figure 6.18 *Depth section obtained by migrating the target-oriented areal shot record of Figure 6.16., using the stabilized inversion as imaging principle (equation (5.13)) ($|\varepsilon|^2$=0.1). The image is clipped at –6dB of the maximum of the image. Note how instabilities disappear in the deeper part of the subsurface due to the fact that the source wave field gets simpler during propagation.*

at the surface (conventional plane wave stacking) followed by areal shot record migration (Figure 6.12), and by synthesis for controlled illumination followed by areal shot record migration (Figure 6.18), we see that the latter gives a much better result.

To see the influence of the stabilization factors three depth sections are shown for stabilization factors $|\varepsilon|^2$=0.1, $|\varepsilon|^2$=0.01 and $|\varepsilon|^2$=0.001 (Figure 6.19). Only the lateral positions from 5000 to 7000m are shown. Note that if the stabilization factor is chosen too low the instabilities will outshine the properly imaged reflections.

If for the imaging principle the least-squares approach is used ($|\varepsilon|^2 = 20.$), we obtain the depth section as shown in Figure 6.20. If we compare the result with the result of Figure 6.18, where the stabilized inversion is used, we see that the least-squares imaging gives a slightly more stable result. This can be explained by the fact that for the least-squares imaging the inversion is stabilized in a broad-band sense, whereas the stabilization in the stabilized inversion acts on monochromatic images.

To see the influence of the stabilization factors three depth sections are shown for stabilization factors $|\varepsilon|^2$=20., $|\varepsilon|^2$=2. and $|\varepsilon|^2$=0.2 (Figure 6.21). Only the lateral positions from 5000 to 7000m are shown. Note again that the results stay more stable compared to the results of the stabilized inversion (Figure 6.19).

From our experiments we may conclude that by controlling the source wave field in a target oriented way (*controlled illumination*) and by using an improved imaging principle, i.e. either
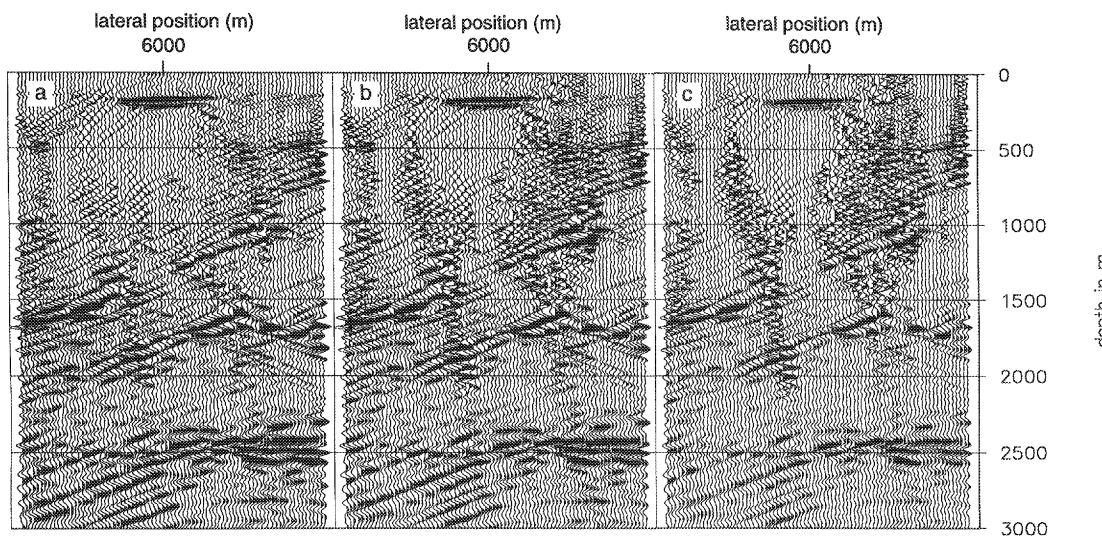
Figure 6.19 *Depth image after depth migration of one target-oriented areal shot record (p=0 at z=2200m) using the true velocity model, using the stabilized inversion as imaging principle. Results for three different stabilization factors are shown: $|\varepsilon|^2=0.1$ (a); $|\varepsilon|^2=0.01$ (b), and $|\varepsilon|^2=0.001$ (c). The images are clipped at −6dB of the maximum value in the individual images. Surface positions from 5000 to 7000m are shown.*
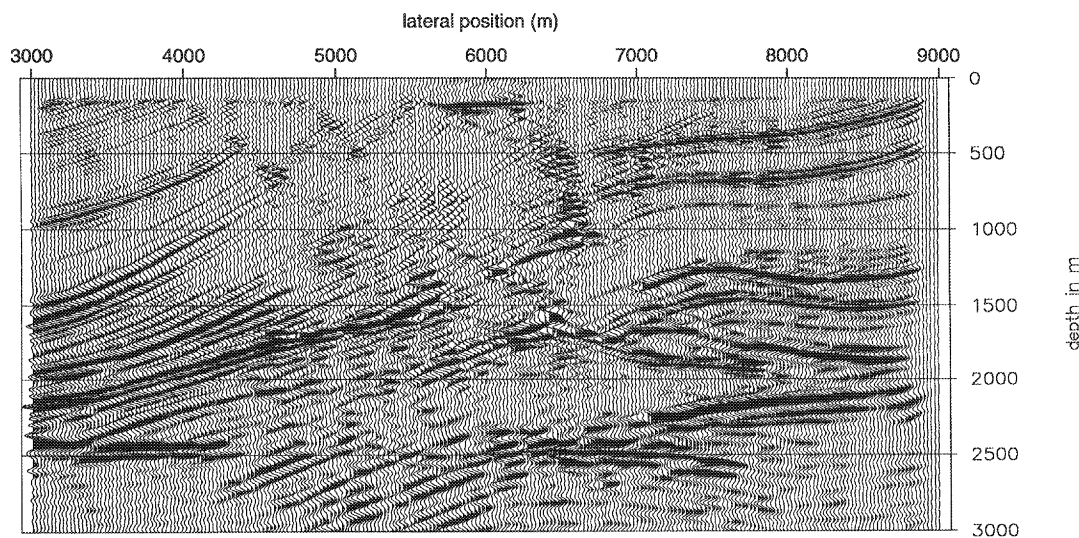
Figure 6.20 *Depth image after depth migration of one target-oriented areal shot record (Figure 6.16), using the least-squares as imaging principle ($|\varepsilon|^2=20.$). The image is clipped at −6dB of the maximum of the image. Note how instabilities disappear in the deeper part of the subsurface due to the fact that the source wave field gets simpler during propagation. Note that the result show more stable than the version where the stabilized inversion is used (Figure 6.18). This is due to the fact that the stabilization is applied in a broad-band sense.*
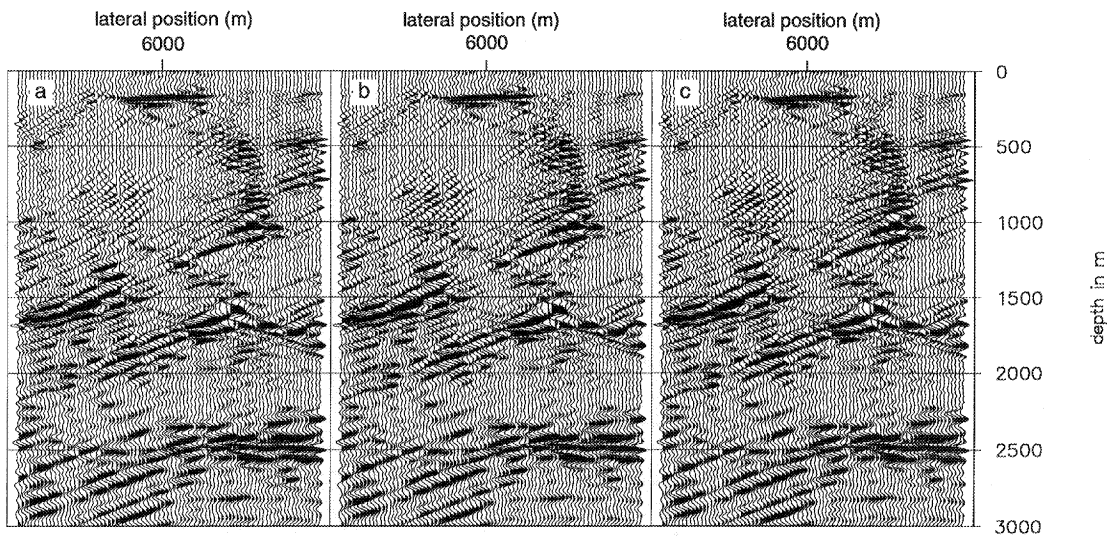
Figure 6.21 *Depth image after depth migration of* one *target-oriented areal shot record* (p=0 at z=2200m) *using the true velocity model, using the least-squares approach as imaging principle. Results for three different stabilization factors are shown:* $|\varepsilon|^2$=20. (a); $|\varepsilon|^2$=2. (b), and $|\varepsilon|^2$=0.2 (c). *The images are clipped at –6dB of the maximum value in the individual images. Surface positions from 5000 to 7000m are shown.*

stabilized inversion or the least-squares approach, a very good image of the target zone can be obtained, even for just *one* illumination angle. Note that the computational effort for the result of Figure 6.18 is comparable to the computational effort of the depth migration of one shot record.

### 6.2.6 Target oriented areal shot record migration for non-zero *p*-values

When an improved imaging principle is used, we saw in the previous section that it was possible to obtain a very good image of the target zone even for just one illumination angle. For parts of the subsurface where the incident source wave field is complex the image is disturbed by instabilities. If we would define a different areal source wave field, compute the synthesis operator, synthesize the areal shot record and migrate it, all the events that correspond to reflectors will be mapped at the same position, whereas the instabilities will appear different. The individual depth sections can be stacked in a true Common Depth Point sense, like in the conventional shot record migration scheme, thus amplifying the reflections and suppressing the instabilities. This holds for both the surface oriented and target oriented areal shot record migration. In this subsection we will show results on two experiments for a target oriented synthesis for non-zero rayparameters. The final stacked depth section for 5 different illumination angles will be shown for both the surface and target oriented areal shot record migration and be compared with the full prestack migration.

As illuminating wave field at depth level z = 2200m wavefronts were chosen for two constant *p*-values, $p = +25$ µs/m and $p = -25$ µs/m (*controlled illumination*). These *p*-values correspond
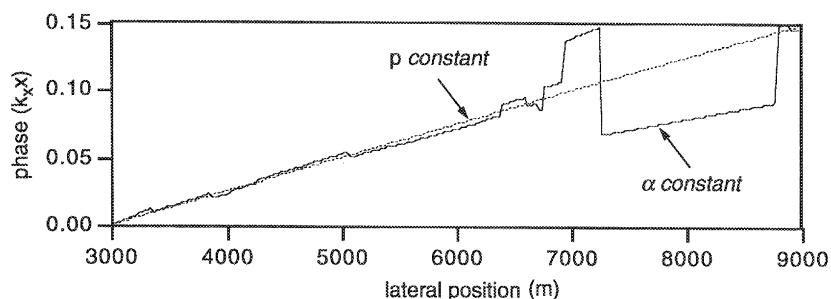
Figure 6.22 *Phase as function of the lateral position for a wave front at depth level $z = 2200m$ with constant angle of incidence (solid line), and constant p-value (dotted line). Note the fast changes of the phase for the illumination by a wave front with a constant angle, due to the lateral velocity variations*

to angles of approx. +5. resp. -5. degrees for a velocity of 3500 ^{m}/s (the average velocity at $z = 2200m$). It is important to realize that the choice for constant p-values was made in favor of a choice in angles of incidence due to the fact that the phase along the wavefront is in that case continuous (Figure 6.22) even in inhomogeneous media.

The two synthesis operators were modeled using the true depth model. The areal shot records after synthesis and the synthesis operators are shown in Figure 6.23 for $p = +25$ $^{\mu s}$/m, and in Figure 6.24 for $p = -25$ $^{\mu s}$/m. Using the areal shot record migration scheme, we obtained the depth sections as shown in Figure 6.25. As imaging principle we have used the stabilized inversion ($|\varepsilon|^2 = 0.1$). The depth section for $p = +25$ $^{\mu s}$/m (Figure 6.25a) shows more detail especially in the deeper part of the section. The reflectors to the left of the potential reservoir, between 2500 and 3000m are better imaged compared to the depth section obtained for $p = 0$ ^{s}/m (Figure 6.18). The depth section for $p = -25$ $^{\mu s}$/m (Figure 6.25b) shows more detail especially in the middle part of the section. The image of the faults has improved compared with the illumination for $p = 0$ and $p = +25$ $^{\mu s}$/m. In the deeper part the reflector at the right hand side of the reservoir is not imaged better. This is due to the limitations of the acquisition aperture at the surface.

Experiments were done over a range of rayparameters (both target and surface-oriented), ranging from −50 $^{\mu s}$/m to +50 $^{\mu s}$/m with steps of 25 $^{\mu s}$/m. All synthesized areal shot record were migrated and finally CDP stacked. For the imaging the stabilized inversion is used ($|\varepsilon|^2 = 0.1$). The stacked image for the surface oriented approach is shown in Figure 6.26a. The stacked image for the target oriented approach is shown in Figure 6.26b. In both cases the quality of the depth image has improved. The instabilities are indeed suppressed in favor of the true reflections, as expected. For the target oriented approach even the shallow events seem to be imaged without any disturbance. For the surface oriented approach is the subsurface below 1500m still disturbed considerably by the instabilities. More surface oriented areal shot records over a wider range or with a finer sampling could solve this problem. Of course, this will degrade the efficiency of the method. The fact that the instabilities vanish more easily with the target oriented approach can be explained by the fact that in the target oriented approach the instabilities are always localized around the same positions and vanish for the deeper parts of the subsur-

(a)

lateral position (m)

(b)

lateral position (m)
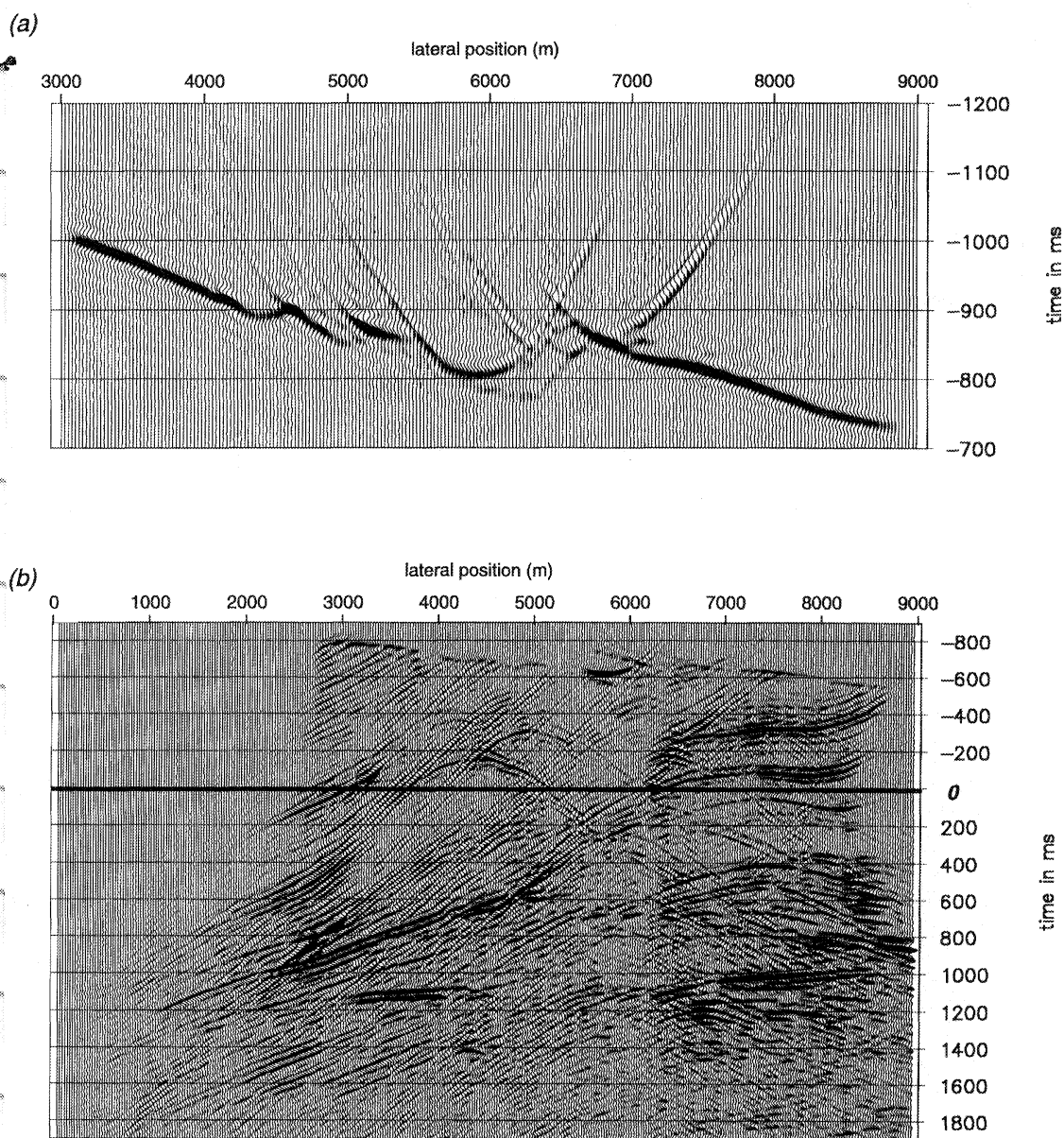
Figure 6.23 *Areal source wave field at the surface (z = 0m) to create desired illumination at depth level z = 2200m for an illumination rayparameter* p = +25 $^{\mu s}/_m$ (a);

(b) *the corresponding areal shot record for the synthesis operator as shown in* (a).

(a)

(b)
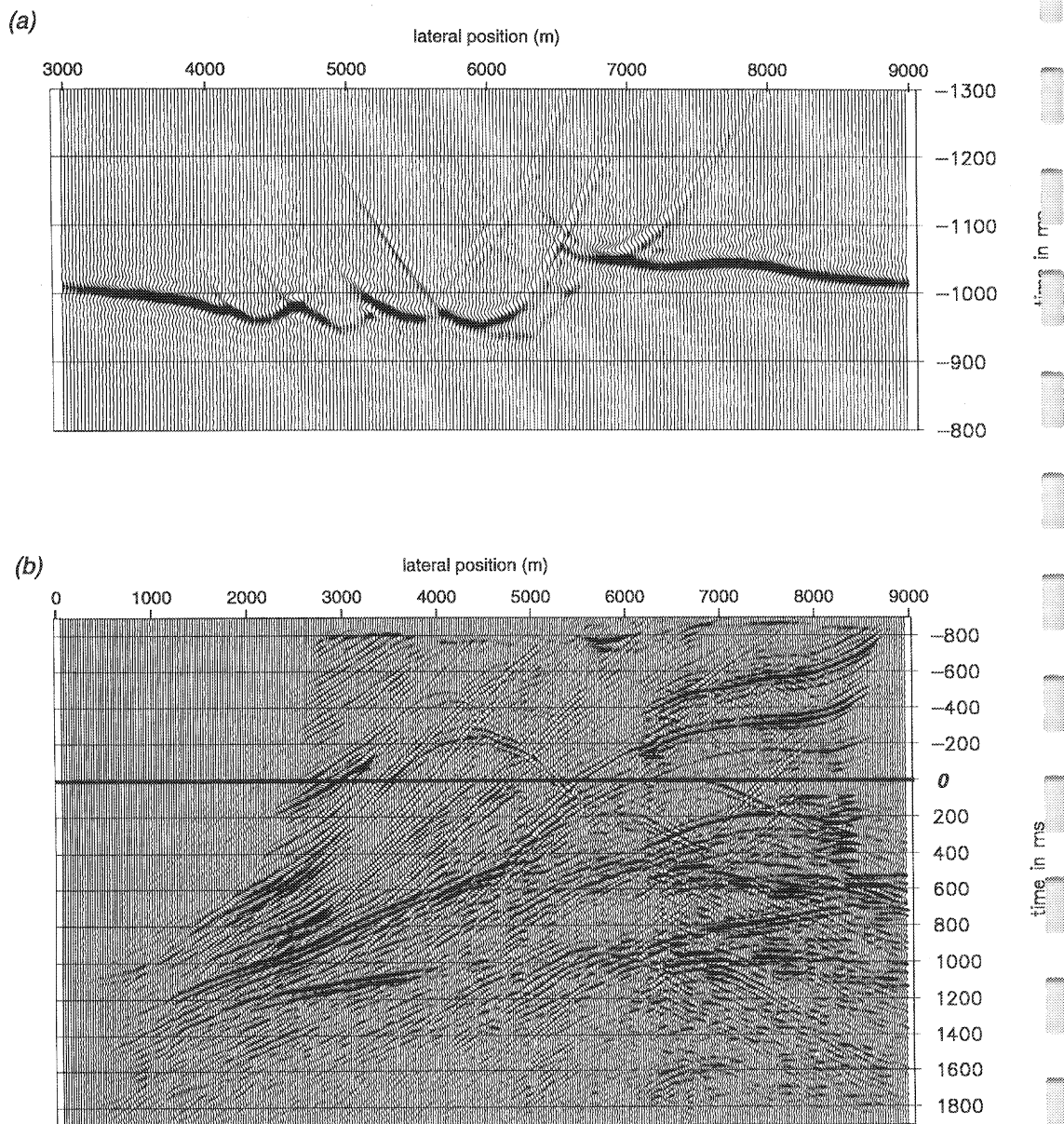
Figure 6.24 *areal source wave field at the surface (z = 0m) to create desired illumination at depth level z = 2200m*
for an illumination rayparameter p = −25 $^{\mu s}/_m$ (a);
(b) *the corresponding areal shot record for the synthesis operator as shown in* (a)

(a)

lateral position (m)

$p = +25 \, ^{\mu s}/_m$

(b)

lateral position (m)
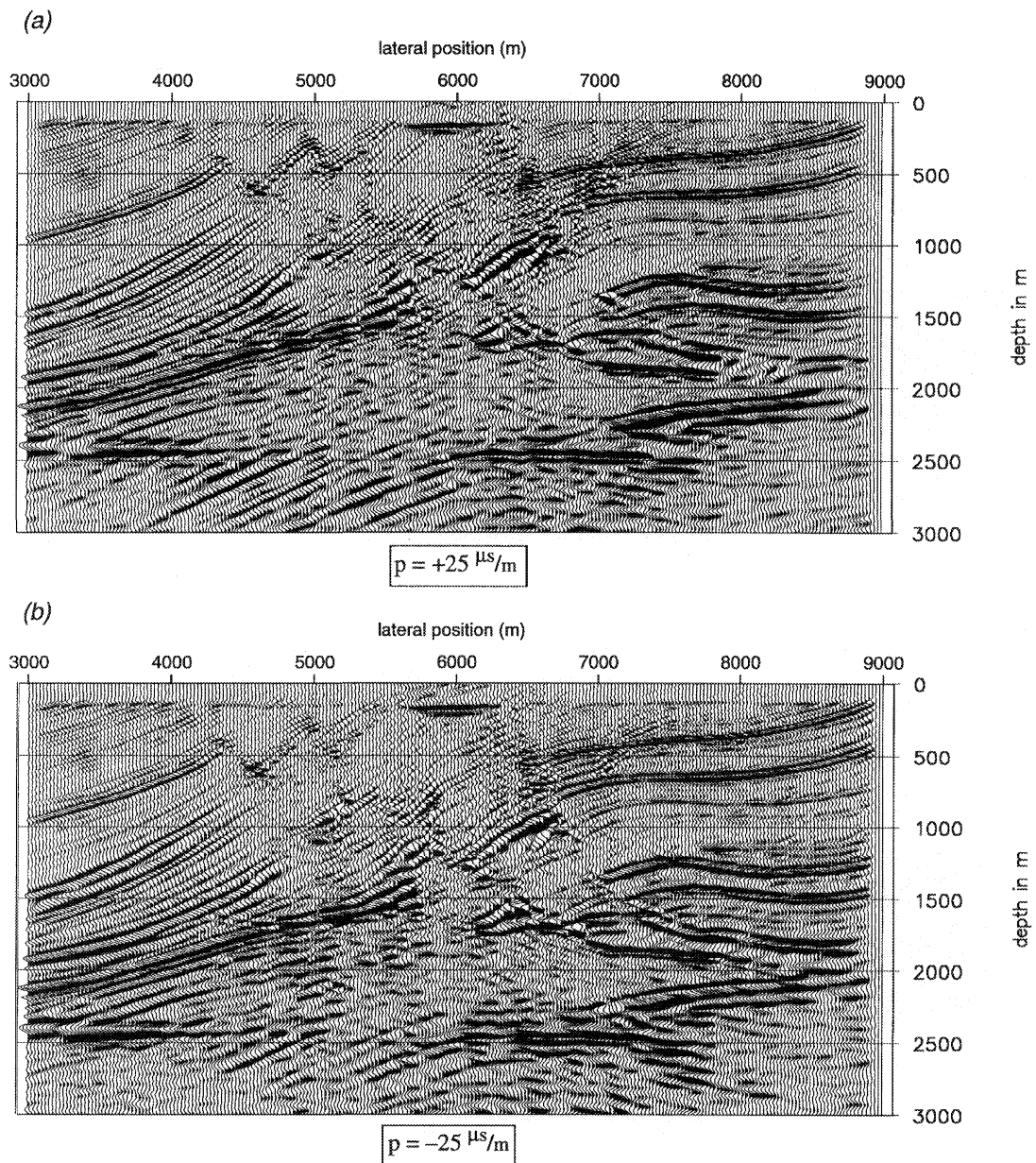
$p = -25 \, ^{\mu s}/_m$

Figure 6.25 *Depth sections obtained by migrating the areal shot records, using the* stabilized inversion *for imaging*
($|\varepsilon|^2 = 0.1$):
(a) $p = +25 \, ^{\mu s}/_m$; *(b)* $p = -25 \, ^{\mu s}/_m$.

(a)

lateral position (m)

surface oriented synthesis

(b)

lateral position (m)

target oriented synthesis
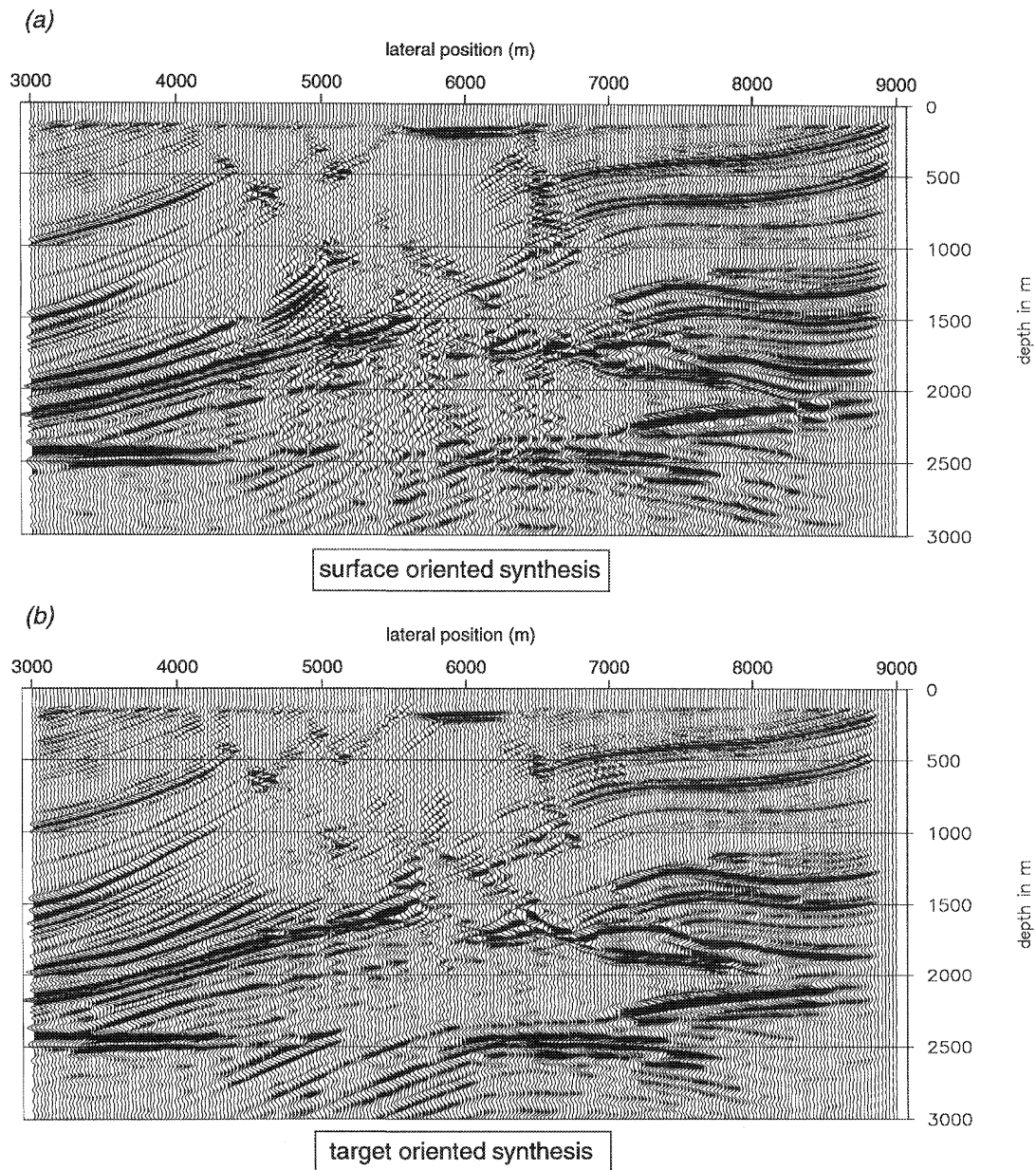
Figure 6.26 *Depth sections obtained by stacking the migration results of 5 areal shot records, using* stabilized inversion *for imaging ($|\varepsilon|^2 = 0.1$). The rayparameters ranged from -50 μs/m to $+50$ μs/m with an increment of 25 μs/m:*

(a) surface oriented synthesis; *(b)* target oriented synthesis.

face. For the surface oriented approach however, the instabilities occur directly beneath the complex structures of the subsurface and are then spread in any direction in the subsurface, depending on the propagation direction of the source wave field.

If we compare the result of the target oriented synthesis followed by areal shot record migration (Figure 6.26b) with the result after full prestack depth migration (Figure 6.3) we see an almost perfect match. By using the method of controlled illumination followed by areal shot record migration we have been able to obtain a depth image with the quality of a prestack depth migration with a reduction of processing time of approximately a factor of 24. For this noise-free situation we could also settle for the result after areal shot record migration of only *one target* oriented areal shot record.

6.3 Field data example

In this section a comparison of the surface-oriented synthesis methods and controlled illumination will be given on a field dataset (courtesy of NAM). Both synthesis methods will be followed by areal shot record migration. Results for different p-values will be generated and finally combined. First a brief review of the model and the acquisition geometry will be given.

6.3.1 The macro model and the field dataset

The field data example is a land data set. The acquisition parameters are shown in Table 1. A macro model (Figure 6.27) was estimated using a traveltime inversion method. In the third layer we have a horizontal gradient, with a linear velocity profile from 3025 $^m/s$ up to 3920 $^m/s$. The target zone is indicated in the model. The goal is to image the reflectors below the salt body at a depth larger than 2300m. The missing near offsets were interpolated using a CMP interpolation technique. This was done to avoid truncation effects during the extrapolations.

Table 1: Acquisition geometry parameters for the field data example

geometry	split spread
number of shots	301
shot spacing	30. m
number of detectors per shot	120
detector spacing	30. m
near offset	115. m
far offset	1935. m
registration time	4. s
time sampling interval	4. ms
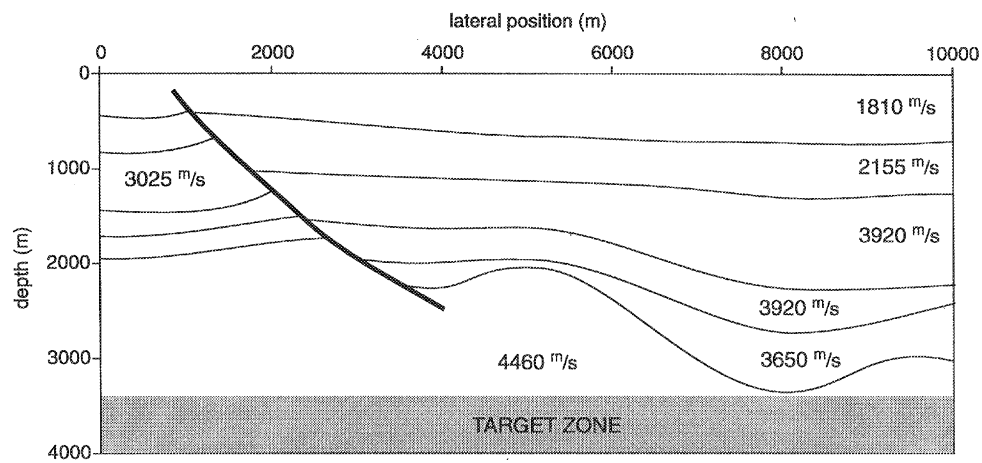
Figure 6.27 *Estimated macro model for the field data example (courtesy NAM). Note the horizontal velocity gradient in the third layer.*

6.3.2 Surface oriented synthesis and areal shot record migration

For the examples in this subsection plane wave responses are generated for a range of angles. All plane wave responses are migrated using the areal shot record migration scheme. The individual migrated sections are stacked in a common depth point sense, generating an image that will be compared with the result after full prestack depth migration (Figure 6.28). The experi-
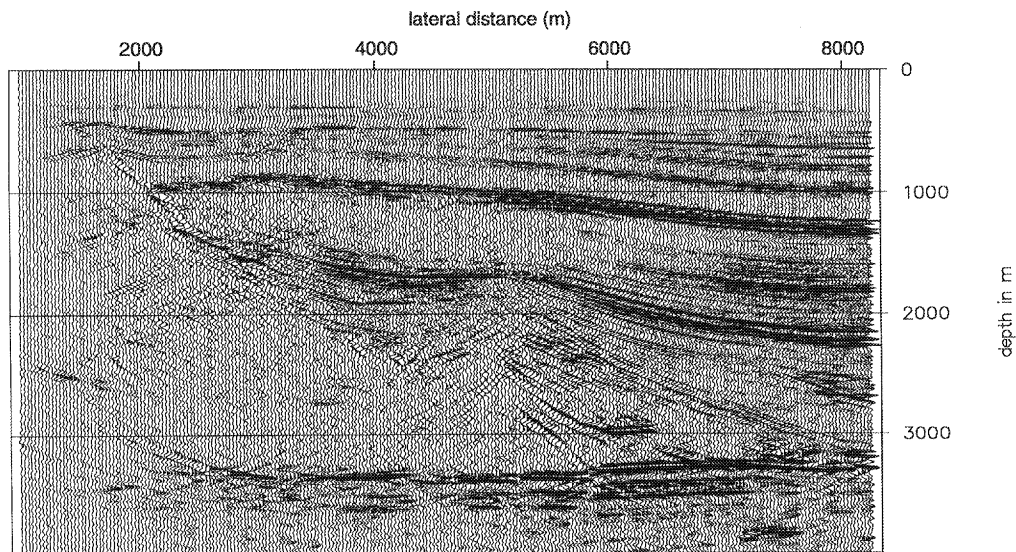
Figure 6.28 *Depth section after full prestack depth migration.*
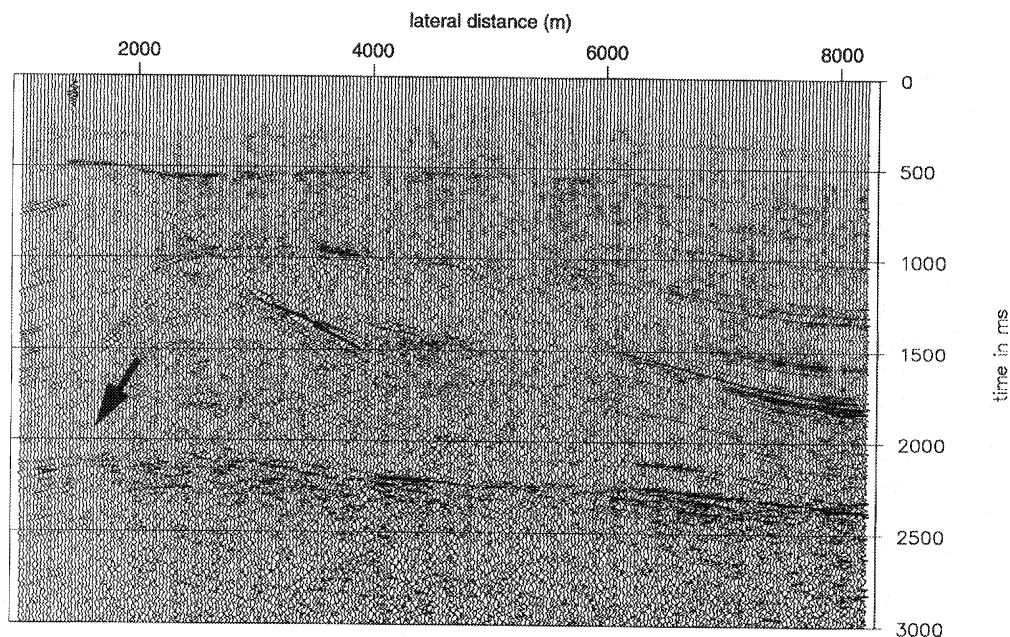
Figure 6.29 Areal shot record after synthesis for a horizontal plane wave at the surface.

ment for $p = 0$ $^{s}/m$ will be presented in detail. For the other experiments are used to obtain the final stacked depth section.

The result of the synthesis for a plane wave at the surface is shown in Figure 6.29. Note that this gather can also be used to control the quality of the data (QC). It is obvious that the geophone station indicated by the arrow was not working properly during the acquisition. If reciprocity is applied (i.e. shot records are treated like common receiver gathers) the same section can be built (Figure 6.30). Here we can clearly indicate bad shot records in the line (indicated by the arrow).

Figure 6.31 shows the depth section obtained after migration of the areal shot record of Figure 6.29. Note that all reflectors are properly positioned, and that most diffraction energy is collapsed. Also note the bad signal-to-noise ration compared to the pre-stack migration image (Figure 6.28). This can be explained by the fact that during the synthesis only the first Fresnelzone contributes constructively to the stacked trace (Appendix B), whereas in prestack migration the whole hyperbola contributes to the final stacked trace, hence, giving an optimal noise suppression. In the case of areal shot records the major noise suppression is achieved during the stacking of the individual migrated depth sections for the different illumination angles, i.e. let the Fresnelzone shift over the hyperbolas.

To increase the SNR, plane wave stacks are generated with a p-range from -275 $^{\mu s}/m$ to 275 $^{\mu s}/m$ (approx. $-30°$ to $30°$) with $\Delta p = 22.3$ $^{\mu s}/m$ (approx. $2.5°$). All responses are migrated. Figure
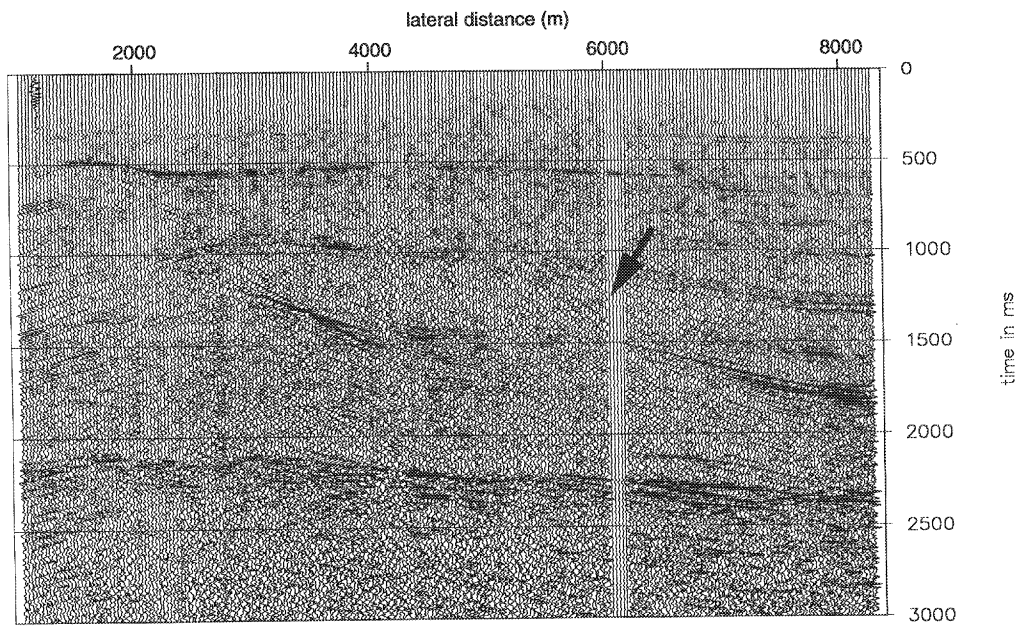
Figure 6.30 *Areal shot record after synthesis for a horizontal plane wave at the surface, if reciprocity is applied.*
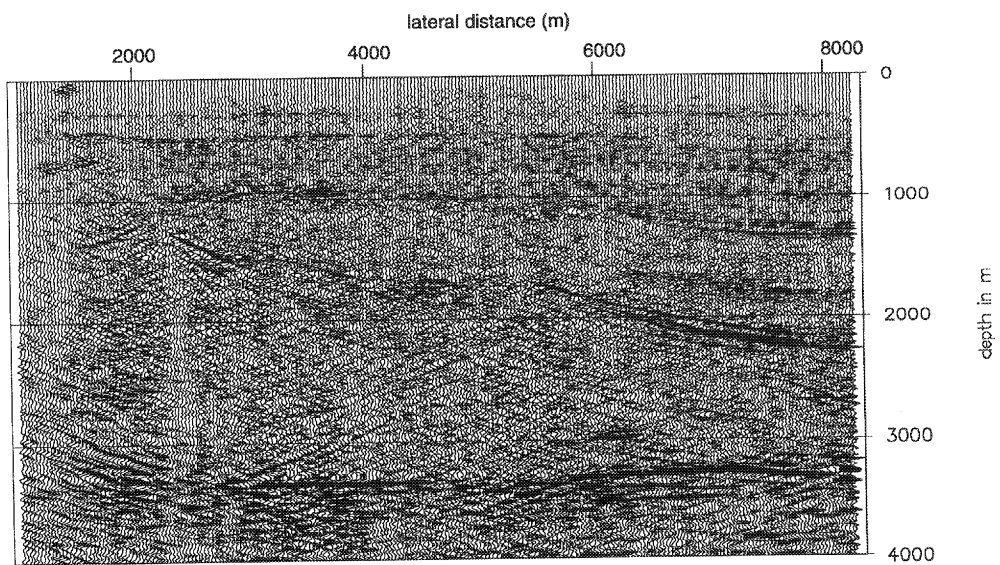
Figure 6.31 *Migrated areal shot record for a plane wave illumination from the surface ($p = 0 \, ^{s}/_{m}$).*
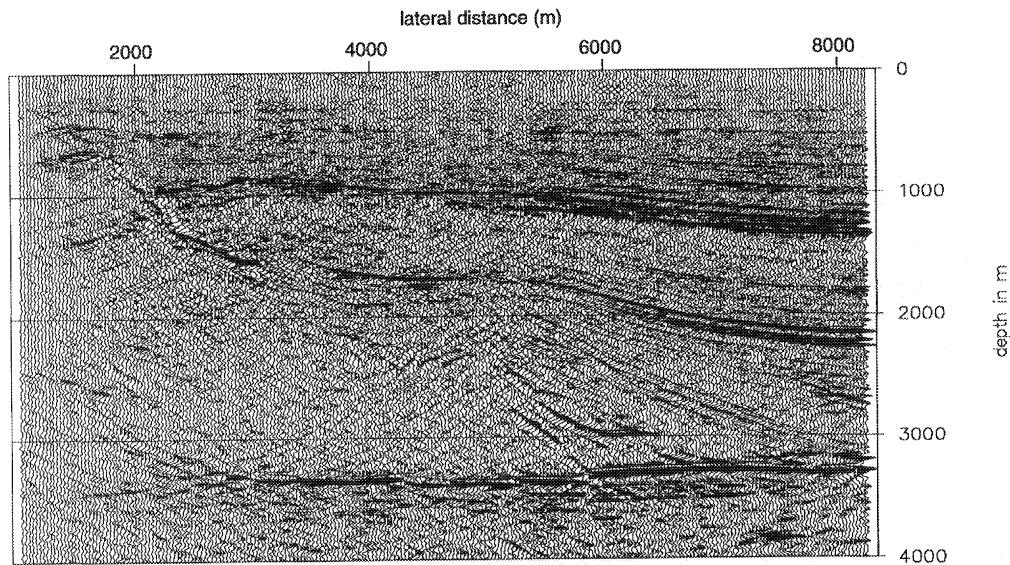
Figure 6.32 Depth section obtained by stacking of 25 individually migrated surface *oriented areal shot records.*

6.32 shows the total section from a stack of all migrated areal shot records. Note that in this final image the signal-to-noise ratio is increased and all reflectors are imaged at the same positions compared to the prestack image (Figure 6.28). However, especially in the target zone the image is of less quality. Note that the result of Figure 6.32 saves about a factor of 6 on the computation time compared to the full prestack migration.

6.3.3 Target oriented synthesis and areal shot record migration

For the examples in this section plane wave responses are generated for a range of rayparameters at a depth of 3250m. All areal shot records are migrated using the areal shot record migration scheme. The individual migrated sections will be stacked in a common depth point sense, generating an image which will be compared with the prestack migrated section (Figure 6.28). Some different aspects of the target oriented synthesis using controlled illumination will be discussed.

Horizontal plane wave ($p = 0$ $^{s}/m$) at $z = 3250$ m

The synthesis operator is modeled using the estimated macro model (Figure 6.27) and is shown in Figure 6.33. The areal shot record is shown in Figure 6.34. This areal shot record is deconvolved with the synthesis operator for display purposes. The migration result is shown in Figure 6.35.

Although the source wave field is designed in a target oriented way, the structure of the target reflector is *not* imaged well. This can be explained by the fact that the designed source wave
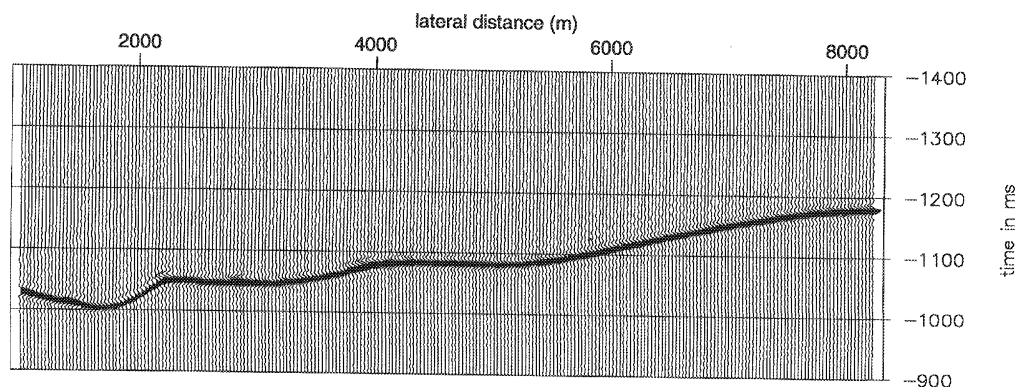
Figure 6.33 Areal source wave field at the surface (z = 0m) to create a horizontal plane wave illumination at depth level z = 3250m.

field, and the structures in the target zone are almost parallel, meaning normal incidence illumination. This means that the main energy contribution of the target reflector will be present at zero offset (Figure 6.36). These are exactly the offsets that are missing in the data, and are interpolated. The interpolation was not done very well for the target response. In Figure 6.37 the common receiver gathers are shown after correction for the illumination, but prior to the actual synthesis. Each gather will result in one trace of the synthesized areal shot record. Clearly it can be seen that for the illumination of $p=0^s/m$, the contribution of the target reflector comes from
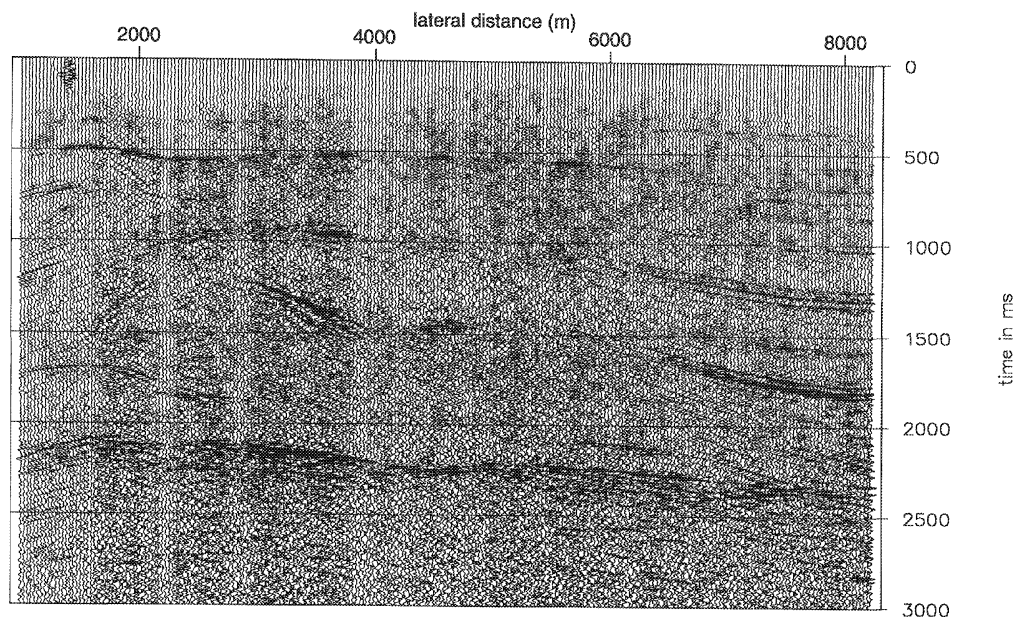
Figure 6.34 Areal shot record for a horizontal plane wave illumination at z = 3250m. The shot record is deconvolved with the synthesis operator (Figure 6.33).
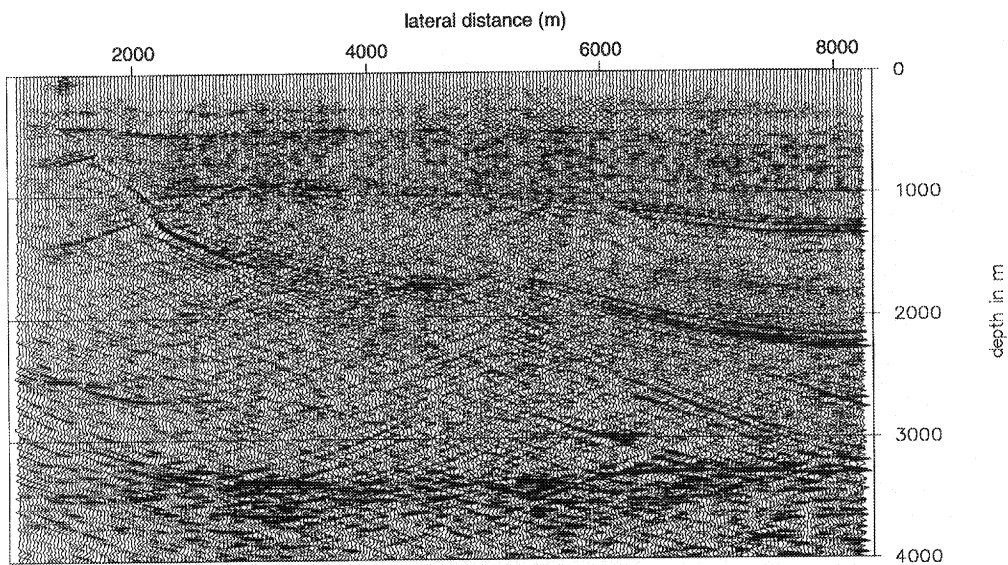
Figure 6.35 *Migrated areal shot record. The illuminating source wave field is a horizontal plane wave at z = 3250 m. Note the bad quality of the image in the target zone, due to the missing near offsets.*
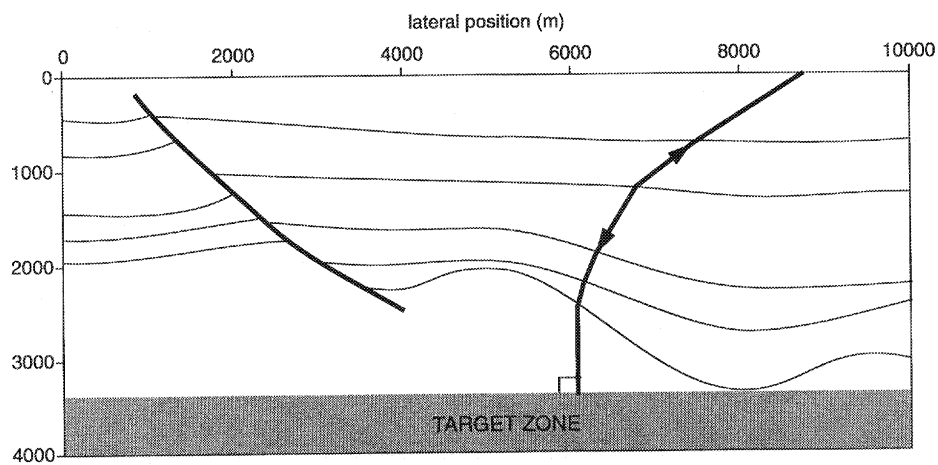
Figure 6.36 *If the structures in the target zone are parallel to the incident source wave field, normal incidence reflection will occur, and the main contribution of the target reflection will come from zero offset.*
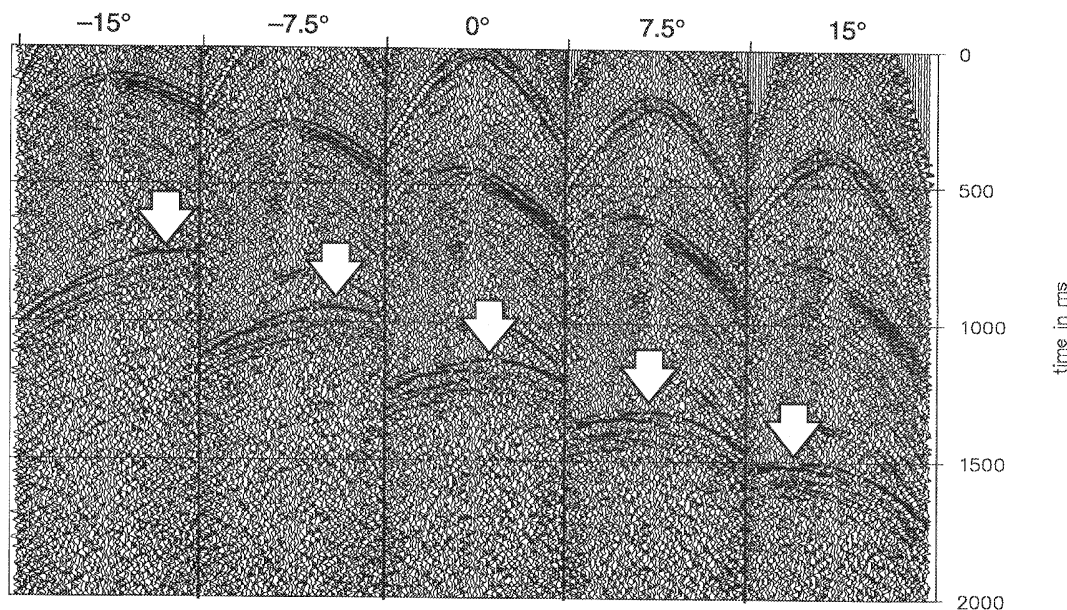
Figure 6.37 *Common receiver gathers after correction for the proper illumination (angles at z = 3250m), prior to stacking. Indicated is the target reflection and the position of the apex of the event, which determines the offset which has the main contribution in the stacked trace.*

zero-offset. It is obvious that in practise never a normal incidence wave field should be chosen if the aim is structural imaging, unless proper zero-offset data is available.

Note that on the one hand the synthesis operator tells us which sources contribute to a certain source wave field at target level, whereas on the other hand the corrected common receiver gathers (so prior to stacking, Figure 6.37) tell us which part of the data is contributing to the areal shot record for the chosen illumination. This means that there is control on both the receiver and the source side whether a certain experiment is indeed sensible for a given acquisition geometry.

Non-zero p-values at z = 3250m

Areal shot records are generated over a p-range from -117 $^{\mu s}/m$ to 117 $^{\mu s}/m$ (approx. $-30°$ to $30°$) with $\Delta p = 9.8$ $^{\mu s}/m$ (approx. 2.5°). All responses are migrated and stacked in a common depth point sense. Figure 6.38 shows the total section from a stack of all migrated areal shot records.

If we compare the result obtained from the surface oriented areal shot records (Figure 6.32) and the one obtained from the target oriented areal shot records (Figure 6.38) it is clear that by putting the control of the incident source wave field at the target a better control of the data used for the migration is obtained, resulting in a better image, not only in the target zone, but also in the other parts of the subsurface. If we compare the target zone response with the response after
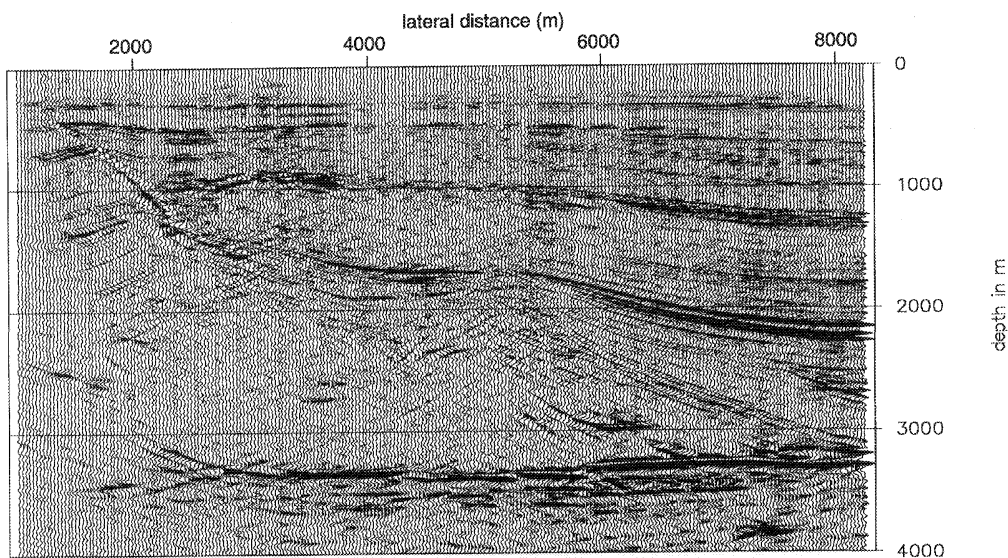
Figure 6.38 *Depth section obtained by stacking 25 individually migrated* target *oriented areal shot records.*

full prestack migration, we see a comparable quality of the depth image, both in resolution and signal-to-noise ratio.

The use of the corrected common receiver gathers prior to the stacking (Figure 6.37) can be used to determine the p-range to be used for the processing of the dataset. If it is clear from these gathers that the main contribution to the areal shot record should come from offsets outside the range of the acquisition geometry used (*near* and *far* offsets), these angles will only cause disturbance of the final image, hence should not be used for further processing.

6.3.4 Generating target oriented z-p gathers

If we have migrated all areal shot records individually, we can construct an image of the target zone as function of the p-value of the incident source wave field (Figure 6.39). These gathers can be used as input for linear AVO inversion (de Bruin, 1992). The alignment in these gathers indicates whether the used macro model indeed describes the propagation properties properly. It is obvious that at the left side of the section the alignment in the z-p gather is not very good for the deeper reflectors, indicating that the macro model is not describing the propagation properties properly. We have already noticed this error in Chapter 4. If we use a simple correlation between the individual migrated section, using a window over 10 traces, and then stack the corrected depth sections, we obtain the depth section as shown in Figure 6.40. The main improvement can be seen at the left deep reflection where some migration smiles are removed. Deeper in the section we see some reflectors appear after correction of the z-p gathers (Figure 6.41). These reflectors were not imaged properly due to errors in the macro model used for the migration of the areal shot records. The deeper reflectors are not available in the prestack migration result, and therefore not shown in the complete depth sections.
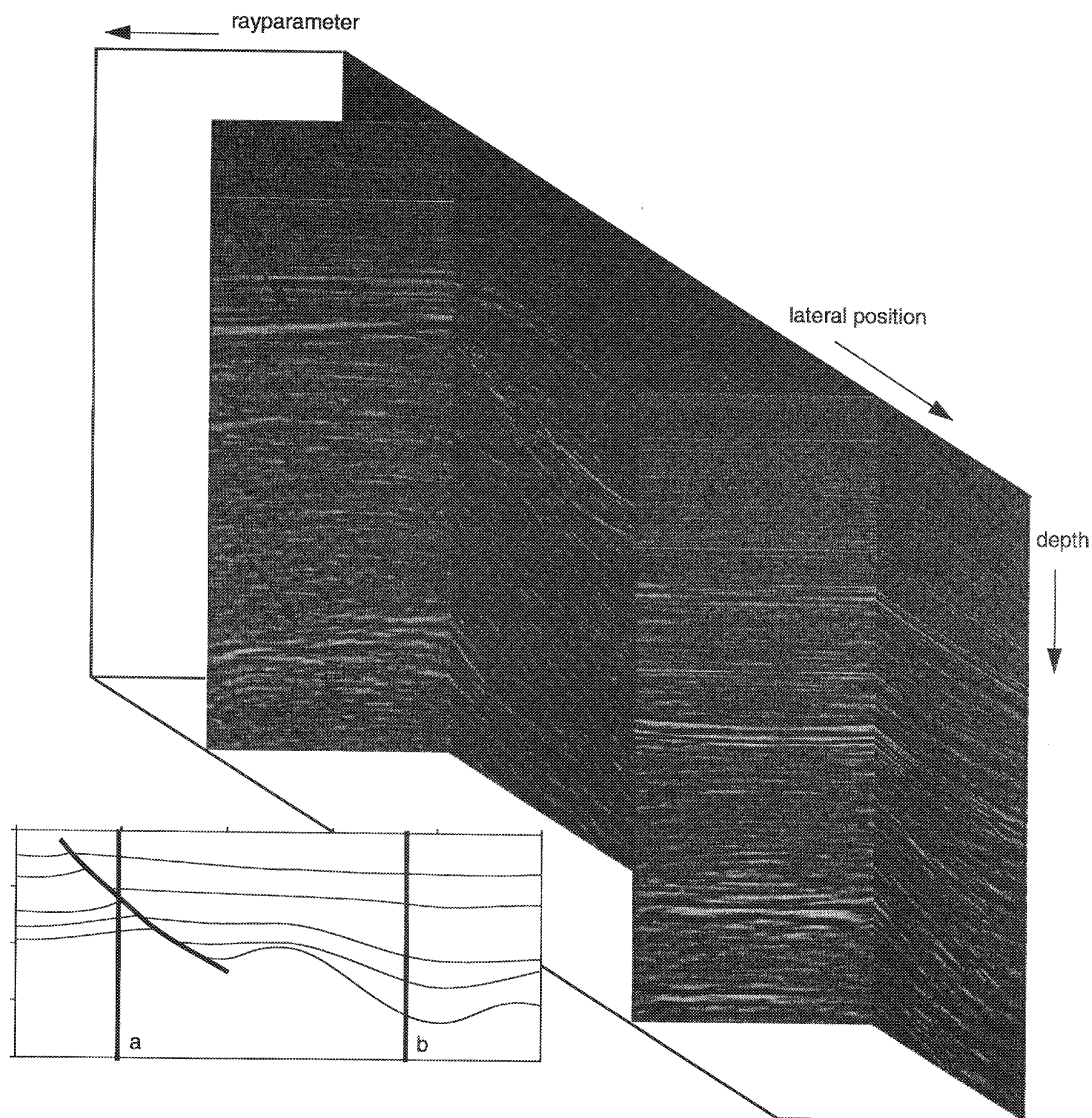
Figure 6.39 *Plot of the 3D data volume that is obtained after migration of the individual areal shot record for different illumination angles. The back plane shows the depth section for* $p = -78.2$ $\mu s/m$. *The two other data planes show z-p gathers for different lateral positions. Note that in plane* b *the events are very well aligned horizontally, indicating a well estimated macro model. In plane* a *however, the deeper events are not aligned anymore, indicating in this case a structural error in the position of the fault plane.*
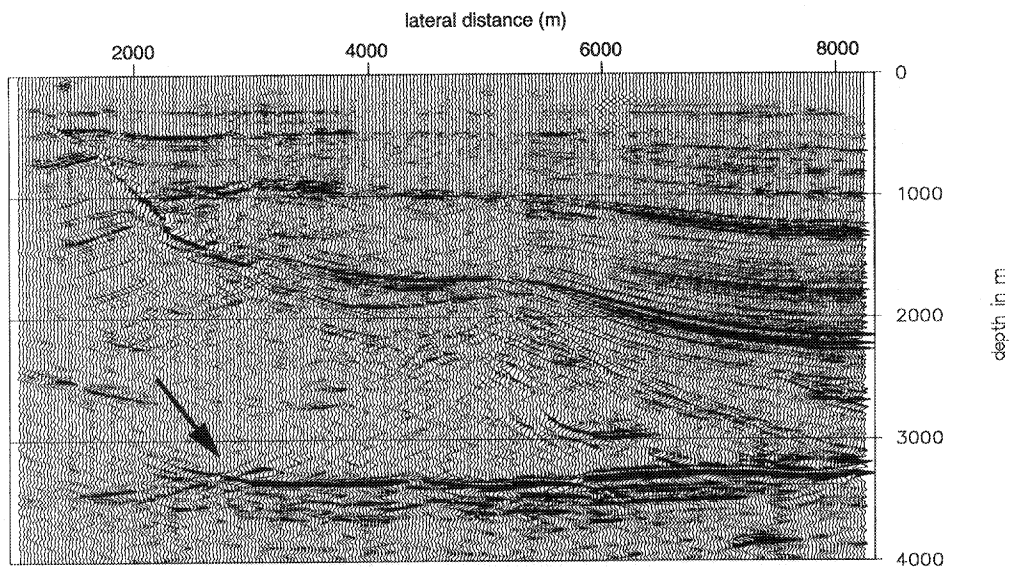
Figure 6.40 *Depth section obtained by using correlations prior to the stacking of the 25 individually migrated depth sections. Note the improved image at left side of the section.*
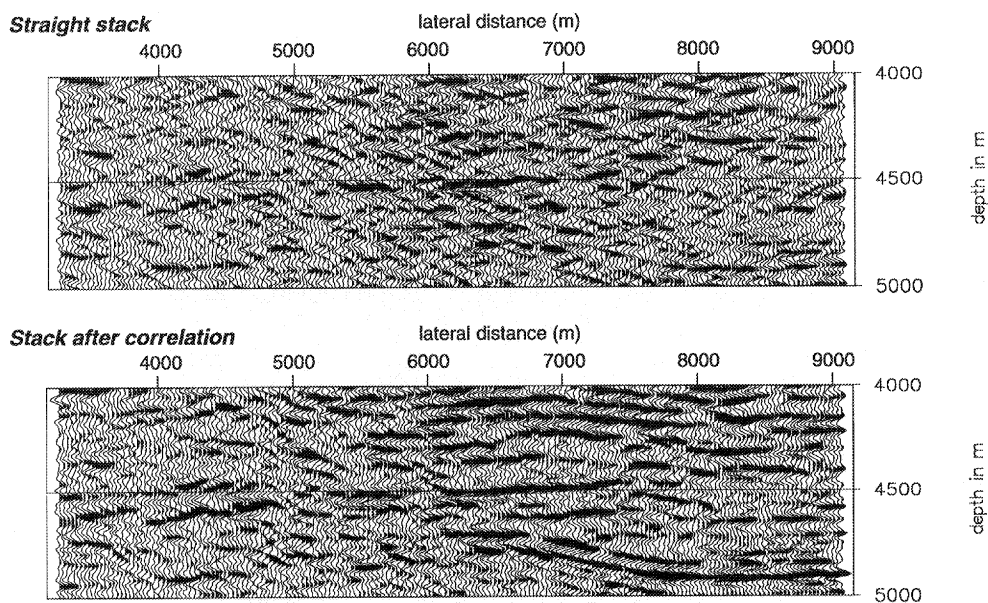
Figure 6.41 *Depth sections from deeper reflectors: (a) the result after a straight stack; (b) the result after correlation and stack. Note the improvement of the image, which was distorted due to errors in the macro model used for the migration of the areal shot records.*

6.3.5 Imaging in selected areas

For the migration of prestack data a description of the macro model is needed. If we use the method of areal shot record migration combined with controlled illumination we use this macro model not only for the migration, but also for the design of the illuminating source wave field at target level. In practice this macro model should be estimated, and will therefore never be exact. Errors in the macro model will give rise to artifacts in the image. These artifacts will not only occur at the position where the macro model is erroneous, but will spread out over the section. Figure 6.38 shows these artifacts at the left side of the section at a depth of approx. 3300m. It is possible that these artifacts will interfere with the image of the target reflector and distort the image severely. The method of controlled illumination is very well suited to focus the energy of the incident source wave field to those positions in the subsurface that we want to image, hence has the capability to avoid problem areas during imaging, by not illuminating them. Doing so will avoid artifacts from the problem areas to spread all over the section. Although the field data set is not too well suited to show this (the macro model is rather well known at all positions, and the artifacts due to errors do not interfere with other reflectors), we perform the experiment of illuminating the target zone at $z = 3250$ m only with a limited lateral aperture, avoiding the area at the left side of the model. The lateral aperture ranged from 3800 m to the end of the model. The stacked result (stack of 25 p-values) is shown in Figure 6.42. Note that indeed we have avoided to image the left side of the model, without sacrificing the quality of the image at the right side of the model. Also note that due to the limited illumination range at target level, we also image a limited area in the other parts of the model.
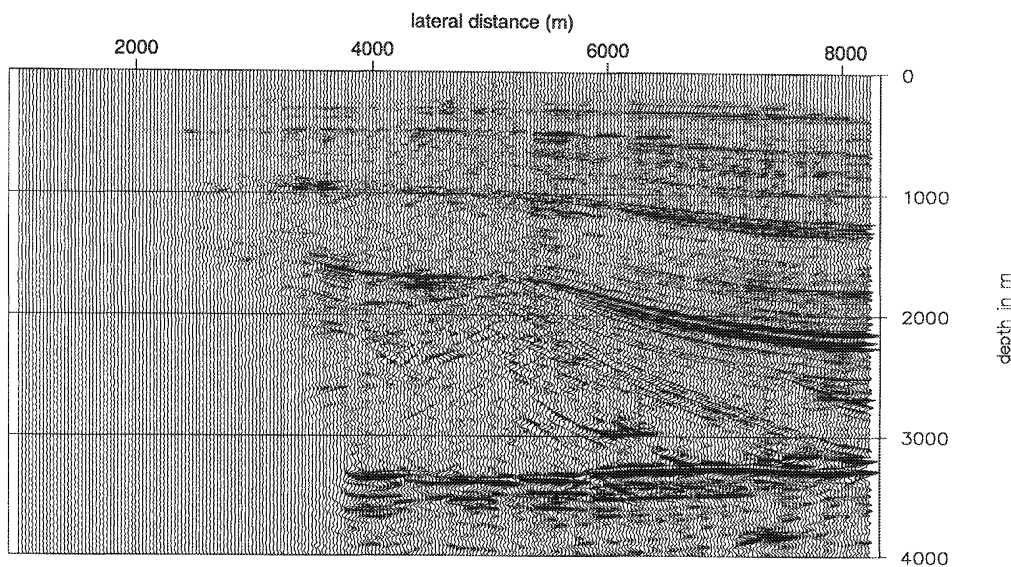
Figure 6.42 *Depth section obtained by stacking 25 individually migrated* target *oriented areal shot records. Only a selected area of the target zone is illuminated.*

6.4 Noise-suppression by Fresnelzone filtering

One of the main problems when processing field data, using the approach discussed in this thesis, is the signal-to-noise ratio (SNR). Due to the fact that in each areal shot record only a part of the data is used (the so-called Fresnel zone, see Appendix B), the increase of the SNR is not as good as in CMP stacking or full prestack migration. The same SNR can be obtained by using *many* areal shot records, but from an economic point of view that would be unfavourable. In this section we will discuss how we can increase the SNR in the individual areal shot records. We will illustrate the effect of the noise filtering on the same field dataset, as shown in the previous subsections.

6.4.1 Where to apply a noise-suppression filter?

If we look at the total processing sequence used in areal shot record technology, we can see several stages where we could apply a noise-suppression filter. The problem with noise-suppression is that the actual data must be affected as little as possible by the filtering. Hence, a noise-suppression filter should be applied in a domain, where data and noise are well-separated, or where we know which part of the data we will use in the further processing.

During the synthesis process, there is a point where we know which part of the data we will use in the further processing. The synthesis process consists of two steps: the first step where we correct the shot records to obtain the desired areal source; and a second step where all traces in a corrected CRG are synthesized into one trace, the actual construction of the areal source response. The second step is a straight stack over all traces, i.e. the selection of the $p = 0$ ^{s}/m component of the corrected CRG. The stage between the two steps seems very well suited to apply a noise-suppression filter.

6.4.2 Which noise-suppression filter to apply?

Keeping in mind that we select the $p = 0$ ^{s}/m component of the data, it might seem advantageous to use a filter in a domain, where all angles are separated, i.e. the wavenumber-frequency or Radon domain. The problem in these domains is that the selection for the angle is already made and that there is no separation between the signal and noise in the $p = 0$ ^{s}/m component of the data. During the transformation to the Radon domain (and back) aliasing effects and noise may be suppressed (Fyfe and Kelamis, 1992), but again, noise which is mapped onto $p = 0$ ^{s}/m cannot be suppressed in the Radon domain. Hence, in the wavenumber domain *no* noise filtering, and in the Radon domain only partial noise filtering can be done, mainly aliased energy.

A desired noise-suppression filter would leave horizontally aligned events in the corrected CRG unharmed and would remove all other energy, leaving thus only that part of each event, that contributes constructively to the areal shot record. Hence we should apply a lateral filter along the spatial coordinate for each point in time, i.e. a filtering along *isotime* lines. The response we should inspect to evaluate the result of the filtering is *not* the filtered corrected CRG, but the filtered trace in the areal shot record, so the output of the total synthesis process.

6.4.3 Fresnelzone filtering

The filter that we will evaluate here is a simple 1-D filter. Although the Fresnelzone does contain events with a small curvature, this curvature is neglected by this filter. The filter evaluates the coherency of the amplitudes along the *isotime* lines. If within the length of the filter all amplitudes have the same polarity, the data point under consideration keeps its value. If one or more data points within the filter length have an opposite polarity from the data point under consideration, this data point is assumed to be *outside* the Fresnelzone and considered as noise. Its value is replaced by zero. An additional threshold allowing one or more samples with opposite polarity, would create a more moderate filter. Figure 6.43 shows the effect of the filter for one iteration and a filter length of $l=7$ on a corrected CRG. The data is modelled over a density contrast, hence does not contain angle-dependent reflectivity. Events with quickly changing polarity are removed, leaving only the data points within the Fresnelzones. Note the increase to signal-to-noise ratio in the trace of the areal shot record after Fresnelzone filtering.

6.4.4 Application of Fresnelzone filtering on corrected common receiver gathers.

We will illustrate the effect of the Fresnelzone filter on the field data example which was shown in the previous subsections. The illumination defined for this experiment is a horizontal plane wave at the surface. Each trace in the gathers to be shown, is the result of Fresnelzone filtering followed by stacking, so the *full* synthesis process, including the filtering mentioned in the previous subsection. The filter is applied for different lengths and different numbers of iterations.

The result for a part of the synthesized areal shot record is shown for a range of different filters in Figure 6.44. Figure 6.45 shows the difference between the original result without filtering, and the filtered areal shot records. Note again that all gathers are plotted with the same absolute amplitude. Long filters (length $l > 5$) filter too strong. Not only the noise, but also the data is affected, even for one iteration. The introduction of a threshold could improve the result. The short filters (length $l \leq 5$) give good results. More iterations will remove more noise, but will also affect the edges of the Fresnelzones, hence the amplitudes in the areal shot record. An appropriate choice seems to be a filter length of $l=3$, using two iterations, or a filter length of $l=5$, using one iteration.

We conclude this subsection with the full areal shot record for two iterations with a filter length of 3 (Figure 6.46). Compare this result with the areal shot record if no filtering is applied (Figure 6.30). Note the increased SNR. In the remainder of this section, we will use the 3-point filter with 2 iterations during the synthesis process, to improve the SNR of the areal shot records.

6.4.5 Implementation considerations

The application of the Fresnelzone filter should be done in the time domain on the corrected common receiver gathers. The correction of the common receiver gather for the defined illumination is done in the frequency domain. Hence, after correction for the illumination the data should be transformed back to the time domain, prior to filtering and stacking, instead of *one* optional inverse Fourier transform of the whole areal shot record after synthesis.
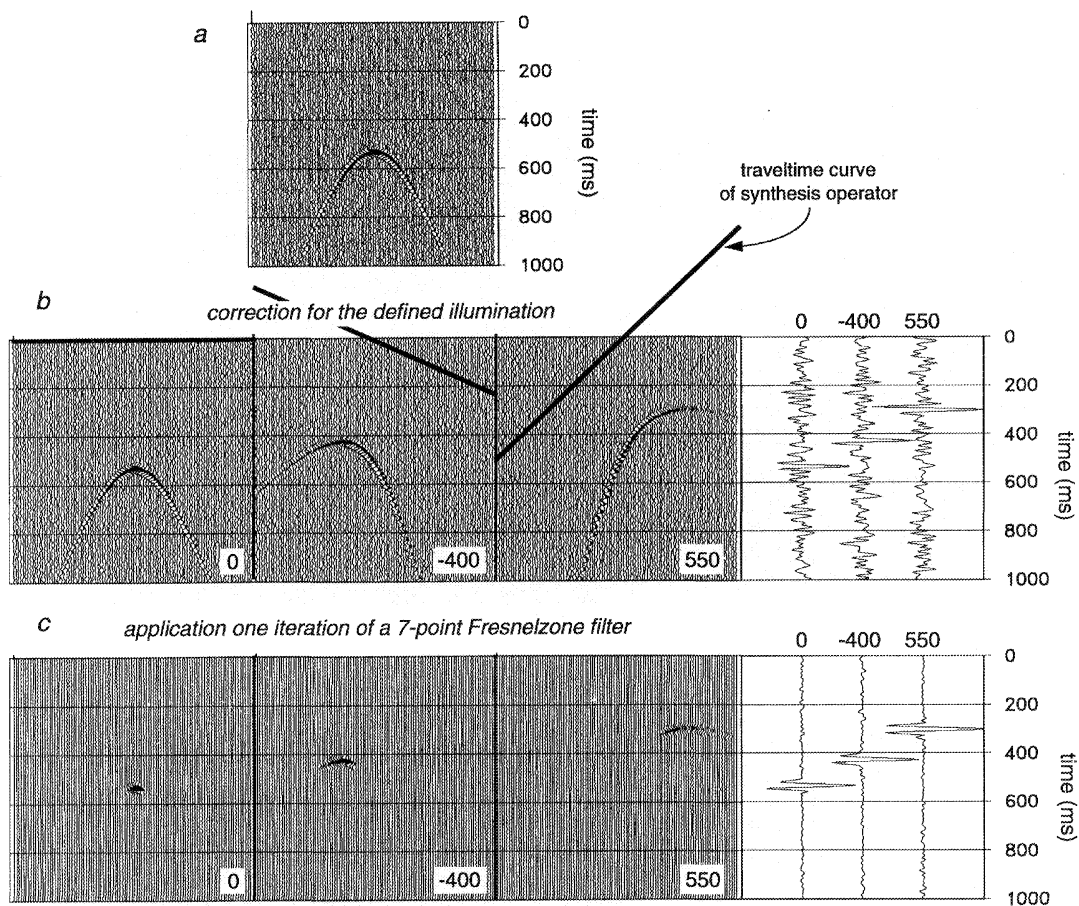
Figure 6.43 *Application of a Fresnelzone filter (7 points, one iteration).* (a) *The original common receiver gather (CRG).* (b) *The CRGs corrected for the defined illumination (p=0, -400, 500 $^{\mu s}$/m). The right-hand side shows the trace of the areal shot record after stacking of the traces in the corrected CRGs.* (c) *The corrected CRGs after filtering with the Fresnelzone filter. The right-hand side shows the trace of the areal shot record after stacking of the traces in the filtered corrected CRGs. Note that only those parts of the data, that are identified as a Fresnelzone, are left unharmed. Also note the increase in signal-to-noise ration in the trace of the areal shot record.*

Also prior to filtering, the data should be reorganized into common receiver gathers. This means that common receiver gathers should be gathered during the synthesis process. This number of CRGs to be kept in memory would approximately be equal to the number of receivers per shot record. However, if *reciprocity* is applied, each shot record can be interpreted as a common receiver gather, avoiding this cumbersome reordening process. The implementation is then straightforward: 1. forward Fourier transformation; 2. correction for the illumination; 3. inverse Fourier transformation; 4, application of the filter; 5. synthesizing the trace of the areal shot record.
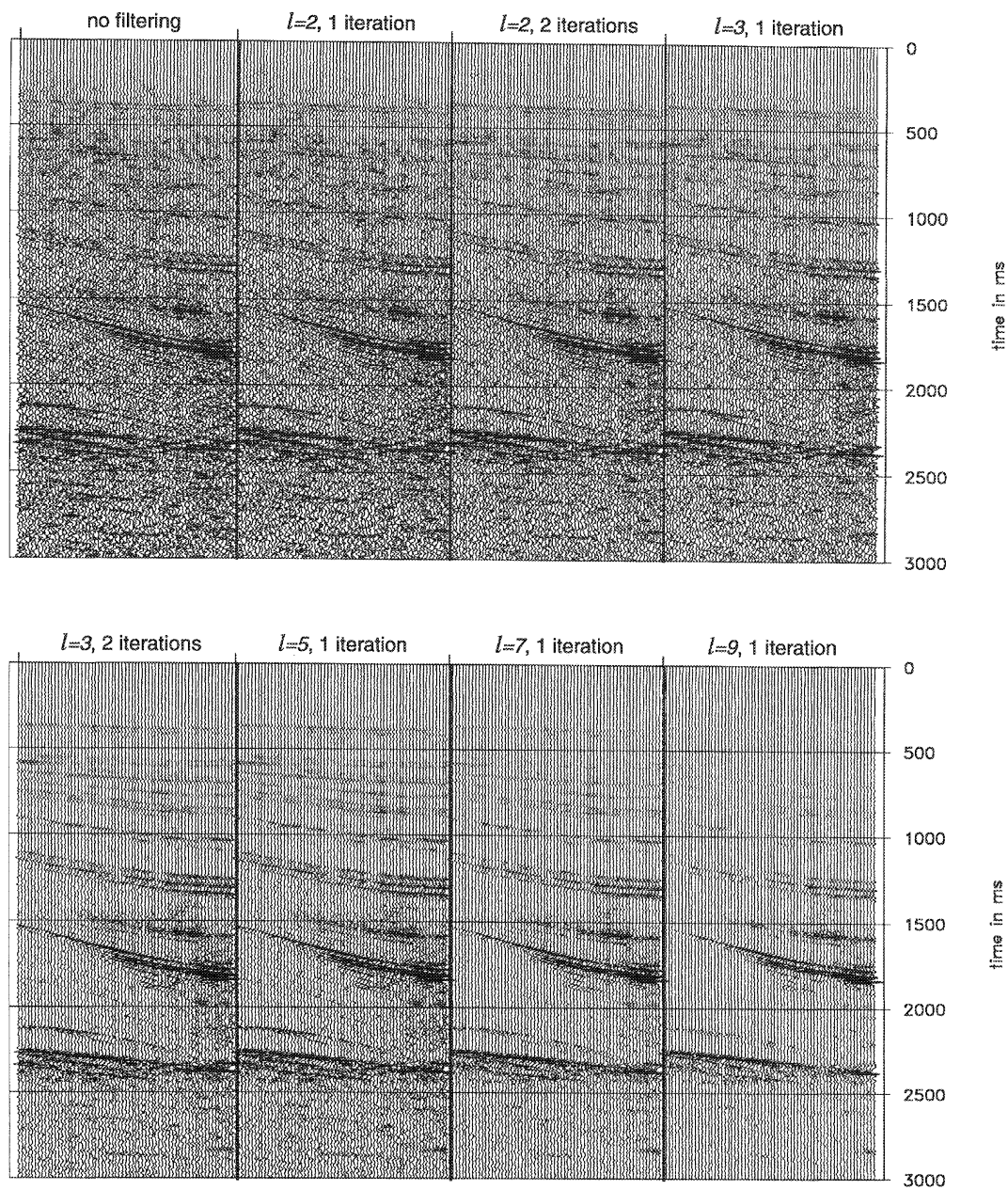
Figure 6.44 *Part of the areal shot record for different Fresnelzone filter lengths l and number of iterations. The areal source wave field is a horizontal plane wave at the surface. All gathers are scaled to the same value. Note how the SNR increases with increasing filter length. Also note that the amplitudes of the events are affected if the filtering is too strong.*
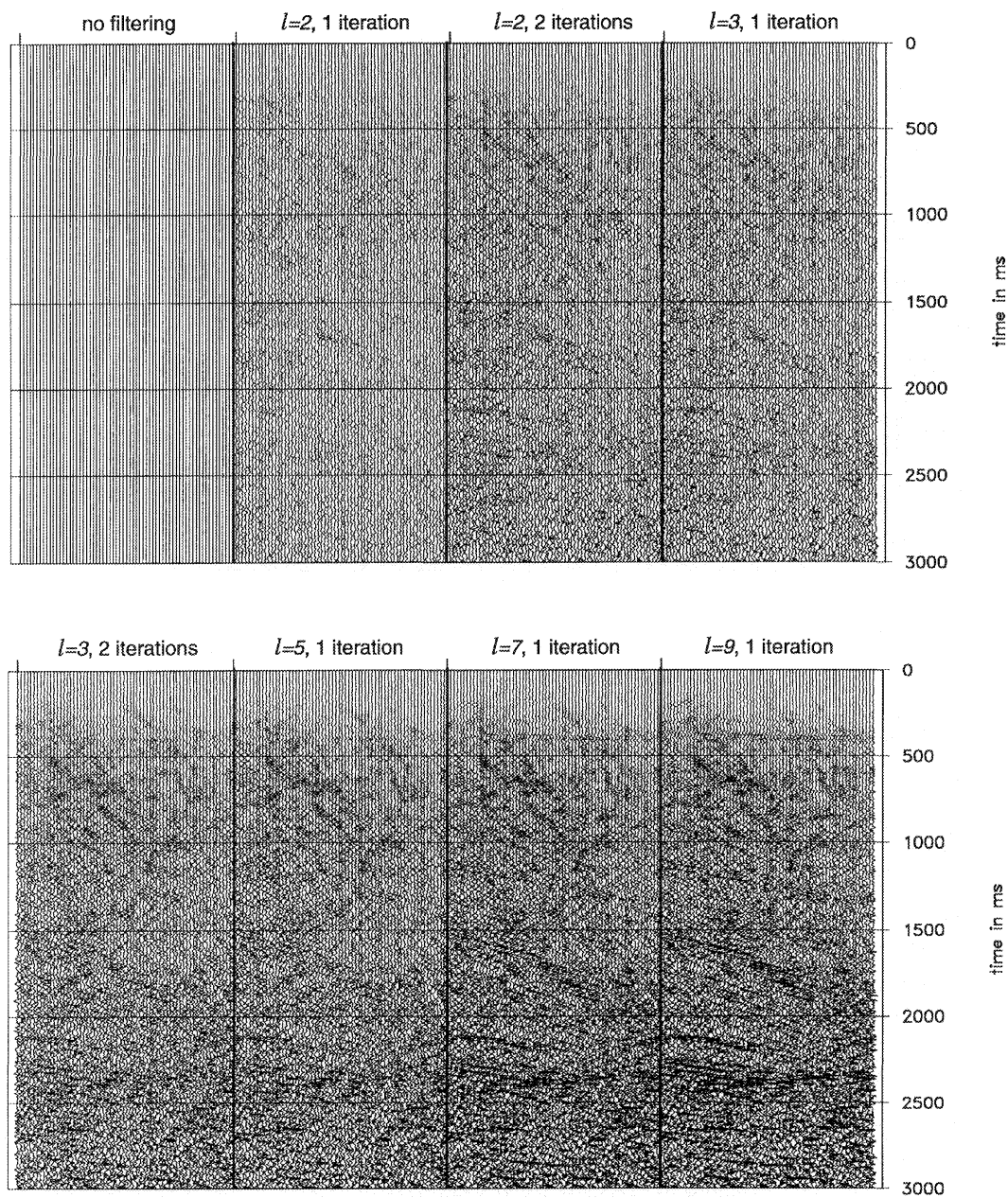
Figure 6.45 *Difference between the areal shot record without filtering, and the filtered areal shot records (Figure 6.44). Note that for longer filters more noise is removed from the areal shot record, but that also the events in the data are affected by the filter. For short filter lengths more iterations are necessary to obtain a sufficient noise suppression.*
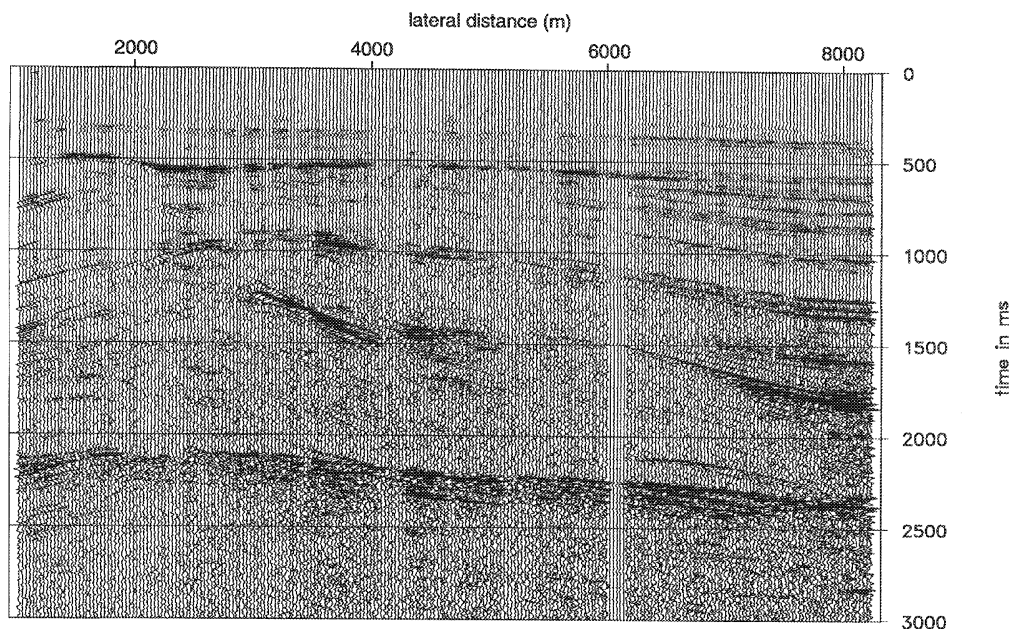
Figure 6.46 *Areal shot record after synthesis for a horizontal plane wave at the surface, using 2 iterations of a Fresnelzone filter with length l=3. Compare this result with Figure 6.30 at page 78. Note the increase in signal-to-noise ratio. Also note that very weak reflections are suppressed by the filter.*

6.4.6 Areal shot record migration after target-oriented synthesis using Fresnelzone filtering

For the examples in this subsection areal shot records are synthesized for plane waves at a depth of 3250m for a range of angles. Reciprocity is applied and the same filter is used during the synthesis process as discussed in the previous subsection. All synthesis operators are modeled using the estimated macro model shown in Figure 6.27. Areal shot records are generated with a p-range from -117 $^{\mu s}/m$ to 117 $^{\mu s}/m$ (ca -30° to 30°) with $\Delta p = 9.8$ $^{\mu s}/m$ at target level. The individual migrated sections are stacked in a common depth point sense. Figure 6.47 shows the total section from a stack of all migrated, filtered areal shot records. Compare this result with the result without filtering (Figure 6.38, page 83). The filter increases the SNR significantly. Only very weak reflections are affected at the left-hand side of the section. The structure of the target zone is very well preserved.

We will now look how we can choose the sampling in the angle (rayparameter) direction Δp. The sampling of $\Delta p = 9.8$ $^{\mu s}/m$ was used to increase the SNR to an acceptable level. We will resample the angle domain with a factor of 2 and 4 and show the results. Figure 6.48 shows the section for a sampling of $\Delta p = 20$ $^{\mu s}/m$. A slight decrease of the SNR is visible. The overall quality of the image is similar to the result where the full range of angles is taken (Figure 6.47) for all depth levels. By controlling the sampling of the illuminating wave fields in the layer with the highest velocity, we oversample the layers with a lower velocity. This means that increasing the angular sampling interval has almost no effect on the resolution. If we increase the angular
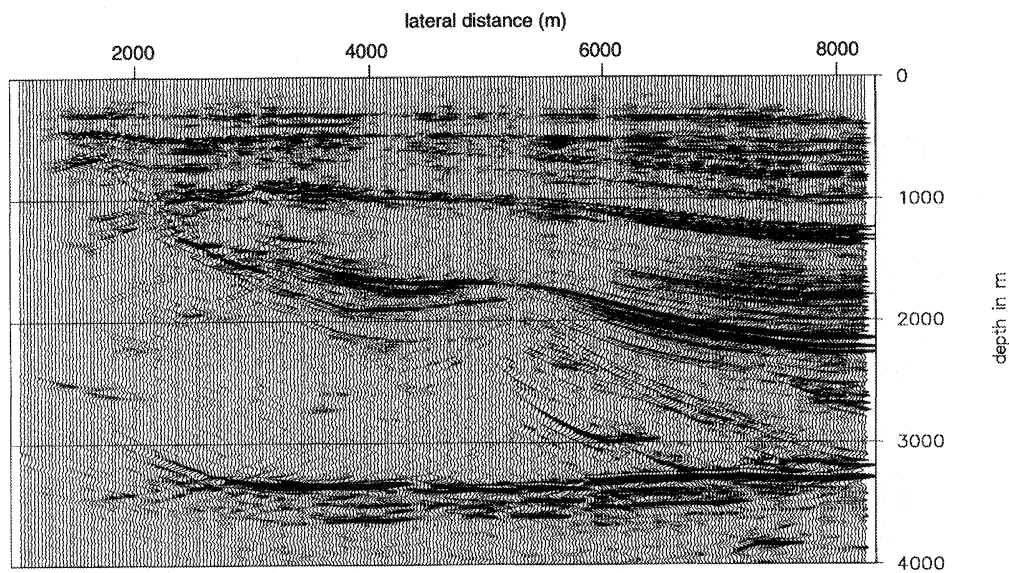
Figure 6.47 *Depth section obtained after migration of 25 filtered target-oriented areal shot records. For the Fresnelzone filtering two iterations of the 3-point Fresnelzone filter are used. Compare this result with the result if no filtering is applied during the synthesis (Figure 6.38, page 83). Note that the signal-to-noise ratio has improved and that some low amplitude events are suppressed at the left-hand side of the section.*
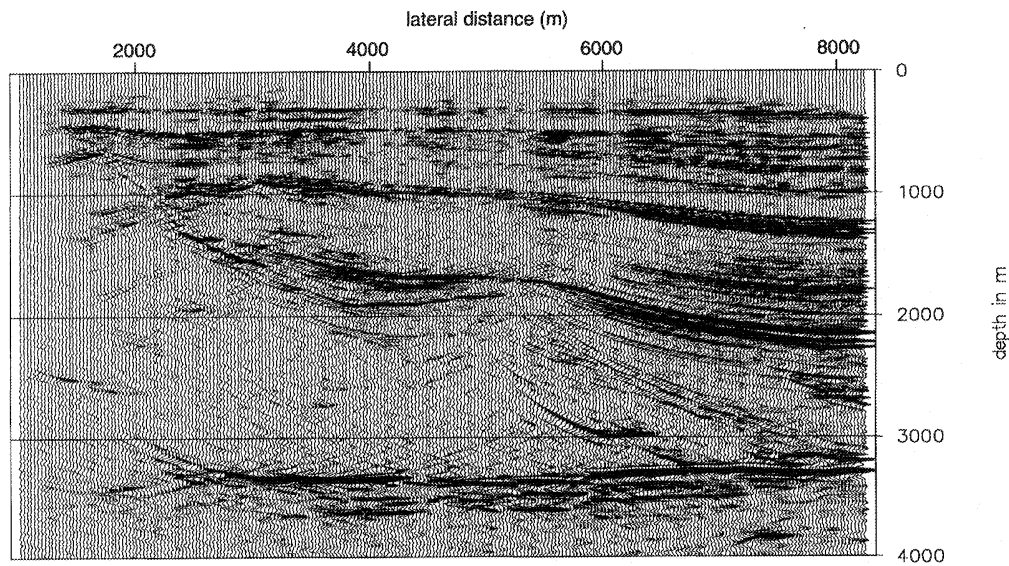
Figure 6.48 *Depth section obtained by stacking 13 individually migrated target-oriented filtered areal shot records. The rayparameter sampling is $\Delta p = 20$ μs/m. For the Fresnelzone filtering two iterations of the 3-point Fresnelzone filter are used. Note that there is a slight decline in the signal-to-noise ratio, compared to the depth section as shown in Figure 6.47.*

lateral distance (m)
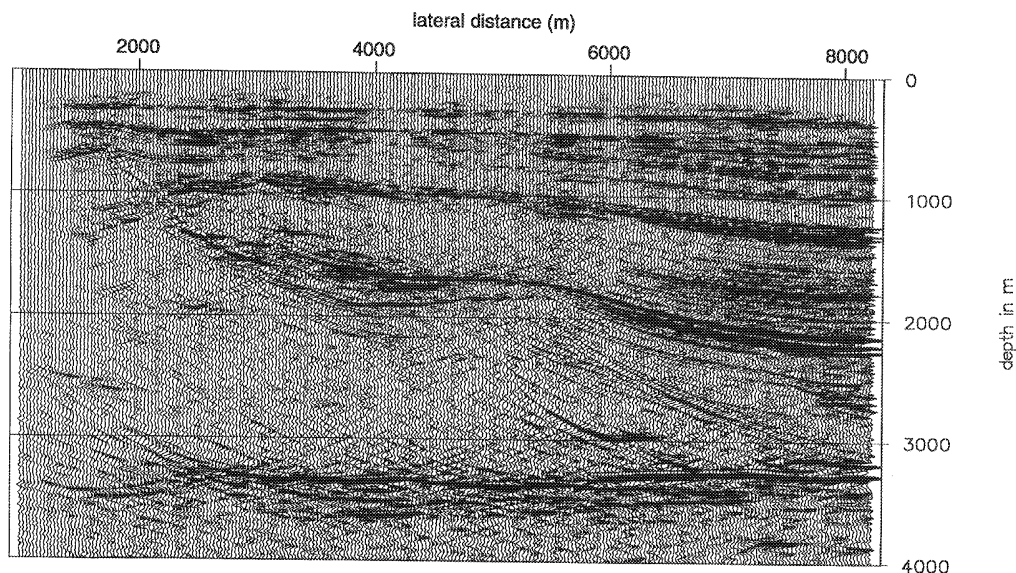
Figure 6.49 *Section obtained by stacking 7 individually migrated target-oriented filtered areal shot records. The rayparameter sampling is $\Delta p = 40$ µs/m. For the Fresnelzone filtering two iterations of the 3-point Fresnelzone filter are used. Note that there is a decline in the signal-to-noise ratio, compare to the depth section as shown in Figure 6.47. Also the image quality in the target zone is affected by the coarse sampling in the rayparameter domain.*

sampling interval to $\Delta p = 40$ µs/m (Figure 6.49), we see a further decrease of the SNR. Only in the target area the noise level disturbs some of the lower amplitude events, and the quality of the image in the target zone is decreased. The quality of the rest of the depth section is similar to the results as shown before in Figures 6.47 and 6.48.

The filter as presented in this section filters along isotime lines and does not honor the curvature which occurs inside the Fresnel zone. If the filter would work on a small timegate, the amplitude conservation would improve, and hence the quality of the areal shot record. The design of such a filter is not straightforward and is beyond the scope of this thesis.

In conclusion we may state that the application of Fresnelzone filters during the synthesis process provides an excellent tool to increase the signal-to-noise ratio in the areal shot records, hence in the migrated sections. This leaves the opportunity for a more sparse sampling in the angle domain, increasing the efficiency of the areal shot record method. The application of the Fresnelzone filter can be used in both the surface-oriented and target-oriented synthesis. The target-oriented approach, using controlled illumination, is favourable over the surface-oriented approach, since by controlling the illuminating source wave field at target level, also the resolution is controlled. Increasing the length of the filter or the number of iterations will remove all noisy events from the data, but will also effect the low S/N events in the areal shot record.

3-D extension and example

7.1 Introduction

If we look at one of the main features of the areal shot record synthesis method, we may conclude that the processing of seismic data becomes more efficient. Since the seismic industry is concentrating on 3-D data, it is obvious that the strength of the method of areal shot record synthesis becomes even more evident. In this section we will discuss how the method of areal shot record migration can be used in 3-D processing. First we will discuss the influence of the spatial sampling in 3-D on the pros and cons of areal shot record synthesis. Next some implementation aspects will be discussed. Finally results will be shown on a simple synthetic data set and on a watertank data set.

7.2 Areal shot record synthesis in three dimensions

If we would have a full 3-D acquisition geometry at our disposal, it would be possible to synthesize areal sources which have lateral extent both in the x- and y-direction. Unfortunately this will never be the case. In *land* acquisition it is common practice to sample the sources sparse in the in-line direction, whereas a proper sampling is used in the cross-line direction (Figure 7.1a). For the *marine* case, several parallel streamers may be used, and the surface is scanned in a line-wise manner (Figure 7.1b). It is obvious that any sparse sampling can cause problems for the synthesis process, especially concerning *aliasing*. To keep control over the effect of aliasing, we suggest to initially use the technique of areal source synthesis in an *line-oriented* mode, using only those sources, which are properly sampled, thus avoiding aliasing. The migration of each line source would result in a 3-D image of that part of the subsurface which is illuminated by that specific line source (Figure 7.1).

If the data are processed in such a way, we keep control over all images per source line. At the end of the areal shot record migration, the depth sections can be combined in *one* depth section,
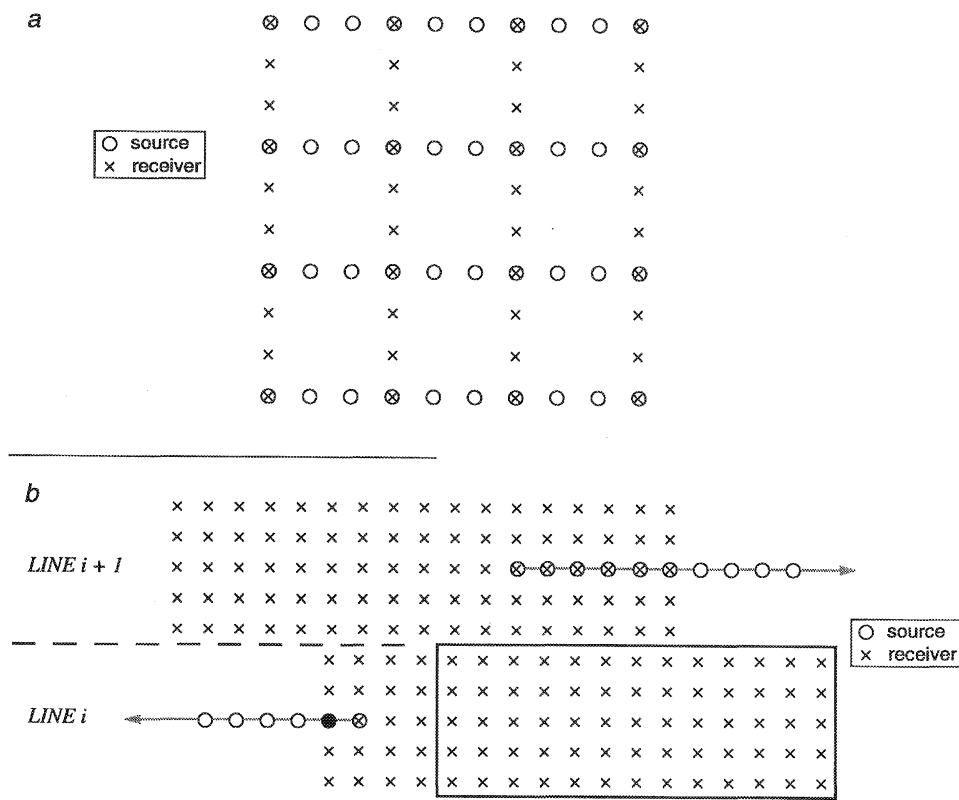
Figure 7.1 *Practical acquisition geometry for a 3-D survey. (a) Land acquisition. (b) Marine acquisition. For the marine acquisition only two shot lines are shown. The window shows the receiver groups used for the indicated shot.*
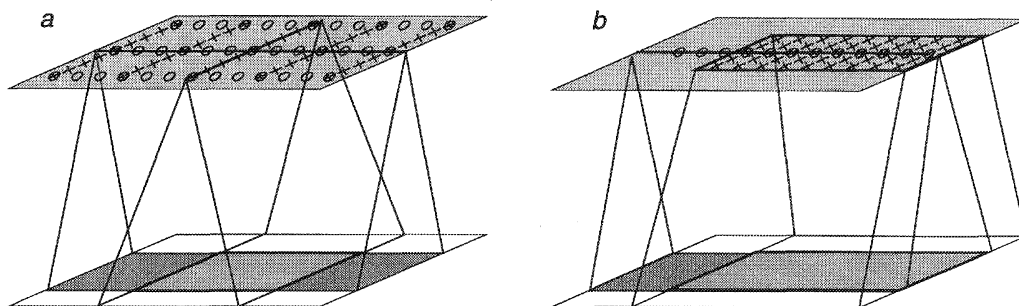
Figure 7.2 *Line-oriented processing of 3-D data. By processing per source, control is kept on the aliasing problem. (a) Land data case; (b) marine case.*

by applying a *common depth point stacking*. Inspection on the alignment of different events in the individually migrated areal shot record can provide information on the quality of the velocity model used for the migration.

For small illumination angle an additional synthesis in the sparse sampled source directions can be performed *prior* to migration, resulting in the response of a 2-D areal surface source. The migration of this *one* areal shot record would result in an image of the whole 3-D subsurface. In the watertank example we will illustrate both methods.

Another problem in 3-D processing is the irregular sampling. Feathering in the marine case and environmental restriction on land can cause a distortion of the desired regular acquisition geometry. Irrespective of the type of processing, both known and unknown irregularities in source and receiver positions will cause a distortion in the subsurface image, if not taken properly into account. Broekers (1994) shows the influence of irregularly sampled data on the areal shot record for the 2-D case. To overcome the problems of irregularly sampled data, he describes a method, which reconstruct prestack data on a regular grid, requiring knowledge of the sampling positions and the (irregularly sampled) data only. This important subject is still under study.

In this chapter we will focus on the influence of sparsely sampled data. A discussion of the regularization problem is beyond the scope of this thesis.

7.3 Implementation aspects

Processing of 3-D data has two bottle-necks. The first one is the total amount of input-output (I/O) operations. The second one is the number of computations involved in the processing itself. The use of areal shot records is the approach discussed in this thesis to solve the second problem. In this section we will discuss the first problem by looking at the data flows involved in the procedure of areal shot record synthesis and migration. We will show two possible data flows: the first one is more suited for the conventional way of processing, using shot records in the time domain as input of the processing scheme, whereas the second one shows the data flow for processing in the frequency domain. The conversion to the time domain is in principle only for display purposes. We will first discuss the data flow for the synthesis process.

The data flow, using the shot records in the time domain as input, is shown in Figure 7.3. We see that the data flow can be split into three levels, two input levels (one for the synthesis operators, and one for the shot records) and one output level. All data on tape is assumed to be in the (x,t)-domain. The first input level shows the storage of the synthesis operators from tape to disk; at the same time the operators are transformed from the (x,t)- to the (x,ω)-domain. It is beneficial to synthesize as many areal shot records as possible in one pass, to avoid several passes of the prestack input data. For the 2-D case this is in general not a problem. For the 3-D case however, the total (computer) memory required for the areal shot records might be too large. Note that the synthesis operator is stored as function of the source *position*. The second input level shows the shot records, which are (piece by piece) stored from tape onto disk. Again,
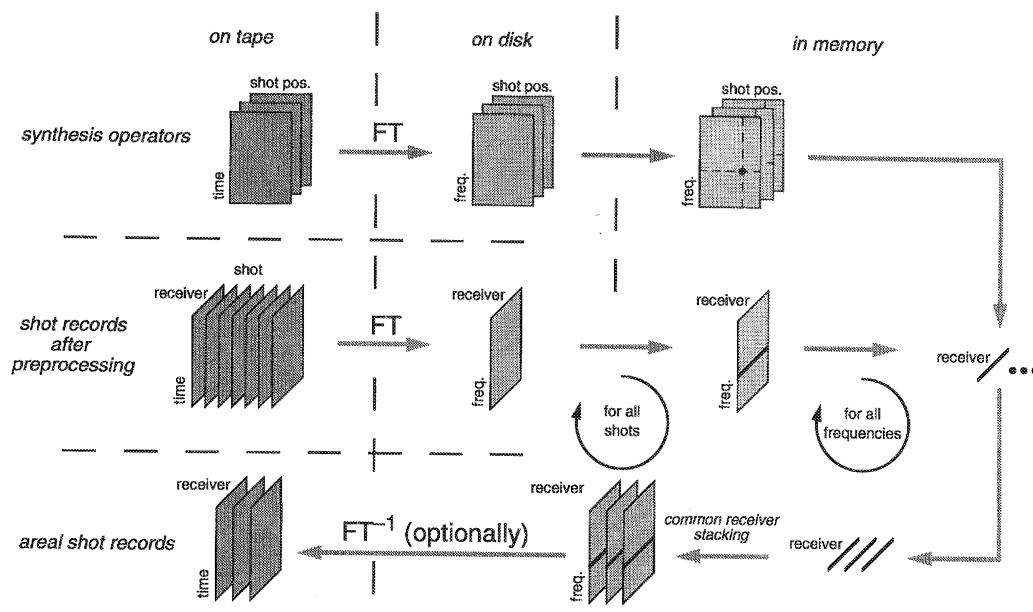
Figure 7.3 Data flow for areal shot record synthesis, using shot records in the time domain as input.

at the same time the data is transformed from the (x,t)- to the (x,ω)-domain. Each frequency component of the shot record is multiplied by the frequency component of the trace of the synthesis operator belonging to the shot position of that shot record. Next, this result is stacked onto the result obtained from the previously processed shot records in a common receiver sense (the actual *synthesis*). If this is done for all the relevant frequency components of the shot record, a new shot record is considered. Note that the areal shot record is not transformed into the (x,t)-domain, unless the user wants to inspect the areal shot record. It can also be stated at this point that the use of a processing scheme, as depicted in Figure 7.3, involves not many more I/O operations than a normal *post-stack* processing scheme.

The second option for the implementation of the algorithm of areal shot record synthesis is shown in Figure 7.4. Here all data is assumed to be already stored in the (x,ω)-domain. This means that the shot records are stored in so-called *frequency files*. These frequency files are in fact the *data matric*es in the forward model as discussed in Chapter 2. If we compare Figure 7.4 to Figure 7.3, it is obvious that the total amount of I/O in the second scheme is less, and that Fourier transformation is only applied for display purposes, and is not part of the processing sequence itself. Furthermore the total processing sequence is very simple and very well suited for vector processing or parallel implementation. Note that the shot record loop and frequency loop are interchanged in Figure 7.4 and Figure 7.3. This allows for a better parallel implementation. It should also be stated here that 3-D data sets do not influence the data flows itself, but 'merely' change the size of the files involved.
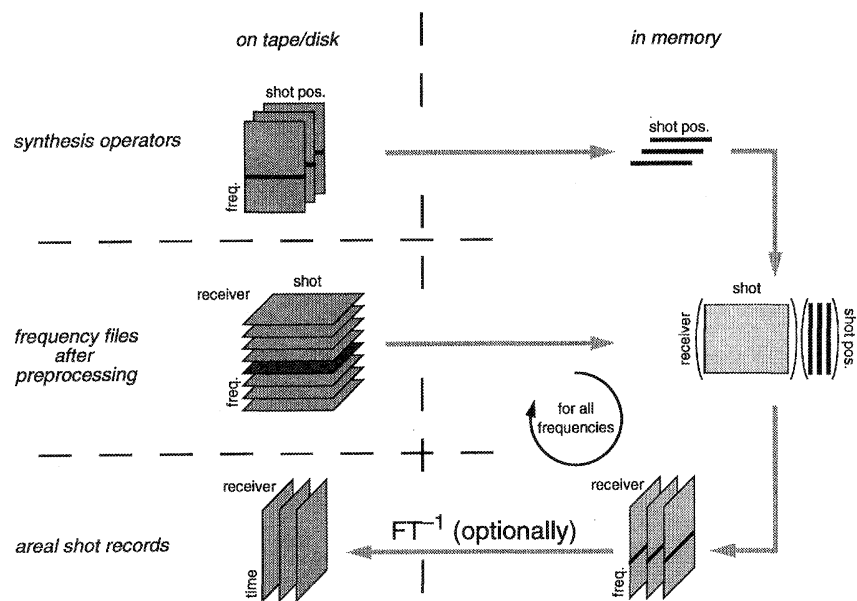
Figure 7.4 *Data flow for areal shot record synthesis, using input data in the frequency domain. Note the simplicity of the data flow (compare Figure 7.3). The frequency files are the output of the surface related preprocessing.*

The data flow for the areal shot record migration following the synthesis for areal shot record synthesis, is fully equivalent to the data flow for normal shot record migration. The areal source wave field is given by the synthesis operator (at the *surface*). The data flow is shown in Figure 7.5. For every depth step the areal source wave field and areal shot record are extrapolated. Note that if a recursive scheme is used for these extrapolations, the results after extrapolation are used as input for the extrapolation to the next depth level. Since all processing is performed in the frequency domain the imaging is nothing more than the stacking of all individually extrapolated frequency components.

The implementation of the areal shot record migration scheme allows for two levels of parallellization: one in the areal shot record direction and one in the frequency direction. The areal shot record direction leaves totally independent experiments. For the frequency direction the extrapolations can be performed parallel, after which all the monochromatic wave fields should be gathered for the imaging step.

In practice the acquisition geometries make it very doubtful whether it is possible to rearrange data in true Common Receiver Gathers (CRG). Even if this is possible, they are often sparsely sampled. The only true gather in practice is the Common Shot Gather (CSG), i.e. the shot record. Ignoring directivity effects (they should be taken care of in the surface related pre-processing) a CSG can be considered a true CRG, using *reciprocity*. If this principle is applied to
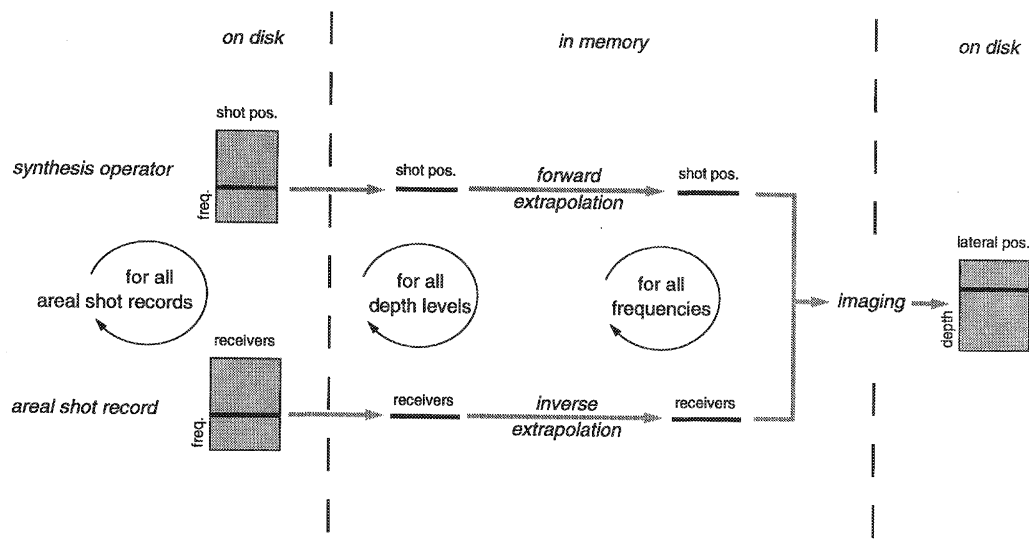
Figure 7.5 *Data flow for the (areal) shot record migration.*

the data, it means that the synthesis of areal shot records can be applied to CSGs in stead of CRGs. Hence, the processing of each shot record results in *one* trace of the areal shot record positioned at the source position.

The migration scheme used for the examples shown in this chapter is a 3-D explicit recursive space-frequency depth migration. Many papers have been written on the subject of 3-D depth migration. Hale (1991) gives an historic overview. Based on the one-way wave equation, explicit extrapolation filters can be designed (Holberg, 1988). Blacquière (1989) extended this method to the 3-D case, using a table-driven implementation, in which a table of pre-computed extrapolation operators is used. Because of the small depth step which is taken in the recursive extrapolation, we can take a *homogeneous* extrapolation operator, which is symmetric around its center. The extrapolation is done by a 2-D convolution of the data with the appropriate extrapolation operators.

7.4 Synthetic example

To illustrate the influence of a sparse acquisition geometry two standard acquisition geometries are investigated. The model used for these experiments consists of a horizontal density contrast at a depth of 400m. In the first experiment the acquisition geometry consists of a 2-D line, 101 sources and receivers, with an in-line spacing of 10m. This acquisition geometry can be seen as a basic building block for 3-D *marine* surveys. A horizontal plane wave is synthesized and the areal shot record is migrated in a 3-D sense. The areal shot record is shown in Figure 7.6a. Figure 7.6b shows an image in the in-line direction, direct below the source positions. The

image of the reflector is positioned at the correct depth. The image in the cross-line direction (Figure 7.6c) shows the well-known zero-offset migration *impulse response*, because we have only zero-offset data in the cross-line direction. The depth slice at 400m is shown in Figure 7.6d. Clearly the reflector can be identified in the in-line direction, whereas in the cross-line direction we do not have the offsets to image the reflector properly. A full image of the reflector can be obtained by combining parallel 2-D lines. This will result in a *post-stack* image in the cross-line direction, whereas we have the possibility to obtain a *prestack* image in the in-line direction.

In the second experiment the acquisition geometry consists of a 2-D source line with the receivers positioned perpendicular to the source line. The source and receiver line cross in the middle of the surface and consist of 101 positions with a lateral spacing of 10m. This acquisition geom-
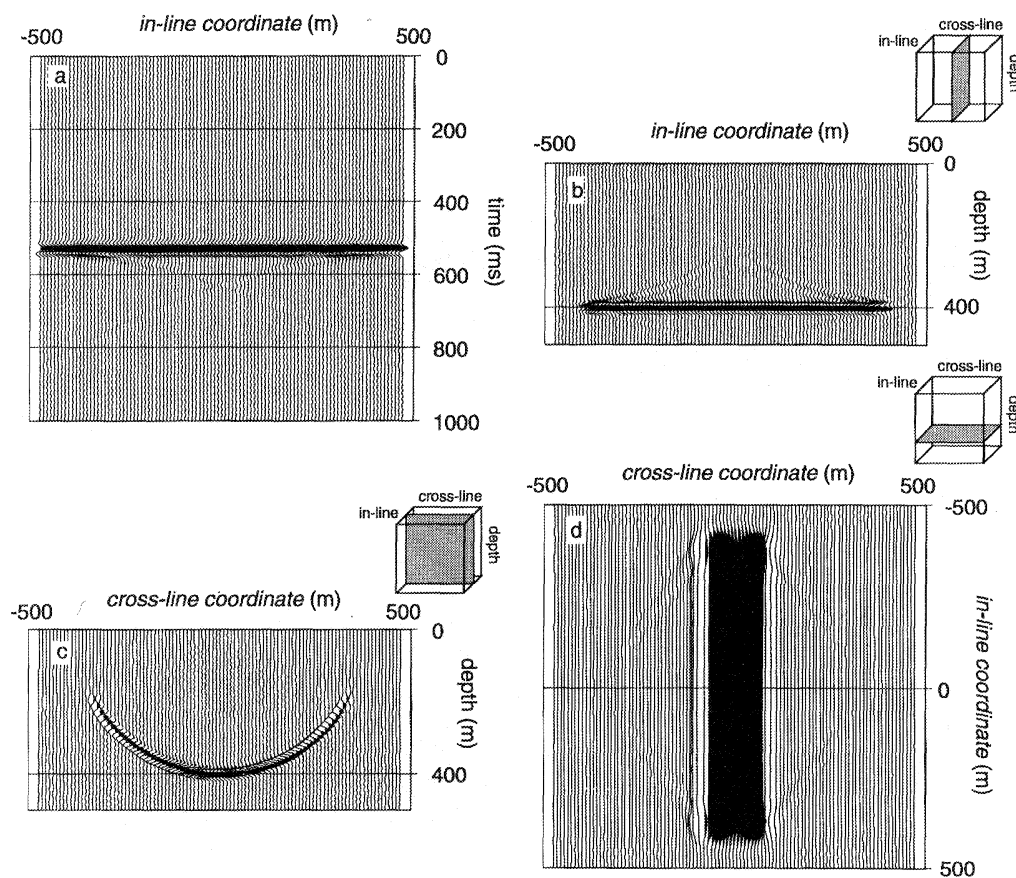
Figure 7.6 (a) *Areal shot record for a horizontal plane wave over a horizontal interface. Sources and receivers are positioned along the same line.* (b) In-line *cross-section of the 3-D migrated areal shot record.* (c) Cross-line *cross-section of the 3-D migrated areal shot record.* (d) *Depth slice at the reflector.*

etry can be seen as a basic building block for 3-D *land* surveys. A horizontal plane wave is synthesized and the areal shot record is migrated in a 3-D sense. The areal shot record is shown in Figure 7.7a. Figure 7.7b shows an image below the receiver line. The image of the reflector is positioned at the correct depth at the position where the receiver line crosses the source line. This image is the impulse response of the migration of a horizontal plane wave. The image below the source line (Figure 7.7c) shows the migration result for one 2-D shot record. Only the illuminated part of the reflector is imaged and positioned at the correct depth. The depth slice at 400m is shown in Figure 7.7d. Clearly visible is the region where the reflector is imaged properly, directly below the crossing of the source and receiver line. It can be imagined that the total reflector can be imaged by combining different overlapping 'patches', where a relative sparse sampling of the source and receiver lines is allowed. The combination of the data should from an aliasing point of view in principle be done *after* migration.
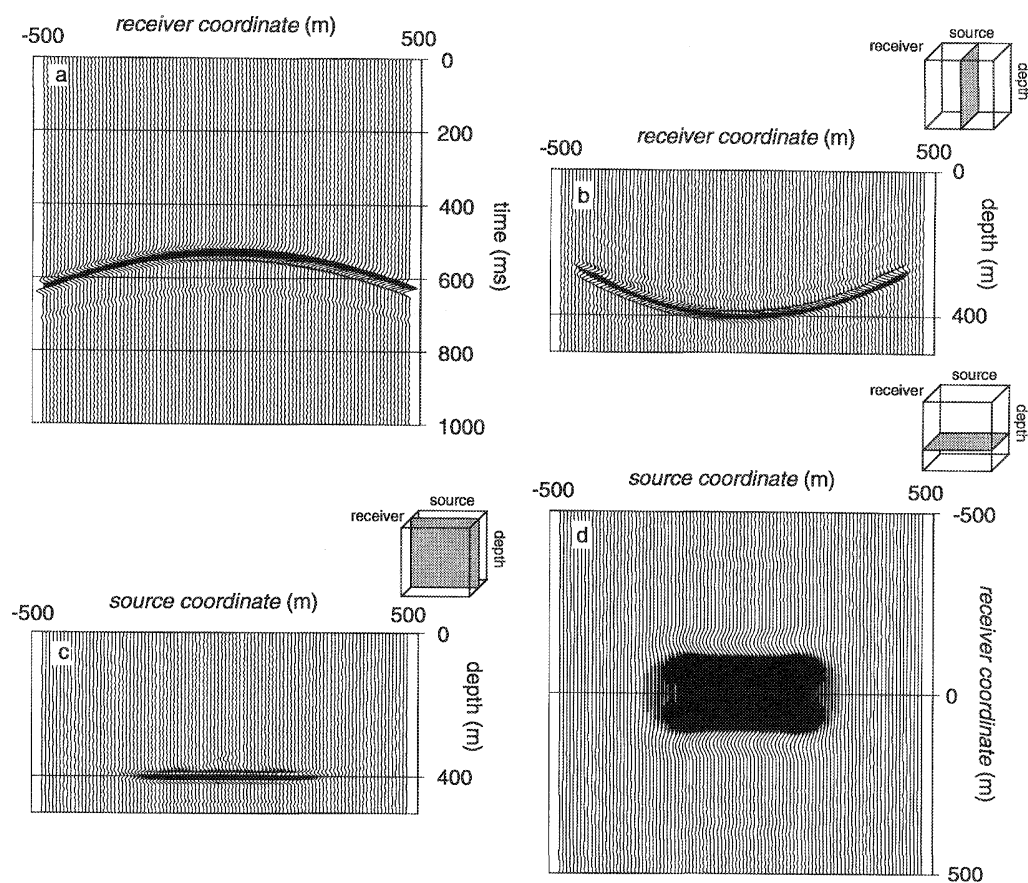
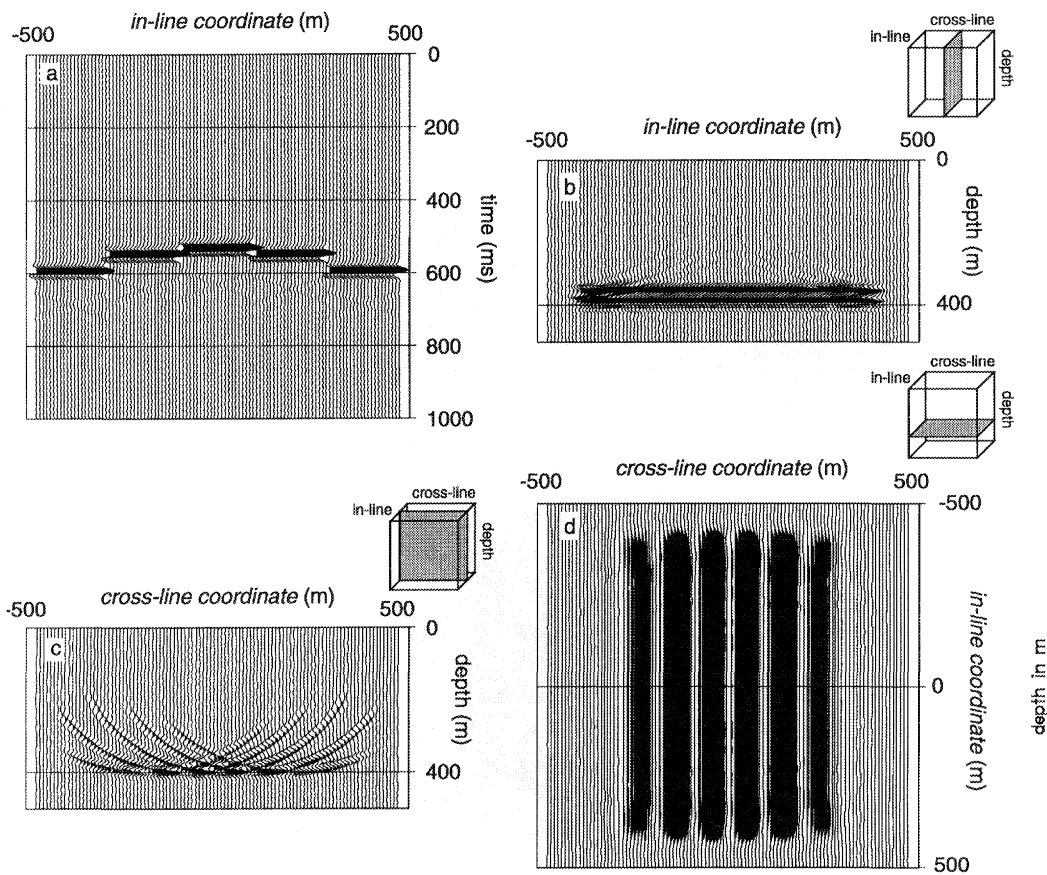
Figure 7.7   (a) *Areal shot record for a horizontal plane wave over a horizontal interface. Source and receiver line are perpendicular to each other, crossing at the center of the model.* (b) *Cross-section of the 3-D migrated areal shot record below the* receiver *line.* (c) *Cross-section of the 3-D migrated areal shot record below the* source *line.* (d) *Depth slice at the reflector.*

In the third experiment the acquisition geometry consists of a 2-D line with 101 sources 5 streamers, containing 101 receivers each, with an in-line spacing of 10m. The cross-line sampling interval of the streamers was 200m. Again, a horizontal plane wave is synthesized and the areal shot record is migrated in a 3-D sense. The middle 20 traces of each streamer of the synthesized areal shot record are shown in Figure 7.8a. Figure 7.8b shows a cross-section in the in-line direction, directly below the areal source. If we compare this response to the response using only one streamer (Figure 7.6b) we observe a degrade of the image due to the interference of the images of the separate streamers. In the cross-line direction (Figure 7.8c) we see that the image of the reflector is better resolved due to the offsets that are now available in the cross-line direction (compare with Figure 7.6c). Due to the coarse sampling in the cross-line direction strong aliasing is visible in the image of the reflector. This can also be seen in the depth slice at the depth of the reflector (Figure 7.8d). Hence, the offsets in the cross-line direction help to

Figure 7.8 (a) *Part of the areal shot record for a horizontal plane wave over a horizontal interface using a parallel streamers. The* cross-line *spacing of the streamers is* 200m. *The in-line spacing is* 20m.
(b) *Cross-section of the 3-D migrated areal shot record in the* in-line *direction.* (c) *Cross-section of the 3-D migrated areal shot record in the* cross-line *direction.* (d) *Depth slice at the reflector.*

resolve the structure of the reflector in this direction, but due to aliasing, the image is too coarse sampled.

In the last experiment the acquisition geometry consists of one 2-D line of 101 sources with a sampling of 10m. The receivers are positioned along 5 parallel lines, perpendicular to the source line, with an in-line sampling of 10m and a cross-line sampling of 200m. Like in all other experiments a horizontal plane wave is synthesized and the areal shot record is migrated in a 3-D sense. The areal shot record consists of 5 streamers with all identical responses (apart from some edge-effects) as shown in Figure 7.7a. In Figure 7.9a an image below the middle receiver line is shown. The image contains the interference pattern of 5 horizontal plane-wave migration pulse responses (compare Figure 7.7b). The envelope reveals the structure of the reflector, but the image is distorted due to aliasing. The image below the source line (Figure 7.9b) shows also a distorted image of the reflector with strong artefacts caused by aliasing. The depth slice at the reflector shows that the structure of the reflector both in the source and the receiver lines direction is correctly resolved. Due to the aliasing the image is very distorted.

Figure 7.9 *An areal shot record for a horizontal plane wave over a horizontal interface is synthesized. Source and receiver lines are perpendicular to each other. Five parallel receiver lines are used with a cross-line sampling of 200m and an in-line sampling of 20m. (a) Cross-section of the 3-D migrated areal shot record below the middle receiver line. (b) Cross-section of the 3-D migrated areal shot record below the source line. (c) Depth slice at the reflector.*
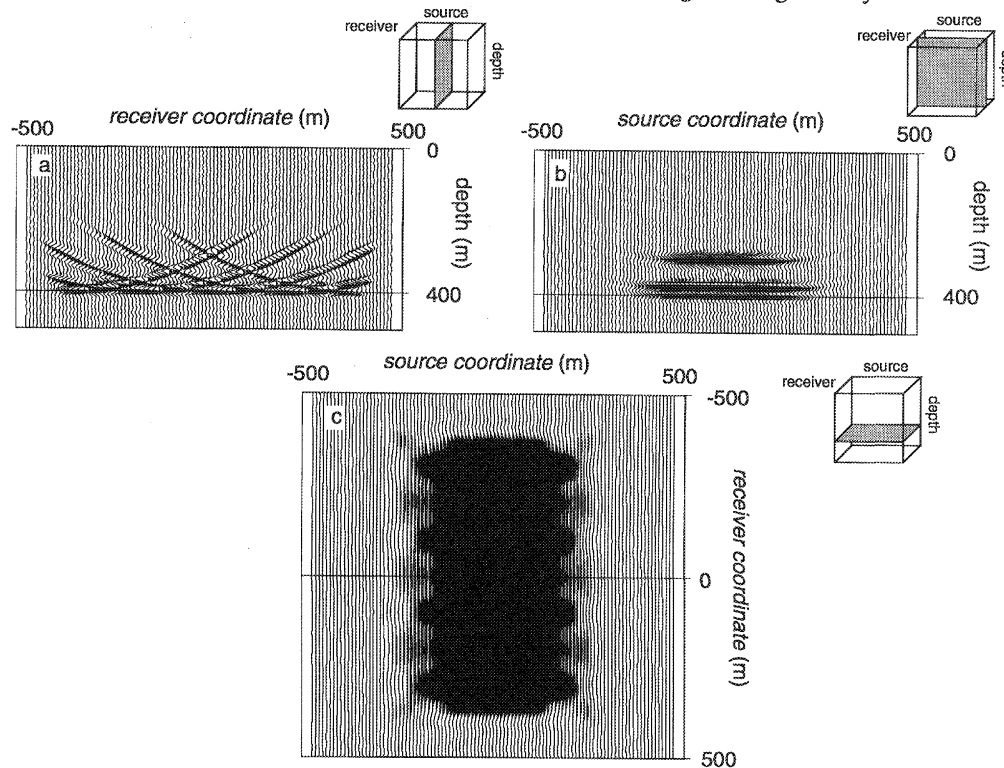
From these experiments we may conclude that 3-D structural information can only be revealed if the acquisition geometry has a 3-D character, i.e. offsets in the in-line and cross-line directions. Aliasing caused by a too coarse sampling will degrade the image severely and can cause a misinterpretation of the imaged 3-D structures.

7.5 Example on a watertank data set

7.5.1 The model and the acquisition geometry

In the measurement facility of the Laboratory of Seismics and Acoustics in Delft, the Netherlands 3-D marine data is acquired in a new watertank. The model used for the measurements is shown in Figure 7.10, together with the model parameters. A description of the measurement facility is given by Koek and Faber (1992, 1995). The model is built with different types of rub-

layer	velocity (m/s)	density (kg/m³)
1	1487	1000
2	1018	959
3	2190	1035
4	1018	959
5	1510	1070
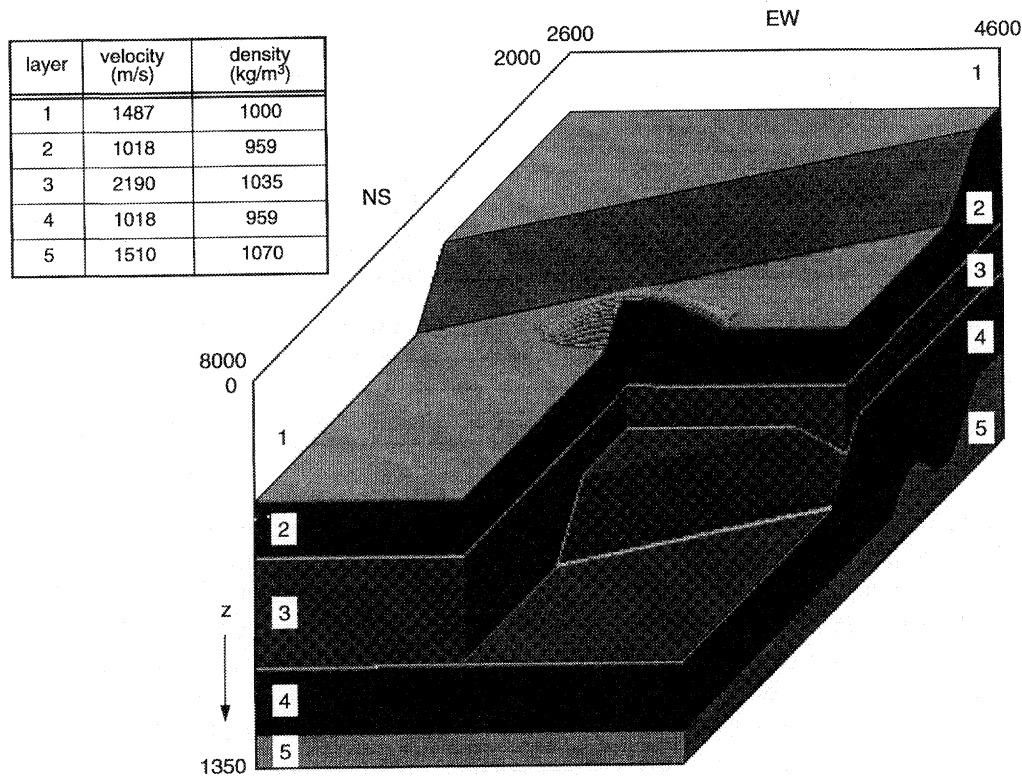
Figure 7.10 *An inside look in the model as used for the watertank measurements. The acquisition level is at z=0m. The medium parameters are shown in the table. A marine data set was acquired, using parallel shot lines with an in-line sampling (x-direction) of 20m and a cross-line sampling (y-direction) of 60m. Hydrophones were used with 7 parallel streamers with an in-line sampling of 20m and a cross-line sampling of 60m, centered behind the source position. Five shot lines were acquired over the center of the model.*
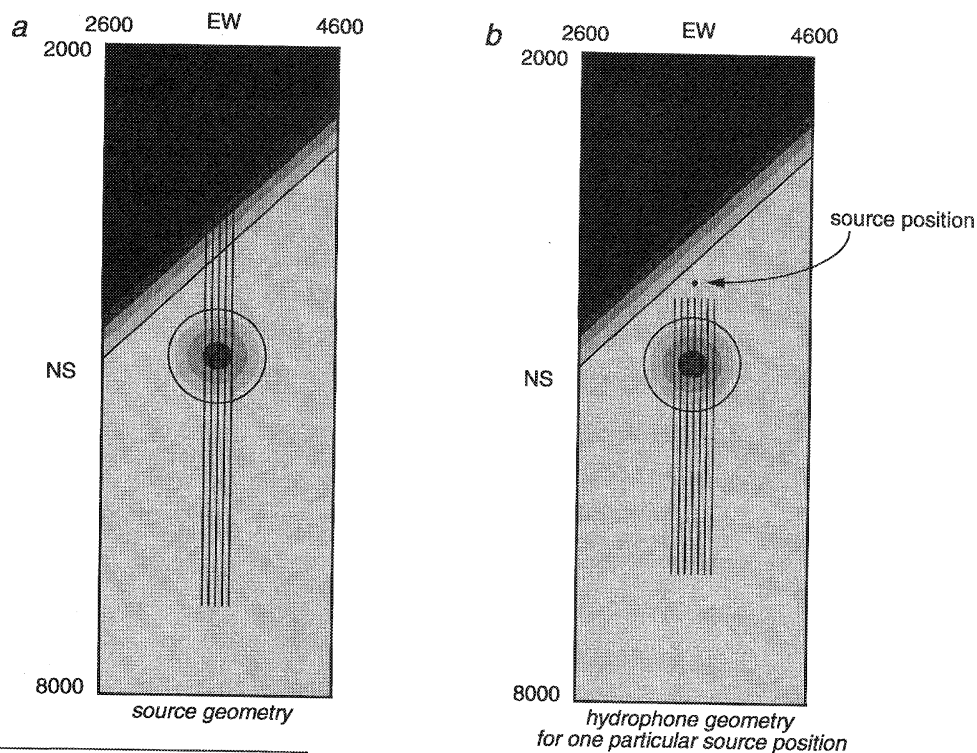
Figure 7.11 *The acquisition geometry plotted over a top view of the first layer. The source geometry consists of 5 parallel lines with an in-line sampling (NS-direction) of 20m and a cross-line sampling (EW-direction) of 60m. The source lines are positioned at EW 3500, 3560, 3620, 3680 and 3740. The hydrophone geometry consists of 7 parallel streamers with an in-line sampling of 20m and a cross-line sampling of 60m, centered behind the source position. The nearest offset for the center streamer is 100m. In (b) the source position associated with the hydrophone positions is indicated.*

ber-like materials, to avoid the excitation of shear waves. The acquisition geometry consists of 5 parallel source lines, in-line spacing *20m*, cross-line spacing *60m* (Figure 7.11a), where each shot record shoots in 7 parallel streamers, symmetrically positioned behind the source (Figure 7.11b), with an in-line sampling of 20m and a cross-line sampling of 60m. Each source line consists of 250 source positions. The source lines are positioned at the coordinates EW3500, EW3560, EW3620, EW3680 and EW3740. On this 3-D marine survey experiments will be done, where plane-waves line sources will be synthesized at surface and migrated in a 3-D sense through the model. Next a true 2-D areal source will be constructed, so a synthesis both in *in*-line *and cross*-line direction. Finally we will show an example of a controlled illumination experiment, illuminating the second boundary by a horizontal plane wave.

7.5.2 Line-oriented plane-wave synthesis at the surface

As argued in the previous section, given the sparse sampling of the sources in the cross-line direction, that we have to restrict ourselves to *line*-oriented synthesis avoiding aliasing effects.

The combination of the various migrated line-oriented areal shot record should be done *after* migration. In this experiment we synthesize cylindrical plane-waves at the surface for rayparameters ranging from $p = 0$ $^{\mu s}/m$ to $p = 450$ $^{\mu s}/m$ (approx. 42°). Only positive angles are used, since this marine acquisition geometry does not contain the negative angles. These could be constructed using *reciprocity*, but this would require the full 3-D data volume to be read for the synthesis of one cylindrical areal source, which increases the total I/O involved in the synthesis and increases the complexity of the implementation of the synthesis process. First the results for line EW3620 will be shown, followed by the final result after stacking all the individually migrated areal shot records.

Synthesis and migration of one areal shot record with cylindrical areal source wave field

Figure 7.12 shows the middle streamer of the synthesized cylindrical areal shot record for rayparameter $p = 0$ $^{\mu s}/m$. Also the traces of all streamers are shown for the part with the reflection of the fault of the top layer. From Figure 7.12a we see that the damping in the indicated layer causes the reflections of lower reflectors to have small amplitude. Some internal multiples are indicated. Figure 7.12b clearly shows the 3-D structure of the fault on the first layer. The different offsets show not only a difference in traveltime caused by the cross-line offset, but also show different reflections of the fault, due to the 3-D nature of the structure.

The areal shot record is migrated using frequencies ranging from *20Hz* to *50Hz* and a depth step $\Delta z = 7.5m$. As imaging principle the correlation is used, this to avoid possible instabilities during imaging. In Figure 7.13a the vertical cross-section is shown of the depth section at position EW3620, i.e. the position of the areal line source. Note that the fault of the first layer is not imaged properly. This is due to the fact that this reflection is mainly an *out-of-plane* event, due to the spatial structure of the fault. Clearly the first two layers can be identified. Below the fault and the dome, the layers are not well illuminated, which causes the image to fade. In Figure 7.13b three depth slices are shown slicing through the first layer at the high ($z=220m$) and the low part ($z=440m$), and through the second layer ($z=650m$). Clearly the structure of the fault can be identified. The slight change in phase along the imaged boundary indicates that the interface is not entirely flat. This is well visible in the slice at $z=650m$. Here clearly the bad illuminated areas can be identified. In the depth slice at $z=440m$ some edge effects are visible at larger cross-line offsets from the source line (EW3620). They are caused by the limited offset in the cross-line direction.

CDP stacking of individually migrated areal shot records

All 5 shot lines are synthesized over a range of rayparameters ($p = 0$ $^{\mu s}/m$ to $p = 450$ $^{\mu s}/m$ (approx. 42°), step $\Delta p = 75$ $^{\mu s}/m$, approx. 6°), and migrated individually. Afterwards all 3-D data volumes are stacked into a final depth image. The result of this processing sequence is shown in Figure 7.14. In Figure 7.14a the vertical cross-section at position EW3620 is shown. Clearly the image has improved. The image shows the both sides of the dome. The fault of the first layer is properly positioned, but weak in amplitude. This is mainly due to the angle-limitation in the extrapolation operator of *60°*. The weak illuminated areas of the second layer have mostly van-
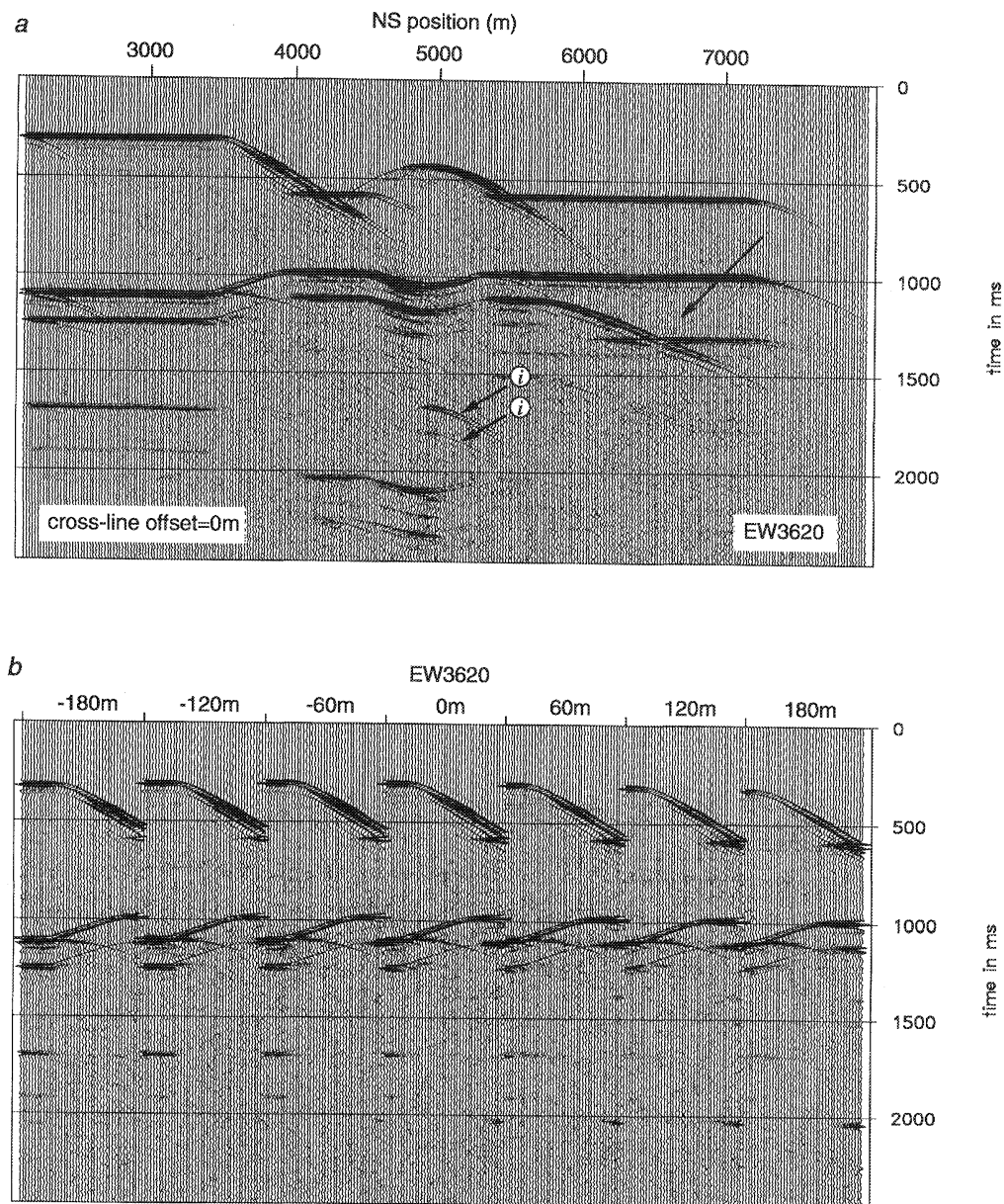
Figure 7.12 (a) *Middle streamer of the areal shot record for a cylindrical horizontal plane wave at position EW3620. Note that the deeper reflectors have a weak amplitude, due to the damping in the indicated layer. Indicated are some internal multiples (i). (b) 40 traces of all streamers of the areal shot record. Note the 3-D structure of the fault in the first layer. The cross-line offsets are indicated at the top of the Figure.*
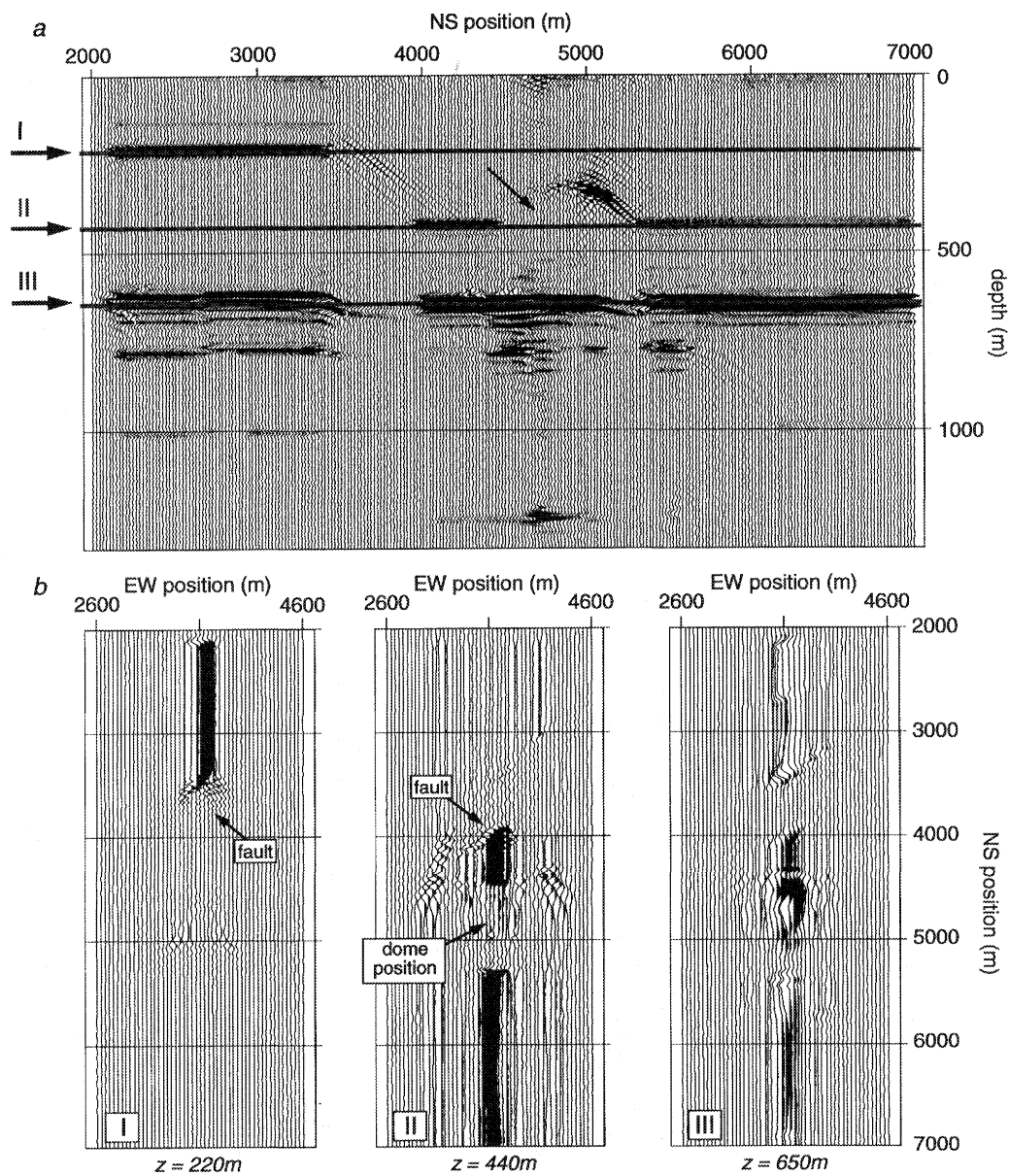
Figure 7.13 *3-D migrated areal shot record (Figure 7.12). (a) A vertical cross-section at position EW3620, directly below the position of the areal source. Clearly the structures of the first layer are visible. Note that due to the acquisition geometry (single-sided shots) only one side of the dome is imaged. (b) Three depth slices at the depths indicated in (a), cutting through the first layer at two depths (I: z=220m and II: z=440m) and through the second layer (III: z=650m). Clearly the structures can be identified, including the position of the dome. Obviously the second layer is not entirely flat, causing a slowly varying phase along the interface. Also some weak illuminated areas are visible below the dome and the fault*
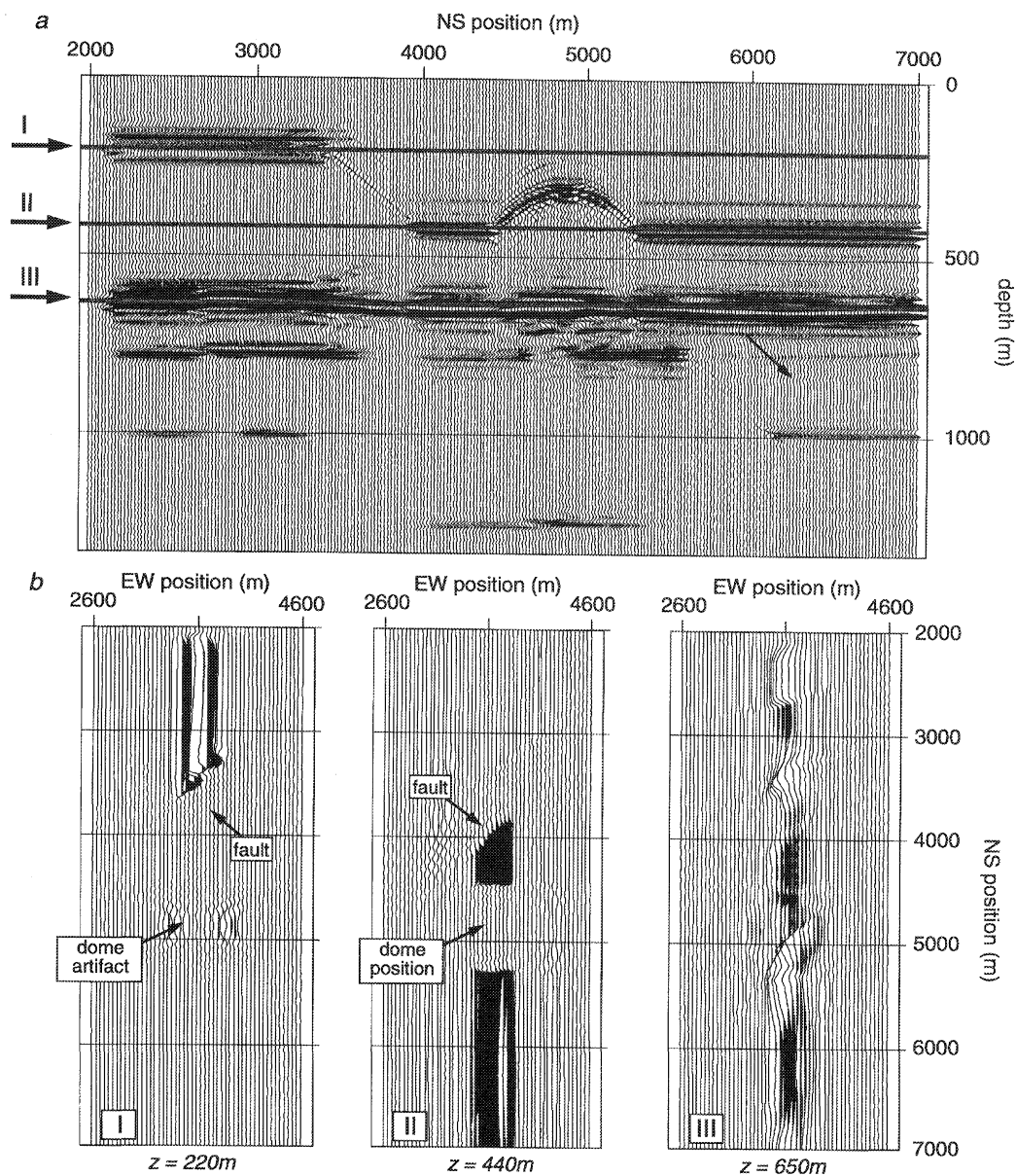
Figure 7.14 *CDP stacked depth sections after migration of all 5 source lines for 7 different rayparameters.*
(a) *A vertical cross-section at position EW3620. Clearly the structures of the first layer are visible.*
(b) *Three depth slices at the depths indicated in (a), cutting through the first layer at two depths (I:*
z=220m and II: z=440m) and through the second layer (III: z=650m). Clearly the structures can be
identified, including the position of the dome. Obviously the second layer (III) is not entirely flat, causing a
slow varying phase along the boundary. Note that the weak illuminated areas are better imaged, because
they are now illuminated from different surface positions and by different rayparameters.

ished. Clearly the wavy structure is visible, especially in the depth slice at $z=650m$ in Figure 7.14b. The depth slices at $z=220m$ and $z=440m$ make an identification of the position of the fault easy. Also the position of the dome is evident. The deeper reflectors are also better visible. The faults are not imaged, basically because of the acquisition aperture. At the right-hand side of the section, the deepest reflector vanishes ($z=1200m$). This is due to the strong damping in the indicated layer. This layer is at that side of the model significantly thicker.

7.5.3 Synthesizing areal sources in both the in-line and cross-line direction

In the previous subsection line-oriented areal shot records were synthesized. This was done because of the sparse sampling in the cross-line direction, which can cause aliasing. Similar to the 2-D or 3-D conventional shot record migration scheme the depth sections can be combined *after* migration. From an economic point of view it would be very attractive to construct from the prestack data as few areal shot records as possible, hence synthesizing areal shot records, containing the response of 2-D areal sources at the surface. In this subsection we will synthesize such an areal shot record and migrate it.

From all the prestack data, i.e. all 5 source lines with 250 shots, one areal shot record is synthesized with a rayparameter in the in-line direction $p_{in} = 75\ ^{\mu s}/m$, and in the cross-line direction $p_{cr} = 0\ ^{\mu s}/m$. The in-line rayparameter was chosen such that is assured that indeed data is used in the synthesis process. E.g. rayparameter $p = 0\ ^{\mu s}/m$ for a horizontal interface requires data at zero-offset. The cross-line rayparameter is chosen small to avoid aliasing effects caused by the sparse sampling. We will not show the areal shot record, which contains *eleven* streamers, of which the middle *three* have a cross-line fold of 5, but suffice with the migration result. The source wave field used in the migration was *not* restricted to the 5 source lines, as, theoretically spoken, would be correct. In the migration the source wave field is sampled with 20m in both the in-line and cross-line direction sampled to avoid aliasing and edge effects.

The migration result of this *one* areal shot record is shown in Figure 7.15. Figure 7.15a shows the vertical cross-section at position EW3620. The top layer is imaged correctly. The left part of the dome is not imaged due to the acquisition geometry. The fault is not imaged properly due to the angle-restriction of the used extrapolation operators. The deeper reflectors show an image comparable to the result of Figure 7.14, but with less resolution. The weak illumination of the second reflector below the fault and the dome, as was visible with the illumination with the cylindrical areal source wave field, is present again. The depth slices (Figure 7.15b) show again clearly the structures of the first layer. Also some aliasing effects are visible in the image at $z=220m$ (the black-white striped pattern). The weak illumination zone below the fault is also clearly visible. If we compare the computational effort required for the image as shown in Figure 7.15 with the image of Figure 7.14 we gain a factor of *35*. Compared to a full 3-D prestack depth migration we gain a factor of *1250*.
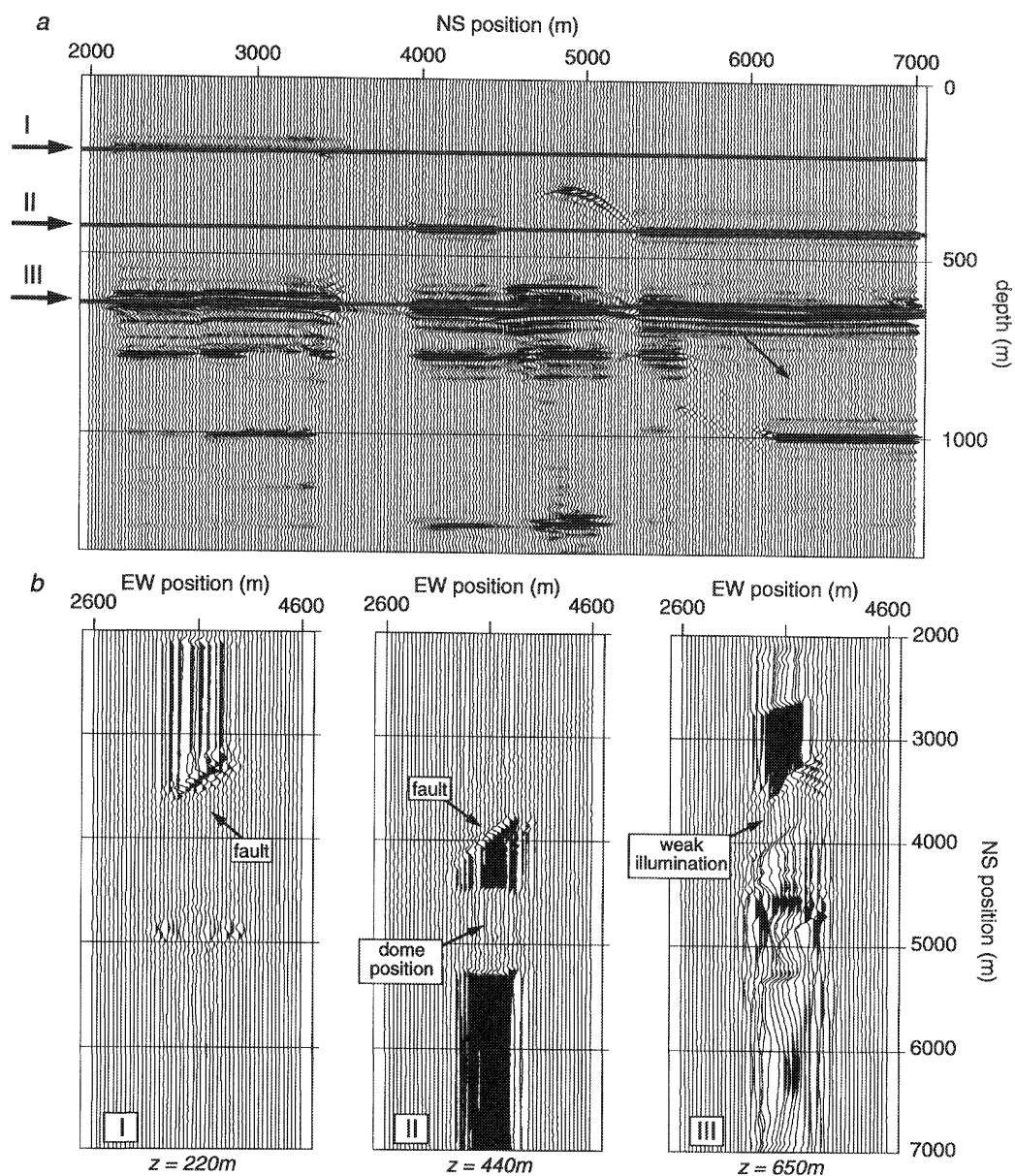
Figure 7.15 *Migration of* one *areal shot record, synthesized in the in-line and the* cross-*line direction*
(a) A vertical cross-section at position EW3620. Note that the dome is imaged only at one side, due to the acquisition geometry. (b) Three depth slices at the depths indicated in (a), cutting through the first layer at two depths (I: z=220m and II: z=440m) and through the second layer (III: z=650m). Clearly the structures can be identified, including the position of the dome. Again the wavy shape of the second layer can be observed. Also note the bad illuminated areas caused by the dome and the fault in the first layer.

7.5.4 Controlled illumination in 3-D

In the previous subsections we have seen how areal shot record synthesis and migration can be used for 3-D prestack seismic migration. Surface-oriented areal shot records were synthesized and migrated. We observed some problems concerning the illumination of deeper reflectors caused by the complexity of the top layer. By using the method of controlled illumination we will try to avoid these illumination problems.

A synthesis operator is computed based on the model as shown in Figure 7.10. A horizontal plane-wave is defined directly below the first layer at z=450m. The defined areal source wave field is defined as a true 2-D plane wave source. The synthesis operator at the surface is shown in Figure 7.16. The synthesis operator is shown for the position EW3620 and NS3700. The synthesis operator is applied to all 5 source lines and the resulting areal shot record is migrated. In the migration the full synthesis operator is taken as source wave field to avoid aliasing and edge effects. The areal shot record consists of eleven streamers with an cross-line fold of 5 for the three middle streamers. The results of the migration are shown in Figure 7.17. The vertical cross-section (Figure 7.17a) shows that the depth section at position EW3620. The image of the top layer is decreased in quality, compared to Figure 7.15a. The illumination of the second boundary (Figure 7.17b,III) has improved. This is due to the fact that the areal source wave field was constructed in such a way that it had an optimum shape at this boundary. Again, like in the previous subsection, all shots were synthesized into one areal shot record. The image shown
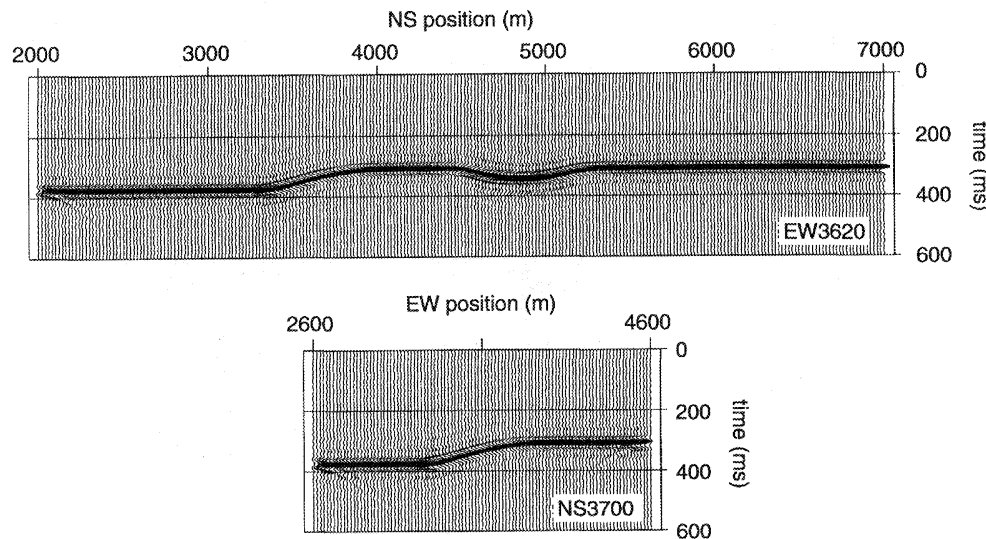
Figure 7.16 *Two slices through the modelled complex conjugated synthesis operator for a horizontal plane-wave illumination just below the first layer at z=450m. The time domain representation is shown. At the top the synthesis operator is shown along position EW3620. The bottom picture shows the synthesis operator along position NS3700. The synthesis operator is applied to the prestack data (all 5 source lines).*

a

NS position (m)

b

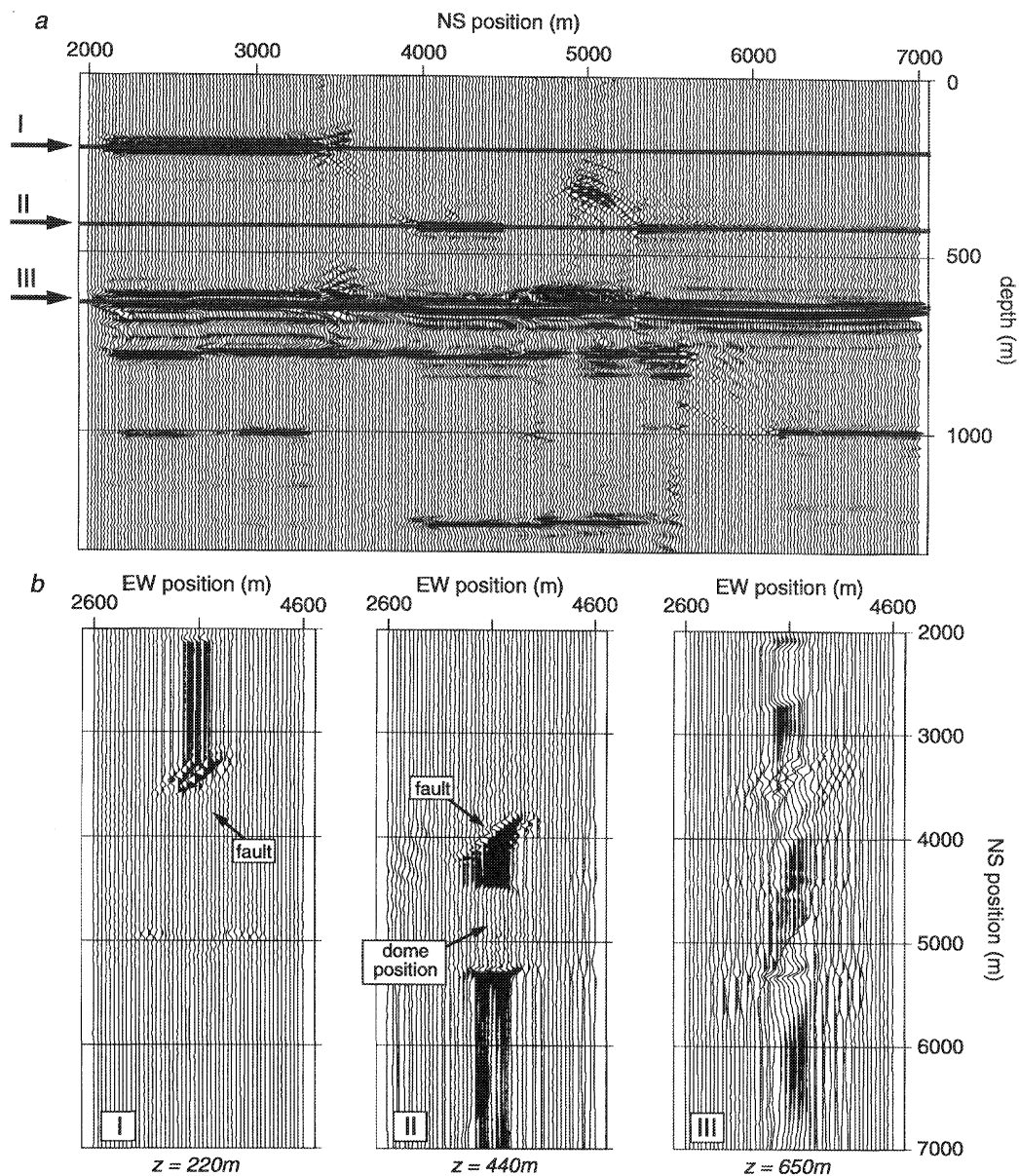**Figure 7.17** *Migration result after synthesis for controlled illumination of the second boundary by a horizontal plane wave. The synthesis was done both in the in-line and the cross-line direction. (a) A vertical cross-section at position EW3620. Note the decrease of image quality of the top layer, due to the complexity of the source wave field. Note that the illumination problem (Figure 7.15) is solved by defining the source wave field at the target boundary. (b) Depth slices at z=220m, z=440m and z=650m. Note that the quality of the top layer (I, II) is less compared to Figure 7.15. The illumination of the second boundary has improved (III).*

here requires just *one* migration of the areal source wave field. Again some aliasing effect are visible in the slice through the top of the first boundary (Figure 7.17b, I). The overall structure of the layers deeper in the section are fairly well imaged, although the signal-to-noise ratio is worst compared to the *line*-oriented approach (Figure 7.14). This is mainly due to the fact that in the *line*-oriented more illumination angles were used.

We may conclude that the first results show that by synthesizing areal shot records in the well-sampled *in*-line direction, these cylindrical source wave fields can be very well used to migrated a prestack data set in a prestack way. By synthesizing only in the *in*-line direction, control is kept on aliasing. The quality of the final image comes from the combination of the all individually migrated depth section, similar to the common depth point stacking in conventional migration schemes.

For illuminating source wave fields with small dips in the *cross*-line direction, the synthesis process may be extended in the cross-line direction, leaving an areal shot record, due to a *2-D* areal source wave field, i.e. covering the whole acquisition geometry. The results of this experiment show that although some aliasing effect are visible on the section, the overall structural information gives a good impression on the reflectors in the 3-D subsurface.

By synthesizing an areal source wave field which illuminated the second boundary as a horizontal 2-D areal plane wave, some illumination problems caused by the structures of the first boundary can be solved.

It may be stated that the results on the application of areal shot record synthesis and migration, including controlled illumination, in three dimensions show promising results. The efficiency ranges from a factor *35* for the *line*-oriented approach, to *1250* for the true *2-D areal source wave field* approach.

Appendix A

The matrices in the forward model

In this appendix the matrices, used in the forward model, as described in chapter 2 of this thesis are discussed in more detail. For a detailed discussion on the forward model and the matrices involved, the reader is referred to Berkhout (1993).

A.1 The data matrix

Consider a 2-D wave field, measured at a constant depth level as a function of lateral position and time, described by

$$p(x,z_0;t), \tag{A.1a}$$

where p is the broadband wave field in terms of acoustic pressure, x is the lateral coordinate of the receivers, z_0 is the depth level of the acquisition surface, and t is the time. After a Fourier transformation from time to frequency this wave field is described by

$$P(x,z_0;\omega), \tag{A.1b}$$

where P is the Fourier transformed wave field and ω is the angular frequency ($\omega = 2\pi f$).

In the following we only consider the frequency domain representation, that is, we assume that the Fourier components $P(x,z_0;\omega_i)$ are available for a range of ω_i values. If T is the total recording time then $\Delta\omega = \omega_{i+1} - \omega_i = 2\pi/T$. Because the earth is a time-invariant medium, all these Fourier components can be treated independently. If we consider one component ω_i only, then the discretized version of the wave field at z_0 can be represented by a *vector*, according to

$$\vec{P}(z_0) = [P(-K\Delta x,z_0;\omega), \dots , P(k\Delta x,z_0;\omega), \dots , P(K\Delta x,z_0;\omega)]^T, \tag{A.1c}$$

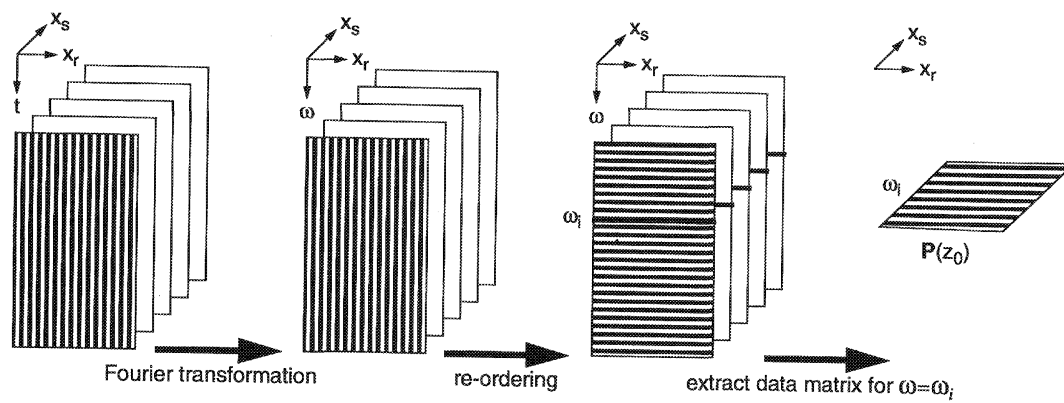where Δx is the distance between the receivers.

Figure A.1   *The relationship between a number of 2-D broadband experiments and the data matrix P(z₀)*

In acoustic imaging this vector represents one Fourier component of the data in one broadband acoustic experiment with one source and $2K+1$ receivers. Let us now write this vector symbolically as

$$\vec{P}(z_0) = [P_{-K}, \dots, P_k, \dots, P_K]^T, \qquad (A.2a)$$
$$x_r \longrightarrow$$

where x_r denotes that the different elements in this vector correspond to the different lateral positions of the receivers. With this notation we can represent all data by a *matrix*, according to

$$x_s \longrightarrow$$
$$P(z_0) = \begin{bmatrix} P_{-K,-K} & \cdots & P_{-K,l} & \cdots & P_{-K,K} \\ \cdot & & \cdot & & \cdot \\ P_{k,-K} & \cdots & P_{k,l} & \cdots & P_{k,K} \\ \cdot & & \cdot & & \cdot \\ P_{K,-K} & \cdots & P_{K,l} & \cdots & P_{K,K} \end{bmatrix} \quad x_r \downarrow \qquad (A.2b)$$

where x_s denotes the different lateral positions of the sources.

Each element $P_{k,l}$ corresponds to a fixed lateral receiver coordinate x_k and a fixed lateral source coordinate x_l. Each column in this data matrix represents one Fourier component of one acoustic experiment; the main diagonal represents zero offset data and a subdiagonal represents common offset data. The procedure for obtaining data matrix $P(z_0)$ is summarized in Figure A.1. For 3-D situations the organization of the data matrix is shown in Figure A.2.

So far we used the matrix notation for the representation of wave fields that are actually measured in a number of acoustic experiments. Of course the same notation may be used for the representation of any type of wave field(s). For example, consider the source $S^+(z_0)$, symbolically written as:
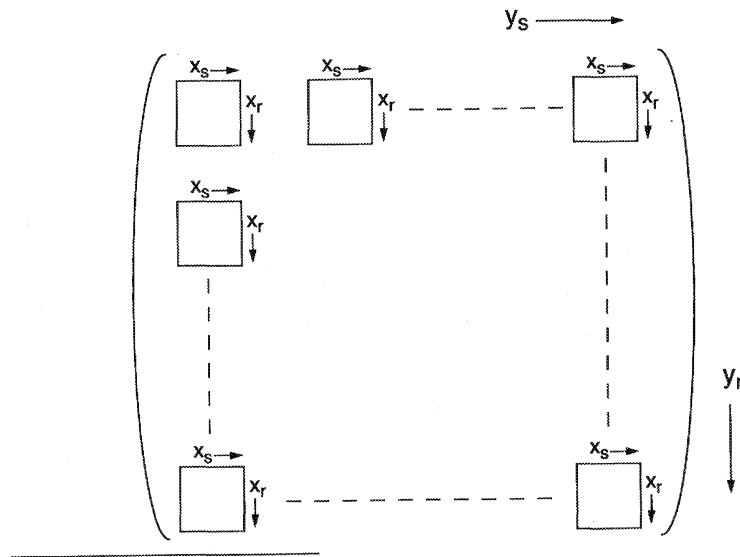
Figure A.2 *Organization of the data for 3-D experiments.*

$$S^+(z_0) = \begin{bmatrix} S^+_{-K,-K} & \cdots & S^+_{-K,l} & \cdots & S^+_{-K,K} \\ \cdot & & \cdot & & \cdot \\ S^+_{k,-K} & \cdots & S^+_{k,l} & \cdots & S^+_{k,K} \\ \cdot & & \cdot & & \cdot \\ S^+_{K,-K} & \cdots & S^+_{K,l} & \cdots & S^+_{K,K} \end{bmatrix} \begin{matrix} x_s \to \\ \\ \\ x_r \downarrow \end{matrix}$$

<div align="right">(A.3a)</div>

Each column vector $\vec{S}^+(z_0)$ in this matrix represents one Fourier component of a downward traveling source wave field (in terms of acoustic pressure) at the data acquisition surface z_0. When dipole sources are used, the downgoing source wave fields at z_0 are represented by spatial delta functions $\delta(x-x_l)$ (this is because the wave fields are described in terms of pressure) or, in discrete notation, δ_{kl}, meaning that $S^+(z_0)$ simplifies to a diagonal matrix, according to

$$S^+(z_0) = \begin{bmatrix} S^+_{-K,-K} & & & \\ & \cdot & & \\ & & S^+_{l,l} & \\ & & & \cdot \\ & & & & S^+_{K,K} \end{bmatrix} \begin{matrix} x_s \to \\ \\ \\ x_r \downarrow \end{matrix}$$

<div align="right">(A.3b)</div>

Here $S^+_{l,l}$ is equal to the complex amplitude of one Fourier component of the source signature in the lth acoustic experiment.

A.2 The propagation matrix

Consider equation (2.2) for downward propagation of the source wave field $\vec{S}^+(z_0)$,

$$\vec{S}^+(z_m) = W^+(z_m,z_0)\,\vec{S}^+(z_0). \tag{A.4a}$$

Here $W^+(z_m,z_0)$ is the downward propagation matrix and $\vec{S}^+(z_m)$ is the downgoing response at z_m due to the downgoing source wave field at z_0. If $\vec{S}^+(z_0)$ denotes the lth column of the diagonal matrix $S^+(z_0)$, given by equation (A.3b), i.e., $\vec{S}^+(z_0)$ represents a single dipole at lateral position x_l, then equation (A.4a) may be symbolically written as

$$\begin{bmatrix} S^+_{-K,l} \\ \cdot \\ \cdot \\ S^+_{k,l} \\ \cdot \\ \cdot \\ S^+_{K,l} \end{bmatrix}_{z_m} = \begin{bmatrix} W^+_{-K,-K} & \cdots & W^+_{-K,l} & \cdots & W^+_{-K,K} \\ \cdot & & \cdot & & \cdot \\ W^+_{k,-K} & \cdots & W^+_{k,l} & \cdots & W^+_{k,K} \\ \cdot & & \cdot & & \cdot \\ W^+_{K,-K} & \cdots & W^+_{K,l} & \cdots & W^+_{K,K} \end{bmatrix} \begin{bmatrix} 0 \\ 0 \\ S^+_{l,l} \\ 0 \\ 0 \\ 0 \\ 0 \end{bmatrix}_{z_0} . \tag{A.4b}$$

Apparently, for this situation vector $\vec{S}^+(z_m)$ is a scaled version of the lth column of matrix $W^+(z_m,z_0)$, the scaling factor being the dipole source strength $S^+_{l,l}$.

Hence, the lth column of downward propagation matrix $W^+(z_m,z_0)$ contains by definition one Fourier component of the downgoing response at z_m due to a unit dipole source at (x_l,z_0) in 2-D
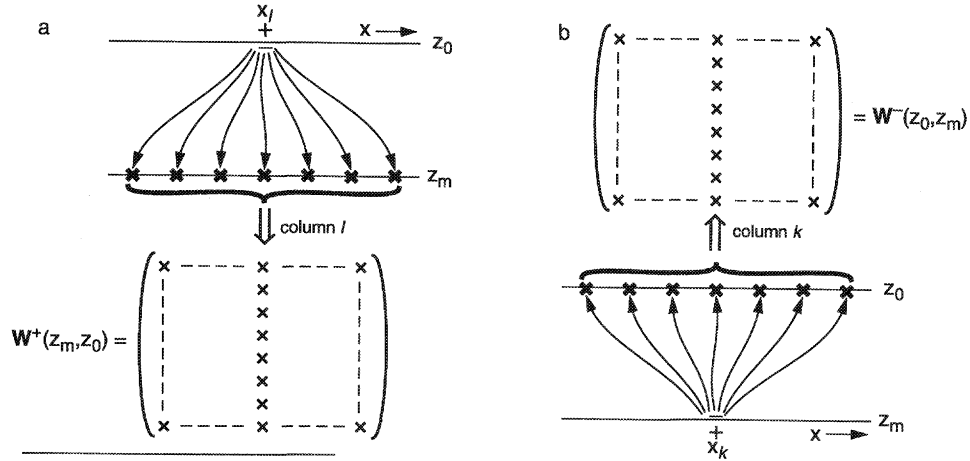
Figure A.3 *Organization of the 2-D propagation matrices: (a) For the downward propagation matrix the column l contains one Fourier component of the response at z_m of a dipole at (x_l,z_0). (b) For the upward propagation matrix column k contains one Fourier component of the response at z_0 of a dipole source at (x_k,z_m).*

(Figure A.3a), or $(\mathring{r}_l, z_0)$ at in 3-D. Similarly, the kth column of upward propagation matrix $W^-(z_0, z_m)$ contains by definition one Fourier component of the upgoing response at z_0 due to a unit dipole source at (x_k, z_m) in 2-D (Figure A.3b), or $(\mathring{r}_k, z_m)$ in 3-D.

Note the similarity of the propagation matrices $W^+(z_m, z_0)$ and $W^-(z_0, z_m)$ with the data matrix $P(z_0)$: the lth column of matrix $P(z_0)$ contains the monochromatic data at z_0, measured in an acoustic experiment with a source at (x_l, z_0) in 2-D, or $(\mathring{r}_l, z_0)$ at in 3-D.

Note also an important difference. Opposed to the data matrix $P(z_0)$, which contains physical wave fields obtained from acoustic experiments (Figure A.1), the propagation matrices contain mathematical wave fields obtained analytically (homogeneous macro model) or numerically (inhomogeneous macro model, Figure A.3). The element $W^+_{k,l}$ for extrapolation from $(\mathring{r}_l, z_0)$ to $(\mathring{r}_k, z_m)$ reads:

$$W^+_{k,l} = \frac{2}{\rho(\mathring{r}_l, z_0)} \frac{\partial}{\partial z}(G^+_{k,l})_{z_0},$$
(A.5a)

and analogously for $W^-_{l,k}$ for extrapolation from $(\mathring{r}_k, z_m)$ to $(\mathring{r}_l, z_0)$:

$$W^-_{l,k} = -\frac{2}{\rho(\mathring{r}_k, z_m)} \frac{\partial}{\partial z}(G^-_{l,k})_{z_m},$$
(A.5b)

where $\rho(\mathring{r}_k, z_m)$ and $\rho(\mathring{r}_l, z_0)$ represents the density $(\mathring{r}_k, z_m)$, resp. $(\mathring{r}_l, z_0)$ and $G^+_{k,l}$ and $G^-_{l,k}$ represent the Green's functions. Note that for homogeneous as well as inhomogeneous macro models these Green's functions obey the reciprocity relation

$$G^+_{k,l} = G^-_{l,k}$$
(A.6)

For the homogeneous situation the Greens's functions read in 3-D:

$$G^+_{k,l} = G^-_{l,k} = \frac{\rho}{4\pi} \frac{e^{-jk\Delta r}}{\Delta r},$$
(A.7a)

with

$$\Delta r = \sqrt{|\mathring{r}_l - \mathring{r}_k|^2 + (z_m - z_0)^2},$$
(A.7b)

or in 2-D:

$$G^+_{k,l} = G^-_{l,k} = -\frac{j\rho}{4} H_0^{(2)}(k\Delta r),$$
(A.8a)

with

$$\Delta r = \sqrt{(x_l - x_k)^2 + (z_m - z_0)^2},$$
(A.8b)

and $H_0^{(2)}$ denoting the zeroth order Hankel function of the second kind, defined by:

$$H_0^{(2)}(k\Delta r) = \sqrt{\frac{2j}{\pi}}\, \frac{e^{-jk\Delta r}}{\sqrt{k\Delta r}}.$$

(A.8c)

A.3 The reflection matrix

Consider one Fourier component of a downgoing plane wave P^+ incident to a horizontal interface between two homogeneous acoustic half-spaces. The velocities in the upper and lower half-space read c_1 and c_2, respectively, the mass densities read ρ_1 and ρ_2.

At z_m, the depth level of the interface, the incident wave is partly reflected and partly transmitted. For the reflected wave we may write:

$$P^-(z_m) = R(\alpha)\, P^+(z_m),$$

(A.9a)

and for the transmitted wave:

$$P_t^+(z_m) = T(\alpha)\, P^+(z_m).$$

(A.9b)

Here the angle-dependent reflection coefficient reads:

$$R(\alpha) = \frac{\rho_2 c_2 \cos\alpha - \rho_1 c_1 \cos\beta}{\rho_2 c_2 \cos\alpha + \rho_1 c_1 \cos\beta},$$

(A.10a)

and the angle-dependent transmission coefficient reads:

$$T(\alpha) = 1 + R(\alpha),$$

(A.10b)

where α is the angle of incidence and where β is determined by Snell's law:

$$\frac{\sin\alpha}{c_1} = \frac{\sin\beta}{c_2},$$

(A.10c)

and where incident and reflected/transmitted wave fields are in terms of pressure.

If we define the wave number k_x, according to

$$k_x = k_1 \sin\alpha = k_2 \sin\beta,$$

(A.11a)

with

$$k_1 = \omega/c_1, k_2 = \omega/c_2,$$

(A.11b)

where ω is the circular frequency, then we may also write for the angle dependent reflection coefficient

$$\tilde{R}(k_x, z_m, \omega) = \frac{\rho_2\sqrt{k_1^2 - k_x^2} - \rho_1\sqrt{k_2^2 - k_x^2}}{\rho_2\sqrt{k_1^2 - k_x^2} + \rho_1\sqrt{k_2^2 - k_x^2}}. \tag{A.12}$$

Let us now assume that an arbitrary downgoing source wave field $S^+(x, z, \omega)$ is incident to the interface at z_m. Then we could use the following procedure to obtain the reflected wave field.

(1) Apply plane wave decomposition to the incident wave field at z_m by means of a spatial Fourier transform from x to k_x:

$$S^+(x, z_m, \omega) \xrightarrow{\text{FT}} \tilde{S}^+(k_x, z_m, \omega). \tag{A.13a}$$

(2) Apply the angle-dependent plane wave reflection coefficient for all k_x, yielding the reflected plane waves:

$$\tilde{P}^-(k_x, z_m, \omega) = \tilde{R}(k_x, z_m, \omega)\,\tilde{S}^+(k_x, z_m, \omega). \tag{A.13b}$$

(3) Apply plane-wave synthesis by means of an inverse spatial Fourier transform from k_x to x, yielding the reflected wave field in the space-frequency domain:

$$P^-(x, z_m, \omega) \xleftarrow{\text{FT}^{-1}} \tilde{P}^-(k_x, z_m, \omega). \tag{A.13c}$$

According to Fourier theory, we can replace these three steps by a simple *spatial convolution*, according to

$$P^-(x, z_m, \omega) = \int R(x-x', z_m, \omega)\,S^+(x', z_m, \omega)\,dx'. \tag{A.14a}$$

Here the reflection operator $R(x, z_m, \omega)$ is related to the angle-dependent plane wave reflection coefficients according to

$$R(x, z_m, \omega) \xleftarrow{\text{FT}^{-1}} \tilde{R}(k_x, z_m, \omega). \tag{A.14b}$$

Note that when $\tilde{R}^+$ is *in*dependent of the incidence angle, according to

$$\tilde{R}(k_x, z_m, \omega) = r_0, \tag{A.15a}$$

the reflection operator is represented by a scaled delta function, according to

$$R(x, z_m, \omega) = r_0\,\delta(x). \tag{A.15b}$$

In this case we call the reflector *locally reacting*. Note that when a velocity contrast exists at z_m the $\tilde{R}$ is angle dependent (equation (A.12)) and, consequently R is not a delta function.

The discretized form of the convolution integral (equation (A.14a)) reads

$$P^-(x_k, z_m, \omega) = \sum_l R(x_k - x_l, z_m, \omega)\,S^+(x_l, z_m, \omega)\,\Delta x. \tag{A.16}$$
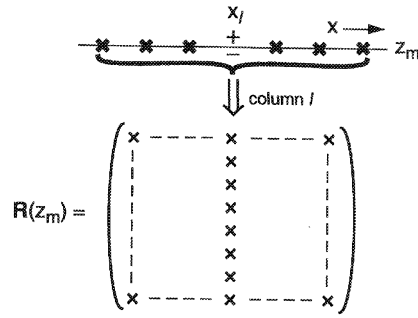
Figure A.4 *Organization of the reflection matrix. Column l contains one Fourier component of the reflection response at z_m of a dipole source at (x_l, z_m).*

Hence, in matrix notation we obtain

$$\vec{P}^-(z_m) = \mathbf{R}(z_m)\, \vec{S}^+(z_m) \tag{A.17a}$$

or, symbolically,

$$
\begin{bmatrix} P^-_{-K} \\ \cdot \\ \cdot \\ P^-_{k} \\ \cdot \\ \cdot \\ P^-_{K} \end{bmatrix}
=
\begin{bmatrix}
R_{-K,-K} & \cdots & R_{-K,l} & \cdots & R_{-K,K} \\
\cdot & & \cdot & & \cdot \\
R_{k,-K} & \cdots & R_{k,l} & \cdots & R_{k,K} \\
\cdot & & \cdot & & \cdot \\
R_{K,-K} & \cdots & R_{K,l} & \cdots & R_{K,K}
\end{bmatrix}
\begin{bmatrix} S^+_{-K} \\ \cdot \\ \cdot \\ S^+_{k} \\ \cdot \\ \cdot \\ S^+_{K} \end{bmatrix},
\tag{A.17b}
$$

where

$$S^+_l = S^+(x_l, z_m, \omega), \tag{A.17c}$$

$$P^-_k = P^-(x_k, z_m, \omega), \tag{A.17d}$$

and

$$R^+_{k,l} = R(x_k - x_l, z_m, \omega)\, \Delta x, \tag{A.17e}$$

Equation (A.17e) expresses that $\mathbf{R}(z_m)$ is a so-called Toeplitz matrix (i.e., the elements along any diagonal are constant).

Similar as for the propagation matrix, the lth column of the reflection matrix $\mathbf{R}(z_m)$ contains one Fourier component of the reflection response at z_m of a unit dipole source at (x_l, z_m), see Figure A.4.

In case of locally reacting (i.e., angle-*in*dependent) reflectivity this response is restricted to the position of the dipole source. Hence, in this special case $R(z_m)$ is a diagonal matrix. A typical example is a pure density contrast at z_m. However, in general the reflection response is *not* restricted to the reflection point, i.e., to the position of the dipole source. In the case we call the reflector *non-locally reacting* and $R(z_m)$ looses its simple diagonal structure. Note that non-locally reacting reflectivity (multi-element columns) corresponds to angle-dependent reflectivity.

When the reflectivity properties at z_m *change* along the x coordinate then the convolution (equation (A.16)) becomes space variant,

$$P^-(x_k, z_m, \omega) = \sum_l R_l(x_k - x_l, z_m, \omega)\, S^+(x_l, z_m, \omega)\, \Delta x. \qquad (A.18a)$$

Hence, the elements in the matrix $R(z_m)$ are given by

$$R_{k,l} = R_l(x_k - x_l, z_m, \omega)\, \Delta x. \qquad (A.18b)$$

The lth column now contains the discretized reflection response R_l, describing the angle-dependent reflectivity properties at (x_l, z_m).

The transmission operator for downgoing waves at z_m reads, in accordance with equation (A.10b),

$$T(z_m) = I + R(z_m). \qquad (A.19a)$$

Appendix B

Influence of missing data

B.1 Introduction

In this appendix the influence of missing data on the synthesized result is discussed. The issue of missing far offsets will be approached theoretically and illustrated on a single reflector example. An attempt is made to find an analytic solution to the minimum offset required for true amplitude processing. Finally the influence of missing near offsets is discussed. The problems concerning these missing near offsets will be attacked using a CMP oriented interpolation process as described by Verschuur (1990).

B.2 The influence of missing data

In seismic practice the acquisition geometries used are usually *moving spread* geometries. This means that our data matrix $P^-(z_0)$ is a *band* data matrix (Figure B.1). The missing near offsets
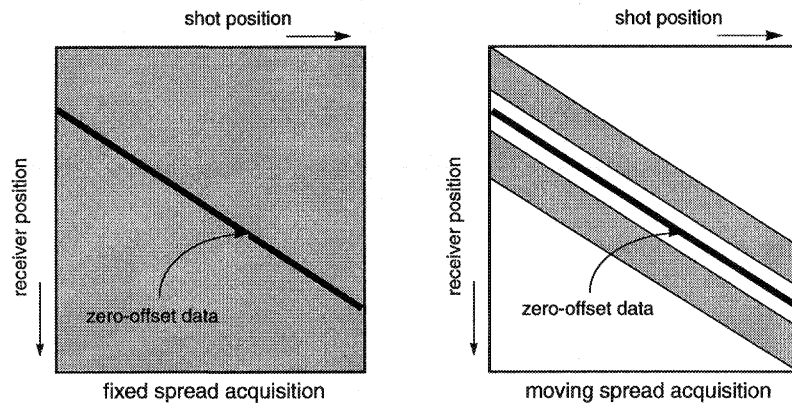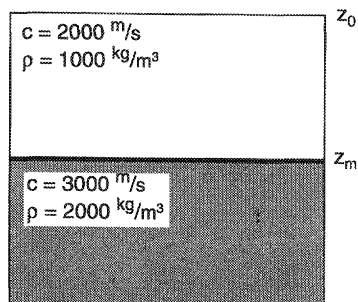

Figure B.1   *Influence of the acquisition on the form of the data matrix.*

Figure B.2 *Model used to investigate the influence of missing offsets on the phase and
amplitude of the synthesized areal shot record.*

result in a gap around the zero-offset position (the diagonal of the matrix). To test the influence
of both the missing near and far offsets on the synthesized result the model as depicted in Figure
B.2 is used (a density contrast over a horizontal interface). Before showing the obtained results,
we will look at the mechanism of synthesizing shot records. We will focus on the influence of
finite offset on the phase and amplitude behaviour of the synthesized result.

 The synthesis process, as described in Chapter 2, involves a *common receiver stacking*. If we
apply reciprocity, each common *shot* gather becomes a common *receiver* gather. Hence, if we
consider as desired source wave field a horizontal plane wave at the surface, the synthesis pro-
cedure is fully equivalent to the stacking of all the traces in each shot record.

For the model as shown in Figure B.2, the shot record can in traveltime also be considered as a
truncated extrapolation operator from the surface z_0 to twice the reflector depth z_m. The ampli-
tudes however, are influenced by the reflection properties of the interface, in this example an
angle *in*dependent reflection coefficient of 0.5. Hence, the problem of synthesizing data with
finite offsets is in this simple case fully equivalent with the extrapolation of a plane wave by a
truncated operator (Figure B.3) over a distance equal to twice the reflector depth z_m. This
extrapolation can be described by the Rayleigh II-integral:
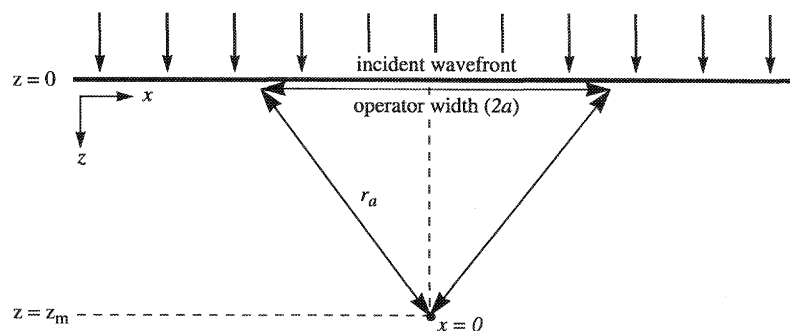
Figure B.3 *The extrapolation of a plane wave by a truncated operator. Explanation of used symbols.*

$$P_a(0,z_m) = \frac{1}{2\pi} \int\limits_{-a}^{a} P(x,0) \left[\frac{\partial}{\partial z}G(x,z)\right]_{z=0} dx, \tag{B.1}$$

where a describes the half-width of the extrapolation operator,

$P(x,z)$ describes the pressure of the wave field at position (x,z); the subscript a indicating that we evaluate the pressure as function of a, and

$G(x,z)$ describes the Green's function from depth level $z=0$ to position $(0,z_m)$.

In the next section we will look at a analytic solution to equation (B.1)

B.3 Theoretical solution to the extrapolation of a plane wave by a truncated operator

In this section we will derive an analytic solution for the extrapolated result of a plane wave through a homogeneous media by a truncated operator (equation (B.1)). The main variable will be the width of the operator, i.e. $2a$. For the derivation an approximation of the Rayleigh II-integral is used as described by Stamnes (1982), which involves a Taylor expansion around the edge points of the operator. Figure B.3 shows the configuration and explains the most important variables used.

Equation (B.1) can for the 2-D case be rewritten as:

$$P_a(0,z_m) = -\frac{j}{2} \int\limits_{-a}^{a} P(x,0) \left[\frac{\partial}{\partial z}H_0^{(2)}(kr)\right]_{z=0} dx, \tag{B.2a}$$

where $H_0^{(2)}$ is the zeroth order Hankel function of the second kind;

k is the wave number defined by ω/c, and

$$r = \sqrt{x^2 + (z_m - z)^2}. \tag{B.2b}$$

Equation (B.2a) can be rewritten as:

$$P_a(0,z_m) = -\frac{j}{2}\left[\int\limits_{-\infty}^{\infty} P(x,0) \left[\frac{\partial}{\partial z}H_0^{(2)}(kr)\right]_{z=0} dx + \right.$$
$$\left. -2\int\limits_{a}^{\infty} P(x,0) \left[\frac{\partial}{\partial z}H_0^{(2)}(kr)\right]_{z=0} dx\right]. \tag{B.3}$$

The first part of equation (B.3) is the response of the incident wave field $P(x,0)$ in point $(0,z_m)$. The second part describes the influence of the missing parts in the extrapolation operator. The incident wave field at $z=0$ however, is a plane wave with amplitude R_0:

$$P(x,0) = R_0, \tag{B.4}$$

simplifying equation (B.3) to:

$$P_a(0,z_m) = R_0 \, exp(-jkz_m) \; + jR_0 \int_a^\infty \left[\frac{\partial}{\partial z} H_0^{(2)} \, (kr) \right]_{z=0} dx. \tag{B.5}$$

The second part of equation (B.5) can be approximated for the far-field ($kr >> 1$):

$$P_a(0,z_m) = R_0 \, exp(-jkz_m) \; - 2R_0 \sqrt{\frac{jk}{2\pi}} \, z_m \int_a^\infty \left[\frac{exp \, (-jkr)}{r\sqrt{r}} \right]_{z=0} dx. \tag{B.6}$$

The second part of equation (B.6) is of the kind of:

$$I(a) = \int_a^\infty g(x) \, exp(jf(x)) \, dx. \tag{B.7}$$

Integrals of this form can be approximated by taking the value of $g(x)$ at the edge point a and applying a second order Taylor expansion to the phase term $f(x)$ around $x=a$. The assumption is that $f(x)$ has no stationary points in the integration interval (Stamnes, 1982), which is indeed the case for equation (B.6). This leads for the second term $P_{a,2}(0,z_m)$ of $P_a(0,z_m)$ to:

$$P_{a,2}(0,z_m) = g(a) \, exp\left[-jkr_a \left(1 - \frac{a^2}{2z_m^2} \right) \right] \int_a^\infty exp \, \{ \frac{-jkz_m^2}{2r_a^3} \left[x + \frac{a^3}{z_m^2} \right]^2 \} \; dx, \tag{B.8a}$$

$$r_a = \sqrt{a^2 + z_m^2}, \text{ and} \tag{B.8b}$$

$$g(a) = -2 \, R_0 \sqrt{\frac{jk}{2\pi}} \, z_m \, \frac{1}{r_a\sqrt{r_a}}. \tag{B.8c}$$

Changing the integral variable x to ξ according to:

$$\frac{\pi}{2} \, \xi^2 = \frac{kz_m^2}{2r_a^3} \left[x + \frac{a^3}{z_m^2} \right]^2, \tag{B.9}$$

leaves equation (B.8a) to:

$$P_{a,2}(0,z_m) = \frac{g \, (a) \, r_a}{z_m} \sqrt{\frac{\pi r_a}{k}} \; exp\left[-jkr_a \left(1 - \frac{a^2}{2z_m^2} \right) \right] \int_{\xi_a}^\infty exp \, \{ \frac{-j\pi\xi^2}{2} \} \, d\xi, \tag{B.10a}$$

with

$$\xi_a = \sqrt{\frac{kr_a}{\pi}} \, \frac{a}{z_m}. \tag{B.10b}$$

The integral in equation (B.10a) can be rewritten as:

$$I = \int_0^\infty \cos\{\frac{\pi\xi^2}{2}\}\, d\xi - j\int_0^\infty \sin\{\frac{\pi\xi^2}{2}\}\, d\xi - \int_0^{\xi_a} \cos\{\frac{\pi\xi^2}{2}\}\, d\xi + j\int_0^{\xi_a} \sin\{\frac{\pi\xi^2}{2}\}\, d\xi. \qquad (B.11)$$

Using the definition of the Fresnel integrals (Abramowitz and Stegun, 1968):

$$C(q) = \int_0^q \cos\{\frac{\pi\xi^2}{2}\}\, d\xi, \text{ and} \qquad (B.12a)$$

$$S(q) = \int_0^q \sin\{\frac{\pi\xi^2}{2}\}\, d\xi, \qquad (B.12b)$$

simplifies equation (B.11) to:

$$I = C(\infty) - jS(\infty) - C(\xi_a) + jS(\xi_a) \qquad (B.12c)$$

Remembering that:

$$C(\infty) = \frac{1}{2};\ S(\infty) = \frac{1}{2} \qquad (B.12d)$$

and substitution of equation (B.12c) into equation (B.10a) leaves:

$$P_{a,2}(0,z_m) = -R_0\ \sqrt{2j}\ exp\left[-jkr_a\left(1 - \frac{a^2}{2z_m^2}\right)\right] \{\frac{1}{2} - C(\xi_a) - j\left[\frac{1}{2} - S(\xi_a)\right]\} \qquad (B.13)$$

with r_a defined by equation (B.8b) and ξ_a defined by equation (B.10b).

Substitution of equation (B.13) in equation (B.6) leaves:

$$P_a(0,z_m) = R_0\ exp(-jkz_m)$$
$$\left[1 - \sqrt{2j}\ exp\left[-jk\{r_a\left(1 - \frac{a^2}{2z_m^2}\right) - z_m\}\right] \{\frac{1}{2} - C(\xi_a) - j\left[\frac{1}{2} - S(\xi_a)\right]\}\right]. \qquad (B.14)$$

Note that for $a \rightarrow \infty$ equation (B.14) leads to:

$$P_\infty(0,z_m)_{a\,\rightarrow\,\infty} = R_0\ exp(-jkz_m), \qquad (B.15a)$$

and for $a \rightarrow 0$ to:

$$P_0(0,z_m)_{a\,\rightarrow\,0} = 0. \qquad (B.15b)$$

B.4 Influence of missing far offsets

Equation (B.14) gives a theoretical prediction of the result of the synthesis for a medium with one reflector and an angle *in*dependent reflection coefficient. In this section we want to compare the theoretical phase and amplitude behaviour of the areal shot record with the results after numerical synthesis.

For a monochromatic experiment (*f = 61 Hz, z = 500 m, c = 2000 m/s*) the theoretical result according to equation (B.14) and the results as obtained from the synthesis are shown in Figure B.4 for a varying maximum offset in the extrapolation operator or the shot record. The results show both the amplitude and the phase behaviour as function of the maximum offset in the extrapolation operator/shot record. Both the small amplitude error as well as the difference in periodicity for large maximum offsets can be explained both, by the fact that the integral of equation (B.1) is approximated in the synthesis due to the discretization, or are due to the approximations in equation (B.14). In Figure B.4 the first Fresnel zone is indicated. The first Fresnel zone is defined as the zone for which there is a $\lambda/2$ difference in length of the raypaths from the mid- and endpoint of the zone to the detector position (Figure B.5) according to Rayleigh (1896). It can be easily derived that half the width of the first Fresnel zone $2a_{F,1}$ can be approximated by:

$$a = \sqrt{\lambda z_m} \; , \qquad\qquad (B.16)$$

with λ the wavelength, and

z_m the extrapolation depth, i.e. twice the depth of the reflector.

From Figure B.4 we learn that the amplitude increases with increasing maximum offset, as long as the offset is within the first Fresnelzone. For offsets exceeding the first Fresnelzone the
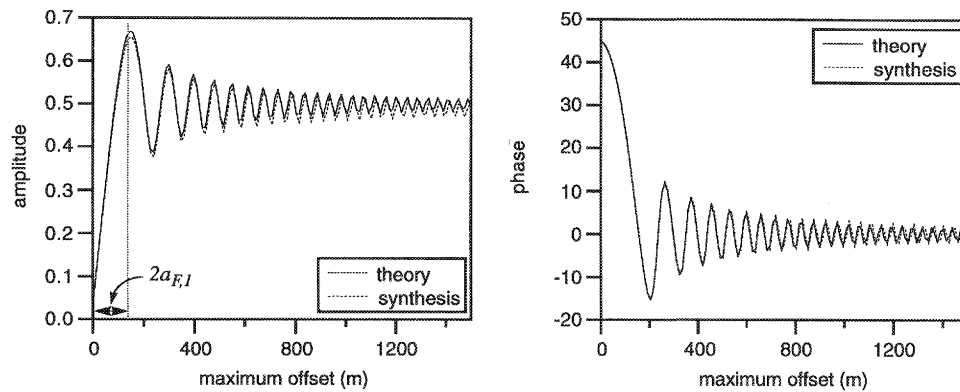
Figure B.4   : *Monochromatic experiment. The amplitude (left) and phase (right) as function of the maximum offset in the extrapolation operator/shot record calculated by equation (B.14) (solid line) and by the synthesis (dotted line). At the left hand side the first Fresnel zone is indicated ($2a_{F,1}$).*
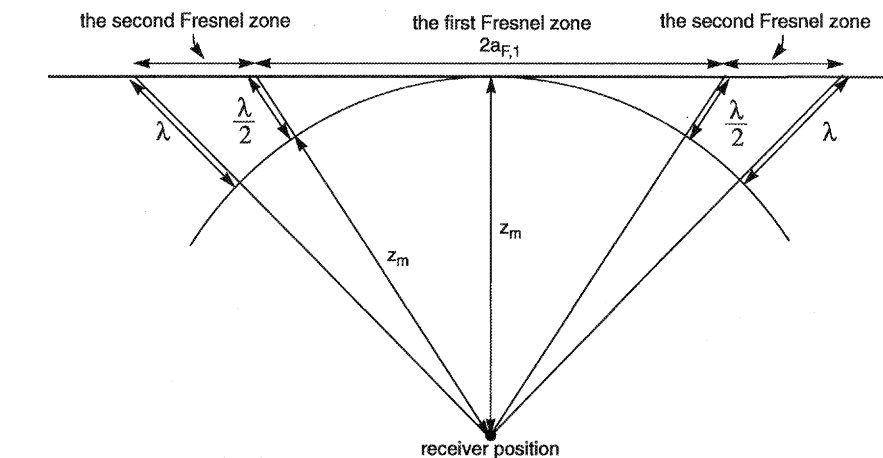
Figure B.5 : *The definition of the first and second Fresnelzone.*

amplitude oscillates around the exact solution. Only for an infinite maximum offset the result will converge to the exact solution (*amplitude R_0 = 0.5, phase = 0°*).

Next we will show the truncation effects, but now with a broad band experiment using a box spectrum (*40 Hz $\leq f \leq$ 80 Hz, λ_{60Hz} = 33m*). The results show the amplitude and phase averaged over the used frequency components (Figure B.6). A small error in the amplitude still exists between the analytic solution and the result after synthesis, however the oscillations match very well. Here we see that both results tend to the exact solution already for a maximum offset of 400 m.

The influence of filtering the frequency spectrum of the wavelet is shown in Figure B.7, for a frequency contents of *0 $\rightarrow$ 60 Hz*, filtered from *0 $\rightarrow$ 5 Hz* and from *55 $\rightarrow$ 60 Hz* by a
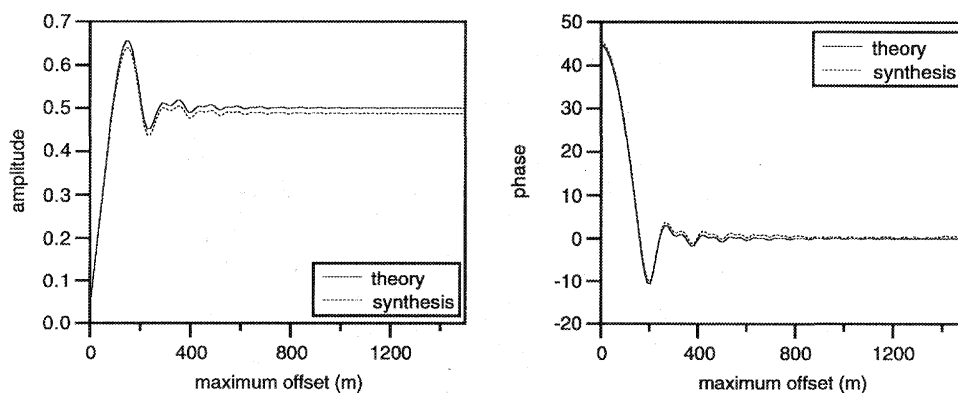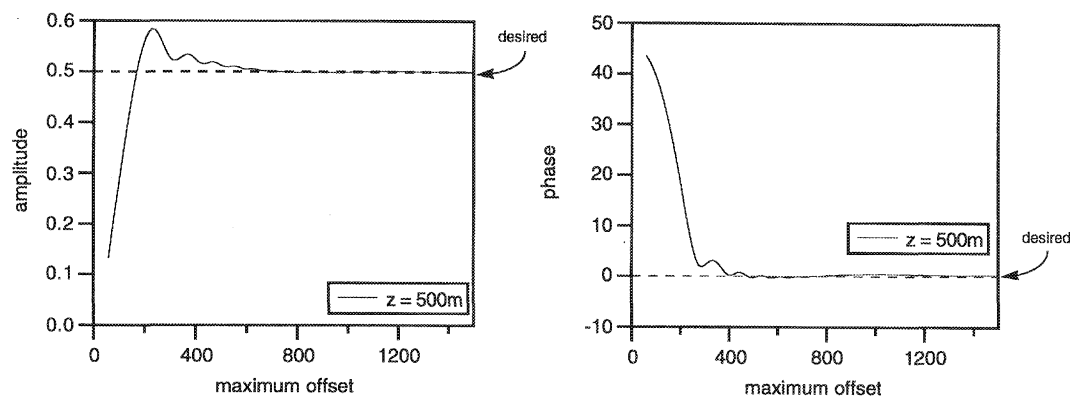

Figure B.6 : *Broad band experiment (box spectrum, 40 - 80 Hz). The amplitude (left) and phase (right) as function of the maximum offset in the extrapolation operator/shot record calculated by equation (B.14) (solid line) and by the synthesis (dotted line).*

Figure B.7   *Broad band experiment for a frequency range of 0 til 60 Hz, filtered from 0 to 5 and from 55 to 60 Hz by a cosine-squared taper. The amplitude (left) and phase (right) behaviour of the synthesized result as function of the maximum offset. Indicated are the exact solutions for a plane wave response (0.5, 0°).*

cosine-square filter. The wavelength λ for the center frequency of 30 Hz is 67m. Only the experimental results are shown. For the synthesis a lateral cosine-square truncation window was applied over 5 traces at each side of the spread, this to improve the results on the phase behaviour. For an offset of approximately 600m the amplitude is correct. The phase is already correct for an offset of 450m. In Figure B.8 the result of the synthesis is shown in the time domain. Each trace represents the result for a specific maximum offset. Note the phase shift of the wavelet for increasing maximum offset.

So far we have shown that it is possible to predict the amplitude and phase behaviour of the synthesized result when a split spread acquisition is performed over a horizontal interface. This theoretical result could be used to predict the minimum offset necessary to obtain a true amplitude and phase after synthesis.

To gain more insight in the minimum offset needed for true amplitude and phase, additional experiments were done with different reflector depths and velocities above the interface. The
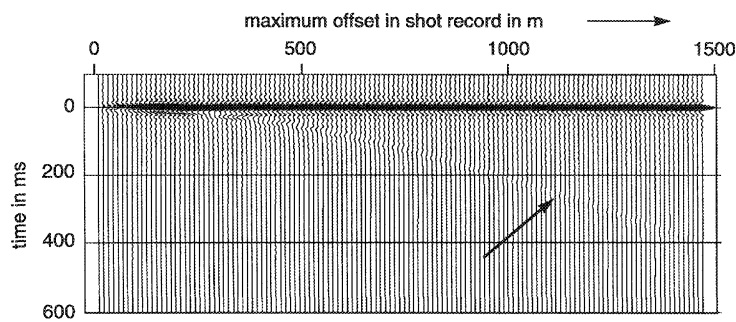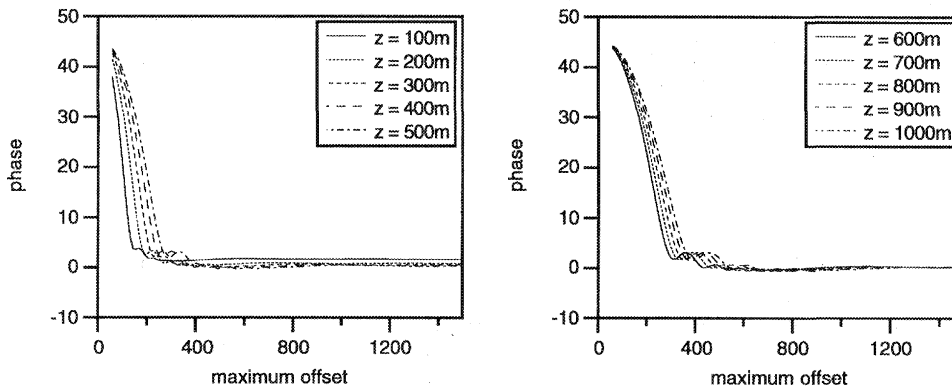

Figure B.8   *The result of the synthesis as function of the maximum offset in each shot record. The arrow indicates the event due to the aperture limitation of the shot record.*
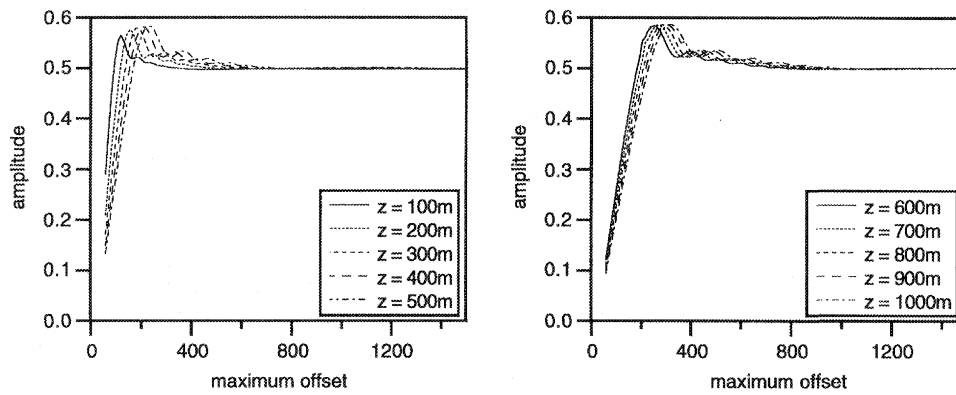
Figure B.9 : *The amplitude of the synthesized result as function of the maximum offset for different reflector depths. The velocity in the model was 2000 m/s.*

results shown are not the results obtained from the theoretical solution, but from the synthesis itself. The depth of the reflector was varied from 100m to 1000m with steps of 100m. The velocities used were $1500 \, ^m/s$, $2000 \, ^m/s$, and $3000 \, ^m/s$. As in the previous experiment, a lateral cosine-square truncation window was applied over 5 traces at each side of the spread, to improve the results on the phase behaviour. The wavelet contained the frequencies from $0 \rightarrow 60 \, Hz$, and was filtered from $0 \rightarrow 5 \, Hz$ and from $55 \rightarrow 60 \, Hz$ by a cosine-square filter, as was the case in the last example. The experiments for a velocity of $2000 \, ^m/s$ will be discussed in detail. For the other velocities we will suffice with just showing the results

Figure B.9 shows the result of the amplitude for varying reflector depth. The results for the phase are shown in Figure B.10. It can be very clearly seen that the offset for which the amplitude and phase are correct increases with increasing reflector depth. It is also clear that for a correct amplitude a larger offset is necessary than for a correct phase. It is possible to find from these graphs the minimum offset range as a function of the depth of the reflector for
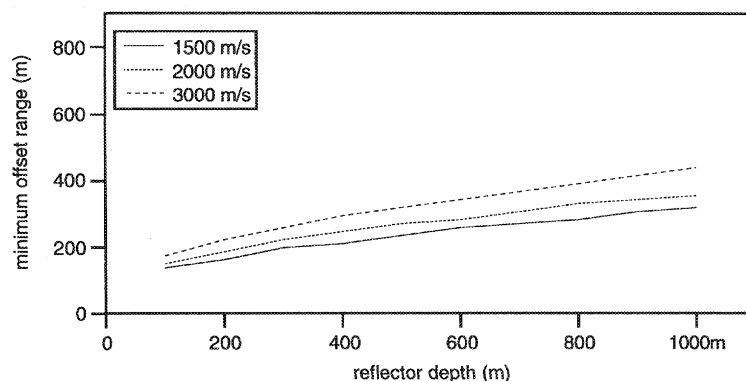

Figure B.10: *The phase of the synthesized result as function of the maximum offset for different reflector depths. The velocity in the model was 2000 m/s.*
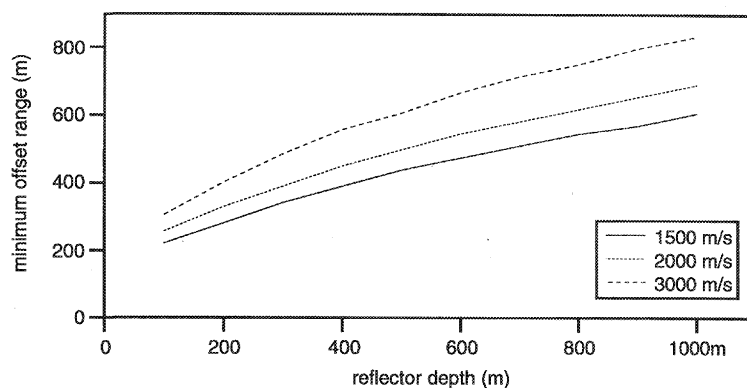
Figure B.11 : *The minimum offset range for which the areal source may be considered a plane wave source according to the* amplitude *behaviour.*

which the amplitude and phase have the correct values. If we look at the amplitude and use as criterion that the amplitude may deviate less than *3%* from the correct value *0.5*, the result as shown in Figure B.11 is obtained. In this figure the results for the three velocities are shown. If we look at the phase and use as criterion that the phase may deviate *5°* maximum from the correct value *0°*, the results as shown in Figure B.12 are obtained. Again the same remark on the picking of the minimum offset should be made. From these last two graphs we can see that the *minimum* offset range needed to obtain correct amplitude or phase after the synthesis increases with increasing reflector depth and increasing velocity. Again we see that to obtain true amplitude results a wider offset range required, compared to a result with 'just' the correct phase. Note that all curves show a curve proportional to the square-root of the reflector depth, equivalent to the Fresnel zone (equation (B.16)).

So far only horizontal plane wave fields were considered. Now we want to focus on the illumination with tilted plane waves. We have used the same range of reflector depths and the same three velocities. We kept the maximum offset in the shot record fixed to 1538 m and investi-

Figure B.12 : *The minimum offset range for which the areal source may be considered a plane wave source according to the* phase *behaviour.*
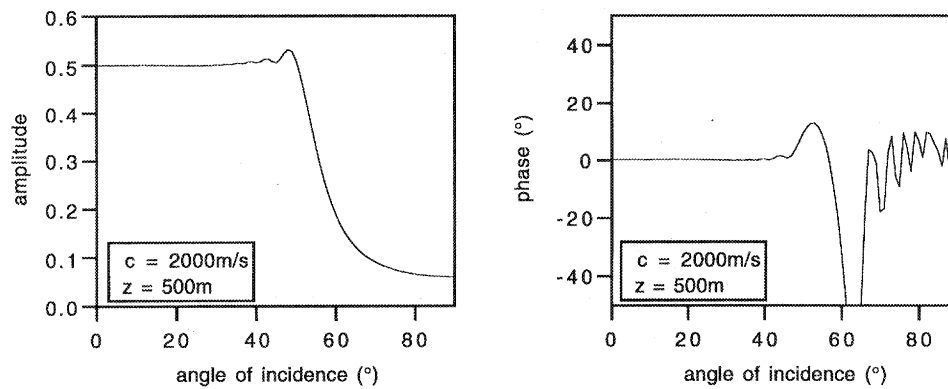
Figure B.13 : *The amplitude and phase of the synthesized result as function of the angle of incidence of the illuminating source wave field for a maximum offset of 1538m.*

gated the amplitude behaviour as a function of the *angle* of the illuminating wave field. For a reflector depth of 500m and a velocity of 2000 ^{m}/s the results are shown in Figure B.13. From those graphs we can again pick the maximum angle for which the illuminating wave field can be considered a true areal plane wave field using the same criteria as discussed previously.

The results are shown in Figure B.14 when using the amplitude, and in Figure B.15 when using the phase. Both figures look very similar. In these graphs also the specular reflection limit is indicated. This limit shows the maximum angle available in the data according to the maximum offset and the reflector depth (Figure B.16) using a raytracing approximation. From Figure B.14 and Figure B.15 it is obvious that for *true amplitude* processing more offsets are required.

It is obvious that this extra offset, required to consider the incident source wave field at the reflector as a true plane wave field, can be related to the first Fresnel zone of the center frequency of the frequency window considered. In Figure B.17 it is shown how the extra offset
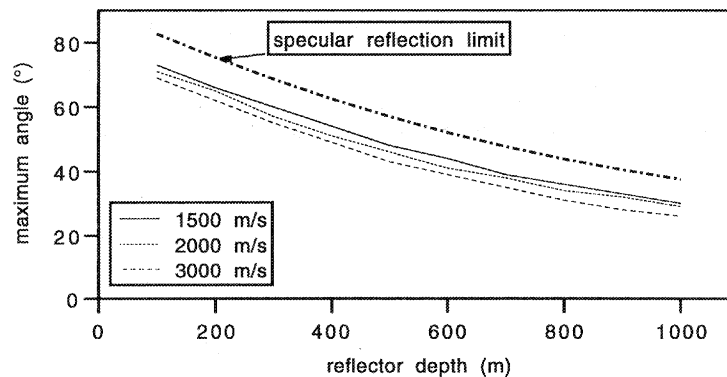
Figure B.14: *The maximum angle of incidence as function of the reflector depth for a maximum offset of 1538 m. For the angle of incidence indicated the illuminating wave field can still be considered a true plane wave field, using the amplitude criterion.*
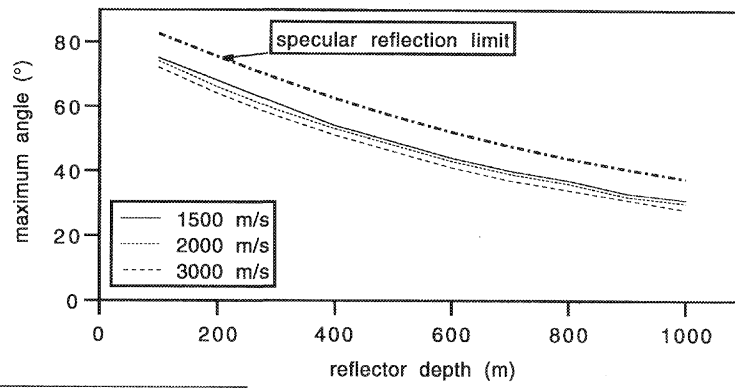
Figure B.15: *The maximum angle of incidence as function of the reflector depth for a maximum offset of 1538m. For the angle of incidence indicated the illuminating wave field can still be considered a true plane wave field, using the* phase *criterion.*

needed to cover the first Fresnel zone can be constructed. Some simple mathematics leads to the simple expression for the minimum offset needed to obtain a true plane wave illumination of a flat reflector at depth z_m:

$$h = h_{spec} + h_{fres},$$ (B.17)

or,

$$h = 2z_m \tan\alpha + \sqrt{\frac{\lambda z_m}{\cos\alpha^3}},$$ (B.18)

where h_{spec} describes the contribution of the specular reflection limit;

h_{fres} describes the contribution of the first Fresnel zone;

α is the angle of illumination;

z_m is the depth of the reflector, and

λ is the wavelength of the center frequency of the used bandwidth.
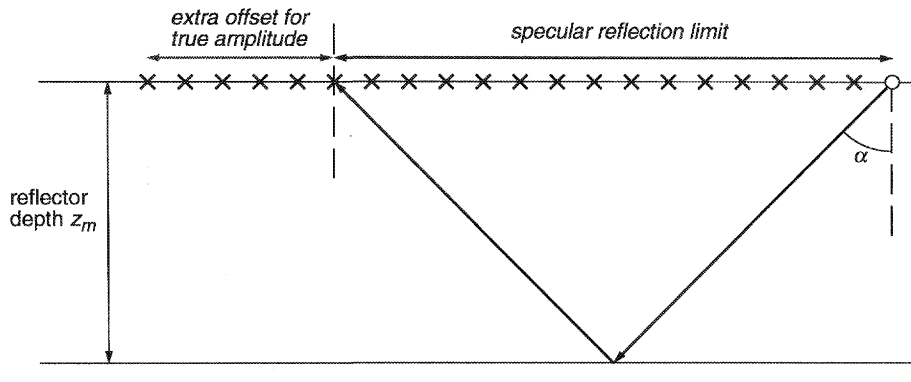
Figure B.16: *Specular reflection limit for illumination angle* α, *and reflector depth* z.
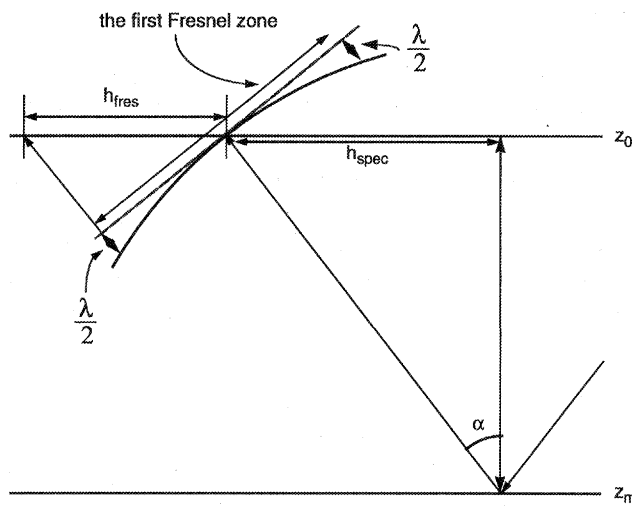
Figure B.17: Projecting the first Fresnel zone for oblique incidence with angle α on the acquisition level; z_m is the depth of the reflector, h_{spec} indicates the specular reflection limit, and h_{fres} the extra offset due to the projection of the first Fresnel zone.

Using equation (B.18) it is possible to calculate similar curves as shown in Figure B.14 and Figure B.15. The result is shown in Figure B.18. Note the similarity between the analytically obtained curve of Figure B.18 and the experimentally obtained curves of Figure B.14 and Figure B.15.

The derived formula (B.18) provides a tool to gain insight in which range of angles can be used for true amplitude processing. It could also be used prior to acquisition to calculate roughly the required maximum offset needed to have the possibility to obtain true amplitude angle dependent seismic information for litho-stratigraphic inversion.
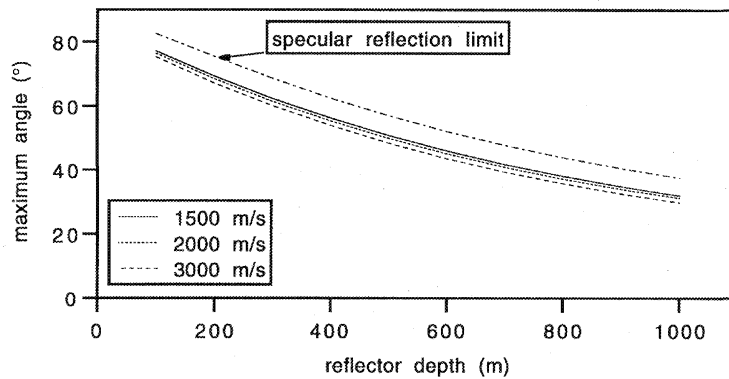
Figure B.18: The maximum angle of incidence as function of the reflector depth for a maximum offset of 1538m calculated with equation (B.18). For the angle of incidence indicated the illuminating wave field can still be considered a true plane wave field. (Compare with the experimental obtained curves, Figure B.14 and Figure B.15.)

B.5 The influence of missing near offsets

In the previous section we have seen that the influence of missing far offsets give mainly rise to an amplitude error and an error in the phase of the wavelet. It was shown that the errors could be related to the first Fresnel zone. However, if we think about missing *near* offsets, we see immediately that for a simple plane wave stack at the surface, these traces are positioned within the first Fresnel zone. This means that strong artifact can be expected. For illumination under different angles of incidence the missing near offsets might not be in the first Fresnel zone. However, since the missing near offsets will be in the apex of most of the reflector responses, the high amplitudes at the edges of the missing offsets will cause strong artifact in the synthesized result.

Experiments were done on the same data sets as were used for the far offsets experiments. In Figure B.19 the results after synthesis are shown for an increasing missing near offset range; the reflector depth was 500m, the velocity 2000 ^{m}/s, and the maximum offset used was 1524m. It is obvious that amplitude and phase are severely distorted.

To obtain reliable results these missing offsets should be interpolated. Verschuur (1990) discusses a robust CMP-based interpolation algorithm. This interpolation technique is used to interpolated the missing near offsets. In Figure B.20 the results of this interpolation are shown for reflector depth of 500m for the velocities 1500 ^{m}/s (a), 2000 ^{m}/s (b) and 3000 ^{m}/s (c). From these results it may be concluded that the interpolation technique fixes missing near offsets up to a range of 300m, both in phase and amplitude. If we would not interpolate the missing near offsets we can expect an image with seriously wrong amplitudes, and mispositioned reflectors.
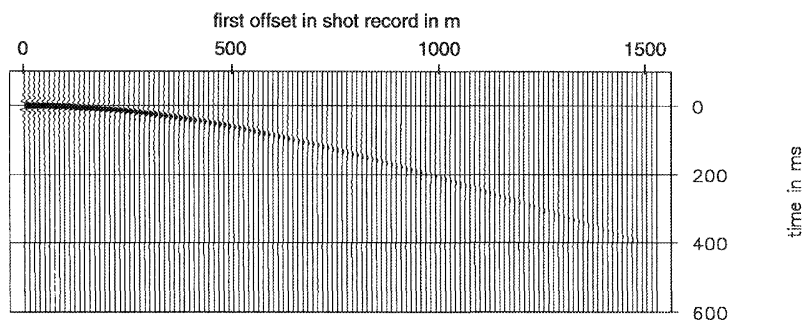
Figure B.19 *The result of the synthesis as function of the first offset in each shot record. The reflector depth was 500 m, the velocity 2000 ^{m}/s. Clearly the importance can be seen of the near offsets for the amplitude and the phase behaviour of the synthesized results.*
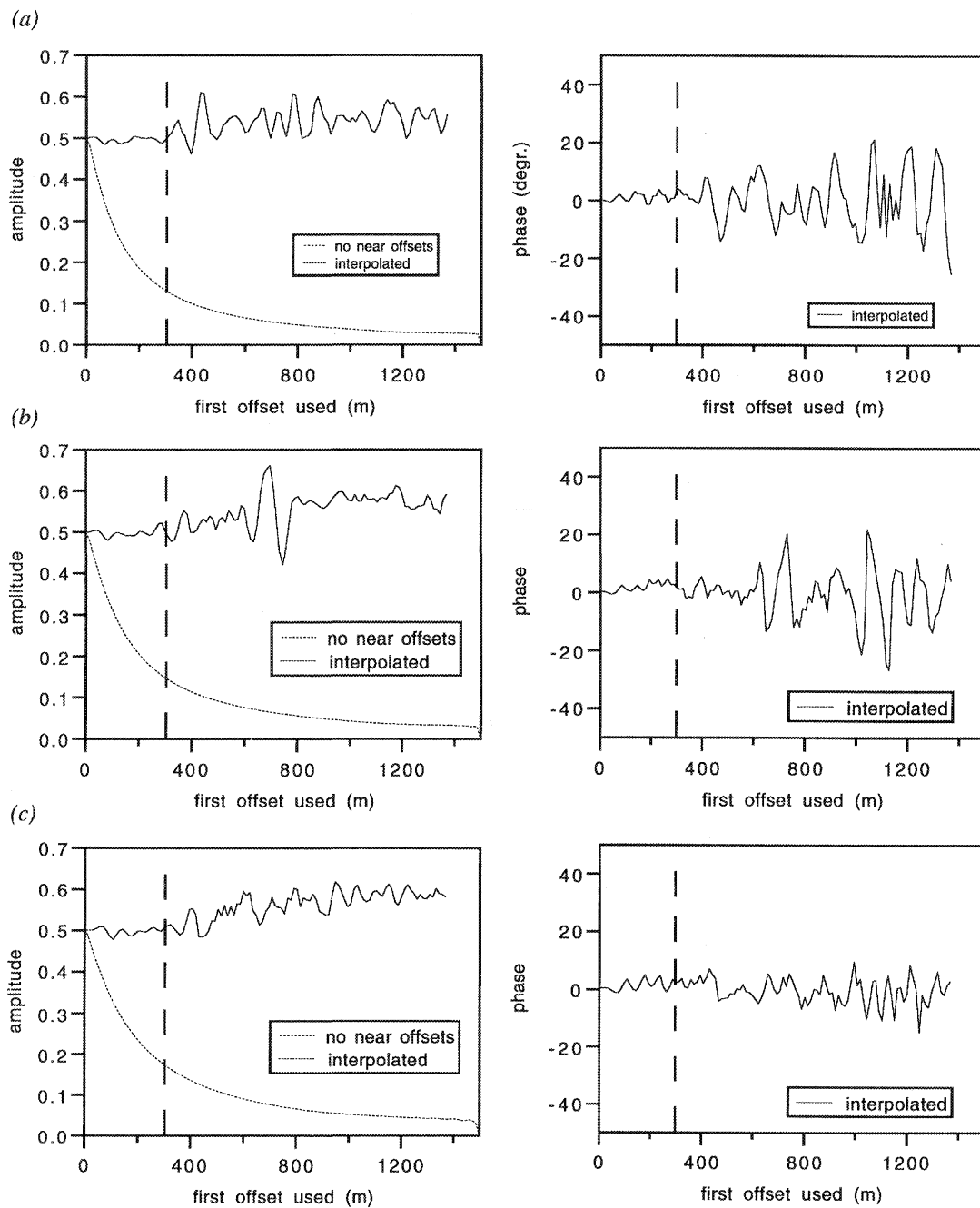
Figure B.20 : *The amplitude and phase as function of the first offset in the data, after interpolation of the missing near offsets. On the left hand side the results for the amplitude are shown, on the right hand side the results on the phase. For the amplitude also the results without interpolation of the missing offsets are shown. The reflector depth was 500m; the velocities were (a) 1500 ^{m}/s, (b) 2000 ^{m}/s and (c) 3000 ^{m}/s.*

References

Abramowitz, M. and Stegun, I.A., 1968, *Handbook of mathematical functions*, 5th edition.

Al-Yahya, K.M., 1989, *Velocity analysis by iterative profile migration*: Geophysics, **54**, 718-729.

Berkhout, A.J., 1985, *Seismic migration: Imaging of Acoustics energy by wavefield extrapolation. A. Theoretical Aspects*, 3rd Ed.: Elsevier Science Publ. Co., Inc.

Berkhout, A.J. and Wapenaar, C.P.A., 1992, *DELPHI, Delft philosophy on acoustics and elastic inversion*: The Leading Edge, **9**, no. 2, 30-34.

Berkhout, A.J., Cox, H.L.H., Verschuur, D.J. and Wapenaar, C.P.A., 1991, *The DELPHI approach to macro model estimation*: Proceedings of the 1990 EAEG workshop on practical aspects of seismic data inversion, EAEG

Berkhout, A.J., 1992, *Areal shot record technology*: J. Seis. Expl., **1**, no. 3, 251-264.

Berkhout, A.J., 1993, *A unified approach to acoustical reflection imaging. I: The forward model*: J. Acoust. Soc. Am., **93**, no. 4, 2005-2016.

Berkhout, .A.J., 1995, *Pushing the limits of seismic imaging - part II: Integration of prestack migration, velocity estimation and AVO analysis*: submitted to Geophysics.

Blacquière, G., 1989, *3D wave field extrapolation in seismic depth migration*: Ph.D. thesis, Delft University of Technology, the Netherlands.

Broekers, E.J.F., 1994, *Regridding of irregularly spaced seismic data*: M.Sc. thesis, Delft University of Technology, the Netherlands.

Bruin, C.G.M. de, 1992, *Linear AVO inversion by prestack depth migration: Imaging angle dependent reflectivity as a tool for litho-stratigraphic inversion*: Ph.D. thesis, Delft University of Technology, the Netherlands.

Claerbout, J.F., 1971,*Towards a unified theory of reflector mapping*: Geophysics, **36**, No. 3, 467-481.

Cox, H.L.H., 1991, *Estimation of macro velocity models by wave field extrapolation*: Ph.D. thesis, Delft University of Technology, the Netherlands

Fyfe, D.J. and Kelamis, P.G., 1992, *Removing coherent noise using linear Radon transformation*: 54th EAEG meeting, Paris, Expanded Abstracts, 550-551.

Gardner, G.H.F., and Lu, L., editors, 1991, *Slant-stack processing*: Geophysics Reprint Series, No. 14, SEG, Tulsa, USA.

Haas, J.C. de, 1992, *Elastic stratigraphic inversion, an integrated approach*: Ph.D. thesis, Delft University of Technology, the Netherlands.

Hale, D., 1991, *3-D depth migration via McClellan transformations*: Geophysics, **56**, 1778-1785.

Holberg, O., 1988, *Towards optimum one-way wave propagation*: Geophysical Prospecting, **36**, 99-114.

Hubral, P., 1984, *Simulating true amplitude reflections by stacking shot records*: Geophysics, **49**, 303-306.

Jeannot, J.P., Faye, J.P., and Denelle, E., 1986, *Prestack migration velocities from depth focussing analysis*: 56th SEG meeting, Houston, Expanded Abstracts, 438-440.

Kinneging, N.A., 1989, *Three-dimensional redatuming of seismic shot records*: Ph.D. thesis, Delft University of Technology, the Netherlands.

Koek, E.A., and Faber, G., 1992, *Seismic physical modelling facility at Delft University*: 54th EAEG meeting, Paris, Expanded Abstracts, B025, 128-129.

Koek, E.A., and Faber, G., 1995, *Measurement facility*: DELPHI annual report, Volume VI, Chapter 2.

Lörtzer, G.J.M., 1990, *An integrated approach to lithologic inversion*: Ph.D. thesis, Delft University of Technology, the Netherlands.

Rayleigh, J.M.S., 1896, *The theory of sound*, 2nd edition.

Rietveld, W.E.A., Berkhout, A.J. and Wapenaar, C.P.A., 1992, *Optimum seismic illumination of hydrocarbon reservoirs*: Geophysics, **57**, 1334-1345.

Rietveld, W.E.A.and Berkhout, A.J., 1994, *Prestack depth migration by means of controlled illumination*: Geophysics, **59**, 801-809.

Schultz, P.S. and Claerbout, J.F., 1978, *Velocity estimation and downward continuation by wavefront synthesis*: Geophysics, **43**, 691-714.

Stamnes, J.J., 1982, *Diffraction, Asymptotics and Catastrophics*: Optica Acta, **29**, no. 6, 823-842.

Taner, M.T., 1976, *Simplan: simulated plane-wave exploration*: 46th SEG meeting, Abstracts, 186-187.

Taner, M.T., 1978, *Simulated plane-wave seismic sections, an update*: 48th SEG meeting, Abstracts, 390.

Temme, P., 1984, *A comparison of common-midpoint, single-shot, and plane-wave depth migration*: Geophysics, **49**, 1896-1907.

Timmerman, J.I.H., 1993, *Removal of finite aperture artefacts in wavefield extrapolation and plane wave decomposition*: M.Sc. thesis, Delft University of Technology, the Netherlands

Verschuur, D.J., Berkhout, A.J. and Wapenaar, C.P.A., 1992, *Surface-related multiple elimination*: Geophysics, **57**, No. 8, 1166-1177.

Verschuur, D.J., 1990, *Multiple elimination*: DELPHI annual report, Volume I, Chapter 3, 55-112.

Versteeg, R. and Grau, G., 1991, *The Marmousi Experience*: Proceedings of the 1990 EAEG workshop on practical aspects of seismic data inversion, EAEG.

Wapenaar, C.P.A. and Berkhout, A.J., 1989, *Elastic wavefield extrapolation: Redatuming of single- and multicomponent seismic data*: Elsevier Science Publ. Co., Inc.

Wapenaar, C.P.A., 1992, *The finite aperture paradox*: J. Seis. Expl., **1**, no. 4, 325-336.

Wapenaar, C.P.A., 1993, *Representation of seismic reflection data; II New developments*: J. Seis. Expl., **2**, no. 3, 247-256.

Whitmore, N.D. and Garing, J.D., 1990, *Interval velocity estimation using iterative prestack depth migration in the constant angle domain*: Proceedings of the 1990 EAEG/SEG research workshop on the Estimation and practical use of seismic velocities, EAEG.

Summary

In this thesis a new approach to prestack depth migration is introduced. In this approach the full prestack migration process is replaced by the migration of a finite number of so-called *areal* shot records. By limiting the number of areal shot records the proposed method will be an efficient approach to prestack depth migration.

An areal shot record is the response of the subsurface due to a source wave field with lateral extend. Such an areal shot record can be constructed from the prestack seismic data using Huygens' principle. In general any type of areal source wave field can be constructed from the distribution of point sources, given by the acquisition geometry used in the seismic survey. The description of how to combine the point sources into the areal source wave field is called *the synthesis operator*.

Using the knowledge of the propagation properties of the subsurface, it is possible to construct from the surface point sources an areal source wave field, which will have a predefined shape, both in amplitude and phase, at a specific position in the subsurface. This technique is called *controlled illumination*. The knowledge of the subsurface used in controlled illumination is the *macro model*, which is also used for the depth migration process.

If a desired areal source wave field is defined along a macro boundary, the quality of this macro boundary can be verified by comparing the synthesis operator with the corresponding event in the synthesized areal shot record. If a focus point at a macro boundary is defined, it is possible to evaluate the depth and the velocity at this depth point. If a normal-incidence wave field is defined along a macro boundary, the lateral extend of the macro boundary can be evaluated.

Since the areal source wave field represents a physical wave field, it is possible to migrate the areal shot record with a modified conventional shot record migration scheme. The modification is that the source wave field is given by the synthesis operator, used for the construction of the areal shot record. This so-called *areal* shot record migration process is a generalization of the conventional shot record migration process. The migration can be described by two steps: first

the extrapolation of the wave fields into the subsurface and second the imaging of the reflectivity from the extrapolated wave fields. In the imaging part of the depth migration, the scaling of the depth image with the energy of the incident source wave field is of main importance. This holds for any type of migration. Since in the discussed method the control of the source wave field is put at the region of interest, the target zone, this scaling is simple and straight forward in this area.

An example on a complex synthetic data set (the Marmousi data set) shows that the target-oriented approach is favourable over the normal surface-oriented approach and gives a depth image comparable to a prestack depth image for only *five* areal shot record. The prestack data set consists of 240 shot records. By combining the depth images obtained by migration of the individual areal shot records, constructed for different illuminations, the quality of the depth image will be improved.

An example on a field data set shows similar results, but the number of areal shot records has to be increased to 25 to obtain an acceptable signal-to-noise ratio in the final depth image. An additional Fresnelzone filtering during the synthesis process, increases the signal-to-noise ratio considerably. The number of areal shot records can be decreased and the efficiency of the method is improved.

In conclusion it may be stated that the combination *controlled illumination - areal shot record migration* gives an efficient and accurate approach to prestack depth migration.

Samenvatting

Het gebruik van gecontroleerde belichting in seismische migratie

Het verkrijgen van een beeld van de ondergrond vanuit seismische metingen wordt *seismische migratie* genoemd. In dit proefschrift wordt een nieuwe methode geïntroduceerd voor seismische migratie. Bij deze nieuwe methode worden de seismische metingen gecombineerd tot zogenaamde *uitgebreide* golfveldresponsies. Door het aantal van deze samengestelde responsies klein te houden, ontstaat een efficiënte methode voor seismische migratie.

De seismische weergave van de ondergrond, veroorzaakt door de uitgebreide bron, wordt samengesteld uit de puntbronmetingen. Hierbij wordt gebruik gemaakt van het principe van Huygens. De beschrijving van de wijze waarop de puntbronnen moeten worden gecombineerd tot het uitgebreide bronveld wordt de *synthese-operator* genoemd.

Gebruik makend van de kennis van de *propagatie*-eigenschappen (globale informatie betreffende de snelheid en dichtheid) van de ondergrond is het mogelijk om een uitgebreid bronveld te construeren met een vooraf bepaalde structuur, zowel in amplitude als in looptijd, op een bepaalde positie in de ondergrond. Deze techniek wordt *gecontroleerde belichting* genoemd. De informatie over de propagatie-eigenschappen van de ondergrond, die gebruikt wordt bij gecontroleerde belichting en ook noodzakelijk is voor het uitvoeren van een seismische migratie, wordt het *macromodel* genoemd.

Indien het beoogde bronveld wordt gedefinieerd langs een laagovergang, dan kan deze in het macro-model geanalyseerd worden door de synthese-operator te vergelijken met de seismische reactie van deze overgang in de samengestelde uitgebreide golfveldresponsie. Als een focuspunt wordt bepaald op de laagovergang, kan de diepte en de snelheid boven dit punt worden geverifieerd. Indien een loodrecht invallend bronveld wordt gedefinieerd langs de hele laagovergang, dan kan de zijdelingse uitbreiding van de laagovergang worden vastgesteld.

Aangezien het geconstrueerde bronveld een fysisch experiment voorsteld, kan de gemeten reactie van de ondergrond op dit bronveld gemigreerd worden met behulp van een aangepast

conventioneel puntbronmetings-migratieschema. De toegepaste wijziging houdt in dat het bronveld wordt verschaft door de synthese-operator, die wordt gebruikt voor het samenstellen van de uitgebreide golfveldresponsie van de ondergrond. Dit gewijzigde schema kan worden gezien als een gegeneraliseerde conventionele puntbronmetingsmigratie. Migratie kan worden beschreven als een tweestaps-proces: het berekenen van de golfvelden als functie van de diepte met behulp van het macro-model èn het afbeelden van de reflectie-eigenschappen van de ondergrond. Tijdens de afbeeldingsstap is het belangrijk om de afbeelding op een bepaalde diepte te vergelijken met de energie van het lokaal invallende bronveld. Dit geldt overigens voor iedere migratieprocedure. Daar de besproken methode van de gecontroleerde belichting het invallende golfveld definieert in het doelgebied is deze vergelijking met bronveldenergie eenvoudig. Het is tevens mogelijk om met behulp van de gecontroleerde belichting hoekafhankelijke reflectiviteit af te beelden, die verder gebruikt kan worden voor het bepalen van de werkelijke mediumparameters in de ondergrond.

Een voorbeeld op een ingewikkeld gemodelleerde dataset laat zien dat de gecontroleerde belichting op een specifieke positie in de aarde een superieure afbeelding geeft van dit gebied in vergelijking met methoden waarbij de kennis van het macromodel niet wordt gebruikt tijdens de samenstelling van uitgebreide golfveldresponsies. Door gebruik te maken van slechts *vijf* doelgerichte uitgebreide golfveldresponsies is het mogelijk om een afbeelding te krijgen van de ondergrond vergelijkbaar met het resultaat dat door de migratie van alle 240 puntbron metingen in de totale dataset wordt bereikt. Door de afbeeldingen verkregen door de migratie van de verschillende uitgebreide golfveldresponsies te combineren, wordt de kwaliteit van de afbeelding verbeterd.

Een voorbeeld op seismische velddata laat vergelijkbare resultaten zien, hoewel het aantal uitgebreide golfveldresponsies toeneemt tot 25 om een acceptabele signaal-ruis verhouding in de afbeelding te krijgen. Indien een additionele Fresnelzone filtering tijdens de synthese wordt toegepast, verbetert de signaal-ruis verhouding aanzienlijk en kan het aantal uitgebreide schoten worden teruggebracht.

Concluderend kan worden gesteld dat de in dit proefschrift beschreven combinatie van gecontroleerde belichting en migratie van uitgebreide golfveldresponsies een efficiënte methode is om de ondergrond vanuit seismische metingen nauwkeurig af te beelden.

Curriculum Vitae

Naam	Rietveld, Walter Eduard Antonius
Geboortedatum	10 april 1963
Geboorteplaats	Rotterdam

OPLEIDING

1969 - 1975	Basis onderwijs te Rotterdam
1975-1981	Gymnasium-ß aan de RKSG Sint-Montfort te Rotterdam
1981-1988	Technische Natuurkunde aan de Technische Universiteit Delft (oude stijl)

4e-jaars werk: "Akoestische bepaling van stroomsnelheden: evaluatie frequentieschatten"
5e-jaars werk: "Full elastic modeling for non-destructive evaluation: a finite difference approach", beide uitgevoerd voor de Technisch Physische Dienst, TNO-TPD te Delft.

WERKERVARING

1985-1988	Student medewerker bij TNO-TPD, Delft.
1988-1994	Toegevoegd onderzoeker aan de Technische Universiteit Delft.